SPECTROSCOPIC CHARACTERIZATION OF NONLINEAR OPTICAL AND BIOPHOTONIC MATERIALS

A Dissertation
Presented to
The Academic Faculty

by

Taylor Gray Allen

In Partial Fulfillment
of the Requirements for the Degree
Doctorate of Philosophy in the
School of Chemistry and Biochemistry

Georgia Institute of Technology
December 2018

SPECTROSCOPIC CHARACTERIZATION OF NONLINEAR OPTICAL AND BIOPHOTONIC MATERIALS

Approved by:

Dr. Joseph W. Perry, Advisor
School of Chemistry and Biochemistry
Georgia Institute of Technology

Dr. Seth R. Marder, Co-Advisor
School of Chemistry and Biochemistry
Georgia Institute of Technology

Dr. John R. Reynolds
School of Chemistry and Biochemistry
Georgia Institute of Technology

Dr. Robert M. Dickson
School of Chemistry and Biochemistry
Georgia Institute of Technology

Dr. Ali Adibi
School of Electrical and Computer Engineering
Georgia Institute of Technology

Dr. Carlos Silva
School of Chemistry and Biochemistry
Georgia Institute of Technology

Date Approved: September 24, 2018

To my wife and parents.

ACKNOWLEDGEMENTS

To begin my acknowledgements, I would like to thank my advisor Prof. Joseph Perry for giving me the opportunity to take the next step in my scientific career and for his teachings and encouragement over the past 5 years. I would also like to thank my co-advisor Prof. Seth Marder for his guidance as a mentor and rigorousness as a collaborator and the rest of my thesis committee members, Prof. John Reynolds, Prof. Robert Dickson, Prof. Carlos Silva, and Prof. Ali Adibi, for their helpful critiques and support of my research endeavors at Georgia Tech.

I have been fortunate to have excellent mentors within the Perry lab, for which I would like to express immense gratitude to Dr. San-Hui "Sarah" Chi, Dr. Vincent Chen, Dr. Mohanalingam Kathaperumal, and Dr. Joel Hales, for their technical mentorship and friendship. I would also like to thank Lucas Johnstone, John Tillotson, Yohan "Johnny" Park and former Perry Lab members Dr. Hyeongeu "Anselmo" Kim, Dr. Yunsang Kim, and Dr. Ariel Marshall for their support, helpfulness as teammates, and friendship.

From extensive collaborations with the Marder lab, I would like to thank Dr. Stephen Barlow, Dr. Iryna Daydenko, Dr. Yulia Getmanenko, Dr. Junxiang Zhang, and Janos Simon for their research efforts, interesting scientific discussions, and putting in many hours writing manuscripts. Likewise, I thank Dr. Canek Fuentes from Prof. Bernard Kippelen's lab for many helpful discussions, research advice, and use of equipment. I would also like to thank Joseph Richardson, Aida Demissie, Dr. Blake Fleichser, Baijie Peng, and MD Islam from the Dickson group and Kevin Benham and Dr. Brant Jones from the Orlando group for always being helpful and generously lending equipment and advice.

TABLE OF CONTENTS

LIST OF TABLES

LIST OF FIGURES

LIST OF SYMBOLS AND ABBREVIATIONS

NLO	Nonlinear optics
AOSP	All-optical signal processing
NIR	Near-infrared
1PA	One-photon absorption
2PA	Two-photon absorption
FOM(s)	Figure(s) of merit
FWHM	Full width at half maximum
λ	Wavelength
N	Number density
N_A	Avogadro's number
APC	Bisphenol A polycarbonate
PS	Polystyrene
PVC	Polyvinylchloride
BPM	Beam propagation method
PA	Poisson-Arago
GM	Göppert-Mayer unit
OL	Optical limiting
δ	Two-photon absorption cross section
F	Photon flux
SOH	Silicon-organic hybrid
TDM	Transition dipole moment
^{t}Bu	tert-butyl
^{n}Bu	n-butyl
Ad	Adamantyl
Ad'	Dimethyladamantyl
D	Debye
eV	Electronvolt

SUMMARY

In this dissertation, three studies were presented that involve the spectroscopic characterization of either nonlinear optical or biophotonic materials. The first study (Chapter 3) proposed judicious bulky substitution of cyanine-like, polymethine dyes with large intensity dependent refractive indices to effectively mitigate aggregation between dyes in thin film polymer blends of interest for all-optical signal processing applications in the near infrared (NIR). Linear characterization and Z-scan measurements of these blends at 1550 nm confirmed that bulky groups suppress aggregation in the solid state, thus lowering two-photon absorption (2PA) and improving the nonlinear optical performance of these films. The second study (Chapter 4) proposed a series of planar, fused-ring, organic, quadrupolar chromophores of type A-π-D-π-A with the potential to demonstrate large 2PA cross-sections for optical limiting applications in the NIR. Nondegenerate 2PA measurements revealed that these compounds have large 2PA cross sections and spectral coverage in the NIR, which can be controlled synthetically via structural changes in the core and acceptor groups at the molecule's periphery. The third study (Chapters 5-6) proposed high refractive index replicas of photonic crystal-like hole patterns harvested from *Coscinodiscus wailessii* diatom frustules as sustainably-producable, biophotonic elements for lensless light focusing of NIR radiation at the micro-scale. Linear spectrophotometric and imaging measurements confirmed that these replicas concentrate NIR light via diffraction, which can be manipulated with changes in the index of the frustule through solid-gas conversion chemistries with excellent shape preservation.

CHAPTER 1. INTRODUCTION

1.1 Organic Materials for All-Optical Signal Processing

1.1.1 *Current and Future Data Transmission Demands in Telecommunications*

The proliferation of streaming services, social media, telemedicine, and large data sharing platforms are a few examples of many contributing factors to the continuously increasing global data transmission demands. [1-4] In a 2017 forecast by Cisco [5], the annual global internet protocol (IP) traffic in 2016 was 1.2 ZB/year (ZB = 10^{21} bytes) and is estimated to reach 3.3 ZB/year by 2021. If accurate, this means that by 2021 global internet traffic will be 127 times the volume of the entire global internet from 2005. In terms of data usage on the consumer level, this forecast estimates internet traffic to reach 30 GB per capita by 2021, increasing threefold from 10 GB per capita in 2016. Additionally, internet traffic access by smart phones and/or tablets is has been dramatically increasing. For example, in the last five years, YouTube saw double the number of viewing hours accessed via smart phones, increasing from 25% in 2013 to 50% of total usage in 2018. [6] By 2021, wireless device traffic, which includes smart phones and tablets, is expected to exceed personal computer (PC) traffic and is estimated to account for 63% of total IP traffic. [5] Although the purpose of this introduction is not to present an extensive overview of the forecasting for global internet demands, the information provided here highlights the necessity for faster, inexpensive, reliable, and low energy consumption telecommunications technology that can keep pace with the globally soaring demands for data transmission. In the following sections, the challenges facing traditional methods of optical signal transmission and processing methods will be discussed, as well as the

potential for hybrid devices made from silicon and organic nonlinear optical (NLO) materials in this field.

1.1.2 *Challenges Facing Traditional Optical Signal Transmission Technologies and the Potential of Organic, Third-Order NLO Materials for All-Optical Signal Processing (AOSP) Applications*

Although advances in optical fiber technology and implementation have provided high rates of data transmission (ca. 10^6-10^9 bits/s) on a commercial and consumer basis, the speed and energy efficiency of networks based on these technologies are inherently limited due to the use of electronic components to process and/or relay signals. [1, 3, 4] In many cases, the signal of interest is switched between the optical and electronic domain, which makes the signal subject to latencies associated with the rise time of these electronic components. This has implications when considering other parameters such as device miniaturization and energy consumption, where devices comprised of optical and electronic components physically require more space for operation and can potentially require multiple power supplies and drivers, each of which is associated with its own set of dissipative heat losses that can decrease the overall device efficiency. [7, 8] Further, the rapid growth of various fields related to data science applications and interest in real-time data analysis from potentially remote locations present an increasingly large challenge for signal processing since, eventually, these optical signals must be read by a computer, which requires optoelectronic transduction and highlights the importance of on-chip or chip-to-chip signal processing. [4, 7, 9]

All-optical signal processing (AOSP) methods have been proposed as an attractive technology space to achieve high-speed data transmission with low-energy consumption, in which the latencies associated with electronic transducers are avoided and one can utilize the wealth of optical phenomena such as amplitude, phase, polarization, and/or wavelength modulation to encode information. [1, 9, 10] In this dissertation, alternative technologies such as photonic elements for on-chip and chip-to-chip AOSP are of interest, which build on the mature crystalline silicon processing technology that exists for wafer production, but also presents many advantages in the design of silicon photonic components. [11-14] Compared to optical fibers historically used for AOSP applications that are typically made from silica or doped with expensive rare-earth materials whose relatively large (typically micrometer-scale) core-cladding structure only gives small-to-moderate refractive index differences, silicon waveguides present a high index, IR transparent material that enables the design of large volumes of high-quality photonic elements with the ability to control optical beams down the nanoscale and is thus of great interest for optical signal processing in the telecommunications window (ca. 1300-1600 nm). [9, 13, 15-17]

As such, silicon has found success in passive linear devices, such as waveguides [12, 13] and sensors [18, 19], but has encountered difficulties as an active component like phase-based switches. [20, 21] For example, although wavelength converting waveguides making use of third-order nonlinearities (see section 2.2) in silicon have achieved switching speeds up to 40 Gbit/s, these devices are impeded by deleterious two-photon absorption (2PA) and 2PA-induced free carrier absorption that results in significant optical losses and limits the switching speed. [22, 23] Considering these limitations, so-called silicon-organic hybrid (SOH) devices have been proposed to circumvent these issues by combining the

3

high field intensities and excellent waveguiding at the nanoscale that silicon affords with the large third-order NLO responses of π-conjugated organic materials to achieve efficient phase modulation with significantly reduced losses associated with one-photon (1PA) and/or 2PA. [23-26]
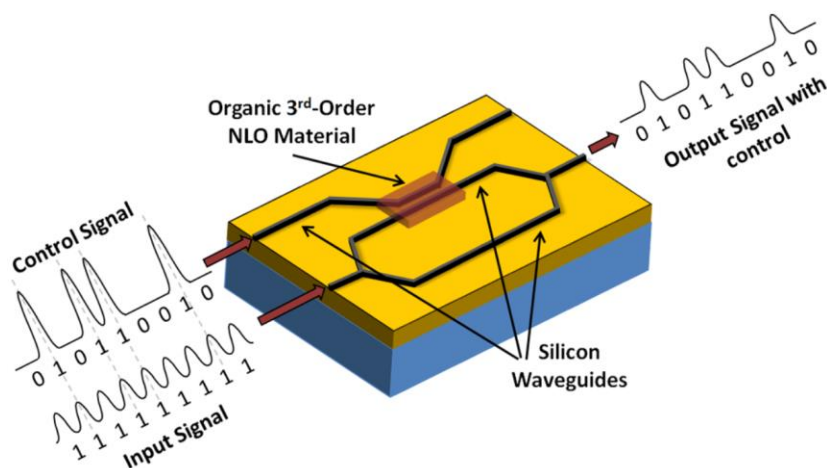
Figure 1.1. Illustration of temporal demultiplexing via all-optical switching in a SOH nonlinear Mach-Zehnder interferometer with silicon waveguides. Reproduced from Hales *et al*. [25] with permission. Copyright 2014 American Chemical Society.

An example of such a device can be found in Figure 1.1, which depicts a Mach-Zehnder interferometer operating via cross-phase modulation. This device aims to all-optically modulate the amplitude of a low intensity signal beam by controlling the change in phase experienced by the signal upon interaction with the organic, NLO cladding material such that the interference with the unimpeded beam from the non-cladded arm will result in controlled constructive or destructive interference at the output. [27] This is hypothetically accomplished using an ultrafast (ca. 100 fs), intense laser pulse to induce intensity-dependent changes in the refractive index (n_2, section 2.2.1) within the organic NLO cladding, where the magnitude of this change depends on the chemical and electronic properties of the cladding material itself. Further, the magnitude of n_2 will determine device

length/size and the operational intensity threshold, which can be rationalized by considering the relation between the change in phase ($\Delta\varphi$) and n_2 expressed as [28]

$$\Delta\varphi = \frac{2\pi}{\lambda} \, n_2 \, I \, D \qquad\qquad (1.1)$$

where D is the path length through the nonlinear medium, I is the control beam intensity driving the nonlinearity, and λ is wavelength of the control beam. From equation 1.1, one can see that large values of n_2 allow for shorter devices, because a large $\Delta\varphi$ can still be achieved over a short distance (D), and the beam intensity needed to obtain an appreciable $\Delta\varphi$ is significantly lower, thus reducing the energy consumption of the device.

Proof-of-concept, all-optical, SOH devices have demonstrated switching at rates of ca. 170 Gbit/s using vapor- and solution-deposited organic NLO chromophores with sizeable nonlinearities, reasonable linear loss (ca. 1 dB cm^{-1}), and minimal 2PA. [9, 23, 26] However, the ability to synthetically tune the optoelectronic properties of these compound is limited, and thus presents room for advancement in terms of material properties that could yield substantial improvements in SOH devices and the realization of terahertz (THz $= 10^{12}$ Hz) AOSP methods that requires dramatically smaller input energies (femtojoule, fJ $= 10^{-15}$ J). Recent studies involving polymethines have shown that these materials demonstrate large values of n_2 and low 2PA that are likely suitable for integration in SOH and have the potential to enable the fabrication of such devices. [25, 29, 30] Therefore, elucidating structure-property relationships that govern the NLO properties of polymethine materials is of interest in this dissertation. The following section will discuss the molecular origins for the NLO response of polymethines and metrics necessary for AOSP.

1.1.3 *Material Metrics for AOSP and Third-Order Nonlinearities of Polymethines*

Practical and scientific interest in polymethine materials stems from a large body of work in the field of π-conjugated organic molecules and polymers that possess highly delocalized electrons and thus have large, ultrafast third-order nonlinearities. [27, 31, 32] As discussed in the previous sections, and in more detail in sections 2.1-2.2, these electronic properties are attractive for phase-based switching because they can afford large nonlinear refractive indices (n_2) and moderate-to-low 2PA that are related to the complex, macroscopic third-order susceptibility ($\chi^{(3)}$) by [28]

$$n_2 = \frac{3}{4\,\varepsilon_0\,n_0{}^2\,c}\,Re(\chi^{(3)}) \tag{1.2}$$

$$\beta = \frac{3\omega}{2\,\varepsilon_0\,n_0{}^2\,c^2}\,Im(\chi^{(3)}) \tag{1.3}$$

where n_0 is the linear refractive index, ε_0 is the permittivity of free space in vacuum, c is the speed of light, ω is angular frequency, and β is the two-photon absorption coefficient. The synthetic tunability of organic materials provides a distinct advantage over the well-studied inorganic semiconductors in that the nonlinearities can be optimized by selective structural changes. [30, 33-40] These efforts were largely focused on achieving increasingly large n_2 ($Re(\chi^{(3)})$) values and minimizing 2PA (i.e. β, $Im(\chi^{(3)})$) to meet or surpass the two-photon figure of merit (2PA-FOM) [41]

$$\left| \frac{Re(\chi^{(3)})}{Im(\chi^{(3)})} \right| \geq 12 \qquad (1.4)$$

that is required for the realization of an all-optical switch utilizing organics as the active $\chi^{(3)}$ material.

Indeed, numerous studies have shown that discrete and polymeric organic systems, such as phthalocyanines [42], porphyrins [43], polydiacetylenes [44], and polyanilines [45], demonstrated values of n_2 that could surpass that of silicon, however, their utility as AOSP materials was largely limited due to concomitant increase in 2PA, which did not satisfy the 2PA-FOMs. Further, one must also consider the processability of the material for device integration. For example, although poly(hexa-2,4-diyne-1,6-diyl bis(para-toluenesulfonate)) demonstrated a sizeable n_2 and reasonable 2PA-FOMs at 1600 nm as a single-crystalline polymer, the difficulty in fabricating devices related to its crystallinity ultimately limited its applicability for AOSP. [46]

In this regard, polymethines present a unique material space with a wealth of synthetic chemistries available to cooperatively optimize NLO performance and enhance processability by tuning chemical properties like thermal and photostability, solubility, and crystallinity. [25, 29, 37, 39, 47-50] Polymethines are a class of linear, π-conjugated, organic chromophores with an odd number of methine groups (=CH–) in their chain and are analogous to polyenes but are ultimately defined by their resonance structures that determine the magnitude of their third-order polarizabilities (γ), which are proportional to $\chi^{(3)}$ (see section 2.1.1, equation 2.7 for details). [38, 48] Originally described by Dähne in 1971 [51], these resonance structures can be divided into two classes: an asymmetrically-

substituted chain with an electron donating group on one end and acceptor on the other, and a charged, symmetrically-substituted chain with either donor (D) or acceptor (A) groups (Figure 1.2). [49] In the asymmetric case, the donor and/or acceptor strength can be tuned to yield one of three resonance forms (A1-3) where A1 describes the neutral polyene-like structure with large, positive bond length alternation (BLA [52], also closely related to bond order alternation, BOA [38, 53]), A2 represents the merocyanine structure with BLA approaching zero, and A3 is the zwitterionic, polyene-like structure with large, negative BLA. The impact these resonance forms have on the linear absorption spectra of such molecules is well-documented where, for example, one can switch between positive (A1) to negative solvatochromism (A2) by increasing the D and A strength of the end groups to facilitate charge separation. [49, 54-57] Additionally, the NLO properties as a function of D-A strength have been extensively investigated, primarily for second-order NLO applications. [58-60]
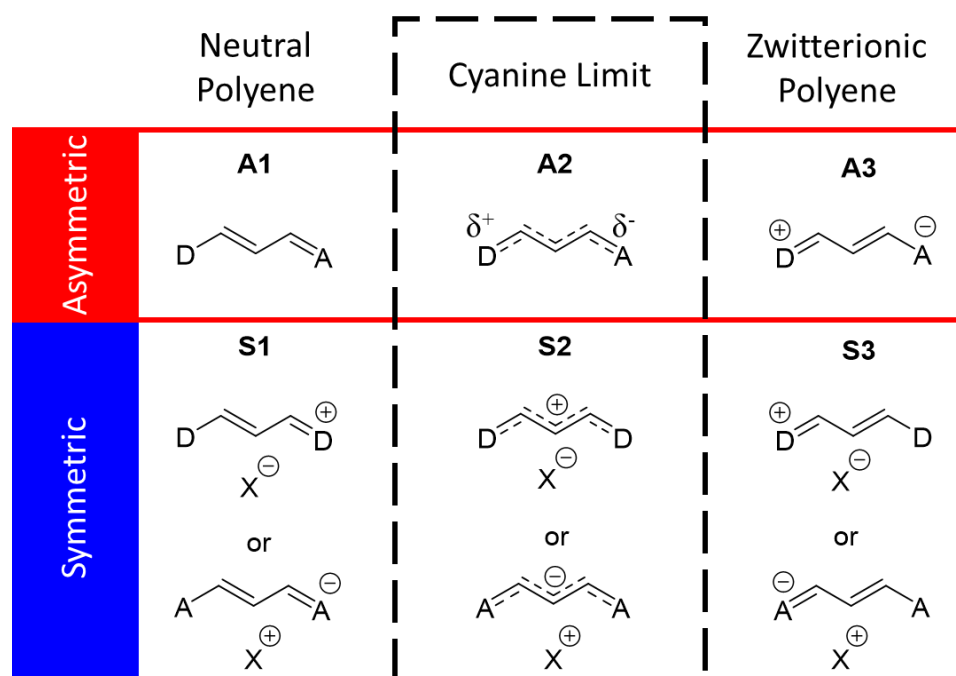
Figure 1.2. Chemical structures for the possible resonance forms of a polyenes and polymethines with three carbon chains.

The symmetric series is of greatest interest for third-order NLO and thus this dissertation due to the so-called cyanine state (S2, Figure 1.2) that can be achieved. This cyanine-like structure is described by negligible BLA (near zero) that maximizes the delocalization of electrons over the chain and results in red-shifted 1PA and large transition dipole moments (TDMs). The other two forms (S1 and S3), where charge is localized on either end of the molecule, are analogous to A1 and A3 with appreciable BLA and broad, charge transfer-like 1PA spectra. [27, 37] S1 and S3 are thought to occur by Peierls-type symmetry breaking, the origins and consequences of which are discussed in section 3.1 and references [49, 61].
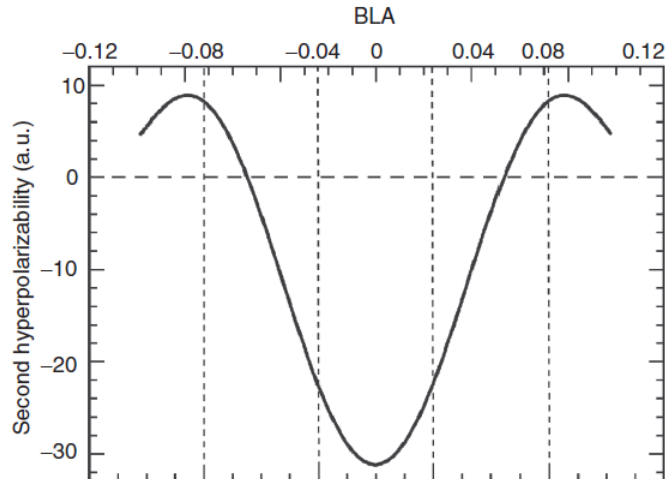
Figure 1.3. Evolution of the second hyperpolarizability (γ) as a function of BLA. Adapted from Hales and Perry [27] with permission. Copyright 2008 CRC Press.

The profound impact of reaching the cyanine limit on the third-order NLO properties of polymethines is plotted in terms of BLA in Figure 1.3, which shows that magnitude of γ reaches a maximum, albeit negative, at the cyanine limit and only smaller positive value can be obtained for unsubstituted and D-A polyene resonance forms. This phenomenon is well described by the sum-over-states (SOS) expressions, which were derived from perturbation theory and describe the linear and nonlinear polarizabilities in terms of the transitions between ground and excited states. [62] To make the interpretation of the SOS expression more tractable, it is typically truncated to only include terms with the strongest resonant denominators and most relevant excited states. [63-68] In the case where the ground state ($|g\rangle$) is coupled strongly with the first excited state ($|e\rangle$) and $|e\rangle$ is itself strongly coupled to a small number of excited states (represented by $|e'\rangle$) the following simplified SOS expression is obtained: [38]

10

$$\gamma = 24\frac{M_{ge}^2\Delta\mu^2}{E_{ge}^3} - 24\frac{M_{ge}^4}{E_{ge}^3} + 24\sum_{e'}\frac{M_{ge}^2 M_{ee'}^2}{E_{ge}^2 E_{ge'}} \qquad (1.5)$$

In this equation, the section in black text is the "D" (dipolar) term, which is negligible for polymethines at the cyanine limit since $\Delta\mu\to0$, the red section is the "N" (negative" term and is the dominant contribution to γ given the 4th and 3rd power-dependence of the TDM for the g$\to$e transition (M_{ge}) and energy gap between g and e (E_{ge}), for which cyanines give large and small values, respectively, and the blue term is the "T" (two-photon) term, which contributes less to the overall value of γ than the "N" term due to quadratic dependence on M_{ge} and E_{ge} and the relatively smaller contributions from transitions to higher-lying excited states ($M_{ee'}$) and large energy gap between g and e' ($E_{ge'}$). Further discussion is provided in references [25, 27, 38].

By pumping with frequencies with small detuning energies from real excited states, cyanine-like polymethines can also benefit substantially from resonance enhancement to yield large values of n_2 and 2PA-FOM in solution that are more than suitable for AOSP. Additionally, a wealth of synthetic modifications are available to tailor the chemical and optical properties of these materials, which affords significant processing flexibility for AOSP and is of significant interest for this thesis. [25] However, as will be discussed in Chapter 3, the largest challenge facing these dyes is the translation of excellent solution nonlinearities into high number density solid films that are needed for AOSP, which is hampered by aggregation effects due to strong dispersion forces between dyes that alter the electronic properties in the solid-state and typically result in greater 2PA, thus lowering the 2PA-FOMs to undesirable levels.

1.2 Optical Limiting

1.2.1 *Past and Present Methods and Materials for Optical Limiting*

The ubiquity and continued growth of lasers in research laboratories calls for appropriate optical limiting (OL) controls that, among other applications, serve to protect sensors and users from bodily harm [69-71], reduce noise [72], and shape pulses [73]. To be considered suitable, OL materials should have high linear transmission, low-turn on threshold, high damage threshold, and large pulse energy suppression over a broad spectral and temporal range. [74] To achieve this, various third-order NLO processes have been implemented, the earliest of which was based on three-photon absorption in semiconductors that was carried out not long after the laser was invented. [75, 76] Some time after these initial experiments, organic OL materials proliferated and have made use of thermal lensing [77], effective $\chi^{(3)}$ processes like reverse saturable absorption [78-80], and charge transfer processes [81]. Although these studies presented significant advances in the field, these OL approaches were largely hampered by poor linear transmission due to 1PA, which prompted the work by Perry and Marder et al. [82-85] and others [72, 86] who utilized 2PA to gain linear transparency while maintaining opacity at higher irradiances. Further, Hales *et al*. [87] and Chi *et al*. [88] have shown that favorable overlap between 2PA and excited state absorption bands in conjugated polymers and related blends can be utilized for effective OL over a broad spectral range in the NIR and over large range of timescales.

Due to the extensive use of NIR lasers (ca. $\lambda = 750\text{-}1600$ nm) in photonics and telecommunications, this dissertation is concerned with OL materials whose 2PA response

12

can be tuned in this spectral range. Although various NIR-absorbing, multicomponent systems have been proposed that were comprised of nanoparticles [89, 90], quantum dots [91], organic-inorganic hybrids [92], and low-dimensional carbon materials [93]; single component organic systems with large 2PA cross sections in the NIR and excellent film processability offer many advantages in terms of cost, toxicity, synthetic tunability, and device fabrication flexibility. [94] In the following section, the potential for small-molecule, π-conjugated, quadrupolar, organic OL materials for these materials is examined.

1.2.2 *Discrete, Quadrupolar, Organic Molecules with Large 2PA*

The degree to which intensity of an optical beam is attenuated by a purely 2PA OL material by can expressed by [28]

$$\frac{\partial I}{\partial z} = -N \, \delta \, F \, I \tag{1.6}$$

where I is intensity, z is the propagation distance in the OL medium, N is the number density, F is the photon flux ($F = I/h\omega$ in units of photons s^{-1} cm^{-2}), and δ is the molecular 2PA absorption cross-section in units of Göppert-Mayer (1 GM = 10^{-50} cm^4 s $photons^{-1}$). [95] From this equation, one can see that a straightforward approach to maximizing OL performance is to incorporate molecules with large values of δ in high N films. In this regard, small-molecule, organic NLO chromophores and the wealth of synthetic chemistries available to tune their chemical and optical properties afford significant advantages in terms of the ability to customize a material's response at certain wavelengths and processability for device purposes. [96-99]

The magnitude of δ is related to the third-order polarizability (γ) by [100]

$$\delta = \frac{16\pi^3 h v^2}{n^2 c^2} L^4 Im\langle\gamma\rangle \tag{1.7}$$

where h is Planck's constant, v is frequency, n is the linear refractive index, c is the speed of light in vacuum, L is the Lorentz local field factor (see section 2.1.1), and the brackets in Im$\langle\gamma\rangle$ signifies an orientational average from an assumed isotropic distribution of molecular transition dipole moments (TDMs). Particularly for discrete organic dyes, the molecular origin of δ has been well described by the sum-over-states model [62, 101] which, for a transition from the ground state (g) to a 2PA-allowed excited state (e') excited by plane polarized light, can be written as (see references [100-102] for further discussion and definitions of certain variables)

$$\delta = \frac{2\pi h v^2 L^4}{\varepsilon_0^2 n^2 c^2 \Gamma_{ge'}} S_{ge'} \tag{1.8}$$

where:

$$S_{ge'} = \left[\sum_e \frac{\langle M_{ge} M_{ee'}\rangle}{(E_{ge} - hv)}\right]^2 \tag{1.9}$$

Focusing on $S_{ge'}$, this formula gives a squared sum comprised of the photon energy (hv), the energy difference (E_{ge}) between the ground (g) and first excited state (e), the TDM between the ground and first excited state (M_{ge}), and the TDM between the first excited state and the second ($M_{ee'}$). After some simplifications, $S_{ge'}$ can be expressed by [101]

14

$$S_{ge\prime} = \frac{1}{5}\left[\left(\frac{\Delta M_{ge\prime} M_{ge\prime}}{h\nu}\right)^2 + \sum_{e \neq g,e\prime}\left(\frac{M_{ge}^2 M_{ee\prime}^2}{(E_{ge} - h\nu)^2}\right)\right] \tag{1.10}$$

where the factor of 1/5 accounts for the reduction in the number of dimensions (now 1D) based on the orientational average, and the expression can be broken down into the "D" (dipolar, black) and "T" (two-photon, red) terms (not to be confused with the "D" and "T" from section 1.1.3). [65, 101] The "D" term is a function of the change in static dipole moment between the g and e' states ($\Delta M_{ge\prime}$), which is zero for the centrosymmetric quadrupolar chromophores of interest in this thesis and thus allows δ to be expressed as

$$\delta \propto \frac{M_{ge}^2 M_{ee\prime}^2}{(E_{ge} - h\nu)^2 \Gamma_{ge\prime}} = \frac{M_{ge}^2 M_{ee\prime}^2}{\Delta^2 \Gamma_{ge\prime}} \tag{1.11}$$

and is now described by a simplified model accounting for the contributions from only three essential states (g, e, e') to the 2PA response. [65, 66] In this equation, $\Gamma_{ge\prime}$ is the full-width at half maximum (FWHM) of the 2PA band and Δ is the detuning energy between the incident photon of frequency (ν) and the energy gap (E_{ge}) between states g and e ($\Delta \equiv E_{ge} - h\nu$), as depicted in Figure 1.4a.
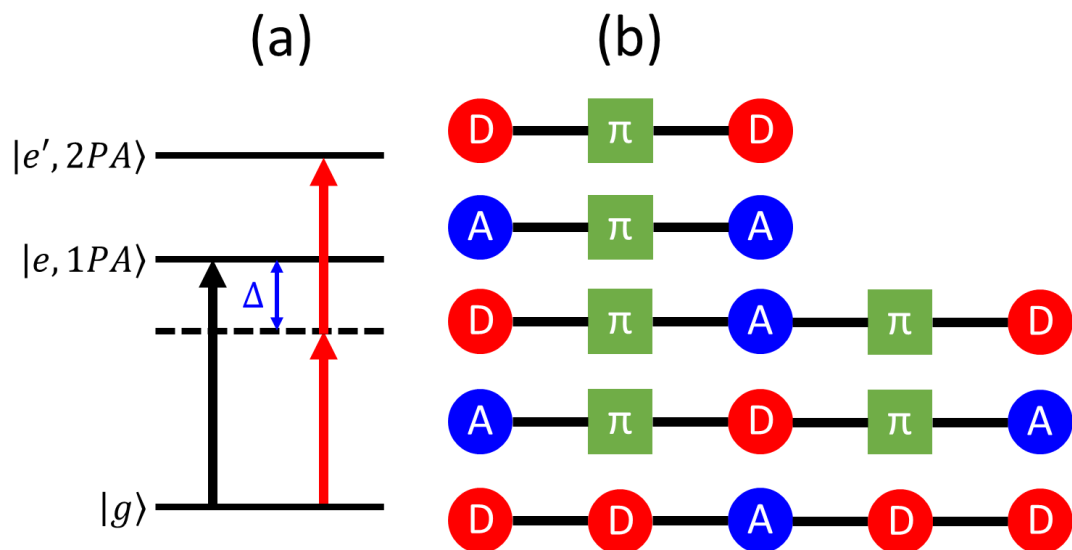
Figure 1.4. (a) Jablonski diagram showing one- (black arrow) and two-photon(red arrows) transitions for a quadrupolar molecule, where Δ is the detuning energy; (b) General structures for quadrupolar dyes showing arrangement of electron donating groups (D), accepting groups (A), and conjugated chains/linkers (π).

Equation 1.11 can be used to inform the design of quadrupolar chromophores with strong 2PA, which typically involves striking a balance between large transfer upon excitation (i.e. large values of M_{ge} and $M_{ee'}$), pumping close to 1PA resonances without being on-resonance (small Δ), and having narrow 2PA bands (small $\Gamma_{ge'}$). As such, a variety of quadrupolar structures (Figure 1.4b) have been studied to elucidate synthetic modifications that can selectively alter the optical properties of these dyes. In a simple example, 2PA responses for D-π-D compounds have been shown to increase with longer chain lengths (π) and stronger D groups, which increase charge transfer from the periphery of the molecule to the center upon excitation. [83, 85] Similar principles have been extended to more complex compounds, like D-π-A-π-D, where combination of alterations in D/A strength and the nature of the π-linkers between D and A groups can be used to

achieve red-shifted 1PA and 2PA bands and obtain large values of Δ due to enhanced charge transfer from the D end groups to the A core. [101, 103-105]

As will be discussed in Chapter 4, the wealth of structural sites with which 2PA behavior can be tuned for A-π-D-π-A chromophores presents a unique opportunity to achieve materials with strong 2PA in the NIR as well as enhance other application-relevant properties like photostability. A structure-property investigation is provided with a focus on how the molecular design for a novel series of organic, fused-ring, quadrupolar compounds influences their 2PA behavior.

1.3   Biophotonic Light Manipulation

1.3.1   *Photonic Elements for Light Concentration and Harvesting*

The ability to control light at small scales (micro-to-nanometers) has been highly desired for various fields, including: photonics [106], imaging [107], biofuels [108], and photovoltaics [109]. As the first example, rapid growth in the solar energy industry in recent years continues to drive the demand for efficient solar panels and farms. [110] In addition to large scale concentrators and collectors, microphotonic elements such as waveguides, microlens arrays, and thin reflectors of similar size to individual cells have been extensively investigated to achieve greater efficiencies. [111-113] Although some advances have been made in this area, the design and fabrication of these microdevices can be expensive and/or difficult to manufacture due to the large number of steps involved and requirement for impeccable reproducibility. [109, 114] In a second example, significant progress has been made in the last 5-7 years in the field of thin film metalenses for which achromatic, sub-diffraction limited focusing has been achieved with carefully-crafted,

17

periodic metastructures. [107, 115, 116] Despite substantial advancements in efficiency, numerical aperture, and field intensities of interest for micro-spectroscopy, even small imperfections can cause poor performance, which is why these metalenses typically require costly, low-throughput, high-precision lithography and atom layer deposition techniques for successful fabrication over a small area. [117, 118]

The above examples highlight a common trade-off in microphotonic elements between performance and manufacturability, which has inspired advances in large area printing and roll-to-roll processing technologies to circumvent these issues, although challenges still exist regarding the reproducibility and precision of fabricating nanoscale features. [119-122] However, an alternative strategy is to use biologically-derived photonic features to achieve high-volume production of microphotonic elements while implementing a sustainable, environmentally-friendly manufacturing model. This concept is similar to the argument made for biofuels production where, to meet 50% of American transport fuel needs, one would need more than 100% of existing American farmland using traditional methods of biodiesel production made from corn, soybean or canola, compared to only 1-3% of existing cropland for microalgae-based photobioreactors. [108, 123] Therefore, farming biophotonic materials could dramatically reduce manufacturing costs that would normally be associated with high-precision lithography, printing, stamping, and characterization equipment and still produce scalable product based on collectable biomass on the kilogram-scale.

The biggest challenge facing this approach is the selection of an appropriate microorganism that demonstrates interesting optical behavior as well as the ability to be harvested with high reproducibility and on large scales. As will be discussed in the

following section, biosilica frustules from marine diatoms possessing photonic crystal-like hole patterns have the potential to satisfy these requirements.

1.3.2 *Potential for Diatoms as Biogenic, Lensless Light Concentrators*

Diatoms are eukaryotic, unicellular microalgae that encase themselves in natural biosilica structures, which are thought to form during the cell wall synthesis stage of their growth due to a catalysed polymerization to form silica using the silicic acid taken up from its environment. [124] For some species, like *Coscinodiscus wailessii* (*C. wailessii*), *C. asteromphalus*, and *Arachnodiscus*, these silica features are described as having two valves (also called frustules) that are held together by a girdle band (see section 5.1.1 for more details). [124-126] If the valves are isolated from the rest of the structure, a photonic crystal-like hole pattern can be found on the surface of each frustule (Figure 1.5a). In an initial study, De Stefano *et al.* [127] observed a focusing-like effect (Figure 1.5b) from individual *C. wailessi* valves and attributed this observation to a complex superposition of diffracted wavelets primarily originating from the hole pattern on the valve surface. Similar results were shown by De Tomassi *et al.* [128] (*C. wailessii*) and Romann *et al.* [129] (*C. wailessii* and *C. centralis*) and were able to be predicted semi-quantitatively by beam propagation simulations and the Rayleigh-Sommerfield diffraction model. Collectively, these observations showed that diatoms have potential as a lensless focusing element, which could can be grown at rates of 5-25 g m^{-2} day^{-1}. [130]
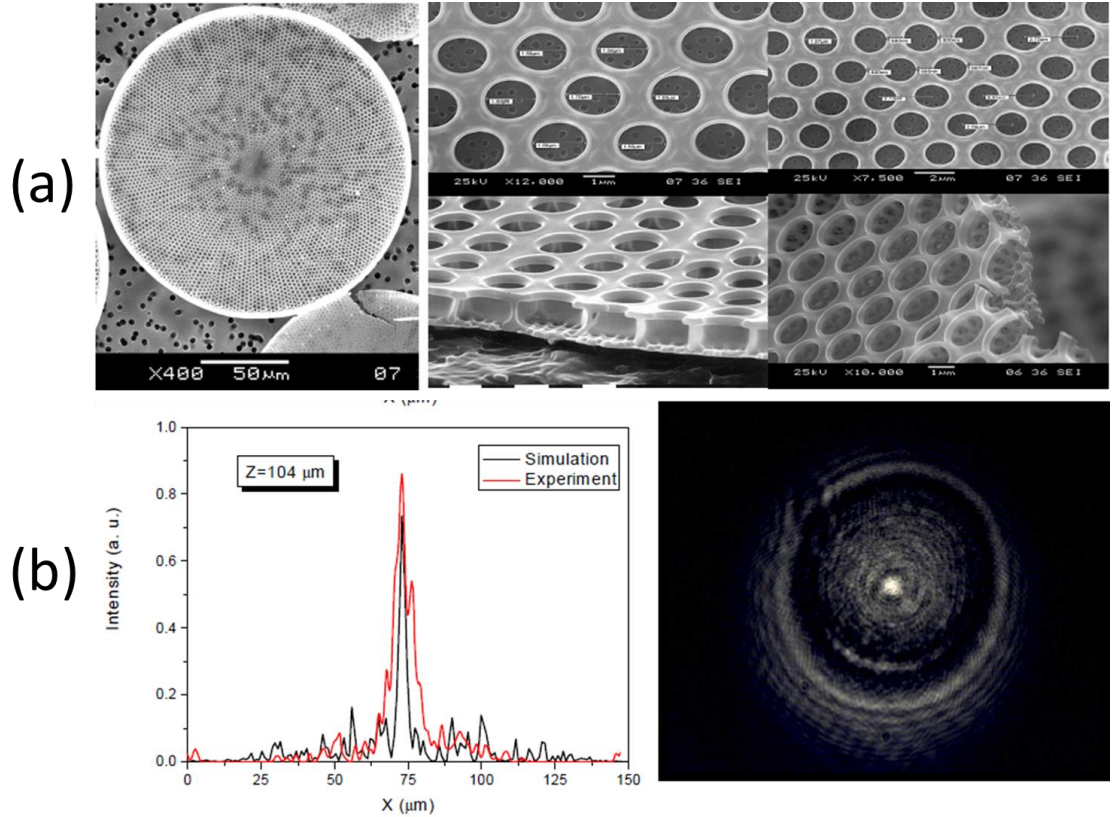
Figure 1.5. (a) Series of SEM images showing overall shape and hole pattern of a *C. wailessii* biosilica valve, (b) Optical micrograph of a focal spot from a *C. wailessii* valve (left) and a plot of the measured intensity profile compared to simulation (right). Adpated from De Stefano *et al*. [127] with permission. Copyright 2007 Optics Express.

However, because these frustules are made of silica, the light-matter interactions will only be appreciable at visible wavelengths, which limits their utility in the NIR (ca. 700-2000 nm). Due to the importance of this spectral region in photovoltaics as well as other photonic applications, the ability to tune the spectral response of these compounds such that the focusing properties of the valves can be translated to the NIR is desirable. Ideally, one would like to preserve the structure of the frustule that is thought to govern its optical properties but enhance interactions with NIR radiation. One feasible way to accomplish this, is by converting the native biosilica frustules into higher refractive index (n) materials through solid-gas conversion chemistries like that shown by Bao *et al*. [131] where an

Aulacoseira frustule was converted in microporous silicon replicas with excellent shape preservation, which began by forming a MgO/Si replica according to the reaction equation:

$$2Mg_{(g)} + SiO_{2\,(s)} \rightarrow 2MgO_{(s)} + Si_{(s)} \tag{1.12}$$
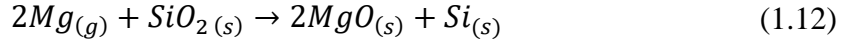
Once fully converted to MgO/Si, the MgO could be selectively dissolved by aqueous HCl, to yield the microporous silicon replica. In doing so, the silicon replica now possessed a substantially larger refractive index (ca. n = 4.0-3.6, [132]) than the native silica (n = 1.46-1.45, [133]) frustules over the same wavelength range, λ = 550-1100 nm, and thus should interact more strongly with NIR photons. Furthermore, even higher index materials, such as magnesium silicide (Mg_2Si, n = 3.74 at 2000 nm, [134]) can be obtained from an additional gas-solid reaction [135]

$$2Mg_{(g)} + Si_{(s)} \rightarrow Mg_2Si_{(s)} \tag{1.13}$$

which affords extremely high refractive indices, even into the mid-IR (ca. λ = 5-15 µm). This presents an opportunity to study the potential of novel, biogenic focusing elements at long wavelengths, assuming good-quality shape preservation of the frustule structure and hole pattern upon conversion to Mg_2Si. Therefore, Chapter 5-6 of this dissertation will detail theoretical and spectroscopic investigations into the optical properties of native silica frustules, MgO/Si (n = 2.15-2.01, λ = 550-1100 nm, see section 5.3.2) replicas, Mg_2Si replicas, and related hole patterns in thin films as a function of their refractive indices in the visible and NIR.

1.4   Thesis Aim and Organization

Chapter 2 presents detailed background on the optical principles of NLO, light interference, diffraction theory, beam propagation simulations, and an overview of the measurement techniques used in this dissertation. This section is meant to serve as a reference for the reader to refer to when unfamiliar theory or measurement principles are discussed in later chapters. Although a comprehensive review of each topic is beyond the scope of this thesis, references are provided for the reader to reinforce their understanding of the subject matter presented here.

Chapter 3 details spectroscopic investigations into the linear and NLO properties of polymethines dyes in the solution and solid-state. Specifically, the ability of bulky groups to mitigate aggregation interactions between polymethines in high number density films is characterized. Additionally, a film processing study is discussed, which systematically identifies the importance of surface chemistries and polymer host identity in dye-polymer blend films of a chalcogenopyrylium heptamethine dye of interest for AOSP.

In Chapter 4, a structure-property study correlating the changes in 2PA behavior and photostability with selective synthetic modifications for a series of organic, fused-ring quadrupolar chromophores is presented. Comparisons are made with other compounds from the literature with strong 2PA in the NIR to assess the suitability for these fused-ring dyes for OL applications.

Chapter 5 presents theoretical experiments and some complementary experimental measurements with the goal of quantifying the impact of hole pattern structure and refractive index have on the optical properties of native silica diatom valves and their high index replicas (MgO/Si and Mg_2Si). The development of a hole pattern analysis algorithm

and related statistical analyses are discussed, as well as beam propagation simulations on standardized patterns in thin films to quantify the effects of index on focusing heavier for simple hole patterns.

Chapter 6 provides experimental comparisons with the theoretical data obtained from Chapter 5 and discusses the possible origins for the complex set of interference phenomena that likely contribute to the observed optical effects in naturally-derived diatom valves and replicas. Chapter 7 concludes this dissertation by providing perspectives and outlook for the materials and technology space discussed in Chapters 3-6.

1.5   References

1.   Willner, A.E., Khaleghi, S., Chitgarha, M.R., and Yilmaz, O.F., *All-Optical Signal Processing.* Journal of Lightwave Technology, 2014. **32**(4): p. 660-680.

2.   Dayal, P., Holman, N., Kissee, J.L., Evans, J., Natale, J.E., Huang, Y., Litman, B., Nesbitt, T., and Marcin, J., *Impact of Telemedicine on Severity of Illness and Outcomes Among Children Transferred from Referring Emergency Departments to a Children's Hospital Pediatric Intensive Care Unit.* Pediatrics, 2018. **141**(1 MeetingAbstract): p. 269-269.

3.   Ramaswami, R., Sivarajan, K.N., and Sasaki, G.H., *Optical Networks: a Practical Perspective*. Third ed. 2010, Burlington, MA: Elsevier.

4.   Taubenblatt, M.A., *Optical Interconnects for High-Performance Computing.* Journal of Lightwave Technology, 2012. **30**(4): p. 448-457.

5.   Cisco. *The Zettabyte Era: Trends and Analysis*. [White Paper] 2017 June; Available from: https://www.cisco.com/c/en/us/solutions/collateral/service-provider/visual-networking-index-vni/vni-hyperconnectivity-wp.pdf.

6.   YouTube. *YouTube for Press*. 2018 [cited 2018 September 6]; Available from: http://www.youtube.com/yt/press/statistics.html.

7.   Caulfield, H.J. and Dolev, S., *Why future supercomputing requires optics.* Nature Photonics, 2010. **4**: p. 261.

8.   Zhang, Y., Chowdhury, P., Tornatore, M., and Mukherjee, B., *Energy Efficiency in Telecom Optical Networks.* IEEE Communications Surveys & Tutorials, 2010. **12**(4): p. 441-458.

9.   Leuthold, J., Freude, W., Brosi, J., Baets, R., Dumon, P., Biaggio, I., Scimeca, M.L., Diederich, F., Frank, B., and Koos, C., *Silicon Organic Hybrid Technology—A Platform for Practical Nonlinear Optics.* Proceedings of the IEEE, 2009. **97**(7): p. 1304-1316.

10.   Moss, D.J., Morandotti, R., Gaeta, A.L., and Lipson, M., *New CMOS-compatible platforms based on silicon nitride and Hydex for nonlinear optics.* Nature Photonics, 2013. **7**: p. 597.

11.   Säynätjoki, A., Karvonen, L., Alasaarela, T., Tu, X., Liow, T.Y., Hiltunen, M., Tervonen, A., Lo, G.Q., and Honkanen, S., *Low-loss silicon slot waveguides and couplers fabricated with optical lithography and atomic layer deposition.* Optics Express, 2011. **19**(27): p. 26275-26282.

12.   Spott, A., Baehr-Jones, T., Ding, R., Liu, Y., Bojko, R., O'Malley, T., Pomerene, A., Hill, C., Reinhardt, W., and Hochberg, M., *Photolithographically fabricated low-loss asymmetric silicon slot waveguides.* Optics Express, 2011. **19**(11): p. 10950-10958.

13.   Levy, J.S., Gondarenko, A., Foster, M.A., Turner-Foster, A.C., Gaeta, A.L., and Lipson, M., *CMOS-compatible multiple-wavelength oscillator for on-chip optical interconnects.* Nature Photonics, 2009. **4**: p. 37.

14.   Almeida, V.R., Barrios, C.A., Panepucci, R.R., and Lipson, M., *All-optical control of light on a silicon chip.* Nature, 2004. **431**: p. 1081.

15.   Leuthold, J., Koos, C., and Freude, W., *Nonlinear silicon photonics.* Nature Photonics, 2010. **4**: p. 535.

16.   Digonnet, M.J.F., Sadowski, R.W., Shaw, H.J., and Pantell, R.H., *Resonantly Enhanced Nonlinearity in Doped Fibers for Low-Power All-Optical Switching: A Review.* Optical Fiber Technology, 1997. **3**(1): p. 44-64.

17.   Haque, S.A. and Nelson, J., *Toward Organic All-Optical Switching.* Science, 2010. **327**(5972): p. 1466-1467.

18.   Dell'Olio, F. and Passaro, V.M.N., *Optical sensing by optimized silicon slot waveguides.* Optics Express, 2007. **15**(8): p. 4977-4993.

19.   Vos, K.D., Bartolozzi, I., Schacht, E., Bienstman, P., and Baets, R., *Silicon-on-Insulator microring resonator for sensitive and label-free biosensing.* Optics Express, 2007. **15**(12): p. 7610-7615.

20. Liu, X., Driscoll, J.B., Dadap, J.I., Osgood, R.M., Assefa, S., Vlasov, Y.A., and Green, W.M.J., *Self-phase modulation and nonlinear loss in silicon nanophotonic wires near the mid-infrared two-photon absorption edge.* Optics Express, 2011. **19**(8): p. 7778-7789.

21. Tsang, H.K., Wong, C.S., Liang, T.K., Day, I.E., Roberts, S.W., Harpin, A., Drake, J., and Asghari, M., *Optical dispersion, two-photon absorption and self-phase modulation in silicon waveguides at 1.5 μm wavelength.* Applied Physics Letters, 2002. **80**(3): p. 416-418.

22. Kuo, Y.-H., Rong, H., Sih, V., Xu, S., Paniccia, M., and Cohen, O., *Demonstration of wavelength conversion at 40 Gb/s data rate in silicon waveguides.* Optics Express, 2006. **14**(24): p. 11721-11726.

23. Koos, C., Vorreau, P., Vallaitis, T., Dumon, P., Bogaerts, W., Baets, R., Esembeson, B., Biaggio, I., Michinobu, T., Diederich, F., Freude, W., and Leuthold, J., *All-optical high-speed signal processing with silicon–organic hybrid slot waveguides.* Nature Photonics, 2009. **3**: p. 216.

24. Vallaitis, T., Bogatscher, S., Alloatti, L., Dumon, P., Baets, R., Scimeca, M.L., Biaggio, I., Diederich, F., Koos, C., Freude, W., and Leuthold, J., *Optical properties of highly nonlinear silicon-organic hybrid (SOH) waveguide geometries.* Optics Express, 2009. **17**(20): p. 17357-17368.

25. Hales, J.M., Barlow, S., Kim, H., Mukhopadhyay, S., Brédas, J.-L., Perry, J.W., and Marder, S.R., *Design of Organic Chromophores for All-Optical Signal Processing Applications.* Chemistry of Materials, 2014. **26**(1): p. 549-560.

26. Esembeson, B., Scimeca, M.L., Michinobu, T., Diederich, F., and Biaggio, I., *A High-Optical Quality Supramolecular Assembly for Third-Order Integrated Nonlinear Optics.* Advanced Materials, 2008. **20**(23): p. 4584-4587.

27. Perry, J.W. and Hales, J.M., *Organic and Polymeric 3rd-Order Nonlinear Optical Materials and Device Applications*, in *Introduction to Organic Electronic and Optoelectronic Materials and Devices*, S.-S. Sun and L.R. Dalton, Editors. 2008, CRC Press: Boca Raton, FL. p. 936.

28. Sutherland, R.L., *Handbook of Nonlinear Optics*. Second ed. 2003: Marcel Dekker, Inc. 971.

29. Li, Z.a., Liu, Y., Kim, H., Hales, J.M., Jang, S.-H., Luo, J., Baehr-Jones, T., Hochberg, M., Marder, S.R., Perry, J.W., and Jen, A.K.-Y., *High-Optical-Quality Blends of Anionic Polymethine Salts and Polycarbonate with Enhanced Third-Order Non-linearities for Silicon-Organic Hybrid Devices.* Advanced Materials, 2012. **24**(44): p. OP326-OP330.

30. Hales, J.M., Matichak, J., Barlow, S., Ohira, S., Yesudas, K., Brédas, J.L., Perry, J.W., and Marder, S.R., *Design of Polymethine Dyes with Large Third-Order*

Optical Nonlinearities and Loss Figures of Merit. Science, 2010. **327**(5972): p. 1485-1488.

31.   Bredas, J.L., Adant, C., Tackx, P., Persoons, A., and Pierce, B.M., *Third-Order Nonlinear Optical Response in Organic Materials: Theoretical and Experimental Aspects.* Chemical Reviews, 1994. **94**(1): p. 243-278.

32.   Nalwa, H.S., *Organic Materials for Third-Order Nonlinear Optics.* Advanced Materials, 1993. **5**(5): p. 341-358.

33.   Dinu, M., Quochi, F., and Garcia, H., *Third-order nonlinearities in silicon at telecom wavelengths.* Applied Physics Letters, 2003. **82**(18): p. 2954-2956.

34.   Hutchings, D.C. and Wherrett, B.S., *Theory of the dispersion of ultrafast nonlinear refraction in zinc-blende semiconductors below the band edge.* Physical Review B, 1994. **50**(7): p. 4622-4630.

35.   Lee, K.-H., Cho, W.-R., Park, J.-H., Kim, J.-S., Park, S.-H., and Kim, U., *Measurement of free-carrier nonlinearities in ZnSe based on the Z-scan technique with a nanosecond laser.* Optics Letters, 1994. **19**(15): p. 1116-1118.

36.   Hurlbut, W.C., Lee, Y.-S., Vodopyanov, K.L., Kuo, P.S., and Fejer, M.M., *Multiphoton absorption and nonlinear refraction of GaAs in the mid-infrared.* Optics Letters, 2007. **32**(6): p. 668-670.

37.   Marder, S.R., Gorman, C.B., Tiemann, B.G., Perry, J.W., Bourhill, G., and Mansour, K., *Relation Between Bond-Length Alternation and Second Electronic Hyperpolarizability of Conjugated Organic Molecules.* Science, 1993. **261**(5118): p. 186.

38.   Meyers, F., Marder, S.R., Pierce, B.M., and Bredas, J.L., *Electric Field Modulated Nonlinear Optical Properties of Donor-Acceptor Polyenes: Sum-Over-States Investigation of the Relationship between Molecular Polarizabilities (.alpha., .beta., and .gamma.) and Bond Length Alternation.* Journal of the American Chemical Society, 1994. **116**(23): p. 10703-10714.

39.   Hales, J.M., Zheng, S., Barlow, S., Marder, S.R., and Perry, J.W., *Bisdioxaborine Polymethines with Large Third-Order Nonlinearities for All-Optical Signal Processing.* Journal of the American Chemical Society, 2006. **128**(35): p. 11362-11363.

40.   Mukhopadhyay, S., Risko, C., Marder, S.R., and Brédas, J.-L., *Polymethine dyes for all-optical switching applications: a quantum-chemical characterization of counter-ion and aggregation effects on the third-order nonlinear optical response.* Chemical Science, 2012. **3**(10): p. 3103-3112.

41.   Stegeman, G.I. *Material figures of merit and implications to all-optical waveguide switching.* in *Proceedings of SPIE.* 1993.

42.   Venkatram, N., Narayana Rao, D., Giribabu, L., and Venugopal Rao, S., *Femtosecond nonlinear optical properties of alkoxy phthalocyanines at 800nm studied using Z-Scan technique.* Chemical Physics Letters, 2008. **464**(4): p. 211-215.

43.   Thorley, K.J., Hales, J.M., Anderson, H.L., and Perry, J.W., *Porphyrin Dimer Carbocations with Strong Near Infrared Absorption and Third-Order Optical Nonlinearity.* Angewandte Chemie International Edition, 2008. **47**(37): p. 7095-7098.

44.   Rangel-Rojo, R., Yamada, S., Matsuda, H., Kasai, H., Nakanishi, H., Kar, A.K., and Wherrett, B.S., *Spectrally resolved third-order nonlinearities in polydiacetylene microcrystals: influence of particle size.* Journal of the Optical Society of America B, 1998. **15**(12): p. 2937-2945.

45.   Osaheni, J.A., Jenekhe, S.A., Vanherzeele, H., Meth, J.S., Sun, Y., and MacDiarmid, A.G., *Nonlinear optical properties of polyanilines and derivatives.* The Journal of Physical Chemistry, 1992. **96**(7): p. 2830-2836.

46.   Lawrence, B.L., Cha, M., Kang, J.U., Toruellas, W., Stegeman, G., Baker, G., Meth, J., and Etemad, S., *Large purely refractive nonlinear index of single crystal P-toluene sulphonate (PTS) at 1600 nm.* Electronics Letters, 1994. **30**(5): p. 447-448.

47.   Scarpaci, A., Nantalaksakul, A., Hales, J.M., Matichak, J.D., Barlow, S., Rumi, M., Perry, J.W., and Marder, S.R., *Effects of Dendronization on the Linear and Third-Order Nonlinear Optical Properties of Bis(thiopyrylium) Polymethine Dyes in Solution and the Solid State.* Chemistry of Materials, 2012. **24**(9): p. 1606-1618.

48.   Marder, S.R., Gorman, C.B., Meyers, F., Perry, J.W., Bourhill, G., Brédas, J.-L., and Pierce, B.M., *A Unified Description of Linear and Nonlinear Polarization in Organic Polymethine Dyes.* Science, 1994. **265**(5172): p. 632-635.

49.   Bouit, P.-A., Aronica, C., Toupet, L., Le Guennic, B., Andraud, C., and Maury, O., *Continuous Symmetry Breaking Induced by Ion Pairing Effect in Heptamethine Cyanine Dyes: Beyond the Cyanine Limit.* Journal of the American Chemical Society, 2010. **132**(12): p. 4328-4335.

50.   Bouit, P.-A., Di Piazza, E., Rigaut, S., Le Guennic, B., Aronica, C., Toupet, L., Andraud, C., and Maury, O., *Stable Near-Infrared Anionic Polymethine Dyes: Structure, Photophysical, and Redox Properties.* Organic Letters, 2008. **10**(19): p. 4159-4162.

51.   Dähne, S. and Radeglia, R., *Revision der Lewis-Calvin-Regel zur charakterisierung vinyloger. Polyen- und polymethinähnlicher verbindungen.* Tetrahedron, 1971. **27**(15): p. 3673-3693.

52. Marder, S.R., Perry, J.W., Tiemann, B.G., Gorman, C.B., Gilmour, S., Biddle, S.L., and Bourhill, G., *Direct observation of reduced bond-length alternation in donor/acceptor polyenes.* Journal of the American Chemical Society, 1993. **115**(6): p. 2524-2526.

53. Gieseking, R.L., Risko, C., and Brédas, J.-L., *Distinguishing the Effects of Bond-Length Alternation versus Bond-Order Alternation on the Nonlinear Optical Properties of π-Conjugated Chromophores.* The Journal of Physical Chemistry Letters, 2015. **6**(12): p. 2158-2162.

54. El-Gezawy, H., Rettig, W., and Lapouyade, R., *Solvatochromic Behavior of Donor−Acceptor-Polyenes: Dimethylamino-cyano-diphenylbutadiene.* The Journal of Physical Chemistry A, 2006. **110**(1): p. 67-75.

55. Grisanti, L., D'Avino, G., Painelli, A., Guasch, J., Ratera, I., and Veciana, J., *Essential State Models for Solvatochromism in Donor−Acceptor Molecules: The Role of the Bridge.* The Journal of Physical Chemistry B, 2009. **113**(14): p. 4718-4725.

56. Bartkowiak, W., *Solvatochromism and Nonlinear Optical Properties of Donor-acceptor π-Conjugated Molecules*, in *Non-Linear Optical Properties of Matter: From Molecules to Condensed Phases*, M.G. Papadopoulos, A.J. Sadlej, and J. Leszczynski, Editors. 2006, Springer Netherlands: Dordrecht. p. 299-318.

57. Würthner, F., Archetti, G., Schmidt, R., and Kuball, H.-G., *Solvent Effect on Color, Band Shape, and Charge-Density Distribution for Merocyanine Dyes Close to the Cyanine Limit.* Angewandte Chemie, 2008. **120**(24): p. 4605-4608.

58. Bourhill, G., Bredas, J.-L., Cheng, L.-T., Marder, S.R., Meyers, F., Perry, J.W., and Tiemann, B.G., *Experimental Demonstration of the Dependence of the First Hyperpolarizability of Donor-Acceptor-Substituted Polyenes on the Ground-State Polarization and Bond Length Alternation.* Journal of the American Chemical Society, 1994. **116**(6): p. 2619-2620.

59. Marder, S.R., Gorman, C.B., Tiemann, B.G., and Cheng, L.T., *Stronger acceptors can diminish nonlinear optical response in simple donor-acceptor polyenes.* Journal of the American Chemical Society, 1993. **115**(7): p. 3006-3007.

60. Würthner, F., Wortmann, R., Matschiner, R., Lukaszuk, K., Meerholz, K., DeNardin, Y., Bittner, R., Bräuchle, C., and Sens, R., *Merocyanine Dyes in the Cyanine Limit: A New Class of Chromophores for Photorefractive Materials.* Angewandte Chemie International Edition in English, 1997. **36**(24): p. 2765-2768.

61. Tolbert, L.M. and Zhao, X., *Beyond the Cyanine Limit: Peierls Distortion and Symmetry Collapse in a Polymethine Dye.* Journal of the American Chemical Society, 1997. **119**(14): p. 3253-3258.

62. Orr, B.J. and Ward, J.F., *Perturbation theory of the non-linear optical polarization of an isolated system.* Molecular Physics, 1971. **20**(3): p. 513-526.

63. Kogej, T., Beljonne, D., Meyers, F., Perry, J.W., Marder, S.R., and Brédas, J.L., *Mechanisms for enhancement of two-photon absorption in donor–acceptor conjugated chromophores.* Chemical Physics Letters, 1998. **298**(1): p. 1-6.

64. Kuzyk, M.G., Singer, K.D., and Stegeman, G.I., *Theory of Molecular Nonlinear Optics.* Advances in Optics and Photonics, 2013. **5**(1): p. 4-82.

65. Dixit, S.N., Guo, D., and Mazumdar, S., *Essential-states mechanism of optical nonlinearity in π-conjugated polymers.* Physical Review B, 1991. **43**(8): p. 6781-6784.

66. Heflin, J.R., Wong, K.Y., Zamani-Khamiri, O., and Garito, A.F., *Nonlinear optical properties of linear chains and electron-correlation effects.* Physical Review B, 1988. **38**(2): p. 1573-1576.

67. Kuzyk, M.G. and Dirk, C.W., *Effects of centrosymmetry on the nonresonant electronic third-order nonlinear optical susceptibility.* Physical Review A, 1990. **41**(9): p. 5098-5109.

68. Dirk, C.W., Cheng, L.-T., and Kuzyk, M.G., *A simplified three-level model describing the molecular third-order nonlinear optical susceptibility.* International Journal of Quantum Chemistry, 1992. **43**(1): p. 27-36.

69. Perry, J.W., Mansour, K., Lee, I.-Y.S., Wu, X.-L., Bedworth, P.V., Chen, C.-T., Ng, D., Marder, S.R., Miles, P., Wada, T., Tian, M., and Sasabe, H., *Organic Optical Limiter with a Strong Nonlinear Absorptive Response.* Science, 1996. **273**(5281): p. 1533-1536.

70. Tutt, L.W. and Kost, A., *Optical limiting performance of C_{60} and C_{70} solutions.* Nature, 1992. **356**: p. 225.

71. Perry, J.W., *Organic and metal-containing reverse saturable absorbers for optical limiters*. 1997, Boca Raton, FL: CRC Press Inc.

72. He, G.S., Weder, C., Smith, P., and Prasad, P.N., *Optical power limiting and stabilization based on a novel polymer compound.* IEEE Journal of Quantum Electronics, 1998. **34**(12): p. 2279-2285.

73. He, G.S., Yuan, L., Bhawalkar, J.D., and Prasad, P.N., *Optical limiting, pulse reshaping, and stabilization with a nonlinear absorptive fiber system.* Applied Optics, 1997. **36**(15): p. 3387-3392.

74. Chi, S.-H., *Third-Order Nonlinear Optical Properties of Conjugated Polymers and Blends*, in *School of Chemistry and Biochemistry*. 2009, Georgia Institute of Technology: Atlanta, GA. p. 187.

75. Geusic, J.E., Singh, S., Tipping, D.W., and Rich, T.C., *Three-Photon Stepwise Optical Limiting in Silicon.* Physical Review Letters, 1967. **19**(19): p. 1126-1128.

76. Ralston, J.M. and Chang, R.K., *Optical Limiting in Semiconductors.* Applied Physics Letters, 1969. **15**(6): p. 164-166.

77. Soileau, M., Williams, W., and Stryland, E.V., *Optical power limiter with picosecond response time.* IEEE Journal of Quantum Electronics, 1983. **19**(4): p. 731-735.

78. Perry, J.W., Mansour, K., Marder, S.R., Perry, K.J., Alvarez, D., and Choong, I., *Enhanced reverse saturable absorption and optical limiting in heavy-atom-substituted phthalocyanines.* Optics Letters, 1994. **19**(9): p. 625-627.

79. Blau, W., Byrne, H., Dennis, W.M., and Kelly, J.M., *Reverse saturable absorption in tetraphenylporphyrins.* Optics Communications, 1985. **56**(1): p. 25-29.

80. Shirk, J.S., Lindle, J.R., Bartoli, F.J., Hoffman, C.A., Kafafi, Z.H., and Snow, A.W., *Off-resonant third-order optical nonlinearities of metal-substituted phthalocyanines.* Applied Physics Letters, 1989. **55**(13): p. 1287-1288.

81. Cha, M., Sariciftci, N.S., Heeger, A.J., Hummelen, J.C., and Wudl, F., *Enhanced nonlinear absorption and optical limiting in semiconducting polymer/methanofullerene charge transfer films.* Applied Physics Letters, 1995. **67**(26): p. 3850-3852.

82. Ehrlich, J.E., Wu, X.L., Lee, I.Y.S., Hu, Z.Y., Röckel, H., Marder, S.R., and Perry, J.W., *Two-photon absorption and broadband optical limiting with bis-donor stilbenes.* Optics Letters, 1997. **22**(24): p. 1843-1845.

83. Albota, M., Beljonne, D., Brédas, J.-L., Ehrlich, J.E., Fu, J.-Y., Heikal, A.A., Hess, S.E., Kogej, T., Levin, M.D., Marder, S.R., McCord-Maughon, D., Perry, J.W., Röckel, H., Rumi, M., Subramaniam, G., Webb, W.W., Wu, X.-L., and Xu, C., *Design of Organic Molecules with Large Two-Photon Absorption Cross Sections.* Science, 1998. **281**(5383): p. 1653.

84. Perry, J.W., Barlow, S., Ehrlich, J.E., Heikal, A.A., Hu, Z.Y., Lee, I.Y.S., Mansour, K., Marder, S.R., Rockel, H., Rumi, M., Thayumanavan, S., and Wu, X.L., *Two-photon and higher-order absorptions and optical limiting properties of bis-donor substituted conjugated organic chromophores.* Molecular Crystals and Liquid Crystals Science and Technology Section B: Nonlinear Optics, 1999. **21**(1-4): p. 225-243.

85. Rumi, M., Ehrlich, J.E., Heikal, A.A., Perry, J.W., Barlow, S., Hu, Z., McCord-Maughon, D., Parker, T.C., Röckel, H., Thayumanavan, S., Marder, S.R., Beljonne, D., and Brédas, J.-L., *Structure−Property Relationships for Two-Photon Absorbing Chromophores: Bis-Donor Diphenylpolyene and*

Bis(styryl)benzene Derivatives. Journal of the American Chemical Society, 2000. **122**(39): p. 9500-9510.

86. He, G.S., Xu, G.C., Prasad, P.N., Reinhardt, B.A., Bhatt, J.C., and Dillard, A.G., *Two-photon absorption and optical-limiting properties of novel organic compounds.* Optics Letters, 1995. **20**(5): p. 435-437.

87. Hales, J.M., Cozzuol, M., Screen, T.E.O., Anderson, H.L., and Perry, J.W., *Metalloporphyrin polymer with temporally agile, broadband nonlinear absorption for optical limiting in the near infrared.* Optics Express, 2009. **17**(21): p. 18478-18488.

88. Chi, S.-H., Hales, J.M., Cozzuol, M., Ochoa, C., Fitzpatrick, M., and Perry, J.W., *Conjugated polymer-fullerene blend with strong optical limiting in the near-infrared.* Optics Express, 2009. **17**(24): p. 22062-22072.

89. Gao, Y., Chang, Q., Ye, H., Jiao, W., Li, Y., Wang, Y., Song, Y., and Zhu, D., *Size effect of optical limiting in gold nanoparticles.* Chemical Physics, 2007. **336**(2): p. 99-102.

90. Belousova, I.M., Mironova, N.G., Scobelev, A.G., and Yur'ev, M.S., *The investigation of nonlinear optical limiting by aqueous suspensions of carbon nanoparticles.* Optics Communications, 2004. **235**(4): p. 445-452.

91. He, G.S., Yong, K.-T., Zheng, Q., Sahoo, Y., Baev, A., Ryasnyanskiy, A.I., and Prasad, P.N., *Multi-photon excitation properties of CdSe quantum dots solutions and optical limiting behavior in infrared range.* Optics Express, 2007. **15**(20): p. 12818-12833.

92. Maciel, G.S., Kim, K.S., Chung, S.J., Swiatkiewicz, J., He, G.S., and Prasad, P.N., *Linear and Nonlinear Optical Properties of an Erbium Two-Photon Dye Salt.* The Journal of Physical Chemistry B, 2001. **105**(16): p. 3155-3157.

93. Chen, K., Su, W., Wang, Y., Ge, H., Zhang, K., Wang, Y., Xie, X., Gomes, V.G., Sun, H., and Huang, L., *Nanocomposites of carbon nanotubes and photon upconversion nanoparticles for enhanced optical limiting performance.* Journal of Materials Chemistry C, 2018. **6**(27): p. 7311-7316.

94. Dini, D., Calvete, M.J.F., and Hanack, M., *Nonlinear Optical Materials for the Smart Filtering of Optical Radiation.* Chemical Reviews, 2016. **116**(22): p. 13043-13233.

95. Göppert-Mayer, M., *Über Elementarakte mit zwei Quantensprüngen.* Annalen der Physik, 1931. **401**(3): p. 273-294.

96. Terenziani, F., Katan, C., Badaeva, E., Tretiak, S., and Blanchard-Desce, M., *Enhanced Two-Photon Absorption of Organic Chromophores: Theoretical and Experimental Assessments.* Advanced Materials, 2008. **20**(24): p. 4641-4678.

97.   Rumi, M., Barlow, S., Wang, J., Perry, J.W., and Marder, S.R., *Two-Photon Absorbing Materials and Two-Photon-Induced Chemistry*, in *Photoresponsive Polymers I*, S.R. Marder and K.-S. Lee, Editors. 2008, Springer Berlin Heidelberg: Berlin, Heidelberg. p. 1-95.

98.   He, G.S., Tan, L.-S., Zheng, Q., and Prasad, P.N., *Multiphoton Absorbing Materials: Molecular Designs, Characterizations, and Applications.* Chemical Reviews, 2008. **108**(4): p. 1245-1330.

99.   Kim, K.S., Lim, J.M., Osuka, A., and Kim, D., *Various strategies for highly-efficient two-photon absorption in porphyrin arrays.* Journal of Photochemistry and Photobiology C: Photochemistry Reviews, 2008. **9**(1): p. 13-28.

100.   Boyd, R.W., *Nonlinear Optics*. Third ed. 2008, Burlington, MA USA: Elsevier Inc.

101.   Pawlicki, M., Collins, H.A., Denning, R.G., and Anderson, H.L., *Two-Photon Absorption and the Design of Two-Photon Dyes.* Angewandte Chemie International Edition, 2009. **48**(18): p. 3244-3266.

102.   Butcher, P.N. and Cotter, D., *The Elements of Nonlinear Optics*, ed. P.L. Knight and W.J. Firth. 1990, New York, NY: Cambridge University Press.

103.   Chung, S.-J., Zheng, S., Odani, T., Beverina, L., Fu, J., Padilha, L.A., Biesso, A., Hales, J.M., Zhan, X., Schmidt, K., Ye, A., Zojer, E., Barlow, S., Hagan, D.J., Van Stryland, E.W., Yi, Y., Shuai, Z., Pagani, G.A., Brédas, J.-L., Perry, J.W., and Marder, S.R., *Extended Squaraine Dyes with Large Two-Photon Absorption Cross-Sections.* Journal of the American Chemical Society, 2006. **128**(45): p. 14444-14445.

104.   Beverina, L., Crippa, M., Salice, P., Ruffo, R., Ferrante, C., Fortunati, I., Signorini, R., Mari, C.M., Bozio, R., Facchetti, A., and Pagani, G.A., *Indolic Squaraines as Two-Photon Absorbing Dyes in the Visible Region: X-ray Structure, Electrochemical, and Nonlinear Optical Characterization.* Chemistry of Materials, 2008. **20**(10): p. 3242-3244.

105.   Pond, S.J.K., Rumi, M., Levin, M.D., Parker, T.C., Beljonne, D., Day, M.W., Brédas, J.-L., Marder, S.R., and Perry, J.W., *One- and Two-Photon Spectroscopy of Donor−Acceptor−Donor Distyrylbenzene Derivatives: Effect of Cyano Substitution and Distortion from Planarity.* The Journal of Physical Chemistry A, 2002. **106**(47): p. 11470-11480.

106.   Tsuchizawa, T., Yamada, K., Fukuda, H., Watanabe, T., Jun-ichi, T., Takahashi, M., Shoji, T., Tamechika, E., Itabashi, S., and Morita, H., *Microphotonics devices based on silicon microfabrication technology.* IEEE Journal of Selected Topics in Quantum Electronics, 2005. **11**(1): p. 232-240.

107. Khorasaninejad, M., Chen, W.T., Devlin, R.C., Oh, J., Zhu, A.Y., and Capasso, F., *Metalenses at visible wavelengths: Diffraction-limited focusing and subwavelength resolution imaging.* Science, 2016. **352**(6290): p. 1190-1194.

108. Erickson, D., Sinton, D., and Psaltis, D., *Optofluidics for energy applications.* Nature Photonics, 2011. **5**: p. 583.

109. Barlev, D., Vidu, R., and Stroeve, P., *Innovation in concentrated solar power.* Solar Energy Materials and Solar Cells, 2011. **95**(10): p. 2703-2725.

110. *Solar Industry Research Data.* 2018 [cited 2018 September 9]; Available from: https://www.seia.org/solar-industry-research-data.

111. Arase, H., Matsushita, A., Itou, A., Asano, T., Hayashi, N., Inoue, D., Futakuchi, R., Inoue, K., Nakagawa, T., Yamamoto, M., Fujii, E., Anda, Y., Ishida, H., Ueda, T., Fidaner, O., Wiemer, M., and Ueda, D., *A Novel Thin Concentrator Photovoltaic With Microsolar Cells Directly Attached to a Lens Array.* IEEE Journal of Photovoltaics, 2014. **4**(2): p. 709-712.

112. Hayashi, N., Inoue, D., Matsumoto, M., Matsushita, A., Higuchi, H., Aya, Y., and Nakagawa, T., *High-efficiency thin and compact concentrator photovoltaics with micro-solar cells directly attached to a lens array.* Optics Express, 2015. **23**(11): p. A594-A603.

113. Yamada, N. and Okamoto, K., *Experimental measurements of a prototype high concentration Fresnel lens CPV module for the harvesting of diffuse solar radiation.* Optics Express, 2014. **22**(S1): p. A28-A34.

114. Debije, M.G. and Verbunt, P.P.C., *Thirty Years of Luminescent Solar Concentrator Research: Solar Energy for the Built Environment.* Advanced Energy Materials, 2012. **2**(1): p. 12-35.

115. Khorasaninejad, M., Shi, Z., Zhu, A.Y., Chen, W.T., Sanjeev, V., Zaidi, A., and Capasso, F., *Achromatic Metalens over 60 nm Bandwidth in the Visible and Metalens with Reverse Chromatic Dispersion.* Nano Letters, 2017. **17**(3): p. 1819-1824.

116. Lu, D. and Liu, Z., *Hyperlenses and metalenses for far-field super-resolution imaging.* Nature Communications, 2012. **3**: p. 1205.

117. Wang, Y. and Zhang, X., *Scale-up of the manufacturing of optical metamaterials.* Npg Asia Materials, 2014. **6**: p. e141.

118. Lalanne, P. and Chavel, P., *Metalenses at visible wavelengths: past, present, perspectives.* Laser & Photonics Reviews, 2017. **11**(3): p. 1600295.

119. Zheng, X., Smith, W., Jackson, J., Moran, B., Cui, H., Chen, D., Ye, J., Fang, N., Rodriguez, N., Weisgraber, T., and Spadaccini, C.M., *Multiscale metallic metamaterials.* Nature Materials, 2016. **15**: p. 1100.

120. Chanda, D., Shigeta, K., Gupta, S., Cain, T., Carlson, A., Mihi, A., Baca, A.J., Bogart, G.R., Braun, P., and Rogers, J.A., *Large-area flexible 3D optical negative index metamaterial formed by nanotransfer printing.* Nature Nanotechnology, 2011. **6**: p. 402.

121. Walia, S., Shah, C.M., Gutruf, P., Nili, H., Chowdhury, D.R., Withayachumnankul, W., Bhaskaran, M., and Sriram, S., *Flexible metasurfaces and metamaterials: A review of materials and fabrication processes at micro- and nano-scales.* Applied Physics Reviews, 2015. **2**(1): p. 011303.

122. Ok, J.G., Youn, H.S., Kwak, M.K., Lee, K.-T., Shin, Y.J., Guo, L.J., Greenwald, A., and Liu, Y., *Continuous and scalable fabrication of flexible metamaterial films via roll-to-roll nanoimprint process for broadband plasmonic infrared filters.* Applied Physics Letters, 2012. **101**(22): p. 223102.

123. Chisti, Y., *Biodiesel from microalgae.* Biotechnology Advances, 2007. **25**(3): p. 294-306.

124. Hildebrand, M., *Diatoms, Biomineralization Processes, and Genomics.* Chemical Reviews, 2008. **108**(11): p. 4855-4874.

125. De Tommasi, E., De Luca, A.C., Lavanga, L., Dardano, P., De Stefano, M., De Stefano, L., Langella, C., Rendina, I., Dholakia, K., and Mazilu, M., *Biologically enabled sub-diffractive focusing.* Optics Express, 2014. **22**(22): p. 27214-27227.

126. Romann, J., Valmalette, J.C., Røyset, A., and Einarsrud, M.A., *Optical properties of single diatom frustules revealed by confocal microspectroscopy.* Optics Letters, 2015. **40**(5): p. 740-743.

127. Stefano, L.D., Rea, I., Rendina, I., Stefano, M.D., and Moretti, L., *Lensless light focusing with the centric marine diatom Coscinodiscus walesii.* Optics Express, 2007. **15**(26): p. 18082-18088.

128. De Tommasi, E., Rea, I., Mocella, V., Moretti, L., De Stefano, M., Rendina, I., and De Stefano, L., *Multi-wavelength study of light transmitted through a single marine centric diatom.* Optics Express, 2010. **18**(12): p. 12203-12212.

129. Romann, J., Valmalette, J.-C., Chauton, M.S., Tranell, G., Einarsrud, M.-A., and Vadstein, O., *Wavelength and orientation dependent capture of light by diatom frustule nanostructures.* Scientific Reports, 2015. **5**: p. 17403.

130. Hildebrand, M., Davis, A.K., Smith, S.R., Traller, J.C., and Abbriano, R., *The place of diatoms in the biofuels industry.* Biofuels, 2012. **3**(2): p. 221-240.

131.   Bao, Z., Weatherspoon, M.R., Shian, S., Cai, Y., Graham, P.D., Allan, S.M., Ahmad, G., Dickerson, M.B., Church, B.C., Kang, Z., Abernathy Iii, H.W., Summers, C.J., Liu, M., and Sandhage, K.H., *Chemical reduction of three-dimensional silica micro-assemblies into microporous silicon replicas.* Nature, 2007. **446**: p. 172.

132.   Green, M.A., *Self-consistent optical parameters of intrinsic silicon at 300K including temperature coefficients.* Solar Energy Materials and Solar Cells, 2008. **92**(11): p. 1305-1310.

133.   Malitson, I.H., *Interspecimen Comparison of the Refractive Index of Fused Silica.* Journal of the Optical Society of America, 1965. **55**(10): p. 1205-1209.

134.   McWilliams, D. and Lynch, D.W., *Indexes of Refraction of Mg₂Si, Mg₂Ge, and Mg₂Sn.* Journal of the Optical Society of America, 1963. **53**(2): p. 298_1-299.

135.   Nayeb-Hashemi, A.A. and Clark, J.B., *The Mg−Si (Magnesium-Silicon) system.* Bulletin of Alloy Phase Diagrams, 1984. **5**(6): p. 584-592.

CHAPTER 2. THEORETICAL AND EXPERIMENTAL METHODS – THIRD-ORDER NONLINEAR OPTICAL RESPONSES AND PRINCIPLES OF DIFFRACTION AND OPTICAL WAVE INTERFERENCE

The purpose of this chapter is to describe the principles behind several characterization techniques used in this dissertation. This begins with an introduction to techniques relevant to Chapters 3 and 4, regarding the origins of ultrafast third-order nonlinear responses from which the intensity-dependent refractive index and two-photon absorption are derived. A theoretical overview and experimentally relevant details of characterization methods used to measure these phenomena, i.e. Z-scan and nondegenerate two-photon absorption (ND2PA), will be given in sections 2.3.1 and 2.3.2. Additionally, an explanation of prism coupling (a complementary technique to NLO measurements on films that measures the linear refractive index and optical loss of NLO films) will be explained in section 2.3.3. Regarding the optical properties of biogenic/biomimetic structures presented in Chapters 5 and 6, qualitative, introductory background on diffraction and the interference of electromagnetic waves is provided in section 2.4.1. From this, concepts are introduced that will be used to interpret results from simulations and measurements regarding the focusing behavior of *C. wailessii* diatom frustules and their high index replicas in sections 2.4.2-2.5.1. Specifically, the principles of ellipsometry, far-field interference imaging, and beam propagation simulations and will be discussed.

2.1 Third-Order Nonlinear Optics
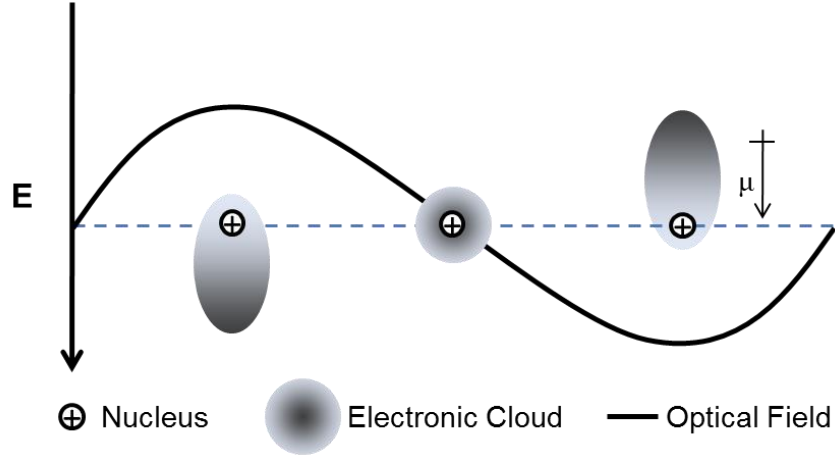
Figure 2.1. Illustration of the oscillation of an electron cloud about its nucleus in response to an electromagnetic or optical field. Reproduced from Perry et al. [27] with permission. Copyright 2008 CRC Press.

At the molecular level, dielectric materials are comprised of charged particles, namely positively charged nuclei and negatively charged electrons. Upon the application of a low-intensity, oscillating electric (optical) field through the medium, the electrons will move in an oscillatory motion away from their positive cores in a harmonic (linear) manner because of their interaction with the applied field, as shown in Figure 2.1. The frequency-dependent induced dipole $\mu_i(\omega)$, considered to be linearly proportional to the strength of the applied field $E_j(\omega)$, that results from the displacement of an electron from its nucleus is given approximately by

$$\mu_i(\omega) = \alpha_{ij}(\omega)E_j(\omega) \tag{2.1}$$

where $\mu_i(\omega)$ and $E_j(\omega)$ are vector quantities. $\alpha_{ij}(\omega)$ is the linear polarizability of the molecule, which is a frequency-dependent quantity that is both complex and tensorial in

nature. The imaginary and real parts of $\alpha_{ij}(\omega)$ describe optical effects such as linear absorption and refraction, respectively. [27, 28]
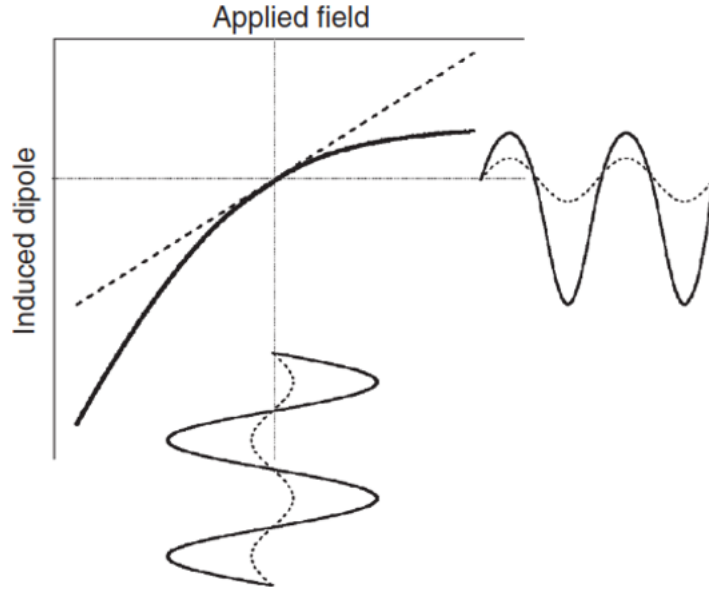
Figure 2.2. Response of an induced dipole as function of the applied field. Reproduced from Perry et al. [27] with permission. Copyright 2008 CRC Press.

At sufficiently high field intensity, the oscillatory behavior of the electrons move away from the linear regime and begin to oscillate anharmonically in response to the applied field as seen in Figure 2.2. The anharmonic oscillation, consequently, results in induced polarization. In this regime, an exact solution for the functional form of $\mu_i(\omega)$ is no longer possible and is expressed as a Taylor series expansion of total dipole μ_i in $E(\omega)$ as

$$\mu_i = \mu_i^o + \alpha_{ij}(-\omega_\sigma; \omega)E_j(\omega) + \frac{1}{2!}\zeta_{ijk}(-\omega_\sigma; \omega_1, \omega_2)E_j(\omega_1)E_k(\omega_2)$$

$$(2.2)$$

$$+ \frac{1}{3!}\gamma_{ijkl}(-\omega_\sigma; \omega_1, \omega_2, \omega_3)E_j(\omega_1)E_k(\omega_2)E_l(\omega_3) + \cdots$$

where μ_i^0 is the permanent dipole, α_{ij} is the first-order polarizability, ζ_{ijk} is the second-order polarizability, and γ_{ijkl} is the third-order polarizability. [27, 100] It is noted that β is the

preferred label for the second-order polarizability in the literature, however, ζ is used here to avoid confusion later with the two-photon absorption coefficient (β) in section 2.2.2. The higher order terms (ζE^2, γE^3, and higher) are responsible for NLO effects and the small size ζ and γ account for the necessity of an intense optical source in order to observe NLO responses. [27]

2.1.1 *Relationship between Microscopic and Macroscopic Nonlinearities*

The polarizabilities (α, ζ, γ) are the microscopic parameters that allow for the analysis of NLO materials at the molecular level. Since most NLO characterization techniques are only able to measure the macroscopic nonlinearities, a relationship between microscopic and macroscopic quantities must be defined. [27] In doing so, first we must define the macroscopic polarization P_I induced in a material

$$P_I = N\langle \mu_i \rangle \tag{2.3}$$

where N is the number density of microscopic dipoles and $\langle \mu_i \rangle$ is the orientational averaging over all microscopic dipoles. Using this relationship, an expansion can be performed that is similar to the one from the induced dipole case, which yields

$$P_I = P_I^{(0)} + \chi_{IJ}^{(1)}(-\omega_\sigma; \omega)E_j(\omega) + \frac{1}{2!}\chi_{IJK}^{(2)}(-\omega_\sigma; \omega_1, \omega_2)E_j(\omega_1)E_k(\omega_2)$$

$$+ \frac{1}{3!}\chi_{IJKL}^{(3)}(-\omega_\sigma; \omega_1, \omega_2, \omega_3)E_j(\omega_1)E_k(\omega_2)E_l(\omega_3) + \cdots \tag{2.4}$$

where $\chi^{(1)}$, $\chi^{(2)}$, and $\chi^{(3)}$ are the first, second, and third-order electric susceptibilities, respectively. A relationship between γ, the microscopic parameter, and $\chi^{(3)}$, the macroscopic parameter, can be found by first considering that the fields (e.g. $E_j(\omega)$) in the

expression for μᵢ are the local fields whereas the fields in Pᵢ are the macroscopic fields. The local fields include contributions from surrounding molecules in addition to the applied macroscopic fields. To account for this, the macroscopic fields can be corrected with Lorentz local field factor. [27, 28] The relationship between the local and macroscopic field is expressed as

$$E_{i,j,k}(\omega_{1,2,or\,3}) = L(\omega_{1,2,or\,3}) \cdot E_{I,J,K}(\omega_{1,2,or\,3}) \tag{2.5}$$

where the Lorentz field factors are given by

$$L(\omega_{1,2,or\,3}) = \frac{n(\omega_{1,2,or\,3})^2 + 2}{3} \tag{2.6}$$

Where n(ω) is the refractive index of the medium at frequency ω. From this expression, a relationship between the microscopic (γ) and macroscopic ($\chi^{(3)}$) parameter can be written as

$$\chi^{(3)}_{IJKL}(-\omega_\sigma; \omega_1, \omega_2, \omega_3)$$
$$= N \cdot L(\omega_\sigma)L(\omega_1)L(\omega_2)L(\omega_3) \cdot \langle \gamma_{ijkl}(-\omega_\sigma; \omega_1, \omega_2, \omega_3) \rangle \tag{2.7}$$

in which N is the number density of microscopic dipoles and L(ωσ) accounts for the local field effects of the modulated output field. [27]

Similar to the linear molecular polarizability αᵢⱼ(ω), $\chi^{(3)}$ is also a complex quantity whose real and imaginary components correspond to nonlinear refraction and absorption, respectively. The NLO phenomena are descried in detail in sections 2.2.1 and 2.2.2.

2.1.2 *Units of $\chi^{(3)}$*

For the purposes of this dissertation, *cgs* units expressed as esu or $cm^2statvolt^{-2}$ are used for $\chi^{(3)}$ quantities. The relation to SI units is given by equation 2.8 below. Conversion between statvolt and volts (V) follows 1 statvolt = 299.79 volts (V). [28]

$$\chi^{(3)}[m^2V^{-2}, SI] = \left(\frac{4\pi}{9} \times 10^{-8}\right)\chi^{(3)}[cm^2statvolt^{-2}, esu] \qquad (2.8)$$

2.2 Third-Order Nonlinear Optical Phenomena

The complex nature of $\chi^{(3)}$ gives rise to nonlinear refraction (NLR) and two-photon absorption (2PA) which, as mentioned previously in Chapter 1, are of interest for AOSP and optical limiting applications, respectively. [136, 137] The real part of $\chi^{(3)}$ is associated with NLR, whose measurable quantity is termed the intensity-dependent refractive index n_2 and its imaginary component is associated with 2PA, whose measurable quantity is defined at the two-photon absorption coefficient (β). Both phenomena are related to the degenerate third-order response, $\chi^{(3)}(-\omega, \omega, -\omega, \omega)$, driven by a single frequency. The positive and negative signs describe the time ordering of interacting photons responsible for these effects, where a sufficiently intense optical field of frequency (ω) incident on a material will induce changes to the amplitude and phase of the field itself, through self-action. The following sections (2.2.1 and 2.2.2) provide a description of the definitions of these measurable quantities and their relation to $\chi^{(3)}$.

2.2.1 *Intensity-Dependent Refractive Index*

The relationship between the intensity-dependent refractive index (n_2) and $Re(\chi^{(3)})$ is expressed by [28, 100]

$$n_2(\omega) = \frac{3}{4\,\varepsilon_0\,n_0(\omega)^2\,c}\,Re\big[\chi^{(3)}(-\omega;\omega,-\omega,\omega)\big] \tag{2.9}$$

where $n_0(\omega)$ is the linear refractive index of the material at frequency, c is the speed of light in vacuum, ε_0 and is the permittivity of free space, giving units of m^2W^{-1} for n_2. True to its name, materials with $Re(\chi^{(3)})$ responses experience a change in refractive index upon illumination by an intense electromagnetic or optical field. The magnitude of this index change is dependent on the intensity (I) of the field and is described by

$$n(\omega, I) = n_0(\omega) + n_2(\omega)I \tag{2.10}$$

where the first term ($n_0(\omega)$) of the observed refractive index ($n(\omega,I)$) over the duration of the intense electromagnetic pulse accounts for the linear index and the second ($n_2(\omega)I$) accounts for the intensity-dependent contribution. The intensity of the optical field (I), is expressed as:

$$I = 2n_0(\omega)\varepsilon_0 c|E(\omega)|^2 \tag{2.11}$$

As a result of the index change, the incident beam experiences a phase change ($\Delta\phi$) as it propagates through the NLO medium. The ability to control this change in phase is the central focus of studying materials with promising $Re(\chi^{(3)})$ responses for phase-based switching applications. Examining how $\Delta\phi$ relates to $n_2(\omega)$ in the expression

42

$$\Delta\phi(\omega, I) = \frac{2\pi}{\lambda} \Delta n \, D = \frac{2\pi}{\lambda} \, n_2(\omega) \, I \, D \qquad (2.12)$$

where Δn is the change in refractive index and D is the length the beam propagates through the NLO material, a straightforward approach to achieving large phase changes is to maximize $n_2(\omega)$ for a given field intensity and propagation length. Although relatively small values of $n_2(\omega)$ could be overcome by increasing the input field intensity and propagation length (e.g. increasing waveguide length or film thickness), these adaptations may not be practical for device purposes where minimizing long-term energy costs and product miniaturization are of great importance. This dilemma highlights the importance of careful material design to enable low energy, compact device structures.

The way the refractive index in a NLO material changes, i.e. positively or negatively, is determined by the underlying electronic properties of the material. For the cyanine-like polymethine materials in this dissertation that show a strongly negative $n_2(\omega)$, the origins of this effect are discussed further in Chapter 3. [25] The sign and magnitude of the index change can significantly impact how spatially non-uniform optical beams (i.e. non-top-hat intensity profile) propagate through a given NLO. Taking the example of a Gaussian beam propagating through large $n_2(\omega)$ material, the center of the beam where intensity is highest will experience a larger phase shift than at the lower intensity edges. For positive $n_2(\omega)$ materials, the NLO material acts as a positive lens which focuses the incident beam. Negative $n_2(\omega)$ materials, on the other hand, act as a negative lens and cause the beam to diverge. The significance of these phenomena in NLO measurements will be discussed further in section 2.3.1 on the topic of the Z-scan technique.

2.2.2 Two-Photon Absorption (2PA)

2PA is the process of simultaneously absorbing two photons to excite an optical transition between two real electronic states of an atom or molecule. [95] The measurable quantity of this effect is the 2PA absorption coefficient (β) which, like n_2, is a macroscopic quantity but is instead related to $Im(\chi^{(3)})$. The relationship between $Im(\chi^{(3)})$ and β is given by [100]

$$\beta(\omega) = \frac{3\omega}{2\,\varepsilon_0\,n_0(\omega)^2\,c^2} Im[\chi^{(3)}(-\omega;\omega,-\omega,\omega)] \tag{2.13}$$

with $\beta(\omega)$ having units of mW^{-1}. 2PA can also be characterized by the molecular cross section (δ, with units of m^4 s $photon^{-1}$), which is related to $\beta(\omega)$ simply by

$$\delta(\omega) = \frac{\hbar\omega\beta(\omega)}{N} \tag{2.14}$$

where $\hbar\omega$ is the energy of the incident beam of frequency ω and N is the number density of the material.

In the presence of linear absorption ($\alpha_0(\omega)$), but at photon fluxes sufficient to achieve 2PA, the expression for the absorption coefficient ($\alpha(\omega)$) of a given material becomes: [28]

$$\alpha(\omega) = \alpha_0(\omega) + \beta(\omega)I \tag{2.15}$$

Further if one imagines a beam propagating through a 2PA medium, the intensity-dependent attenuation of the incident beam's amplitude along the direction of propagation (z) is described by

$$\frac{\partial I}{\partial z} = -(\alpha_0(\omega)I + \beta(\omega)I^2) \tag{2.16}$$

and in terms of transmission as

$$T = \frac{I(L)}{I_0} = \frac{T_0}{1 + I_0\beta(\omega)ID_{effective}} \tag{2.17}$$

where linear transmission (T_0) is related to linear absorption (α_0) and the length of propagation (D) through a 2PA medium according to

$$T_0 = \exp(-\alpha_0 D) \tag{2.18}$$

and the effective propagation distance ($D_{effective}$) is given by.

$$D_{effective} = (1 - \exp(-\alpha_0 D))\alpha_0 \tag{2.19}$$

Since the illumination conditions necessary for 2PA are quadratically-dependent on intensity, 2PA is typically only observed when using high power, pulsed, ultrafast lasers sources or from laser beams confined to small focal volumes. For this reason, 2PA has been essential to the development of 3D lithographic techniques for the fabrication of microstructures with nanoscale features, where photopolymerization of organic resins are

only achieved within the femtoliter focal volumes of a focused femtosecond laser beam and thus give line sub-micron line widths. [138]

2.2.3 *Effective $\chi^{(3)}$ Processes – Excited State Absorption*

When one of the optical frequencies involved in a $\chi^{(3)}$ process approaches resonance with a real electronic transition, linear absorption occurs and can result in substantial population of electronic excited states with strong input fields. Since most interesting $\chi^{(3)}$ materials, such as semiconductors, highly conjugated molecules and polymers, have a high density of excited states the probability of transitions to even higher-lying states is also large, given that the available relaxation pathways (e.g. k_{10}, k_{21}, and k^T_{21} from Figure 2.3. Five-state Jablonksi diagram showing the transitions between the lowest single and triplet excited states.) are sufficiently slow. Under these conditions, the successive transitions between electronic states results in a cumulative $\chi^{(1)}$ process that is known as a $\chi^{(1)}$: $\chi^{(1)}$ or effective $\chi^{(3)}$ Process. [27, 28, 100]
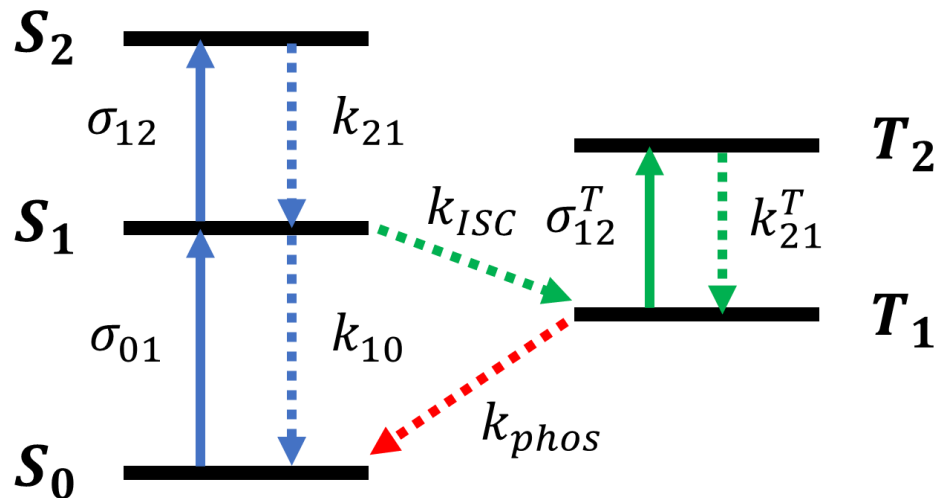
Figure 2.3. Five-state Jablonksi diagram showing the transitions between the lowest single and triplet excited states.

Figure 2.3 shows the various photophysical pathways possible for a five-state Jablonksi diagram after an electron is excited from its singlet ground state (S_0) to higher singlet states S_n. For molecules with large ground state absorption cross sections (σ_{01}) and appreciable excited state absorption cross sections (e.g. σ_{12}), excitation to higher lying states (including triplet states, T_n, if the rate of intersystem crossing, k_{ISC}, and triplet absorption cross section, e.g. σ^T_{12}, is sizeable) is efficient and results in a change in the ratio of molecules that occupy excited states versus those still in the ground state. In addition to the transition cross section, the magnitude of this change depends significantly on the number density of molecules initially found in the ground state (N_0) prior to excitation. Taking the example of linear absorption from S_0 to S_1 (associated with the imaginary part of $\chi^{(1)}$), the absorption coefficient (α_0) is given by

$$\alpha_0 = \sigma_{01} N_0 \tag{2.20}$$

If one only considers the transitions between S_0-S_1 and S_1-S_2, the change in the ground state population (ΔN) of molecules being promoted to S_1, and then potentially S_2 is used to describe the effective absorption coefficient ($\alpha_{effective}$), which gives: [28]

$$\alpha_{effective} = \sigma_{01}(N_0 - \Delta N) + \sigma_{12}\Delta N = \sigma_{01}N_0 + (\sigma_{12} - \sigma_{01})\Delta N \tag{2.21}$$

This can also be written as

$$\alpha_{effective} = \alpha_0 + (\sigma_{12} - \sigma_{01})\Delta N = \alpha_0 + \Delta\alpha \tag{2.22}$$

where the second term (($\sigma_{12} - \sigma_{01})\Delta N = \Delta\alpha$) accounts for intensity-dependent changes in absorption, much like the case of nonlinear absorption in equation 2.15.

Of the photophysical parameters discussed thus far, the relative magnitudes of the absorption cross sections most profoundly influence the type of nonlinear absorption behavior observed in effective $\chi^{(3)}$ processes. A classic example is saturable absorption, which is described by a population inversion to an excited state with a lower absorption cross section than the ground state (i.e. $\sigma_{12} < \sigma_{01}$), using Figure 2.3 as an example) that decreases $\alpha_{effective}$ as beam intensity increases. In the opposite case of reverse saturable absorption, $\alpha_{effective}$ is found to increase with intensity due to a larger excited state absorption cross section relative to the ground state ($\sigma_{12} > \sigma_{01}$). These phenomena have many practical applications, such as saturable absorbing components that enable some passively Q-switched lasers [139] and optical limiting for materials with strong reverse saturable absorption. [71] For the polymethine materials presented in Chapter 3 of this dissertation, the ability to experimentally identify effective $\chi^{(3)}$ processes becomes important for compounds with red-shifted linear absorption bands that take advantage of a pre-resonance enhancement in the telecommunications wavelength window (ca. 1300 – 1600 nm). Since these materials are of interest for AOSP, any linear absorption or effective processes will introduce absorption losses that could deleteriously effect device efficiency and performance. [25, 41] Further, the quantification of 2PA cross sections for highly conjugated polycyclic organic compounds in Chapter 4 will utilize these descriptions to distinguish between short-lived 2PA signals that are spectrally similar to excited state absorption processes but that occur on different time scales.

2.3 Characterization Techniques

2.3.1 *Z-Scan*

Z-scan is a single beam technique by which nonlinear absorption and refraction can be simultaneously measured in solids, liquids, and solutions. In this technique, a sample of a known thickness is translated through the focus of a beam with a Gaussian spatial profile and the nonlinear transmission through the sample is measured as a function of the longitudinal coordinate along the beam axis (*Z*-axis), as seen in Figure 2.4. [140] The open-aperture detector, which monitors the transmitted beam, is only sensitive to nonlinear absorption and is used to obtain the nonlinear absorption coefficient β, from which $Im(\chi^{(3)})$ is calculated. With β known, the closed-aperture detector then provides complementary information in the form of nonlinear refraction by giving n_2 and thus $Re(\chi^{(3)})$. [140] Prior to meeting the first focusing lens, a small portion of the beam is picked and set to a reference detector (detector 1, Figure 2.4) to remove power fluctuations during measurements and improve signal to noise.
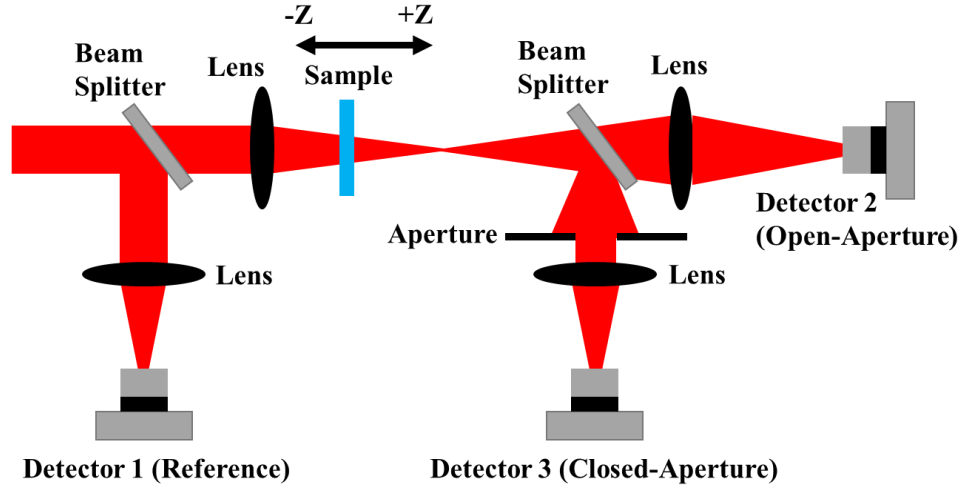
Figure 2.4. Illustration of Z-Scan measurement setup.

For Z-scan measurements, the derivation of n_2 and β is based on strict assumptions such as the incident beam being a diffraction-limited Gaussian beam and the sample thickness is much thinner than the Rayleigh range. Therefore, the beam quality must be carefully quantified prior to actual measurements. Before entering the main measurement line, the laser beam undergoes spatial filtering using a 50 µm diameter diamond-filled circular aperture to obtain at least a 94% Gaussian beam – calculated by a beam profiler (Electrophysics Micronviewer 7290A). Meticulous alignment is crucial to this measurement to where even small misalignments to any of the lenses can easily deform wavefronts. Beam quality is quantified prior to each Z-scan measurement using the Knife-Edge method [141] to determine the beam divergence half-angle (θ) and waist (w_0, i.e. radius at the focus). The product of these two quantities ($\theta \cdot w_0$), called the beam parameter product, is used to establish an relationship with the beam quality factor (M^2), expressed as: [141]

$$M^2 = \theta \, w_0 \, \frac{\pi}{\lambda} \tag{2.23}$$

Perfect, diffraction-limited Gaussian beams give $M^2 = 1$ and values less than one are not physically possible. For the work in this dissertation, only beams with M^2 between 1.0-1.1 were considered usable for measurements. From this information, an additional parameter called the Rayleigh range (Z_R) – defined as the distance from the beam waist in the propagation direction where the beam cross section has increased by a factor of $\sqrt{2}$ – can be calculated. Z_R quantifies the tightness of focusing and is critical for accurately fitting Z-scan data, as the derivation assumes the sample thickness is thinner than the Rayleigh range. For Gaussian beams, Z_R is related to the radius at the beam waist (w_0) and wavelength (λ) by: [141, 142]

$$Z_R = \frac{\pi \, w_0^2}{\lambda} \tag{2.24}$$

Since Z-scan measurements are sensitive to the changes in the spatial and temporal properties of the beam, measurements in this dissertation are carefully calibrated using well-established nonlinearities of references such as fused silica [143], ZnS [144, 145], and ZnSe [145]. Small deviations (ca. ±8%) from the literature values can be used to determine a correction factor that accounts for nonideal beam quality. It is necessary for scans to be taken at multiple irradiances to ensure the measured nonlinearities are of the correct order since Z-scan is sensitive to NLO phenomena of different orders. [146, 147] Additionally, one should be cognizant of other effects like thermal lensing, which can be induced by ultrashort-pulsed, high repitition rate lasers and can obscure the data obtained from Z-scan.

[28, 148] For the work in this dissertation, thermal effects in solution are avoided by lowering the repetition rate to 50 Hz from 1 kHz.
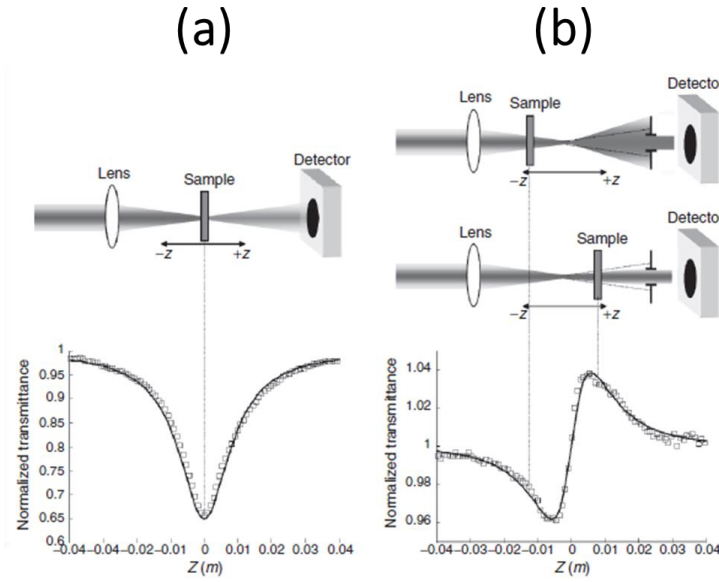
Figure 2.5. Illustration of open- and closed-aperture measurement geometries and typical appearance of scans for (a) a two-photon-absorbing material and (b) a material with positive n_2. Adapted from Perry et al. [27] with permission. Copyright 2008 CRC Press.

Example Z-scan traces are shown in the bottom of Figure 2.5a, where the open-aperture (left) detector shows that, as the sample approaches the focus, the increase in irradiance induces nonlinear absorption and results in decreased transmittance. Once past the focus, the irradiance quickly decreases, and the transmittance is recovered. For third-order nonlinearities, the two-photon absorption coefficient (β) is related to the transmittance with respect to beam axis position $\Delta T(Z)$ by [140]

$$\Delta T(Z) \approx \frac{q}{2\sqrt{2}} \frac{1}{1 + \frac{Z^2}{Z_R^2}} \tag{2.25}$$

and

$$q = \beta I_0 D_{effective} \qquad (2.26)$$

Where I_0 is the irradiance at the focus and $D_{effective}$ is the effective path length, a function

of the linear absorption coefficient (α_0) and sample thickness D), written as:

$$D_{effective} = (1 - \exp(-\alpha_0 D))\alpha_0 \qquad (2.27)$$

With all other parameters known, the two-photon absorption of a sample can be found by

fitting equation 2.25 to the open-aperture transmittance data and iterating the value of β to

obtain the best fit. [28, 140]

Figure 2.5b shows examples of closed-aperture traces for a material with a positive

n_2. The decrease and increase in transmittance with Z-position is explained by simply

thinking of the sample as a lens. A material experiencing an increase in refractive index

(positive n_2) as it approaches the focus (i.e. increasing irradiance) will shift the focus

toward the negative Z direction (-Z, Figure 2.4) and lead to greater beam divergence in the

far field (+Z), which decreases transmission to the closed-aperture detector. This

transmitted intensity is recovered directly after the focus where the positive n_2 sample

collimates the beam. For negative n_2 materials, the opposite trend is expected. The

nonlinear phase change ($\Delta\phi$) can be calculated using the difference in peak and valley

transmittance (ΔT_{PV}) recorded by the closed-aperture detector given

$$\Delta T_{PV} = T_P - T_V \qquad (2.28)$$

$$\Delta T_{PV} \cong 0.406(1 - S)^{0.25}|\Delta\varphi| \qquad (2.29)$$

and

$$\Delta\varphi = \frac{2\pi}{\lambda}n_2 I_0 D_{effective} \qquad (2.30)$$

where is S is the transmittance of the aperture (typically 40%). With known values of I_0 and $D_{effective}$, one can then calculate n_2. [140]

2.3.2   *Nondegenerate Two-Photon Absorption*

Nondegenerate two-photon absorption (ND2PA) is an ultrafast pump-probe technique that is used to obtain 2PA spectra and cross sections of materials in the solution and solid-state. [149, 150] This method is operated much like white light transient absorption, spectroscopy (Figure 2.6), where a strong pump beam excites a sample and is then is "probed" by a weaker white light beam (called the probe beam) whose arrival time after the pump is varied using a delay line. [28, 100] The transmission of probe beam is monitored over discretized time delays and, from the changes in the absorption spectra, one can extract a multitude of kinetic and spectral information of significant importance to physical chemists and spectroscopists such as excited state lifetimes of compounds and polymers and charge generation/separation dynamics that generally take place on the picosecond-to-nanosecond timescale. [87, 151] How ND2PA differentiates itself from standard transient absorption methods is, rather than measuring 1PA transitions, 2PA transitions are examined. Further, because 2PA typically occurs on the femtosecond timescale), long-lived transients are no longer of interest and one would look to track the

appearance and disappearance of 2PA bands within much smaller windows of time closely

after an excitation pulse and with greater temporal resolution to properly capture the 2PA

signal.
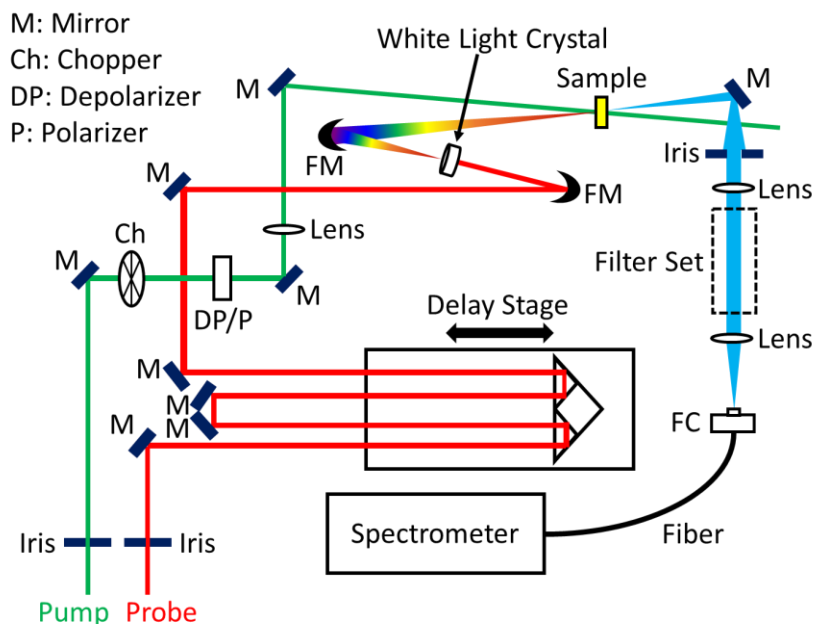
Figure 2.6. Illustration of transient absorption / ND2PA measurement setup.

As the name suggests, ND2PA measurements require that 2PA is accomplished

nondegenerately (i.e. the 2PA transition is completed using two photons of two different

frequencies) rather than degenerately (2PA occurs with two photons of the same

frequency). This is illustrated in Figure 2.7, where the first photon (red arrow) at a

frequency (v_e) lower than the degenerate frequency (v_D) excites the molecules to the

nondegenerate virtual state ($|V_{ND}>$) and is followed by a second photon at a larger

frequency (v_p) to complete the 2PA transition. The subscripts in v_e and v_p indicate that these

frequencies belong to the excitation (i.e. the pump) and probe beam, respectively, and

highlight the key element in setting up a ND2PA experiment: one must excite the sample

with a pump beam of a frequency appreciably less than half the total transition energy (E_{trans}) or, alternatively, total transition wavelength (λ_{trans}). [149] Since the frequency of probe absorption depends on the frequency of the excitation beam, data from ND2PA measurements are reported with respect to E_{trans} which, in terms of wavelength can be written as

$$E_{trans} \propto \frac{1}{\lambda_{trans}} = \frac{1}{\lambda_{ex}} + \frac{1}{\lambda_{probe}} \tag{2.31}$$

where λ_{ex} and λ_{probe} are the wavelengths of the excitation beam and probe beam, respectively.
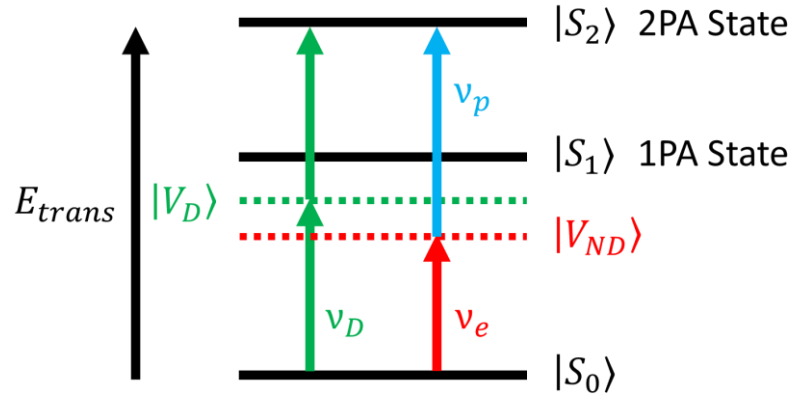
Figure 2.7. Three level Jablonski diagram showing the difference between degenerate (green arrows) and nondegenerate (red + blue arrows) 2PA transitions.

To extract quantitative, physically meaningful information from ND2PA, one must properly account for the attenuation of the excitation and probe beams through the sample, which is expressed as: [28]

$$\frac{dI_e}{dz} = -\alpha_e I_e - 2\sqrt{\frac{\omega_e}{\omega_p}}\beta_{ep}I_e I_p - \beta_{ee}I_e^2 \qquad (2.32)$$

$$\frac{dI_p}{dz} = -\alpha_p I_p - 2\sqrt{\frac{\omega_p}{\omega_e}}\beta_{pe}I_p I_e - \beta_{pp}I_p^2 \qquad (2.33)$$

In these equations, α and β are the linear and nonlinear absorption coefficients and, again, the subscripts e and p indicate the excitation and probe beams, respectively. As such, the left-most term in equations 2.3 and 2.33 accounts for linear absorption losses, the middle terms represents the attenuation due to nondegenerate 2PA, and the right-most terms describe degenerate (self-induced) 2PA of the excitation beam. Since the excitation wavelength of ND2PA measurements is purposefully kept far from any one photon resonances, the left and right terms are considered negligible. Further, because the excitation frequency is less than that required for degenerate 2PA and the probe beam is taken to be weak, the right-most terms in equations 2.3 and 2.33 are ignored, which reduce these expressions to:

$$\frac{dI_e}{dz} = 2\sqrt{\frac{\omega_e}{\omega_p}}\beta_{ep}I_e I_p \qquad (2.34)$$

$$\frac{dI_p}{dz} = 2\sqrt{\frac{\omega_p}{\omega_e}}\beta_{pe}I_p I_e \qquad (2.35)$$

Under these conditions and when the size of the excitation beam is larger than the probe, the probe experiences exponential loss as it propagates through the sample and is quantified by the exponential loss factor (Γ_0)

$$\Gamma_0 \cong 2\sqrt{\frac{\lambda_e}{\lambda_p}} \beta_{ep}(1 - R_e)I_{e0}L \tag{2.36}$$

Where λ_e and λ_p are the excitation and probe wavelengths, respectively, R_e is the Fresnel reflection loss of the excitation beam, is the initial intensity of the excitation beam, and L is the sample thickness. Γ_0 is related to probe transmittance ($T \equiv I_p/I_{p0}$) by

$$T = (1 - R_p)^2 exp(-\Gamma_0) \tag{2.37}$$

with R_p accounting for Fresnel reflection losses of the probe beam. [28]

By carefully characterizing the 1/e beam diameters and input energy, one can obtain the nondegenerate 2PA coefficient (β_{ND}) by way of analysing the 2PA response of the sample as a function of pulse energy at the sample and the excitation volume of the excitation and probe beams. Building on equation 2.13, β_{ND} can written as

$$\beta_{ND}(\omega_e, \omega_p) = \frac{3\omega_p}{2\,\varepsilon_0 n_e n_p\,c^2} Im\left[\chi_{ep}^{(3)}(-\omega_p; \omega_p, -\omega_e, \omega_e)\right] \tag{2.38}$$

where ω_p is the angular frequency of the probe and $n_e n_p$ is the product of the refractive index of the sample at the excitation and probe absorption wavelength, respectively. Experimentally, values of β_{ND} are determined by iterating to obtain a calculated probe transmittance value (or, equivalently, ΔOD that one obtains directly from transient absorption) that matches that of a sample at a given energy. This value is then converted into the ND2PA cross section (δ_{ND}) according to:

$$\delta_{ND}(\omega_e, \omega_p) = \frac{2\,\hbar\,\omega_p \beta_{ND}(\omega_e, \omega_p)}{N} \qquad (2.39)$$

For this thesis, ND2PA is used to obtain 2PA spectra and of highly conjugated, quadrupolar, polycyclic molecules in chloroform solutions that are of interest for NIR optical limiting applications. This data, complemented by Z-scan measurements, is presented in Chapter 4.

2.3.3 *Prism Coupling*

Prism coupling is spectroscopic technique used to measure the thickness, refractive index and linear optical losses of thin films. [152-154] Compared to other techniques like ellipsometry and reflectance spectroscopy, prism coupling provides a simple and expeditious way to obtain accurate optical information about a variety of organic and inorganic thin film materials, gratings and waveguides with good precision without complex modelling or alignment. [152, 155] Such information is critical for the understanding how a given thin film material will perform in optical device applications and whether the limiting factor for an emerging technology is inherently limited by its chemical and/or optical properties or if the fabrication of a thin film is not satisfactory for the desired application.
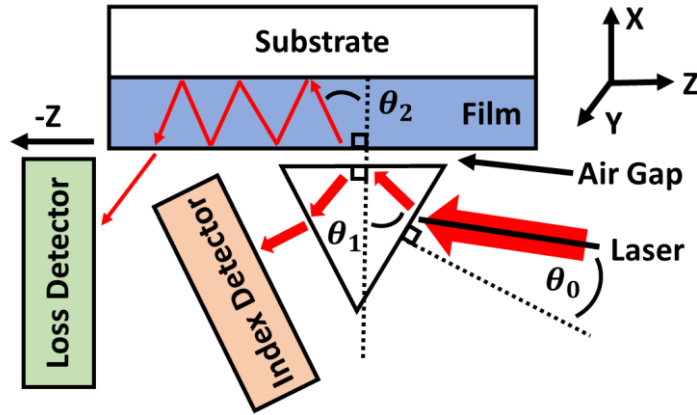
Figure 2.8. Illustration of the prism coupling for refractive index and linear loss measurements of a high index film on a fused silica substrate. Drawings not to scale.

Focusing first on refractive index measurements, this setup consists of a high index prism and a photodetector mounted on a rotational stage which is illuminated by a transverse electric (TE) CW laser beam with narrow line width on one side of the prism, as show in Figure 2.8. To begin measurements, the film of interest in brought into contact with the base of the prism with a pneumatic actuator only separated by a small air gap (100-200 nm), depending on the roughness of the prism and film surfaces. At most angles of incidence (θ_0), the laser beam is refracted into the prism and undergoes total internal reflection (TIR) by reflecting off the base of the prism which then is relayed to the index photodetector. However, for values of θ_0 larger than prism's critical angle, the TIR condition no longer holds and light travels across the air gap and couples into the film. The angles at which coupling occurs result in a loss of reflected intensity on the index photodetector and can be plotted as seen in Figure 2.9a.
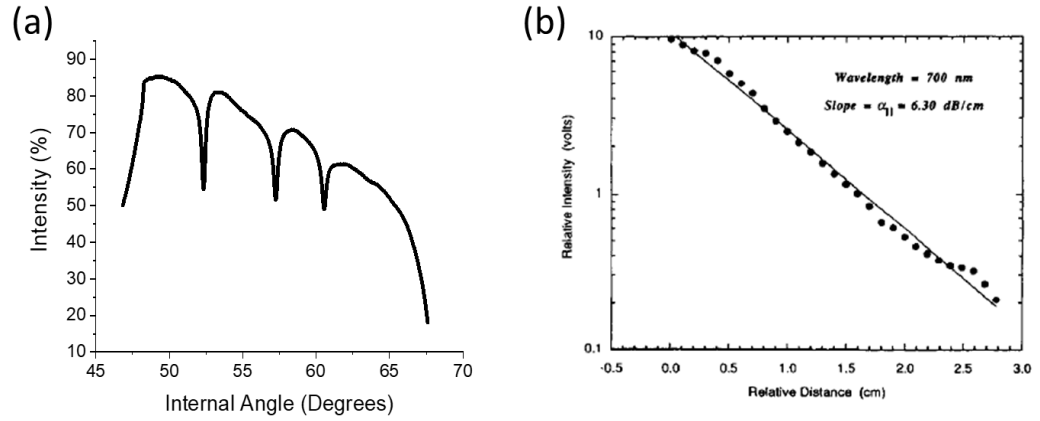
Figure 2.9. Plot of (a) three sharp, guided modes coupled within 50-62° incidence (b) example of linear loss scan and exponential fit of mylar on silicon wafer – reproduced from Bai et al. [156] with permission. Copyright 1992 John Wiley & Sons, Inc.

Each dip corresponds to individually coupled modes at specific coupling angle and can be used to solve for the refractive index and thickness of the film. For the mth mode (where m = 0 for the mode with the largest, positive angle) one can accomplish this by numerically solving an eigenvalue equation, commonly referred to as the mode equation: [157, 158]

$$\frac{2\pi n}{\lambda} Cos(\theta_2)T + \Psi_{fa} + \Psi_{fs} = m\pi \ (m = 0, 1, 2, ..., n) \qquad (2.40)$$

In the mode equation, Ψ_{fa} and Ψ_{fs} are the Fresnel phase shifts at the film-air and film-substrate interfaces, respectively, λ is the incident wavelength, θ_2 is the refraction angle of light upon entering the film and T is the film thickness. Prior to calculation, individual modes that are identified by the incidence angle at which they reach a local minimum. If two or more modes are identified, this set of complex transcendental equations can be used to simultaneously obtain the thickness and refractive index of a given film. If only one

61

mode is found, one must specify either the film thickness to calculate refractive index and vice versa. [153, 158]

For films higher in refractive index than their substrates, as is the case for films studied in this dissertation, the coupled beam propagates as a guided mode. [152] In this sense, the film acts as a waveguide which, for all real systems, exhibits some degree of optical loss as modes propagate down the length of the film and could be caused by factors such as film defects, variations in thickness and/or linear absorption. [156, 159] As shown in Figure 2.8, propagation loss measurements, referred to as linear loss measurements in this thesis, are accomplished by scanning a fibre optic probe over the length of a film and monitoring the light intensity scattered from the surface of the film over a specified distance. This measurement assumes that every point along the direction of propagation where light is scattered and measured by probe is proportional to the light remaining in the film. [152, 158] A plot of light intensity against distance is obtained and is fit by an exponential, like in Figure 2.9, to quantify the optical loss in units of dB cm^{-1}.

For the purposes of this dissertation, this technique is used to measure the optical properties of polymer and blend films doped with NLO chromophores to complement Z-scan measurements by providing refractive indices for accurate data fitting, supporting information about film quality and physical interactions in the solid state, and linear loss data to further assess optical quality and potential device relevance for a given film.

2.3.4 *Ellipsometry*

Spectroscopic ellipsometry is a technique used to extract optical information such as refractive index, absorption coefficient, and the dielectric constant (a complex function

of the index and absorption coefficient) by monitoring changes in polarization of a light beam that is reflected or transmitted from a material. [160, 161] If more material parameters are known, the optical information can also be used to solve for useful physical quantities such as submicron layer thickness, roughness, material composition, and crystallinity. [161-164] In addition to the flexibility of this technique in measuring different materials, the speed and ease with which one can measure samples has made this characterization method a staple in materials science and has found uses in several fields in other areas of science and engineering. [165]
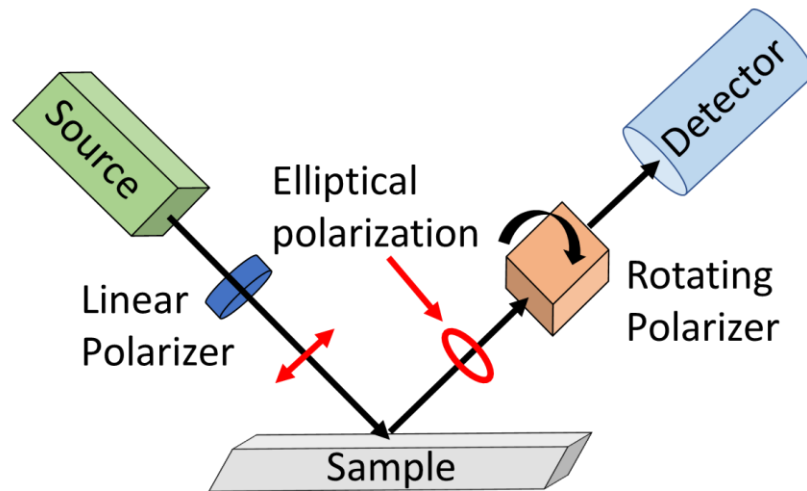
Figure 2.10. Depiction of reflection ellipsometry measurement setup in the rotating analyzer (i.e. rotating polarizer) geometry.

A typical reflection ellipsometry setup is illustrated in Figure 2.10 and can be concisely summarized in four steps. [166] First, a low-intensity light source passes a beam through a linear polarizer to produce linearly polarized. Second, this linearly polarized light reflects off the sample and is converted to elliptical polarization (denoted by red ellipse). Third, the elliptically polarizer light interacts with a rotating polarizer (a.k.a. rotating

analyzer) that records the polarization of the reflected light at certain angles with the amount of transmitted light dependent on change in elliptical polarization induced by the sample. Fourth, light beams of a certain polarization pass through the rotating polarizer and are read by a photodetector. In the first step, the polarization of the beam is oriented between the s- and p-polarized planes, where s-polarization (derived from senkrecht – German for perpendicular) are light waves whose electric field propagates perpendicular to the plane of incidence and p- are waves whose electric fields are parallel to the plane of incidence. [160] This is done so that the incident linearly polarized beam is composed of in-phase s- and p-polarized waves of equal amplitudes. With this polarization is known, the complex reflectance ratio ($\rho = r_p/r_s$) is found by analysing the polarization data obtained via the rotating analyzer. This ratio is related to the difference in amplitude ratio ($\tan(\Psi)$) and phase shift (Δ) of the reflected beam by: [160]

$$\rho = \frac{r_p}{r_s} = tan(\Psi)e^{i\Delta} \tag{2.41}$$

Despite the simplicity in collecting (ρ), for most materials and especially multilayer systems, ellipsometry can only indirectly solve for optical parameters, which is typically achieved through modelling. Although many models exist, one must make sure that the model accurately describes the physical description of the sample and fits the data well (i.e. minimizes mean squared error (MSE)) to get physically reasonable results. For known materials with optical or dielectric data characterized by other methods, it is common to use trusted, tabulated data to reduce the number of free variables and simplify analysis.
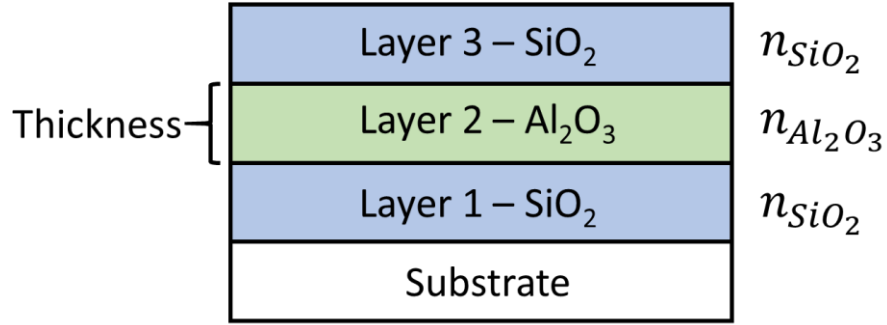
Figure 2.11. Depiction of multilayer film structure consistent of two silica layers and one alumina layer and the relevant parameters to define for ellipsometric fitting.

For example, if one were looking to obtain the effective refractive index of a multilayer stack of silica and alumina thin films (Figure 2.11), one could model this system by specifying an estimated thickness for each layer and then fit against tabulated index data. Additionally, for measurements with white light illumination, rather than adjusting optical properties at each wavelength from tabulated data, fitting can be accomplished using a dispersion relation such as the Sellmeier equation [163]

$$n^2(\lambda) = 1 + \frac{B_1\lambda^2}{\lambda^2 - C_1} + \frac{B_2\lambda^2}{\lambda^2 - C_2} + \frac{B_3\lambda^2}{\lambda^2 - C_3} \qquad (2.42)$$

to determine the effective index for the multilayer structure by empirically solving for the Sellmeier coefficients (B_{1-3}, C_{1-3}) to optimize the fit. Compared to simpler dispersion relations, like the Cauchy formula, the Sellmeier is constrained by the Kramers-Kronig consistency which ensures that the refractive index information obtained maintains a physically reasonable shape. [160] As will be shown in Chapter 5, it is also possible for the dispersion curve (dependence of refractive index on wavelength) to be modelled with an effective medium approximation (EMA), that more closely accounts for the index

dispersion of composite materials, like MgO/Si. [163, 167] The expression for common EMAs is expressed by [168]

$$\frac{\langle \varepsilon \rangle - \varepsilon_h}{\langle \varepsilon \rangle + \gamma \varepsilon_h} = \sum_j f_j \frac{\varepsilon_j - \varepsilon_h}{\varepsilon_j + \gamma \varepsilon_h} \tag{2.43}$$

where $\langle \varepsilon \rangle$ is the dielectric function of the effective medium, ε_h is the dielectric function of the host material, f_i is the fraction of the jth component, and γ is a parameter related to the screening and shape of inclusions, e.g. $\gamma = 2$ for 3-dimensional spheres. [163] The fitting procedure is characterized by using preloaded material files containing optical information of each material that are used to define the dielectric functions of the host and other components. The fraction of the other component is then specified based on elemental analysis techniques, such as energy dispersive X-ray spectroscopy (EDX) for a given sample and the routine is iterated to obtain the best fit, adding additional roughness layers, if necessary. [169]

In Chapter 5 of this dissertation, spectroscopic ellipsometry is used to confirm the refractive index of amorphous silica films made from pyrolyzed, spin-coated tetraethylorthosilicate (TEOS) solutions and higher refractive index MgO/Si films made from converted silica films. These measurements were accomplished using a M-2000UI Ellipsometer (J.A. Woollam).

2.3.5   *Far Field Diatom Interference Imaging*

As will be discussed in Chapters 5 and 6, diatom frustules give bright spots in the far field behind the frustule plane that resemble focal spots because of a complex

superposition of interference phenomena. [125, 127, 129] In order to capture the distance at which these local intensity maxima appear, a modular microscope setup was built to image far field diffraction patterns with spatial and imaging resolution sufficient for capturing sub-micron-sized features. Illustrated in Figure 2.12, diatom frustules and their high index replicas adsorbed on sapphire substrates are mounted onto a 3D translation stage and held by a polydimethylsiloxane-covered coverslip. Alignment began by roughly centring an approximately monochromatic laser beam ca. 3-5 mm in diameter (depending on wavelength) on the objective directly behind the sample holder. Diatom samples were then located and centred within the field of view of the objective and the beam alignment to the sample was then fine-tuned by maximizing intensity on the CCD camera while adjusting an input mirror.
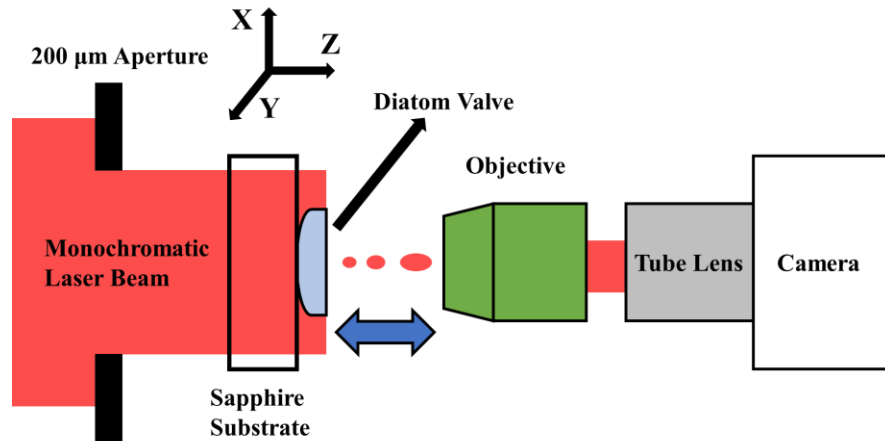
Figure 2.12. Illustration of focal spot imaging measurement setup. Drawings not to scale.

Once the sample was in focus and the beam is properly aligned, it was necessary to eliminate diffraction from other sources such as substrate defects near the frustule and debris from other broken frustules on the same substrate. This was accomplished by carefully placing a 200 µm aperture ca. 1 cm before the plane of the diatom to reduce the

illumination area to circular area just around the periphery of the frustules. At this distance from the frustules, the beam divergence from the aperture is negligible and provides reasonably collimated beams with which measurements can be performed. [127] Using a LabVIEW-controlled stage, measurements proceed by starting at the plane where the diatom frustule is in focus and then translating the sample away from the objective along the beam axis (Z-axis) in discrete steps with sufficient resolution (typically 2-5 µm) to image subtle changes in the resulting interference pattern at each step as one travels further into the far field. All the images collected for a single frustule at a given wavelength are then examined to determine the distance at which local intensity maxima appear and disappear. Given a complete set of interference information for a diatom at multiple wavelengths, the trend in focal distance data is correlated to the physical properties of the diatom, such as hole pattern, diatom size and refractive index of the native frustules and high index replicas.

In this dissertation, this measurement setup is utilized to quantify the dependence of focal distance on wavelength for native biosilica frustules and their higher index, MgO/Si and Mg_2Si, replicas as a function of refractive index. Additionally, this technique is used to image interference patterns from of synthetic hole arrays made in thin films of silica, MgO/Si and Mg_2Si to determine the relationship between refractive index and focusing distance, as well as observe focal behavior for non-diatom-like hole patterns.

2.4 Diffraction Theory and the Interference of Electromagnetic Waves

2.4.1 *Diffraction and Interference Theory*

The general phenomenon of diffraction occurs when a wavefront, from a sound, matter, or light wave, is obstructed in any way that results in a change in amplitude or phase upon interaction with the obstruction. [170] In this section, the origins of this effect will be discussed within the framework of classical wave theory to provide context for the discussion of the optical effects of diatoms and related structures in Chapters 5-6. For the purposes of this thesis, only diffraction relevant to interactions of optical waves in the visible and IR wavelength range will be discussed.

Starting from the description of a harmonic wave, which adequately explains the orthogonal components of electromagnetic radiation (EMR) from a classical standpoint, a one-dimensional propagation of the wave is described by an oscillatory function like sine or cosine. As such, the wavefunction ($\psi(x, t)$) for a progressive wave traveling at velocity (v) in the x-direction can be expressed as [171]

$$\psi(x, t) = A \sin\big(k(x - vt)\big) \tag{2.46}$$

where t is time, A is the amplitude and the propagation constant is defined as $k = 2\pi/\lambda$, taking λ as the wavelength. Often, this equation is written in terms of angular frequency ($\omega = 2\pi v$) which then gives:

$$\psi(x, t) = A \sin(kx - \omega t) \tag{2.47}$$

This form of the wave equation is useful when discussing an important concept of diffraction and the interference of EMR: phase ($\phi(x,t)$), which is defined as a singular point in time and space of a wave cycle and is described by the argument of sine in the wave equation

$$\phi(x,t) = kx - \omega t + \varepsilon \tag{2.48}$$

with ε representing the initial phase. [171] Taking an optical wave as an example, when a light wave travels through a typical dielectric medium the phase velocity (v) is reduced due to the refractive index (n) of that medium (with $n > 1$) as shown in:

$$v = \frac{c}{n} \tag{2.49}$$

where c is the speed of light (ca. $3x10^8$ m/s). Upon exiting the medium, the propagating wave will have obtained a different phase compared to a wave from the same source that did not interact with the medium that still possesses the initial phase (ε). This is illustrated in Figure 2.13, where the black curve shows a sine wave that did not pass through the medium, the red curve shows a wave that did propagate through the medium and is shifted out of phase by 90º (or $\pi/2$ radians) upon transmission relative to the black curve, and the blue wave that is 180º (π radians) out of phase, which also passed through the medium. The exact phase difference depends on the magnitude of the refractive index and the path length of the medium through which a beam propagates. [170, 171]
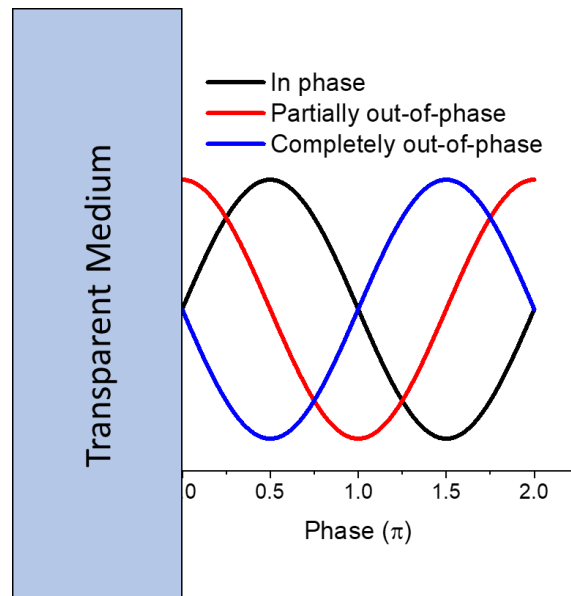
Figure 2.13. Hypothetical illustration of three beams spatially overlapping with different phases. (black) freely propagating wave, (red) transmitted wave 90° out of phase, (blue) transmitted wave completely out of phase by180°

Thinking of these waves in the optical domain with a visible frequency, a superposition of waves (i.e. the sum of wave amplitudes upon overlap in space and time) can create in a pattern of dark and bright areas that are the result of interference between waves. In the case of the bright areas, two waves overlap with the same phase and amplitudes which doubles the amplitude as a result of constructive interference. In the opposite case, destructive interference, two waves of equal amplitude interact completely out-of-phase (i.e. have a phase difference of π), which results in amplitude cancellation and thus no visible light intensity. Using Figure 2.13 as a visual guide, constructive interference can be rationalized by considering the interference of two like waves such as two black waves of the same phase interfering without passing through the medium, or even two red waves interfering having experienced the same phase shift after exiting the medium. On the other hand, total destructive interference is accomplished when the black

71

and blue waves overlap. Naturally, there are varying degrees of destructive interference. One such example can be visualized by considering the interference between the black and red wave, which are only $\pi/2$ out-of-phase but will still result in some partial destructive interference, resulting in a slight reduction in the overall amplitude which, for visible light, could appear as dimming to the eye. [170, 172] These types of interference are similar to what might be obtained from a transmission phase grating and are important concepts for understanding the behavior of periodically ruled structures or transparent films with pseudo-periodic differences in material thickness, like diatom foramen patterns. [127, 129]

As will be discussed in Chapters 5 and 6, the holes patterns of diatoms are also analogous to the classic double (or more) slit on an opaque screen experiment, the diffraction from which is described differently than the phase-shifting phenomena described earlier. Prior to discussing diffraction from a slit, it is salient to define the Huygen-Fresnel Principle, which states that every unobstructed point of a wavefront serves as a source of spherical secondary wavelets of the same frequency as the primary wave and that the amplitude of the optical field at any point beyond is a superposition of all the wavelets. [170] This is illustrated in Figure 2.14, where the diffraction of a plane wave by a single slit gives a secondary wavelet originating from unobstructed parts of the incoming plane wave that interact with points A and B at the edge of the slit. Taking P to represent an arbitrary observation point, the maximum optical path length difference (Λ_{max}) between point sources from which secondary wavelets are generated is: [170]

$$\Lambda_{max} = |\overline{AP} - \overline{BP}| \tag{2.50}$$

Acknowledging that Λ_{max} is less than or equal to $\overline{AB}$, with the later only holding true at large values of P, when the wavelength of the incident wave (λ) is greater than $\overline{AB}$, then it follows that $\lambda > \Lambda_{max}$. Since the diffracted waves were initially in-phase, they will all interfere constructively (to varying degrees) where P happens to be. As such, if the wavelength is much larger than the slit, the waves will necessarily spread out to larger diffraction angles in the region past the slit. Further, the smaller the slit is the more circular the diffracted wave comes. [170] Although the discussion thus far is qualitative, the concept of wavelength dependent diffraction angles is referred to frequently when discussing the focusing distance phenomena from diatom valves in Chapters 5-6.
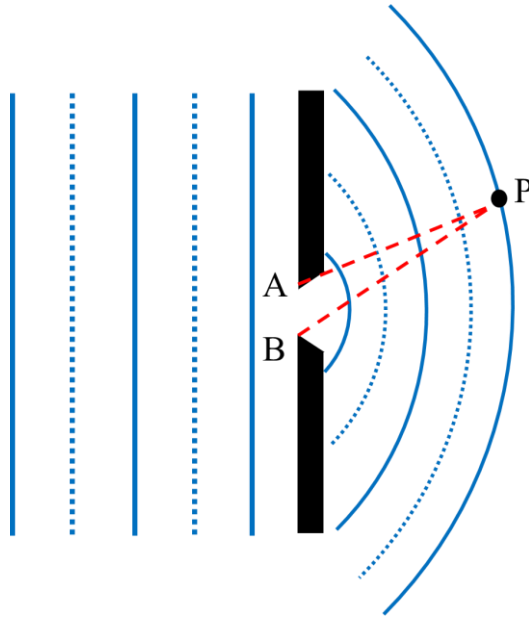
Figure 2.14. Diffraction of a plane wave by a small aperture of width $\overline{AB}$.

Despite the information gained from the single slit picture, diatoms consist of many holes and the resulting interference pattern will be a complex superposition of the wavelets diffracted by these features. This is analogous to a screen bearing many slits and thus is salient to discuss an analogous, well-established theoretical framework for describing the

73

diffraction from such arrays. A simple example that describes these phenomena well is Young's famous double slit experiment. [172, 173] As depicted in Figure 2.15, this experiment involved the illumination of two slits separated by known distance (a). At a known wavelength (λ) diffraction occurs and is projected onto a screen (Σ_o) far from the diffracting screen (Σ_a) and where a fringe, i.e. spot of constructive interference, is observed at P.
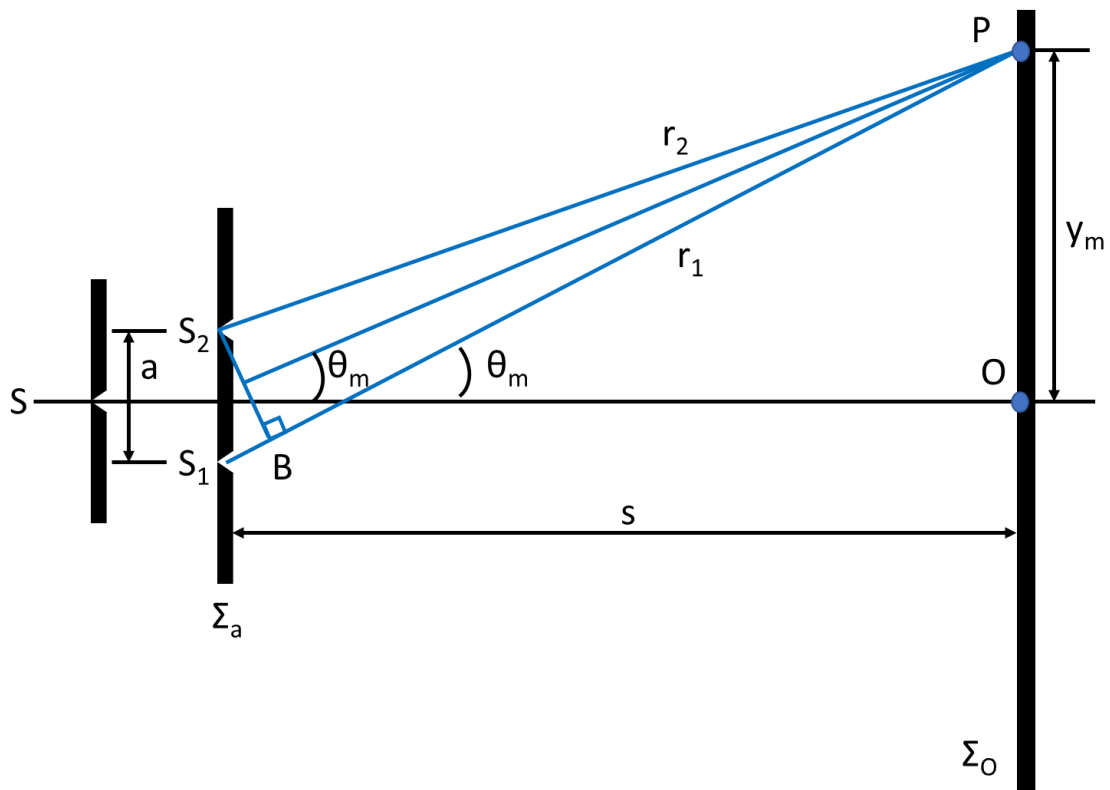
Figure 2.15. Young's double slit experiment showing the geometric parameters used to derive the relationship between the diffraction angle (θ_m), wavelength, and slit spacing (a). Point "O" is the origin point directly across from the center of the diffracting screen where zeroth order diffraction occurs, S_1 and S_2 are the diffracting slits, s is the distance between the diffracting screen and the observation screen, wavelets illuminating the diffraction screen are shown to be generated by a single slit at S, y_m is the distance between arbitrary orders of diffraction, and B is the point where a perpendicular segment approximate is made to derive θ_m .

From Young's experiment, a simple relation was derived to determine the spacing between orders of diffraction (m) in the fair field that is related to the distance between slits (a) by

$$\theta_m = \frac{m\,\lambda}{a} \tag{2.51}$$

where is θ_m the diffraction angle for a fringe of order m, and λ is the incident wavelength (see reference [172] for full derivation). From this expression, increasing the incident wavelength or, equivalently, decreasing the spacing between the slits increases the diffraction angle and thus causes an increase in y_m, assuming a fixed observation screen position. As will be discussed with diatom samples (section 5.2), this is analogous to wavelets diffracted by neighboring holes in the foramen layer interfering at distances closer to the plane of the valve when illuminated by longer wavelength radiation or when the hole spacings are brought closer together, as in the case of synthetic hole arrays whose hole positions can be controlled.

2.4.2 *Fresnel and Fraunhofer Diffraction*

This section presents a brief and qualitative introduction to the two types of diffraction phenomena related to diatom interference patterns. Classically, these phenomena are characterized by the point at which ones observes the diffracted wavefronts, which are illustrated in Figure 2.16. Starting from a point source (S), one can see that, in the field close to S, the waves still possess significant curvature. If this wave were to interact with a single slit in a diffracting screen in this short distance regime, the slit would be illuminated by spherical wavefront, which means the distance between S and where the

wavefront reaches the aperture will be different for each point. As a result, the strength of the electric field will vary point-to-point along the diffracting screen and describes what is called Fresnel diffraction or near-field diffraction. In this case, the propagation of waves and thus the evolution of the electric field over this distance range is described by the Fresnel equation. [173]
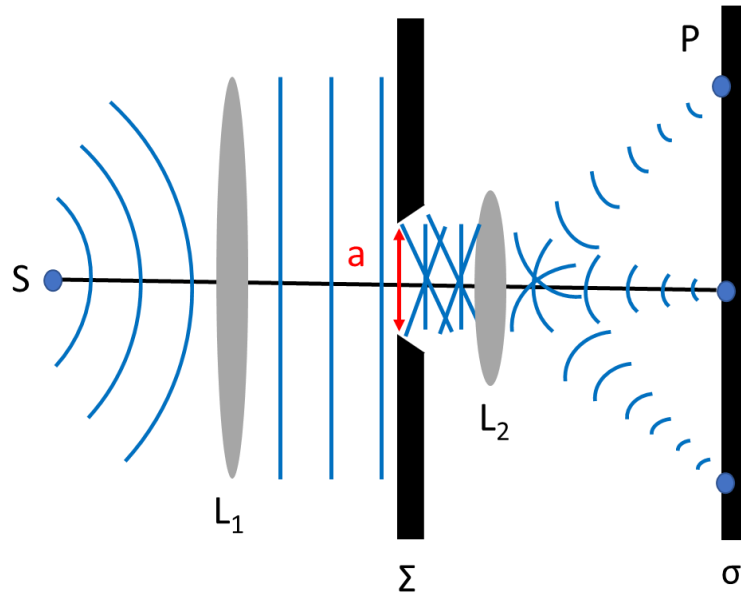
Figure 2.16. Practical realization of the optical setup for observing Fraunhofer diffraction in a compact arrangement. S is the point source, L_1 is a collimating lens to flatten wavefronts from S, a is the width of the slit, L_2 is a positive lens to focus plane waves diffracted from the slit to shorter observable distance, and P are the observation points on the observation screen (σ).

In the opposite regime, called Fraunhofer diffraction, waves are encountered in the far field where one finds that the wavefronts have flattened to the point where they can be considered plane waves. This also applies to focused beams, where the wavefronts are found to be approximately flat in areas with small cross sections. The evolution of the electric field in this diffraction regime is then described by the Fraunhofer equation. [170,

173] For systems like diatoms with complex layer and hole structures, the ability to ascribe diffraction from specific layers to the either the Fresnel or Fraunhofer regime will enable a better understanding of how light propagates through the frustule. As a practical rule-of-thumb, Fraunhofer diffraction will occur at a diffracting object according to

$$R > \frac{a^2}{\lambda} \qquad (2.52)$$

where R is the smaller of the two distances from the point source (S) to the diffracting screen (Σ) and from Σ to the observation point (P), and a is the width of the diffracting object. Although a comprehensive review of the mathematical physics is beyond the scope of this thesis, a more detailed explanation of these diffraction phenomena and how they can be used to solve for the magnitude of the electric field in the near and far fields, respectively, can be found in references [170, 172, 173].

2.4.3 *Poisson-Arago Diffraction*

Poisson-Arago (PA) diffraction, otherwise known as Poisson's spot, is a diffraction phenomenon that describes the appearance of a bright spot in the dark plane behind the center of an opaque, circular object illuminated by a plane wave (Figure 2.17a). [170] This effect is relevant to diatoms due to the presence of a well-defined edge for *C. wailessii* valves, as well as other circular diatoms species. Although the diatom valves do not fit the traditional definition of an opaque object, the index contrast between the valve and air, particularly for higher index replicas, is sufficient to induce diffraction. This was confirmed experimentally by Di Caprio et al. [174] for ca. 200 µm-wide *C. wailessii* frustules using digital holography.
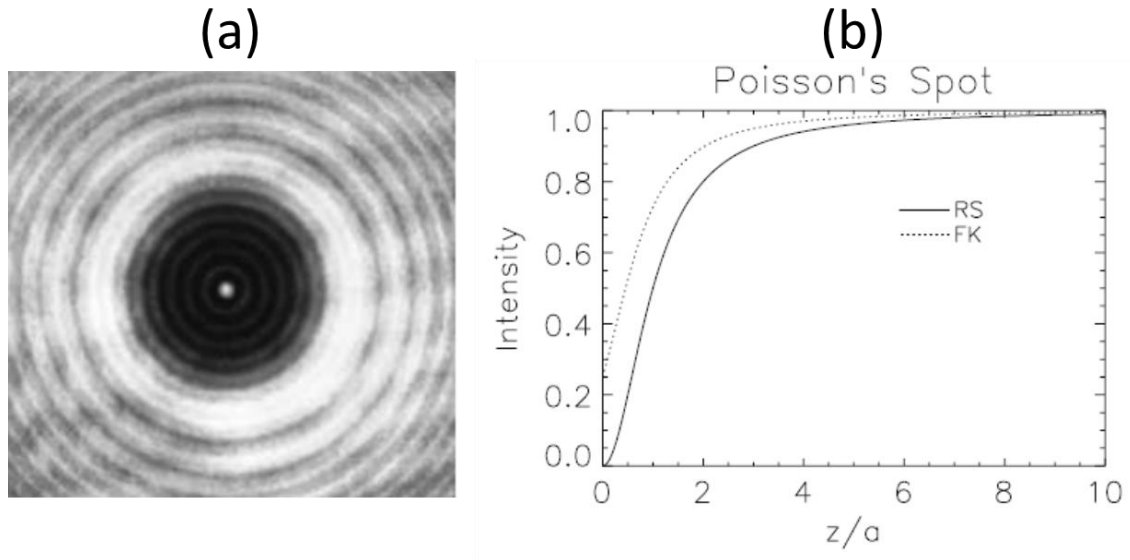
Figure 2.17. (a) Image showing PA diffraction from a 1/8 inch-diameter ball bearing glue to a microscope slide and illuminated by a HeNe laser. Reproduced from Hecht et al. [170] with permission. Copyright 2002 Pearson. (b) Plot showing the intensity distribution along the central beam axis (z) in the dark plane behind an obstruction of radius (a) as predicted by the Rayleigh-Sommerfield (RS) and Fresnel-Kirchhoff (FK) models. Reproduced from Lucke [175] with permission. Copyright 2006 European Journal of Physics.

It has been shown that the Rayleigh-Sommerfield diffraction model can accurately predict the distance at which PA diffraction appeared in the dark plane and the intensity distribution as a function of distance. [175, 176] As seen in Figure 2.17b, the spot intensity reaches 50% of its maximum value at a distance that follows $1 = z / a$, and saturates at nearly 100% according to $4 = z / a$. Using the ball bearing from Figure 2.17a, this means that Poisson's spot reaches 50% maximum intensity just 1/16 inches away from the ball bearing and 100% at approximately 1/4 inches. As will be discussed in Chapter 6, diffraction from the edge of smaller diatom valves may have a significant contribution to the overall interference pattern. Simple calculations like those presented here will be discussed within the context of interference imaging measurements and simulations.

2.5   Simulation Methods

2.5.1   *Beam Propagation Simulations*

The program employed in this dissertation is RSoft CAD Environment 7.0, using the BeamPROP package to compute the propagation of light waves in waveguide geometries. Since diatom valves and replicas are approximately comprised of slabs of silica, MgO/Si, or Mg_2Si, the waveguide description was deemed appropriate. This technique uses finite difference beam methods (BPM) [177, 178] to solve parabolic approximation of the Helmholtz equation and assumes transparent boundary conditions as described in reference [179]. To briefly describe the critical parts of this technique, the scalar field assumption allows the wave equation to be written in the form of the Helmholtz equation for monochromatic waves

$$\frac{\partial^2 \varphi}{\partial x^2} + \frac{\partial^2 \varphi}{\partial y^2} + \frac{\partial^2 \varphi}{\partial z^2} + k(x,y,z)^2 \varphi = 0 \tag{2.53}$$

Here the scalar electric field has been written as

$$E(x,y,z,t) = \varphi(x,y,z)e^{-i\omega t} \tag{2.54}$$

and the notation $k(x,y,z) = k_0 n(x,y,z)$ has been introduced for the spatially-dependent wavenumber, with $k_0 = 2\pi/\lambda$ being the wavenumber in free space. As such, the geometry of the problem is defined entirely by the refractive index distribution $n(x,y,z)$.

Considering that, for a typical waveguide problem, the most rapid variation in the field (φ) is the phase variation due to propagation along the guiding axis (assumed to be the Z-direction), this factored out by introducing a slowly varying field (u) via the approach

$$\varphi(x, y, z) = u(x, y, z)e^{i\bar{k}z} \tag{2.55}$$

In this expression, $\bar{k}$ is a constant that represents the average phase variation of the field (φ), called the reference wavenumber. This quantity is frequently expressed in terms of a reference refractive index ($\bar{n}$), via $\bar{k} = k_0\bar{n}$. Introducing equation 2.55 into equation 2.53, one obtains an expression for the slowly varying field, which after some rearrangements gives: [178]

$$\frac{\partial u}{\partial z} = \frac{i}{2\bar{k}}\left(\frac{\partial^2 u}{\partial x^2} + \frac{\partial^2 u}{\partial y^2} + \left(k^2 - \bar{k}^2\right)u\right) \tag{2.56}$$

Equation 2.56 is said to be the basic BPM equation in three dimensions. In this form, with a known index profile (n(x,y,z)) an input field (u(x,y,z)) can be defined (for this dissertation all incident fields are plane waves) and thus the evolution of the field while interacting with the waveguiding structures (hole patterns, diatoms, etc.) can be determined for real, positive values of z. The procedure for importing index profiles will be discussed in section 5.4.4.

Although a comprehensive review of this method is beyond the scope of this dissertation, additional information about the operations of this technique can be found in references [177, 178, 180, 181]. In Chapter 5, beam propagation simulations will be used

to determine the theoretical effect of refractive index on the focusing behavior for hole

pattern arrays. Results will then be discussed in Chapter 6 to corroborate experiments.

2.6   References

25.   Hales, J.M., Barlow, S., Kim, H., Mukhopadhyay, S., Brédas, J.-L., Perry, J.W., and Marder, S.R., *Design of Organic Chromophores for All-Optical Signal Processing Applications.* Chemistry of Materials, 2014. **26**(1): p. 549-560.

27.   Perry, J.W. and Hales, J.M., *Organic and Polymeric 3rd-Order Nonlinear Optical Materials and Device Applications*, in *Introduction to Organic Electronic and Optoelectronic Materials and Devices*, S.-S. Sun and L.R. Dalton, Editors. 2008, CRC Press: Boca Raton, FL. p. 936.

28.   Sutherland, R.L., *Handbook of Nonlinear Optics.* Second ed. 2003: Marcel Dekker, Inc. 971.

41.   Stegeman, G.I. *Material figures of merit and implications to all-optical waveguide switching*. in *Proceedings of SPIE*. 1993.

71.   Perry, J.W., *Organic and metal-containing reverse saturable absorbers for optical limiters*. 1997, Boca Raton, FL: CRC Press Inc.

87.   Hales, J.M., Cozzuol, M., Screen, T.E.O., Anderson, H.L., and Perry, J.W., *Metalloporphyrin polymer with temporally agile, broadband nonlinear absorption for optical limiting in the near infrared.* Optics Express, 2009. **17**(21): p. 18478-18488.

95.   Göppert-Mayer, M., *Über Elementarakte mit zwei Quantensprüngen.* Annalen der Physik, 1931. **401**(3): p. 273-294.

100.   Boyd, R.W., *Nonlinear Optics.* Third ed. 2008, Burlington, MA USA: Elsevier Inc.

125.   De Tommasi, E., De Luca, A.C., Lavanga, L., Dardano, P., De Stefano, M., De Stefano, L., Langella, C., Rendina, I., Dholakia, K., and Mazilu, M., *Biologically enabled sub-diffractive focusing.* Optics Express, 2014. **22**(22): p. 27214-27227.

127.   Stefano, L.D., Rea, I., Rendina, I., Stefano, M.D., and Moretti, L., *Lensless light focusing with the centric marine diatom Coscinodiscus walesii.* Optics Express, 2007. **15**(26): p. 18082-18088.

129.   Romann, J., Valmalette, J.-C., Chauton, M.S., Tranell, G., Einarsrud, M.-A., and Vadstein, O., *Wavelength and orientation dependent capture of light by diatom frustule nanostructures.* Scientific Reports, 2015. **5**: p. 17403.

136. Barlow, S., Brédas, J.-L., Getmanenko, Y.A., Gieseking, R.L., Hales, J.M., Kim, H., Marder, S.R., Perry, J.W., Risko, C., and Zhang, Y., *Polymethine Materials with Solid-State Third Order Susceptibilities Suitable for All-Optical Signal-Processing Applications.* Mater. Horiz., 2014. **1**: p. 577-581.

137. Perry, J.W., Mansour, K., Lee, I.Y.S., Wu, X.L., Bedworth, P.V., Chen, C.T., Ng, D., Marder, S.R., Miles, P., Wada, T., Tian, M., and Sasabe, H., *Organic optical limiter with a strong nonlinear absorptive response.* Science, 1996. **273**: p. 1533-1536.

138. Haske, W., Chen, V.W., Hales, J.M., Dong, W., Barlow, S., Marder, S.R., and Perry, J.W., *65 nm feature sizes using visible wavelength 3-D multiphoton lithography.* Optics Express, 2007. **15**(6): p. 3426-3436.

139. Degnan, J.J., *Optimization of Passively Q-Switched Lasers.* IEEE Journal of Quantum Electronics, 1995. **31**(11).

140. Sheik-Bahae, M., Said, A.A., Wei, T.H., Hagan, D.J., and Stryland, E.W.V., *Sensitive measurement of optical nonlinearities using a single beam.* IEEE Journal of Quantum Electronics, 1990. **26**(4): p. 760-769.

141. Siegman, A.E. *Defining, measuring, and optimizing laser beam quality*. in *OE/LASE'93: Optics, Electro-Optics, and Laser Applications in Scienceand Engineering*. 1993. SPIE.

142. Siegman, A.E. *New developments in laser resonators*. in *OE/LASE '90*. 1990. SPIE.

143. Milam, D., *Review and assessment of measured values of the nonlinear refractive-index coefficient of fused silica.* Applied Optics, 1998. **37**(3): p. 546-550.

144. Krauss, T.D. and Wise, F.W., *Femtosecond measurement of nonlinear absorption and refraction in CdS, ZnSe, and ZnS.* Applied physics letters, 1994. **65**(14): p. 1739-1741.

145. Said, A.A., Sheik-Bahae, M., Hagan, D.J., Wei, T.H., Wang, J., Young, J., and Van Stryland, E.W., *Determination of bound-electronic and free-carrier nonlinearities in ZnSe, GaAs, CdTe, and ZnTe.* Journal of the Optical Society of America B, 1992. **9**(3): p. 405-414.

146. Van Stryland, E.W. and Sheik-Bahae, M., *Z-scan technique for nonlinear materials characterization*. 1998, New York, NY: Marcel Dekker.

147. Van Stryland, E.W. and Sheik-Bahae, M., *Z-scan measurements of Optical Nonlinearities*, in *Characterization Techniques and Tabulations for Organic Nonlinear Materials*, M. Kuzyk and C. Dirk, Editors. 1998, Marcel Dekker, Inc.: New York, NY. p. 655-692.

148. Kovsh, D.I., Hagan, D.J., and Stryland, E.W.V., *Numerical modeling of thermal refraction in liquids in the transient regime.* Optics Express, 1999. **4**(8): p. 315-327.

149. Negres, R.A., Hales, J.M., Kobyakov, A., Hagan, D.J., and Stryland, E.W.V., *Experiment and analysis of two-photon absorption spectroscopy using a white-light continuum probe.* IEEE Journal of Quantum Electronics, 2002. **38**(9): p. 1205-1216.

150. Negres, R.A., Hales, J.M., Kobyakov, A., Hagan, D.J., and Van Stryland, E.W., *Two-photon spectroscopy and analysis with a white-light continuum probe.* Optics Letters, 2002. **27**(4): p. 270-272.

151. Gélinas, S., Rao, A., Kumar, A., Smith, S.L., Chin, A.W., Clark, J., van der Poll, T.S., Bazan, G.C., and Friend, R.H., *Ultrafast Long-Range Charge Separation in Organic Semiconductor Photovoltaic Diodes.* Science, 2014. **343**(6170): p. 512-516.

152. Tien, P.K., *Light Waves in Thin Films and Integrated Optics.* Applied Optics, 1971. **10**(11): p. 2395-2413.

153. Ulrich, R. and Torge, R., *Measurement of Thin Film Parameters with a Prism Coupler.* Applied Optics, 1973. **12**(12): p. 2901-2908.

154. Kersten, R.T., *A new method for measuring refractive index and thickness of liquid and deposited solid thin films.* Optics Communications, 1975. **13**(3): p. 327-329.

155. Adams, A.C., Schinke, D.P., and Capio, C.D., *An Evaluation of the Prism Coupler for Measuring the Thickness and Refractive Index of Dielectric Films on Silicon Substrates.* Journal of The Electrochemical Society, 1979. **126**(9): p. 1539-1543.

156. Bai, S.J., Spry, R.J., Zelmon, D.E., Ramabadran, U., and Jackson, J., *Optical anisotropy of polymeric films measured by waveguide propagation mode determination.* Journal of Polymer Science Part B: Polymer Physics, 1992. **30**(13): p. 1507-1514.

157. Kersten, R.T., *Numerical solution of the mode-equation of planar dielectric waveguides to determine their refractive index and thickness by means of a prism-film coupler.* Optics Communications, 1973. **9**(4): p. 427-431.

158. Corporation, M., *Metricon Model 2010 Prism Coupler Thin Film Thickness/Refractive Index Measurement System Operation and Maintenance Guide.* 2003. p. 124.

159. Wang, X.-L., Wang, K.-M., Fu, G., Li, S.-L., Shen, D.-Y., Ma, H.-J., and Nie, R., *Low propagation loss of the waveguides in fused quartz by oxygen ion implantation.* Optics Express, 2004. **12**(20): p. 4675-4680.

160. Humlíček, J., *1 - Polarized Light and Ellipsometry*, in *Handbook of Ellipsometry*, H.G. Tompkins and E.A. Irene, Editors. 2005, William Andrew Publishing: Norwich, NY. p. 3-91.

161. Schubert, M., *9 - Theory and Application of Generalized Ellipsometry*, in *Handbook of Ellipsometry*, H.G. Tompkins and E.A. Irene, Editors. 2005, William Andrew Publishing: Norwich, NY. p. 637-717.

162. Sakatani, Y., Grosso, D., Nicole, L., Boissière, C., de A. A. Soler-Illia, G.J., and Sanchez, C., *Optimised photocatalytic activity of grid-like mesoporous TiO$_2$ films: effect of crystallinity, pore size distribution, and pore accessibility.* Journal of Materials Chemistry, 2006. **16**(1): p. 77-82.

163. Jellison, G.E., *3 - Data Analysis for Spectroscopic Ellipsometry*, in *Handbook of Ellipsometry*, H.G. Tompkins and E.A. Irene, Editors. 2005, William Andrew Publishing: Norwich, NY. p. 237-296.

164. Collins, R.W. and Ferlauto, A.S., *2 - Optical Physics of Materials*, in *Handbook of Ellipsometry*, H.G. Tompkins and E.A. Irene, Editors. 2005, William Andrew Publishing: Norwich, NY. p. 93-235.

165. Arwin, H., *12 - Ellipsometry in Life Sciences*, in *Handbook of Ellipsometry*, H.G. Tompkins and E.A. Irene, Editors. 2005, William Andrew Publishing: Norwich, NY. p. 799-855.

166. Collins, R.W., An, I., and Chen, C., *5 - Rotating Polarizer and Analyzer ElliPsometry*, in *Handbook of Ellipsometry*, H.G. Tompkins and E.A. Irene, Editors. 2005, William Andrew Publishing: Norwich, NY. p. 329-432.

167. Aspnes, D.E., Theeten, J.B., and Hottier, F., *Investigation of effective-medium models of microscopic surface roughness by spectroscopic ellipsometry.* Physical Review B, 1979. **20**(8): p. 3292-3302.

168. Aspnes, D.E., *Optical properties of thin films.* Thin Solid Films, 1982. **89**(3): p. 249-262.

169. Goldstein, J.I., Newbury, D.E., Echlin, P., Joy, D.C., Lyman, C.E., Lifshin, E., Sawyer, L., and Michael, J.R., *X-Ray Spectral Measurement: EDS and WDS*, in *Scanning Electron Microscopy and X-ray Microanalysis: Third Edition*. 2003, Springer US: Boston, MA. p. 297-353.

170. Hecht, E. and Ganesan, A.R., *Diffraction*, in *Optics*. 2002, Pearson: New York, USA. p. 420-480.

171.   Hecht, E. and Ganesan, A.R., *Wave Motion*, in *Optics*. 2002, Pearson: New York, USA. p. 10-31.

172.   Hecht, E. and Ganesan, A.R., *Interference*, in *Optics*. 2002, Pearson: New York, USA. p. 366-416.

173.   Born, M. and Wolf, E., *Elements of the theory of diffraction*, in *Principles of optics*. 1999, Cambridge University Press: New York. p. 412-514.

174.   Di Caprio, G., Coppola, G., Stefano, L.D., Stefano, M.D., Antonucci, A., Congestri, R., and Tommasi, E.D., *Shedding light on diatom photonics by means of digital holography.* Journal of Biophotonics, 2014. **7**(5): p. 341-350.

175.   Robert, L.L., *Rayleigh–Sommerfeld diffraction and Poisson's spot.* European Journal of Physics, 2006. **27**(2): p. 193.

176.   Harvey, J.E. and Forgham, J.L., *The spot of Arago: New relevance for an old phenomenon.* American Journal of Physics, 1984. **52**(3): p. 243-247.

177.   Scarmozzino, R. and Osgood, R.M., *Comparison of finite-difference and Fourier-transform solutions of the parabolic wave equation with emphasis on integrated-optics applications.* Journal of the Optical Society of America A, 1991. **8**(5): p. 724-731.

178.   Scarmozzino, R., Gopinath, A., Pregla, R., and Helfert, S., *Numerical techniques for modeling guided-wave photonic devices.* IEEE Journal of Selected Topics in Quantum Electronics, 2000. **6**(1): p. 150-162.

179.   Hadley, G.R., *Transparent boundary condition for the beam propagation method.* IEEE Journal of Quantum Electronics, 1992. **28**(1): p. 363-370.

180.   Yevick, D. and Hermansson, B., *Efficient beam propagation techniques.* IEEE Journal of Quantum Electronics, 1990. **26**(1): p. 109-112.

181.   Chung, Y. and Dagli, N., *An assessment of finite difference beam propagation method.* IEEE Journal of Quantum Electronics, 1990. **26**(8): p. 1335-1339.

CHAPTER 3. LINEAR AND NONLINEAR OPTICAL CHARACTERIZATION OF PLOLYMETHINES IN SOLUTION AND SOLID STATE; AND FILM PROCESSING FOR ALL-OPTICAL SIGNAL PROCESSING APPLICATIONS

3.1   Chapter Introduction

Recent experimental demonstrations of SOH all-optical switches made use of an amorphous organic material, namely 2-[4-(dimethylamino)phenyl]-3-([4-(dimethylamino)phenyl]ethynyl)buta-1-3-diene-1,1,4,4-tetracarbonitrile (DDMEBT), which has been used to obtain optical-quality films via vapor deposition [23] and spin coating from dichloromethane solution [182] with linear losses ca. 1 dB cm^{-1}. Although the $|\text{Re}(\chi^{(3)})|$ for this material is sizeable (ca. 1.4×10^{-11} esu) at $\lambda = 1.5$ µm and it demonstrated an ultrafast (<1 ps) optical response with promising switching contrast (4 dB), recent work on ionic polymethine dyes in neat and amorphous APC blend films demonstrated larger $|\text{Re}(\chi^{(3)})|$ than that of DDMEBT and linear loss values were reported as low as 4 dB cm^{-1}; presenting an opportunity for advancement in this material space. [30, 136, 183, 184]
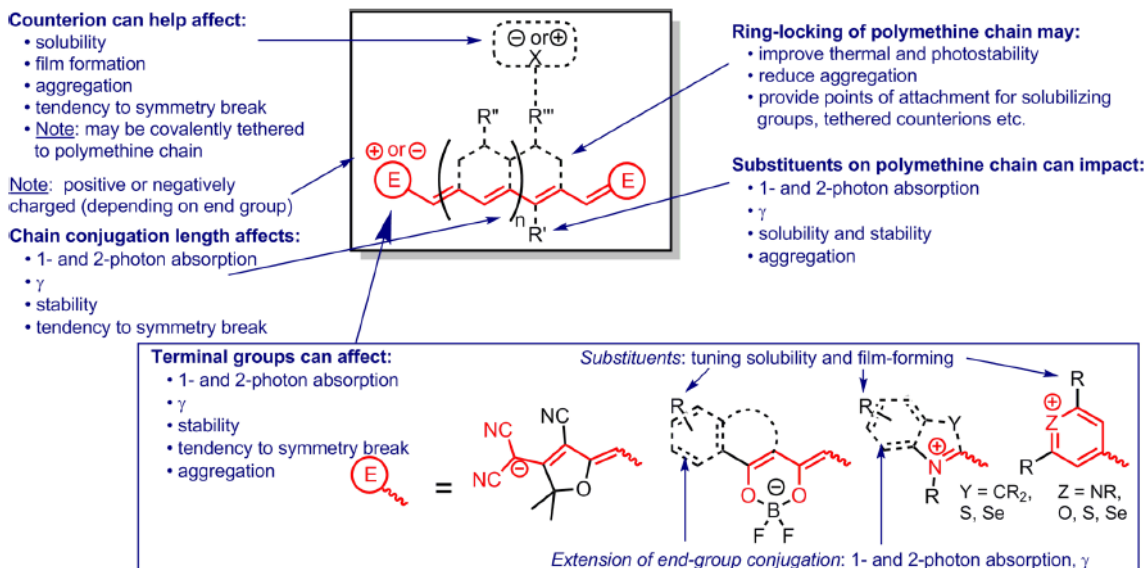
Figure 3.1. Schematic of structural features of polymethine dyes that can be varied and how they can affect material properties. Reprinted from Hales *et al.* [25] with permission. Copyright 2014 Chemistry of Materials.

A clear advantage that polymethines have over DDMEBT and other donor-substituted cyanoethynylethene molecules [185] is the greater synthetic flexibility for tuning chemical, electronic, and optical properties. An extensive review by Hales *et al.* [25] highlights the importance of various structural factors (Figure 3.1) and their respective impacts on specific material properties. To concisely highlight properties of interest for this dissertation, early attempts to enhance Re(γ) for a given polymethine involved lengthening the conjugated chain. This strategy, however, was limited by the tendency for long polymethine chains to undergo Peierls-type symmetry breaking [61, 186], which can result in significant electronic changes that introduce new states and result in increased 2PA, while also reducing the transition dipole moment (TDM) for the ground (g) to first 1PA excited state (e) transition (M_{ge}) and increasing the energy of this transition (E_{ge}). As such, because cyanine-like polymethines have a large contribution from the N-term

(Equation 3.1) from the sum-over-states model, values of |Re(γ)| dramatically decrease as a result. [25, 38]

$$\gamma \propto \frac{M_{ge}^4}{E_{ge}^3} \tag{3.1}$$

Acknowledging this limitation, alternative approaches were developed to maximize |Re(γ)| for a fixed conjugation length (below the symmetry-breaking threshold) by varying the identity of the "end" groups (labeled "E" in Figure 3.1). [30] In doing so, the addition of end groups that possessed significant overlap with frontier orbitals of the conjugated chain allowed for greater effective conjugation length (L), defined as

$$L = N_\pi + 2\,N_{term} \tag{3.2}$$

where N_π is the number of π-electrons on the chain and N_{term} is the effective number of π-electrons contributed by the terminal group. [61, 187] This, in turn, minimizes E_{ge} (scales as 1/L) and maximizes M_{ge} (scales with L), and thus maximize |Re(γ)|. This is illustrated in Figure 3.2 where, of the end groups examined, selenopyrylium "end" groups were found to give the largest M_{ge} and smallest E_{ge}. In addition to chain length and tuning delocalization with "end" groups, the use of larger, less-polarizing counterions have been shown to reduce the tendency for symmetry breaking and to aid in solubility. [30, 49] Furthermore, ring-locking along the backbone has led to improvements in thermal stability and enabled additional synthetic flexibility. [25]
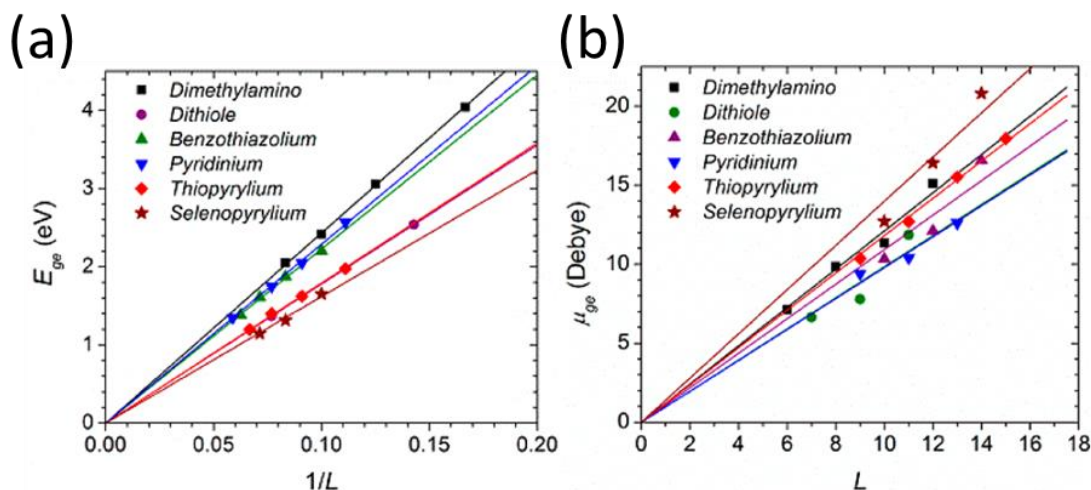
Figure 3.2. (a) E_{ge} .vs. 1/L and (b) M_{ge} (labeled in graph as μ_{ge}) .vs. L for polymethines with various terminal groups. Reproduced from Hales *et al.* [30] with permission. Copyright 2010 American Association for the Advancement of Science.

Despite the success of the aforementioned strategies to maximize $|Re(\gamma)|$, the translation of these properties from solution to the solid state, i.e. into large $|Re(\chi^{(3)})|$ with 2PA-FOM $\geq$ 12, is limited by aggregation in the high number density films made from these materials. The aggregation is a result of strong van der Waals interactions between dyes due to the large linear polarizabilities of polymethines. These strong interactions then induce electronic changes that alter the optical properties in the solid state. The degree to which this occurs, and the type of aggregate formed, i.e. J- aggregate [188-191] or H-aggregate [192-194], are functions of the various structural factors discussed above. [40]

To circumvent this issue, synthetic strategies have been developed with the aim of adding steric bulk to polymethines to separate molecules from one another in the solid state and thus reduce or mitigate aggregate effects. Of particular interest to this dissertation is the work by Barlow *et al.* [195], regarding the judicious substitution of chalcogenopyrylium-terminated dyes to achieve large $|Re(\chi^{(3)})|$ and suitable 2PA-FOM.

This work, and theoretical studies provided by Gieseking *et al*. [196], demonstrated that rigid, out-of-plane bulky groups attached to specific areas of the polymethine can effectively reduce ion-pairing and other polarizing interactions between the conjugated chains of neighboring dyes to preserve solution-like linear and NLO properties. The investigation by Davydenko, Y. A., Allen, T. G. *et al*. [197] outlined in section 3.2 will explore the generality of this method in further detail for an expanded series of bulky-substituted chalcogenopyrylium dyes as well as investing the role of the polymer host environment on select dyes. Additionally, from the work of Davydenko *et al.* [183], an alternate, synthetically-convenient, bulky group (Pd(PPh$_3$)$_2$Cl) will be explored in section 3.3, with the aim of quantifying the impact this group has on the solution and solid state NLO properties of benzoindole-terminated heptamethines. To conclude this chapter, studies on the influence of surface chemistry and polymer identity for 50% wt blend films of a bulky-substituted thiopyrylium dye on silica and silicon substrates will be presented with regards to the impact of processing conditions on device relevant properties such as coverage, uniformity, and adhesion.

3.2   Linear and Third-Order Nonlinear Optical Properties of Chalcogenopyrylium-Terminated Heptamethine Dyes with Rigid, Bulky Substituents

3.2.1 *Background and Experimental Approach*

Earlier work attempting to mitigate aggregation between cyanines, such as that by Scarpaci *et al*. [47], involved attaching Frechet-type dendrons to chalcogenopyrylium dyes to act as a spacer in solid films to prevent direct intermolecular interactions between neighboring molecules. Although some success was found in suppressing aggregation,

both neat and blend films were found to have high linear loss at 1550 nm. Further, because of the large size (in terms of molecular weight) of these dendrons, the additional molecular mass resulted in a dilution effect in the solid state; limiting the highest achievable $|Re(\chi^{(3)})|$.
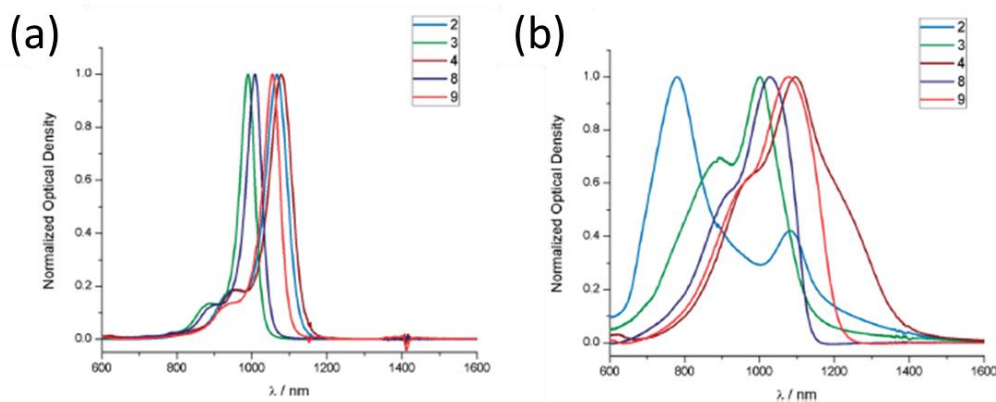
Figure 3.3. Normalized absorption spectra of chalcogenopyrylium-terminated heptamethines in (a) dilute chloroform solutions and (b) 50% wt APC blend films. Adapted from Barlow *et al.* [195] with permission. Copyright 2014 Materials Horizons.

To effectively prevent aggregation in highly concentrated films but still retain a large number density of chromophores, Barlow *et al*. [195] recently reported a molecular design strategy that selectively substituted "front", "back", and "end" positions in thio- and selenopyrylium-terminated heptamethine dyes (see top left generic structure in Figure 3.4) with rigid, bulky, out-of-plane organic groups to render the conjugated backbone inaccessible to neighboring molecules in the condensed phase. As shown in Figure 3.3, amorphous polycarbonate (APC) blend films containing dyes with little-to-no bulky substitution in the center of the molecule, i.e. **2** (X=S, R^1=Cl, R^2-R^3=H-H, R^4=Phenyl) and **3** (X=S, R^1=Cl, R^2-R^3=H-H, R^4=^{t}Bu), show absorption spectra indicative of H-aggregate-like bands whereas bulky-substituted compounds **8** (X=S, R^1=Cbz, R^2-R^3=^{t}Bu-H, R^4=Ad) and **9** (X=Se, R^1=Cbz, R^2-R^3=^{t}Bu-H, R^4=Ad) give solution-like spectra with relatively

minimal broadening. Further, replacing phenyl "end" groups with tertiary alkyl substituents effectively suppressed J-aggregate-like absorption features. As a result of judicious substitution, large $|Re(\chi^{(3)})|$ (ca. 2-3x10^{-11} esu) and 2PA-FOM in APC blends suitable for AOSP ($\geq$12) were demonstrated for two thiopyrylium-terminated heptamethines and one possessing a selenopyrylium "end" group. Moreover, these blends also exhibited relatively low linear loss (ca. 4 dB cm^{-1}).

In this study, the approach by Barlow *et al.* [195] is explored further to better understand the structure property relationships and potential limitations of these methods by investigating the impact of systematic variations in bulky substitution on absorption spectra and NLO properties at 1550 nm for a series of selenopyrylium and telluropyrylium-terminated dyes (see for structural information for compounds **Ia-t**). Additionally, the structure of a pentamethine analogue (**IIa**), for which the crystal has been determined, and the mechanisms for various chalcogenopyrylium salts and target dyes (I) are shown in Figure 3.4 and Figure 3.5, respectively. NLO values will be characterized via femtosecond Z-scan at 1550 nm in solution, neat films, and 50% wt blends with APC and, for **Ij** and **Ip**, polystyrene (PS) and polyvinylchloride (PVC) to quantify the success with which promising Re(γ) values and 2PA-FOM from solution can be translated into the high number density films. For blends in different polymer hosts, host-dependent nonlinearities will be discussed in terms of the impact that polymer identity and processing conditions have on the optical properties of dyes in the solid state. To complement NLO data, prism coupling measurements at 1550 nm will be performed on neat and 50% wt blend films to determine the effectiveness of bulky-substitution on reducing linear loss (α). Results from NLO and loss measurements for dyes **Ia-p** will be compared to DDMEBT, a vapor-deposited

material, whose acceptable 1PA-FOM ($|\text{Re}(\chi^{(3)})/\alpha|$) was utilized to accomplish AOSP at speeds up to ca. 100 Gbit/s in a silicon-organic hybrid waveguide device. [23]
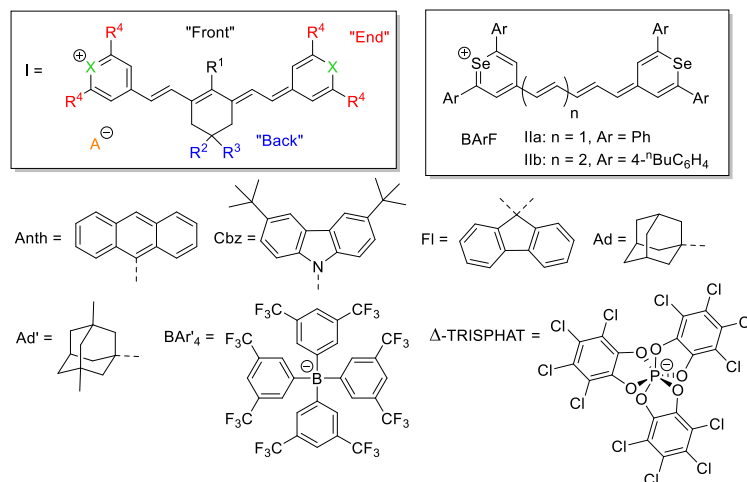
Dye	R₁	R₂	R₃	R₄	X	A
Ia	Cbz		Fl	^{t}bu	S	BAr′₄
Ib	Cbz	^{t}bu	H	^{t}bu	S	BAr′₄
Ic	Cbz	^{t}bu	H	^{t}bu	S	Δ-TRISPHAT
Id	Cbz	H	H	^{t}bu	S	BAr′₄
Ie	Cbz		Fl	Ad	S	BAr′₄
If	Cbz	^{t}bu	H	Ad	S	BAr′₄
Ig	Cbz		Fl	^{t}bu	Se	BAr′₄
Ih	Cbz	^{t}bu	H	^{t}bu	Se	BAr′₄
Ii	Cbz		Fl	Ad	Se	BAr′₄
Ij	Cbz	^{t}bu	H	Ad	Se	BAr′₄
Ik	Cbz	^{t}bu	H	Ad	Se	Δ-TRISPHAT
Il	Cl	^{t}bu	H	^{t}bu	S	BAr′₄
Im	Anth	^{t}bu	H	^{t}bu	S	BAr′₄
In	Cbz	^{t}bu	H	Ad′	S	BAr′₄
Io	Cbz	^{t}bu	H	Ad′	Se	BAr′₄
Ip	Cbz	^{t}bu	H	Ad′	Te	BAr′₄
Iq	Cl	^{t}bu	H	Ad	Se	BAr′₄
Ir	Anth	^{t}bu	H	Ad	Se	BAr′₄
Is	Cl	H	H	Ph	S	BAr′₄
It	Cbz	H	H	Ph	S	BAr′₄

Figure 3.4. Structure of chalcogenopyrylium dyes **Ia-r**, structure of a selenopyrylium dye **IIa**, the single-crystal structure of which is reported here, and structures of related compounds mentioned in the text (**Is,t** and **IIb**).
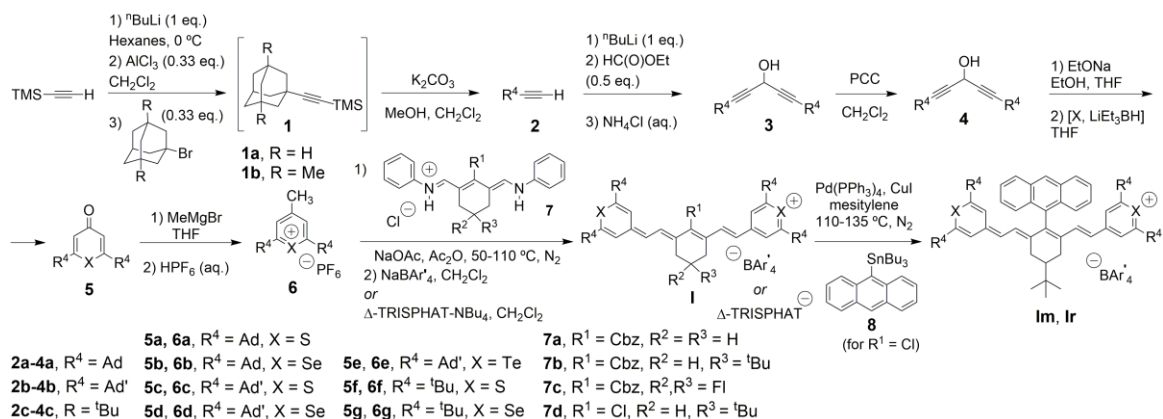
Figure 3.5. Synthesis of chalcogenopyrylium salts **6** and target dyes **I**. Provided by Dr. Yulia Getmanenko – Marder Group, Georgia Tech.

3.2.2 *Results and Discussion*

3.2.2.1 Solution Optical Properties

Linear absorption properties in dilute dichloromethane solutions are summarized in Table 3.1 and Table 3.2, respectively, for several chalcogenopyrylium dyes. As mentioned in previous work [195, 198] the absorption maxima of the dyes with alkyl "end" substituents, R^4, are significantly blue-shifted relative to those seen for comparable dyes with aryl R^4 groups; for example, $\lambda_{max} = 1078$ nm for **It**. [195] The absorptivities and TDMs (M_{ge}) are also lower; M_{ge} values of close to 20 D have been determined for thio- and selenopyrylium heptamethines **Is** and **IIb** [30, 47] with R^4 = aryl "end" groups. Within the series of compounds examined, the structural variable that most significantly affects the position of the solution absorption maximum is the identity of the chalcogen, X, with successive red shifts being observed from S to Se to Te, consistent with the trends seen the previous work. [199, 200]

Table 3.1. Linear Absorption Data[a] and NLO Properties at 1550 nm[b] for Select Dyes in Solution. Some data provided by Dr. Hyeongeu Kim and Dr. Yulia Getmanenko from the Perry and Marder Groups at Georgia Tech, respectively.

Compound	λ_{max} (nm)	ε_{max} (10^5 M^{-1}cm^{-1})	M_{ge} (D)[d]	Re(γ) (10^{-32} esu)	|Re(γ) / Im(γ)|	Re(γ)$_{\text{2-level}}$[e] (10^{-32} esu)
Ia [195]	988	-	-	−1.6	9.0	-
Ib [195]	997	-	-	−1.7	13	-
Id [195]	993	2.86	15.9	−1.8	13	–2.3
Ie	991	3.08	16.9	−1.5	6.3	–2.9
If [195]	1008	-	-	−2.0	14	-
Ig	1030	-	-	−2.2	24	-
Ih	1039	2.88	17.0	−2.4	30	–4.4
Ii	1041	-	-	−2.3	28	-
Ij [195]	1050	3.13	17.3	−2.2	36	–5.2
Il	986	-	-	−1.8	11	-
Im	976	-	-	−1.4	10	-
In	1006	3.37	16.7	−2.2	15	–3.1
Io	1054	3.18	17.2	−2.3	33	–5.3
Ip	1143	2.40	16.5	−4.7	29	–10.4

a) In CH_2Cl_2, b) In $CHCl_3$, uncertainties in Re(γ) and Im(γ) are estimated to be ca. ± 8% and uncertainty in |Re(γ)/Im(γ)| to be ± 11%, c) Calculated according to $M_{ge} = 0.09584 \times (\int \varepsilon \, d\nu / \nu_{max})^{0.5}$, d) Calculated from experimental values of λ_{max} and M_{ge} using equation from c). Data from from reference [195].

Table 3.2. Summary of optical properties for I dyes. Some data provided by Dr. Hyeongeu Kim and Dr. Yulia Getmanenko from Perry and Marder Groups at Georgia Tech, respectively.

Sample	λ_{max} (nm)[b]	λ_{max} (nm)[c]	$n_0{}^a$	$Re(\chi^3)_{ext}$ $(10^{-11}$ esu$)^d$	$Im (\chi^{(3)}{}_{ext}$ $(10^{-11}$ esu$)$	$Re(\chi^{(3)}) /$ $Re(\chi^{(3)})_{extr}$	$Im(\chi^{(3)}) /$ $Im \chi^{(3)})_{extr}$
Ia:APC	982	994	1.65	−1.77	0.19	1.41	2.23
Ib:APC	992	999	1.66	−2.01	0.15	1.34	1.49
Id:APC	993	1016		−2.49	0.19	1.04	1.60
Ie:APC	992	1010	1.65	−1.42	0.23	1.76	1.91
If:APC	1004	1022	1.65	−1.99	0.14	1.21	1.29
Ih:APC	1039	1067		−3.05	0.10	1.11	2.91
Ij:APC	1050		1.67	−2.20	0.06	1.50	4.59
Ij (neat)	1050	1074	1.83	−6.86	0.19	0.74	1.26
Ij:PS	1050	1056	1.71	−2.46	0.07	1.42	5.29
Ij:PVC	1050	1063	1.68	-2.26	0.06	1.33	3.83
Il:APC	986	995	1.72	−2.96	0.26	0.88	2.58
Im:APC	976	1009		−1.99	0.20	1.06	1.16
In:APC	1006	1036	1.66	−2.13	0.15	0.99	2.33
Io:APC	1054	1089	1.68	−2.25	0.07	1.60	3.79
Io (neat)	1054		1.81	−6.47	0.20	0.74	1.57
Ip:APC	1143	1160	1.70	−4.66	0.16	1.62	N/A
Ip:PS	1143	1158	1.69	−4.53	0.15	2.04	N/A
Ip:PVC	1143	1152	1.60	−3.52	0.12	0.34	N/A
Iq	1048	1089					
Ir	1035						

a) Measured by prism coupling, b) In CH_2Cl_2 solution, c) Thin neat film, d) Refractive index, e) For the films for which n_0 was not measured, value of 1.7 was used for calculations of $Re(\chi^{(3)})_{extr}$ and $Im(\chi^{(3)})_{extr}$.

Electrochemical oxidation and reduction potentials (Table 3.3) show very similar trends to those previously observed for squarylium and croconate chalcogenopyrylium dyes [200] and suggest that the red-shift in absorption from S to Se to Te can be mainly attributed to the stabilization of the LUMO. M_{ge} values determined for selected thio-, seleno-, and telluropyrylium dyes fall in the range 15.9-17.3 D (Table 3.1). The identity of R^1-R^4 has a relatively small effect on the linear optical properties in solution; replacement of R^1 = Cbz with Anth leads to a slight blue shift, compounds with R^2, R^3 = Fl have blue-

shifted maxima relative to their R^2, R^3 = ^{t}Bu,H analogues, and increasing the size of the R^4 tertiary alkyl substituent from ^{t}Bu to Ad to Ad^t leads to small successive red shifts.

Table 3.3. Cyclic voltammetry and DSC data for selected I dyes. Data provided by Dr. Yulia Getmanenko – Marder Group, Georgia Tech.

Cmpd	$E_{1/2}{}^{ox2}$ (V)[a]	$E_{1/2}{}^{ox1}$ (V)[a]	$E_{1/2}{}^{red1}$ (V)[a]	$E_{1/2}{}^{red2}$ (V)[a]
Ib	+0.71	+0.08	–0.86	–1.88
Ij	+0.70	+0.09	–0.83	–1.83
In	+0.72	+0.06	–0.90	–1.93
Io	+0.71	+0.10	–0.81	–1.83
Ip	+0.64	+0.07	–0.74	–1.75

a) Cyclic voltammograms were recorded in 0.1 M Bu$_4$NPF$_6$ in dichloromethane using FeCp$^*_2{}^{+/0}$ (–0.55 V .vs. FeCp$_2{}^{+/0}$) as internal reference.

Table 3.1 also summarizes the microscopic NLO properties determined in dilute chloroform solutions (ca. 2–5 mM) using the femtosecond Z-scan technique with λ_{exc} = 1550 nm. For polymethine dyes, the off-resonant NLO response of the dye in the cgs units of esu can be estimated by the two-level expression: [30, 201]

$$Re(\gamma)_{2-level} = -3.264 \times 10^{-38} \frac{M_{ge}^4}{\left(E_{ge} - \hbar\omega\right)^3} \tag{3.3}$$

where E_{ge} and M_{ge} are the transition energy in eV and TDM in Debye (D), respectively, linking the ground and first excited states, and $\hbar\omega$ is the energy in eV of the excitation photons. A comparison of this value with the observed values give an indication of the extent to which the two-level model holds for these compounds. The trends in measured values of Re(γ) for the thiopyrylium species are in reasonably good agreement with the expectations from the two-level model, Re(γ)$_{2\text{-level}}$ (Table 3.1), although are overestimated by a factor of 1.2-1.9. Similarly, the two-level model overestimates Re(γ) by 1.8-2.4 for the selenopyrylium dyes and by 2.2 for the telluropyrylium dye.

The largest discrepancies, quantified by $Re(\gamma)_{\text{2-level}}/Re(\gamma)_{\text{meas}}$, are found for the compounds with longest wavelength of maximum absorption, which can, in part, be attributed to the omission of a damping term in equation 3.. In addition, equation 3. ignores the effects on the dispersion of $Re(\gamma)$ of two-photon resonances associated with vibrationally assisted excitation into the low-lying electronic state. Values of the $Re(\gamma)$ measured for R^4 = alkyl thio- (-1.5×10^{-32} to -2.2×10^{-32} esu) and selenopyrylium dyes (-2.2×10^{-32} to -2.4×10^{-32} esu) are somewhat smaller in magnitude than those previously reported values for R^4 = aryl thio- (-2.4 to -3.6×10^{-32} esu for **Is** and **It**) [47] and selenopyrylium (-4.4×10^{-32} esu for **IIb**) [30] dyes at the same wavelength. This can be attributed to the smaller values of M_{ge} and larger values of E_{ge} for compounds with alkyl "end" groups.

The values of $Im(\gamma)$ are attributed to 2PA; cyanine-like dyes typically show vibronically assisted 2PA into S_1 [30, 202], with the transition energy corresponding to the 2PA peak being ca. 0.2 eV greater than that for the 1PA peak; i.e., for S-, Se-, and Te-containing dyes of type **I** with alkyl "end" groups, maxima would be expected at transition energies of ca. 1.44, 1.38, and 1.29 eV, respectively. Thus, the photon energy of the incident beam, 0.8 eV (corresponding to a 2PA transition energy of 1.6 eV), more closely approaches 2PA resonance for the thiopyrylium derivatives, which accounts for the values of $Im(\gamma)$ for the thiopyrylium derivatives being ca. twice those for analogues containing the heavier chalcogens, resulting in smaller values of the 2PA-FOM, $|Re(\gamma)/Im(\gamma)|$. Nonetheless, in most cases, the values of $|Re(\gamma)/Im(\gamma)|$ would be sufficient for AOSP applications if successfully translated to high-chromophore density films.

3.2.2.2   Optical Properties of High-Chromophore Density Films

To investigate the optical behavior of **Ia-p** in high-chromophore density films, 50 wt% blends with APC and, for selected dyes, neat films and 50 wt% blends with polystyrene (PS) and poly(vinylchloride) (PVC) were examined. Linear absorption spectra of the films (see Figures 3.6, 3.8, 3.9, 3.12, and 3.14-3.16) are, to a first approximation, similar to one another and the absorption maxima are only slightly red-shifted relative to those seen in solution, although the absorption bands are generally somewhat broader, and the high-energy shoulders more strongly pronounced in the films.

All substitution patterns preserve solution-like spectral shapes in the solid state, although the degree of peak broadening increases from S to Se to Te examples. Values of α at 1550 nm were determined by prism coupling measurements and are tabulated in Table 3.4. Losses were measurable for all samples except for 50 wt% **Ip**:PS, the high loss for which (exceeding the linear detection limit of ca. 20 dB cm^{-1}) is attributable to absorption at 1550 nm due to appreciable optical density on the low-energy side of the broadened primary absorption band, exacerbated a by substantial film thickness (ca. 2.5 μm). For the other blend films, linear losses were typically less than 6.5 dB cm^{-1} with some values as low as 3.3 dB cm^{-1}. Re($\chi^{(3)}$) and Im($\chi^{(3)}$) values at 1550 nm obtained for the films using femtosecond Z-scan measurements are summarized in Table 3.4.
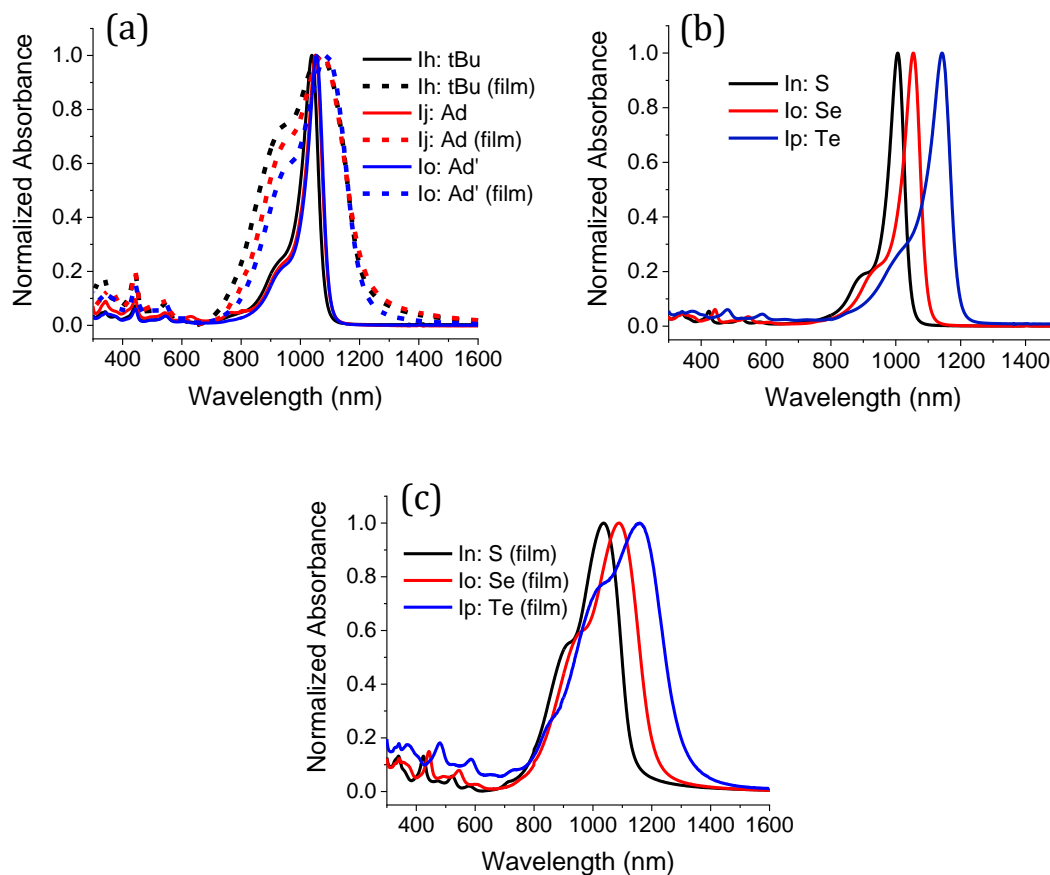
Figure 3.6. Selected examples of dichloromethane solution and thin neat film spectra for chalcogenopyrylium-terminated dyes comparing (a) the influence of the "end" substituent R^4 (^{t}Bu vs. Ad vs. Ad') on the absorption spectra of Cbz/^{t}Bu/R^4/Se/BAr'$_4$ dyes, and (b,c) the influence of the chalcogen "X" (S vs. Se vs. Te) in the series of Cbz/^{t}Bu/Ad'/X/BAr'$_4$ dyes. Data provided by Dr. Yulia Getmanenko – Marder Group, Georgia Tech.

Table 3.4. NLO properties (measured and extrapolated from solution) and linear loss at 1550 nm for dyes in films[a]. Some data courtesy of Dr. Hyeongeu Kim – Perry Group, Georgia Tech.

Cpd:host	$\text{Re}(\chi^{(3)})_{\text{extr}}$ $(10^{-11}\,\text{esu})$ [b]	$\text{Re}(\chi^{(3)})$ $(10^{-11}\,\text{esu})$	$\text{Im}(\chi^{(3)})$ $(10^{-11}\,\text{esu})$	$|\text{Re}(\chi^{(3)})\,/\,\text{Im}(\chi^{(3)})|_{\text{extr}}$ [b]	$|\text{Re}(\chi^{(3)})\,/\,\text{Im}(\chi^{(3)})|$	α (dB cm^{-1})
Ia:APC[195]	−1.8	−2.5	0.42	9	6.0	4.1
Ib:APC[195]	−2.0	−2.7	0.23	13	12	3.5
Id:APC[195]	−2.5	−2.6	0.31	13	8.6	10
Ie:APC	−1.4	−2.5	0.44	6.3	5.6	4.7
If:APC[195]	−2.0	−2.4	0.18	14	13	4.6[c]
Ih:APC	−3.1	−3.4	0.30	30	11	4.9
Ij:APC[195]	−2.2	−3.3	0.28	36	12	4.4
Ij (neat)[195]	−6.9	−5.1	0.24	36	21	8.2
Ij:PS	−2.5	−3.5	0.37	36	9.5	6.2
Ij:PVC	−2.3	−3.0	0.23	36	13	4.8
Il:APC	−3.0	−2.6	0.67	11	3.8	7.3
Im:APC	−2.0	−2.1	0.23	10	9.2	5.4
In:APC	−2.1	−2.1	0.36	15	5.9	4.7
Io:APC	−2.3	−3.6	0.26	33	14	4.3
Io (neat)	−6.5	−4.8	0.31	33	15	6.5
Ip:APC	−4.7	−7.6	e	29	d	6.4
Ip:PS	−4.5	−9.2	e	29	d	>20
Ip:PVC	−3.5	−1.2	e	29	d	4.3

a) Either 50 wt% blends with the polymers specified in the first column or neat films, estimated uncertainties in $\text{Re}(\chi^{(3)})$, $\text{Im}(\chi^{(3)})$, $|\text{Re}(\chi^{(3)})/\text{Im}(\chi^{(3)})|$, and α are ±13, 13, 18, and 20%, respectively, b) $\text{Re}(\chi^{(3)})_{\text{extr}}$ values were extrapolated from solution $\text{Re}(\gamma)$ values assuming a film density of 1.1 g cm^{-3} and using the linear refractive index values summarized in Figure 3.12, while $|\text{Re}(\chi^{(3)})/\text{Im}(\chi^{(3)})|_{\text{extr}}$ values are identical to the $|\text{Re}(\gamma)/\text{Im}(\gamma)|$ values of Table 3.1, c) A lower value was reported in ref. [195], but repeated measurements afford the present value, d) Saturable absorption observed, precluding quantification.

Macroscopic values of $\chi^{(3)}_{extr}$, were extrapolated from solution (γ) values (Table 3.1) via the relation $\chi^{(3)} = N L^4 \gamma$, using the refractive index (n_0) and the projected chromophore density (N) (assuming film density of 1.1 g/cm^3) for each dye in its corresponding film and with $L = (n^2 + 2)/3$. Values of $Re(\chi^{(3)})_{extr}$, extrapolated from solution $Re(\gamma)$ values (Table 3.1), the refractive index, and the projected chromophore density in the films, are generally in reasonable agreement with the experimentally measured values (Table 3.4, Figure 3.7), although the magnitudes of $Re(\chi^{(3)})$ determined for APC and PS blend films incorporating the Te dye **Ip** are much larger than those extrapolated from solution. However, a different picture emerges comparing values of $Im(\chi^{(3)})_{extr}$ extrapolated from solution data and experimentally determined $Im(\chi^{(3)})$, or, equivalently, comparing solution values of $|Re(\gamma)/Im(\gamma)| \equiv |Re(\chi^{(3)})/Im(\chi^{(3)})|_{extr}$ and film values of $|Re(\chi^{(3)})/Im(\chi^{(3)})|$. As shown in Figure 3.7, the experimental values of $Im(\chi^{(3)})$ for APC blends are generally larger than those extrapolated from solution. Larger deviations are observed for the selenopyrylium dyes ($Im(\chi^{(3)})_{meas}/Im(\chi^{(3)})_{extr}$ ratios vary from 1.3 to 5.3) than their thiopyrylium counterparts (1.1 to 2.6). The increase in $Im(\chi^{(3)})$ in the solid state in many cases leads to values of $|Re(\chi^{(3)})/Im(\chi^{(3)})|$ that no longer meet the criterion for AOSP; this increase is attributable to broadening or strengthening of the above-mentioned vibronically assisted 2PA band [30] as a result of dye-dye or dye-host interactions. Differences in the ratios of $Im(\chi^{(3)})_{meas}/Im(\chi^{(3)})_{extr}$ seen for polymer blends and neat films for some dyes suggest both types of interaction may play a role (vide infra). In the following sections the effects of the different structural variables (R^1-R^4, chalcogen, and host material) on the linear absorption spectra, linear loss, and NLO properties of the films are examined in detail.
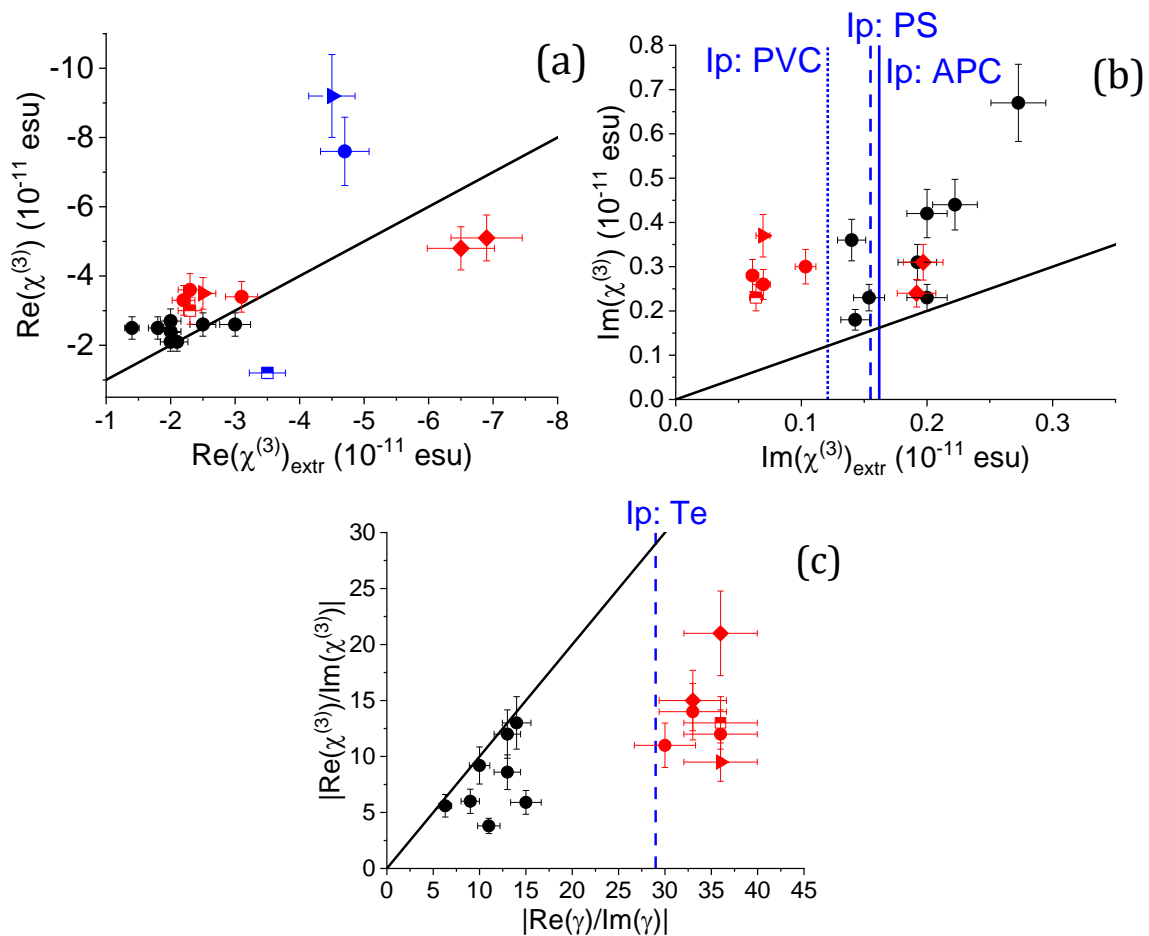
Figure 3.7. Plots of experimental values of (a) Re($\chi^{(3)}$), (b) Im($\chi^{(3)}$), and (c) 2PA-FOM for high-chromophore density films containing dyes of type **I** vs. the values extrapolated from solution measurements of Re(γ) and Im(γ). The straight lines indicate the relationships expected in the case of an ideal translation of solution values to the solids. Plotted data shows neat films (diamonds), 50 wt% blends with APC (solid circles), PS (triangles), and PVC (half-filled squares). Data for S, Se, and Te dyes are shown in black, red, and blue, respectively. For blends of the Te dye Ip, for which Im($\chi^{(3)}$) values were not measurable, blue lines indicate the values of Im($\chi^{(3)}$)$_{extr}$ and |Re(γ) / Im(γ)|.

3.2.2.3   Influence of the "Front" Group R[1]

The most frequently employed R[1] substituent in this study is the 3,6-di(*tert*-butyl)carbazol-9-yl (Cbz) group, which was chosen based on the expectation that intramolecular steric interactions would lead to a significant angle between the plane of the carbazole and that of the π-system of the chromophore. This is corroborated by DFT (B97XD/cc-pVDZ) calculations for model heptamethine thiopyrylium dyes that gave a torsion angle of 57.6° between the plane of the polymethine chain and carbazole "front" substituent and an angle of 90° for that of the anthracene group (values provided by Dr. Rebecca Gieseking, Bredas Group – Georgia Tech). As such, these substituents should be sufficient to prevent π-stacking of the delocalized polymethine chains of the chromophore.

The effects of different R[1] substituents were compared by examining thiopyrylium compounds **Ib**, **Il** and **Im**, all of which share ᵗBu "back" and "end" groups as well as the BAr'$_4$ counterion, but differ in having Cbz, Cl, and Anth "front" groups, respectively. It is noted that a similar trend was also seen in the solution spectra for **Ij**, **Iq**, and **Ir** (Figure 3.8). For the dye with the least bulky substituent, **Il** with R[1] = Cl, the neat-film absorption band is broader (full width at half maximum, FWHM, = 420 meV) than that of dyes with the larger Cbz (**Ib**, 340 meV) or Anth (**Im**, 360 meV) moieties and has a more pronounced high-energy shoulder (see Figure 3.8 and Figure 3.9). Although the absorption peak of the anthracene dye **Im** is slightly blue-shifted relative to that of **Ib** in solution, this difference is not seen in the neat-film absorption spectra. Despite the similarity in neat film spectra, the linear loss for 50 wt% APC blends is larger (and the 1PA-FOM lower) for anthracene-based **Im** than for Cbz-substituted **Ib** and is only slightly less than Cl-substituted **Il**. This

suggests that the ^{t}Bu groups on the carbazole are effective in separating the molecules (related findings for the "back" groups are discussed in section 3.2.2.4).

The values of Re(γ) and the 2PA-FOM in dilute solution at 1550 nm varied only slightly across the series discussed above, consistent with the similarity in the UV-vis-NIR spectra (Figure 3.8). In 50 wt% APC films, dyes substituted with bulkier groups such as Cbz and Anth (**Ib** and **Im**) retain the 2PA-FOM observed in solution, whereas the dyes with smaller Cl substitution in the "front" position (**Il**) show a marked reduction in the 2PA-FOM. The stronger 2PA in the latter may be associated with the more pronounced absorption seen on the high-energy side of the absorption maximum in the neat film spectrum, indicating greater vibronic coupling of S_0 and S_1.

To summarize the results from this section, a moderately bulky "front" group is essential for obtaining a reasonably "solution-like" spectrum and an acceptable 2PA-FOM in high chromophore density films, and, of the two out-of-plane R^1 groups examined here, the Cbz moiety appears to be somewhat more effective than Anth.
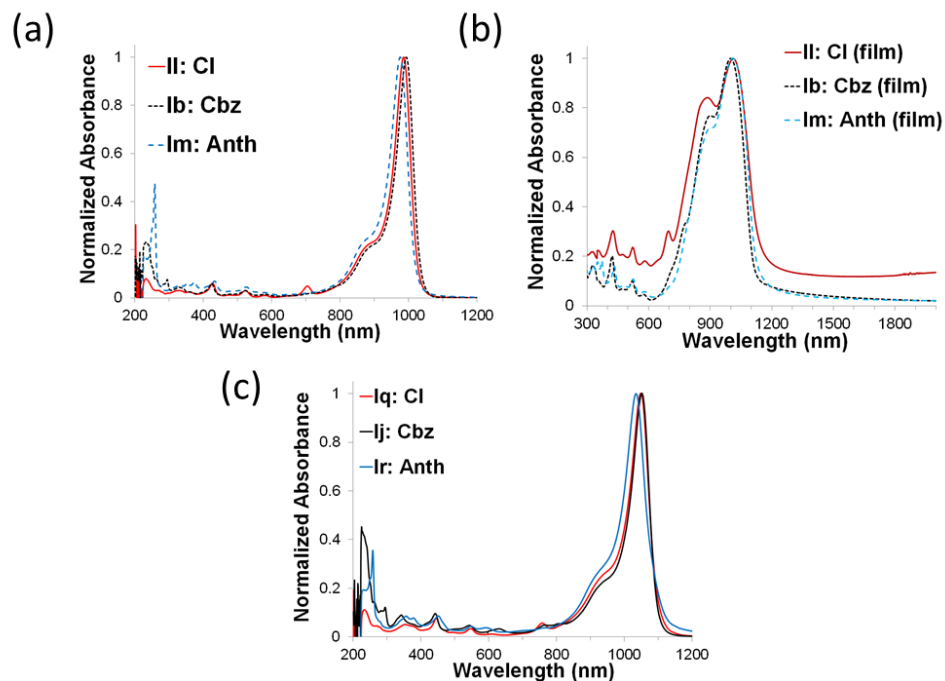
Figure 3.8. Influence of the "front" R^1 substituent (Cl vs. Cbz vs. Anth) on the UV-vis-NIR spectra of two series of $R^1/{}^tBu,H/R^4/X/BAr'_4$ dyes: (a) $R^4 = {}^tBu$, X = S dyes in dichloromethane solution and (b) same dyes in neat thin films cast from 1,2-dichloroethane, respectively, and (c) R^4 = Ad, X = Se dyes in dichloromethane solution. Data provided by Dr. Yulia Getmanenko – Marder Group, Georgia Tech.
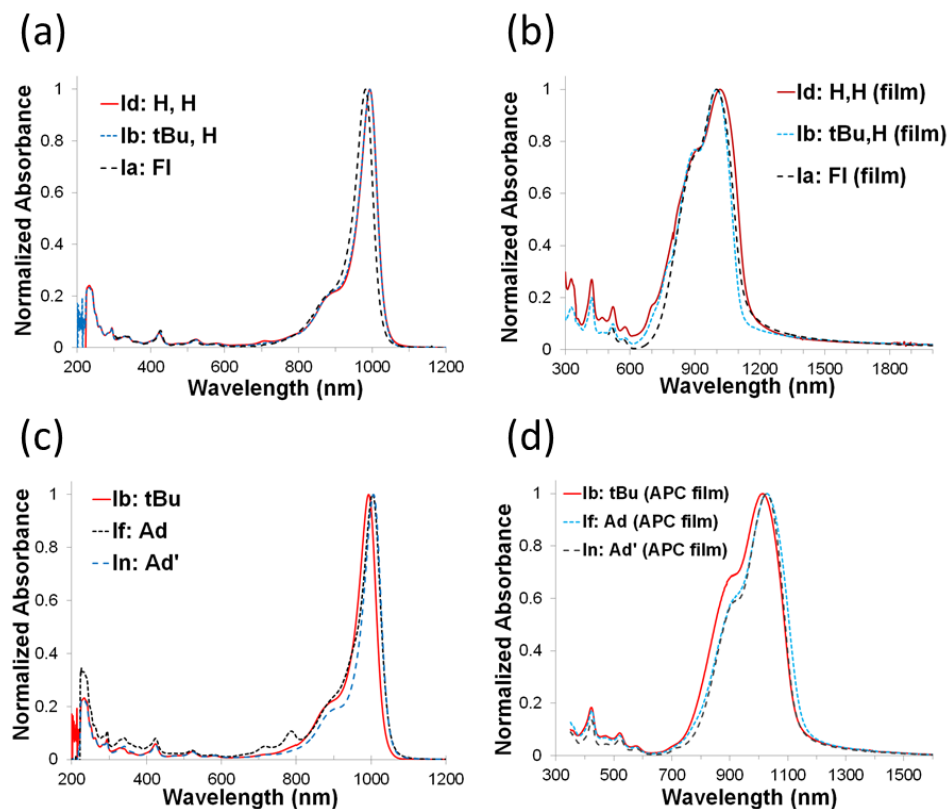
Figure 3.9. Influence of (a-b) "back" substituents (R^2, R^3 = H,H vs. ^{t}Bu,H vs. Fl) in a series of Cbz/R^2,R^3/^{t}Bu/S/BAr'$_4$ dyes, (c-d) "end" substituents (R^4 = ^{t}Bu vs. Ad vs. Ad') in a series of Cbz/^{t}Bu,H/R^4/S/BAr'$_4$ dyes on the UV-vis-NIR spectra, (a,c) dichloromethane solutions and (b,d) thin neat films from 1,2-dichloroethane. Data provided by Dr. Yulia Getmanenko – Marder Group, Georgia Tech.

3.2.2.4 Influence of the "Back" Groups, R^2 and R^3

Thiopyrylium dyes **Ia**, **Ib** and **Id** differ in the R^2 and R^3 groups at the "back" position, with R^2, R^3 = Fl, 'Bu,H and H,H, respectively. The choice of "back" groups has little effect on the shape and position of the bands in solution or in films, [195] although the absorption maximum in solution for **Ia** is slightly blue-shifted relative to that for **Ib** and **Id**, similar to the blue shifts observed for other Fl vs. 'Bu,H comparisons (Table 3.1). Despite the similarity in the absorption spectra of the films (Figure 3.9), the linear loss at 1550 nm for 50 wt% APC films is reduced by the presence of the bulky "back" substituents (**Ia**, **Ib** vs. **Id**). Furthermore, although loss values between Fl and 'Bu,H analogues (i.e. **Ia** .vs. **Ib** and **Ie** .vs. **If**) are similar, slightly higher loss for **Ia** and **Ie** may suggest that, much like the comparison of "front" groups, planar π-systems that project above and below the plane of the chromophore π-system and that themselves do not possess additional bulky substituents are not generally the most effective groups for reducing optical loss.

Consistent with the trends in the solution absorption spectra, similar solution values of Re(γ) and |Re(γ)/Im(γ)| are found for **Ib** and **Id**. For the fluorene derivative **Ia**, a larger Im(γ) results in a smaller value of |Re(γ)/Im(γ)| (9.0) than that of **Ib** and **Id** (both 13). These results are consistent with the blue shift in the linear absorption, which results in a smaller pre-resonance enhancement of Re(γ) and a concomitant blue shift of the 2PA state closer to 1550 nm excitation. Similar differences are seen between other Fl vs. 'Bu analogues, such as **Ie** and **If**.

In the 50 wt% APC films, both Fl-substituted dyes (**Ia** and **Ie**) exhibit lower 2PA-FOMs (5.6–6.0) than their 'Bu,H analogues (12 and 13 for **Ib** and **If**, respectively) (Table 3.4); **Ia** also has lower a 2PA-FOM than H,H-substituted dye **Id**. These low 2PA-FOMs are

108

largely due to large discrepancies between the measured $Im(\chi^{(3)})$ values of Fl-dyes in APC films and the values extrapolated from the solution $Im(\gamma)$ values; i.e. $Im(\chi^{(3)})_{meas}/Im(\chi^{(3)})_{extr}$ ratios for Fl-containing dye films range from 1.9-4.6 while their ^tBu,H and H,H analogues show ratios between 1.3 and 1.5. The different size and shape of the "back" substituent may lead to differences in the distribution of possible dye-dye and dye-counterion interactions; however, the specific origin of the larger discrepancies for the Fl-containing dyes is unclear.

In summary, the comparisons between R^2,R^3 patterns examined in this section suggest that the introduction of three dimensional $R^2 = {}^tBu$ group, which is relatively straightforward from a synthetic point of view, leads to materials with more promising characteristics for AOSP than that of the larger (in terms of molecular weight and out-of-plane projection), but planar R^2,$R^3 = $ Fl group, or use of the unsubstituted (R^2,$R^3 =$H,H) ring.

3.2.2.5 Influence of the "End" Groups, R^4

Previously, it was found that tertiary-alkyl R^4 groups suppress red-shifted features in the spectra of solid-state compared to dyes with aryl "end" groups, such as **Is** and **It**. Here three different such alkyl substituents are compared: ^tBu, Ad, and Ad'. While single crystals of these dyes were not obtainable, single-crystal structures of several chalcogenopyranone precursors, **5a** (X = S; $R^4 = $ Ad) and **5c-e** (X = S, Se, and Te respectively; $R^4 = $ Ad'), were determined, along with that of an aryl (Ph) substituted analogue, **5h** (X = Se; $R^4 = {}^nBu$-Ph, not pictured in Figure 3.5). In the structure of **5h**, aryl groups of neighboring molecules are located above and below the selenopyranone ring with some intermolecular distances between sp^2 carbon atoms of 3.5-3.6 Å. No comparable

interactions between sp^2 carbon atoms are found in the structures of Ad- and Ad'-substituted chalcogenopyranones, consistent with the observed suppression of J-aggregate-like features in the corresponding dyes. However, the structures of **5c-e** show short intermolecular O···X contacts (Figure 3.10) indicating that even the dimethyladamantyl substituents are not sufficiently bulky to protect the chalcogen atom itself from interacting with neighboring moieties. The effect of the identity of the chalcogen on the molecular geometries and on possible intermolecular interactions are discussed further in the following section.
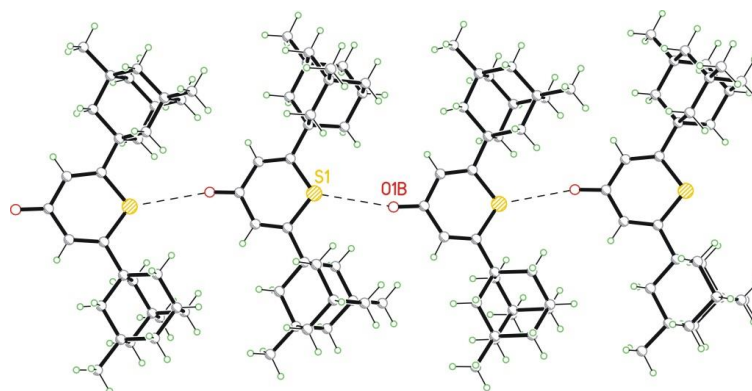
Figure 3.10. Fragment of a ribbon in the crystal structure of **5c** with short intermolecular C=O···S contacts. The structures of its Se (**5d**) and Te (**5e**) analogues are isomorphous. Data provided by Dr. Yulia Getmanenko – Marder Group, Georgia Tech.

Increasing the size of the tertiary-alkyl R^4 substituents (**Ia** to **Ie**; **Ib** to **If** to **In**; **Ig** to **Ii**; **Ih** to **Ij** to **Io**) has little effect on solution linear or nonlinear optical properties, apart from giving rise to small red shifts in the absorption band (Figure 3.6 and Figure 3.9). However, in the APC and neat films, bands for the Ad and Ad' species are narrower than for their ^{t}Bu analogues (Figure 3.6; FWHM are 390, 360, and 330 meV for neat films of **Ih**, **Ij**, and **Io** respectively) and the high-energy shoulder is less pronounced. Dilution from neat films to 50 wt% blends with APC has decreasing effects with increasing alkyl group

size where the bandwidths and half-height for **Ih** (^{t}Bu), **Ij** (Ad), and **Io** (Ad') were found to decrease by 47, 32, and 8 meV, respectively, upon blending. Thus, of the "end" groups chosen for this study, the choice of R^4 has little impact on the linear losses and NLO properties of 50 wt% blends with APC.

3.2.2.6 <u>Influence of the Chalcogen</u>

Consistent with previous reports on chalcogenopyrylium-terminated polymethines, [198] the choice of chalcogen has a profound effect on the linear optical properties of the dyes in both solution and in films. Increase of the atomic number of the chalcogen is correlated with successive red shifts of the absorption maxima, and increases in the relative absorbance of the high-energy shoulder and in the width of the band; e.g. FWHM for **In** (S), **Io** (Se), and **Ip** (Te) are 69, 73, and 80 meV in solution, and 270, 290, and 310 meV in neat films (Figure 3.6b,c). Despite the noticeable red shift in the absorption maxima of Se- and Te-dyes relative to their S-analogues, the linear optical losses for the corresponding 50 wt% APC films at 1550 nm show no clear trend and are generally fairly similar (**Ib** vs. **Ih** and **In** vs. **Io** vs **Ip**).

Substitution of S with Se results in a significant enhancement of the solution value of $|Re(\gamma)/Im(\gamma)|$ at 1550 nm, a consequence of both moderately increased $|Re(\gamma)|$ and substantially decreased $Im(\gamma)$, consistent with the expected increased detuning of the peak of the vibronically allowed 2PA S_0-S_1 transition away from excitation photon energy. On the other hand, while replacing Se (**Io**) with Te (**Ip**) results in a further increase in $|Re(\gamma)|$ consistent with increased pre-resonance enhancement, $Im(\gamma)$ also increases, presumably owing to 2PA to a higher lying state than S_1, resulting in a 2PA-FOM (29) slightly lower

than that of its Se analogue (33). The enhancement of the solution 2PA-FOMs seen for selenopyrylium dyes **Ih** and **Ij** relative to those of their sulfur analogues **Ib** and **If** is essentially eliminated in the 50% wt APC films, such that comparable 2PA-FOMs are observed for analogous structures (Table 3.4), largely due to a substantial increase in $Im(\chi^{(3)})$ for the Se compounds relative to the values extrapolated from $Im(\gamma)$. In the case of **Io** and **In** APC blends, the 2PA-FOMs for both S and Se compounds are significantly reduced relative to the corresponding solution values.

The Te-containing **Ip**:APC exhibits a $Re(\chi^{(3)})$ value (-7.6×10^{-11} esu) much larger in magnitude than that extrapolated from the solution $Re(\gamma)$ value. However, the 2PA-FOM could not be quantified due to the observation of saturable absorption in the open-aperture Z-scans; this precludes reliable measurement of $Im(\chi^{(3)})$. In principle, dye-dye or dye-host interactions might be responsible for weak NIR linear absorption involved in this saturable absorption. To examine the possibility of the latter we examined the Te dye as 50 wt% films with two other polymers, polystyrene (PS) and poly(vinylchloride) (PVC), as described in more detail in the following section. However, saturable absorption was seen in all three cases, indicating that there is appreciable linear absorption at 1550 nm in all three **Ip** films, despite linear losses remaining low to moderate. In part, absorption at 1550 nm may be because, of all the chromophores examined here, **Ip** exhibits the lowest energy absorption maxima (in both solution and films). Moreover, a weak absorption band centered at ca. 1750 nm, suggestive of J-type aggregation, can be detected for $CHCl_3$ solutions of **Ip** at concentrations as low as 0.05 mM (Figure 3.11d). With regards to Z-scan, this feature was evidently sufficiently weak and/or red-shifted enough to not impact the solution open-aperture Z-scans. No comparable low-energy absorption features are

found for S and Se dyes (Figure 3.11a-c) at similar concentrations. Thus, it is likely that similar weakly-absorbing aggregate features to those seen in **Ip** solution may contribute to the saturable absorption seen in the **Ip**-based films.
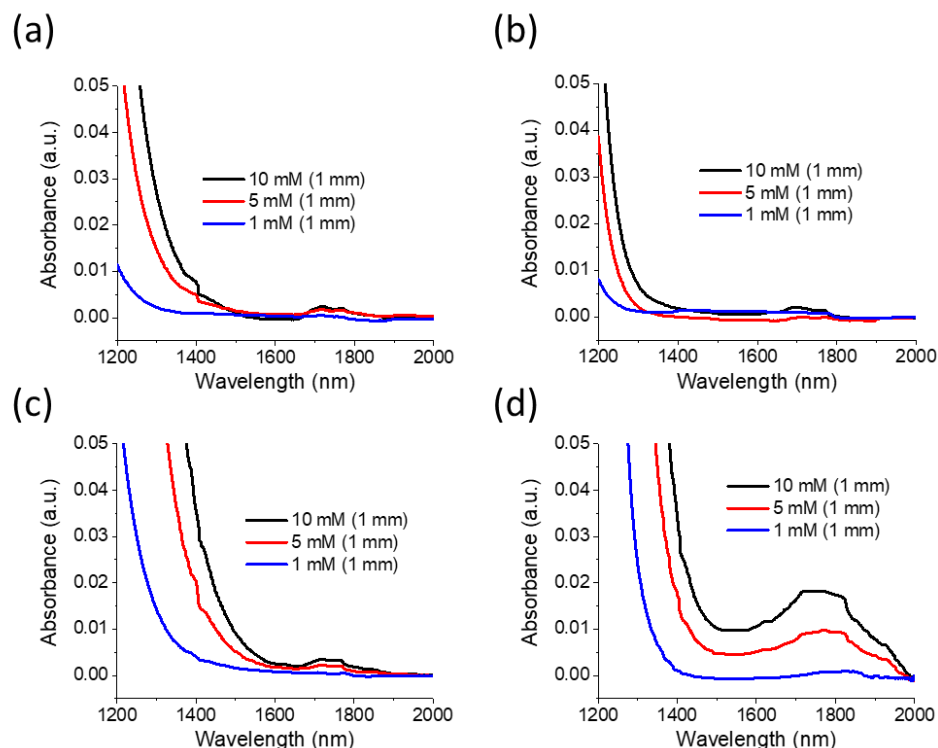
Figure 3.11. Concentration-dependent absorption spectra (smoothed using a percentile filter) in chloroform for (a) **Ie** (S-dye), (b) **Il** (S-dye), (c) **Ij** (Se-dye), and (d) **Ip** (Te-dye).

Telluropyrylium species may exhibit greater tendencies to aggregate than their thio- and selenopyrylium analogues due to their greater polarizabilities and to the reduced steric blocking of the chalcogen by the R^4 groups. The series of crystallographically characterized chalcogenopyryliums, **5c-e** (Table 3.6 in appendix), indicate decreasing C–X–C (X = S, Se, Te) bond angles and increasing C–X bond lengths with increasing chalcogen weight, resulting in increasing Ad'–X–Ad' angles and increasing Ad'–Ad' H–H separations (Figure

3.17), indicating increasing poor steric masking of the chalcogen. Similar trends can be expected in the corresponding chalcogenopyrylium dyes.

To summarize, the selenopyrylium dyes examined here generally exhibit larger 1PA- and 2PA-FOMs than their thiopyrylium counterparts (see Figure 3.13). The telluropyrylium dye example can also (depending on the host) exhibit good 1PA-FOMs, however, this compound did show saturable absorption during Z-scan measurements that precludes reliable measurement of 2PA-FOMs and would adversely affect its use in AOSP. However, whether this is a general phenomenon, is unclear. Indeed, a Te-dye with a bulky Pd(PPh$_3$)$_2$Cl "front" group shows 2PA-FOM > 10. [184] As such, more work on telluropyrylium dyes using the approach to deaggregation described here may be worthwhile, in particular, using bulkier "end" groups that further reduce the steric accessibility of the Te atoms.

3.2.2.7 Influence of the Host

As noted above, the Te dye **Ip** was investigated as a 50 wt% blend with three different polymers, chosen for their potential different interactions with the dye: APC (polar, aromatic), PS (non-polar, aromatic), and PVC (polar, non-aromatic). The Se eye **Ij** was also examined in the same three polymers. For **Ij** (Se), absorption spectra (Figure 3.12) and values of Re($\chi^{(3)}$) and 2PA-FOM (Table 3.4) vary little between the three hosts, suggesting that the bulky substitution pattern of **Ij** is effective in preventing deleterious aggregation independent of host structure. The bulkiness also likely aids miscibility of the dye and host, as evidenced by comparable values of α and narrow range of refractive indices 1.67-1.71 (Figure 3.12), which is indicative of similar film quality and composition

in all hosts. Thus, even in non-ideal hosts, blend films of **Ij** demonstrate NLO performance potentially suitable for AOSP, which may afford extraordinary flexibility regarding film processing for devices.
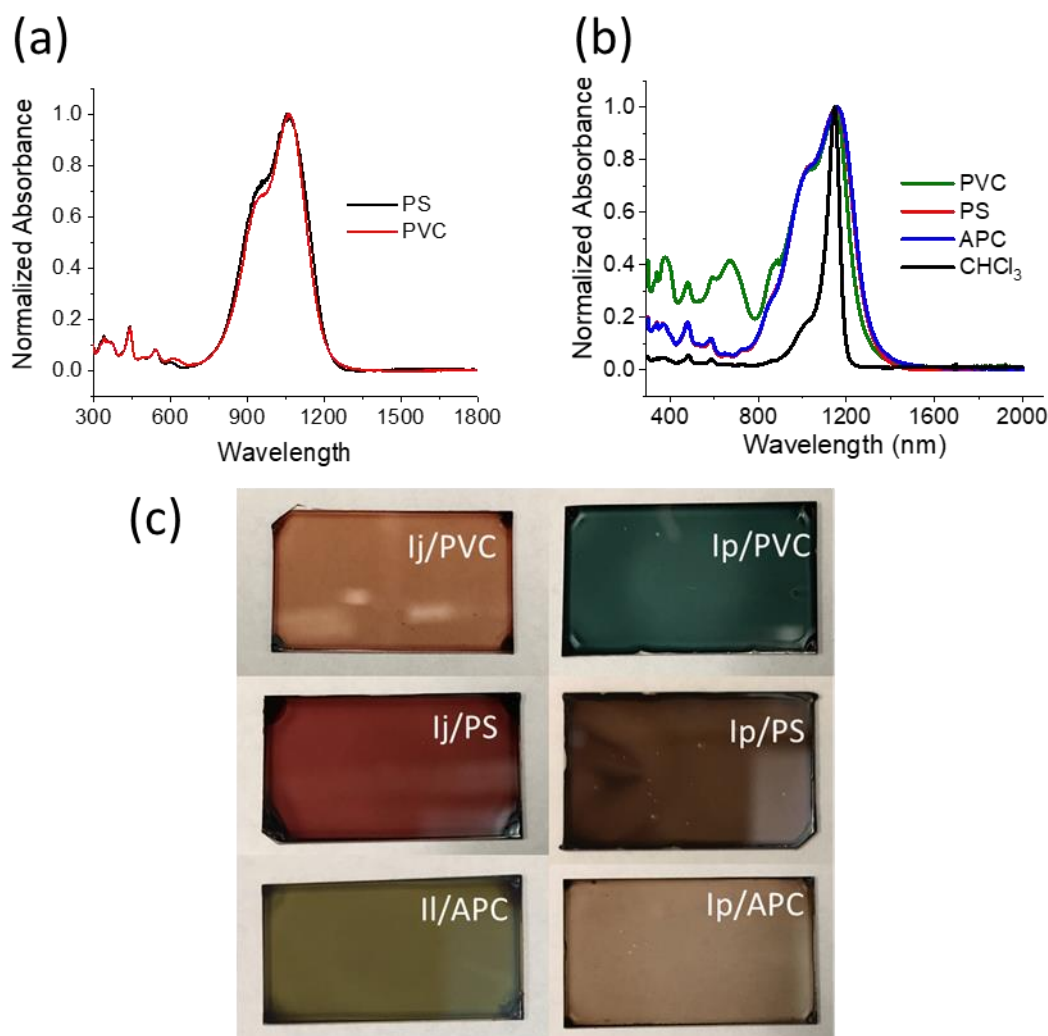
Figure 3.12. Influence of host on (top) UV-vis-NIR absorption spectra and (bottom) film appearance: absorption spectra of (a) 50 wt% films of **Ij** in PS and PVC and (b) **Ip** solution in chloroform and in 50 wt% films from APC, PS, and PVC; (c) photographs of 50 wt% blend films of **Il**, **Ij**, and **Ip** with various polymers.

In contrast to **Ij** (Se), NLO values for **Ip** (Te) blend films (Table 3.4) show significant host-dependence, with $Re(\chi^{(3)})$ ranging from -9.2×10^{-11} esu in PS to -1.2×10^{-11} esu in PVC. APC and PS films exhibited nearly identical absorption spectra (Figure 3.12b), but the PVC blends show a slight blue shift, a noticeably stronger shoulder ca. 900 nm, and some new and significantly higher relative absorbance in the 300-800 nm range. Indeed **Ip**:APC and **Ip**:PS films appear brown, while **Ip**:PVC appear dark blue film (Figure 3.12c). Additionally, the refractive index in the PVC blend (1.60) was significantly lower than APC (1.70) and PS (1.69), possibly due to a lower solubility of **Ip** in the polymer, resulting in dye loss through filtering during film preparation.

In summary, variation of the host has different effects depending on the dye in question. Nevertheless, the dependence of the optical properties of **Ip** on the host indicates that further host variation may in some cases be a useful means of improving AOSP materials.

3.2.3   *Summary and Conclusions*

A series of chalcogenopyrylium-terminated heptamethine dyes with tertiary alkyl "end" substituents and with bulky out-of-plane aromatic or aliphatic "front" and/or "back" substituents has been synthesized and characterized with a goal of understanding the influence of these substituents on the linear and nonlinear optical properties in different film blends, and in obtaining materials that exhibit values of $|Re(\chi^{(3)})|$, 2PA-FOM, and 1PA-FOM suitable for AOSP.

As shown in Figure 3.7a, solution values of $Re(\gamma)$ generally translate reasonably well into film values of $Re(\chi^{(3)})$, which fall in the range -1.2×10^{-11} to -9.2×10^{-11} esu.

Values of $|Re(\chi^{(3)})|$ are somewhat larger in magnitude than those extrapolated from solution data, which is consistent with increased pre-resonance enhancement associated with the slight red shifts seen between solution and film data. Compared to benchmark materials Si ⟨111⟩ and GaAs (Table 3) reported by Dinu *et al.* [33] at 1550 nm, films representative of the trends seen in Table 2, **In**:APC, **Io**:APC, and **Ip**:APC, gave absolute values of $|Re(\chi^{(3)})|$ that were larger than that of Si ⟨111⟩ by a factor of 1.6, 2.8, and 5.8, respectively. For GaAs, only **Ip**:APC from this series gave a larger $|Re(\chi^{(3)})|$ by a factor of 1.6. Further, the $|Re(\chi^{(3)})|$ of GaAs was found to be only slightly smaller than the values from neat films of **Ij** and **Io** but was most greatly surpassed by the **Ip**:PS blend (Table 3.4 and Table 3.5). In contrast, values of $Im(\chi^{(3)})$ for S and Se dyes generally show an even greater increase over the corresponding extrapolated values than those of $|Re(\chi^{(3)})|$ (Figure 3.7b), likely due to strengthening and/or broadening vibronically assisted 2PA into S_1, resulting in values of 2PA-FOM for films that are lower than those for solution (Figure 3.7c), especially in the case of Se-based dyes. For the Te dye, **Ip**, aggregation in the solid state leads to linear absorption that precludes measurement of $Im(\chi^{(3)})$. Despite the general reduction of 2PA-FOMs found on going from solutions to films, some of the films do exhibit 2PA-FOMs that closely approach or exceed the requirement for AOSP (Figure 8). Indeed, the 2PA-FOM for all films of thio- and selenopyrylium dyes showed marked improvements over Si ⟨111⟩ and GaAs with the increase typically becoming larger with chalcogen size, as seen in the data for most selenopyrylium compounds in neat and blend films relative to thiopyrylium dyes (Table 3.4 and Table 3.5).

Table 3.5. Macroscopic NLO values of Si, GaAs, **In**:APC, **Io**:APC, and **Ip**:APC. NLO values of Si and GaAs from reference [33].

Sample	$Re(\chi^{(3)})$ / 10^{-11} esu	$|Re(\chi^{(3)})/Im(\chi^{(3)})|$
Si $\langle 111 \rangle$	1.3	4.0
GaAs	4.7	1.3
In:APC	-2.1	5.9
Io:APC	-3.6	14
Ip:APC	-7.6	-

Despite the general reduction of 2PA-FOMs found on going from solutions to films, some of the films do exhibit 2PA-FOMs that closely approach or exceed the requirement for AOSP (Figure 3.13). Although the linear losses for the present materials are all higher than that reported for DDMEBT (1.6 dB cm^{-1}) [23], these are, to some extent, compensated for by larger $|Re(\chi^{(3)})|$, leading to values of the 1PA-FOM for a few examples that closely approach that for DDMEBT (ca. 0.87×10^{-11} esu dB^{-1} cm, Figure 3.13) with which AOSP has been successfully demonstrated. The 1PA-FOM for **Ip**:APC even exceeds that for DDMEBT, although the saturable absorption observed for this blend makes it unsuitable for AOSP due to excited state effects.

In this study, several materials – in particular, the selenopyrylium materials **Ij**:PVC, **Io**:APC, and neat **Io** – demonstrated large $Re(\chi^{(3)})$ that possess both 2PA-FOMs $\geq$ 12 and suitable 1PA-FOMs. This represents a significant advance in the field of π-conjugated organic dyes for AOSP.

Figure 3.13. Plot of 2PA-FOM ($|\text{Re}(\chi^{(3)})/\text{Im}(\chi^{(3)})|$) vs. 1PA-FOM ($|\text{Re}(\chi^{(3)})/\alpha|$) for films of chalcogenopyrylium polymethines. Data shows neat films (diamonds), 50 wt% blends with APC (solid circles), PS (triangles), and PVC (half-filled squares). Data for S- and Se-dyes are shown in black, and red, respectively. Values of blends $\text{Im}(\chi^{(3)})$, and thus the 2PA-FOM, could not be determined for blends incorporating the Te chromophore **Ip**; the blue lines indicate values of the 1PA-FOM (for **Ip**:PS there is some uncertainty in α, the value reported for 1PA-FOM is an upper limit). The horizontal dashed line corresponds to 2PA-FOM = 12, while the vertical, green dashed line represents the 1PA-FOM value for DDMEBT. [23]

3.2.4   *Appendix for Section 3.2*

Table 3.6. Summary of selected bond lengths and bond angle of pyranones **5a**, **5c-e**, and **5h**.

*Compunds, X(1)	Bond Lengths (Å)		Bond Angle (°)
	X(1)-C(1)	X(1)-C(5)	C(1)-X(1)-C(5)
5a, S	1.744(3)	1.735(3)	104.85(6)
5c, S	1.740(4)	1.742(3)	104.47(6)
5d, Se	1.888(2)	1.887(2)	100.66(3)
5e, Te	2.088(2)	2.092(2)	95.31(2)
5h, Se	1.875(5)	1.875(4)	99.83(18)
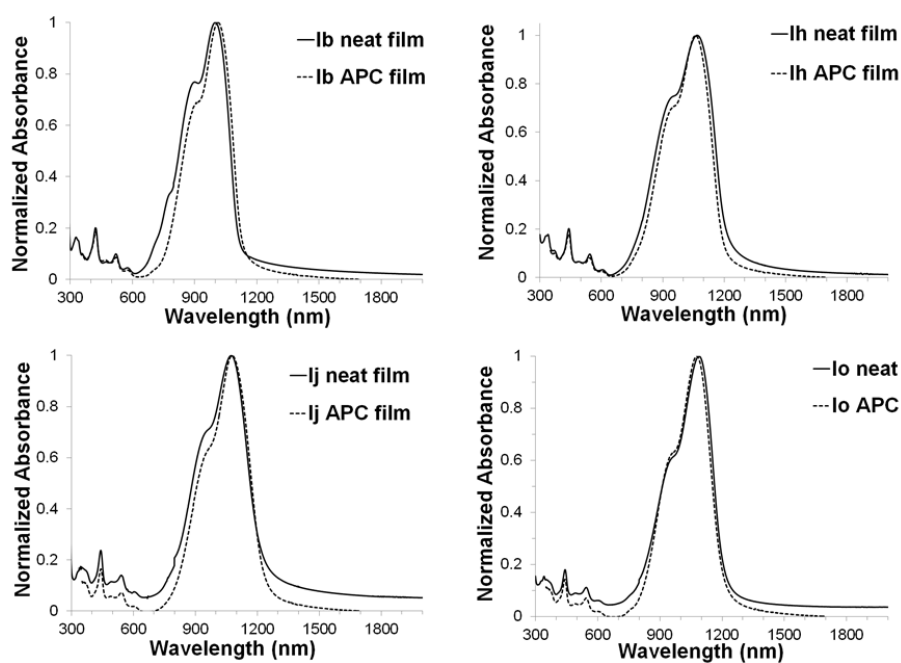
Figure 3.14. UV-vis-NIR absorption spectra of dyes **Ib**, **Ih**, **Ij** and **Io** in thin APC and thin neat films and spectra of **Ij** and **Ip** dyes in neat, APC films. Data provided by Dr. Yulia Getmanenko – Marder Group, Georgia Tech.
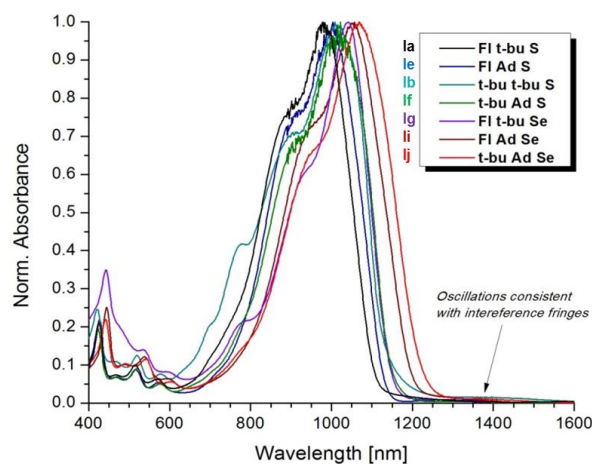
Figure 3.15. UV-vis-NIR absorption spectra of selected dyes **I** in thick APC films. Data provided by Dr. Yulia Getmanenko – Marder Group, Georgia Tech.
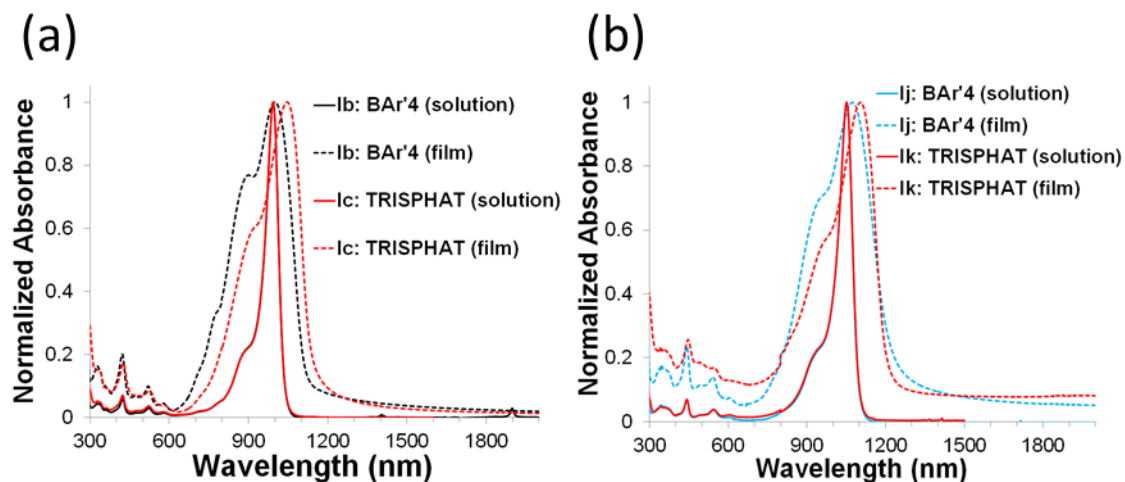
Figure 3.16. Influence of the counterion (BAr'$_4$ vs. Δ-TRISPHAT) in (a) Cbz/^{t}Bu,H/^{t}Bu/S/counterion dyes **Ib** and **Ic** and (b) Cbz/^{t}Bu,H/Ad/Se/counterion dyes **Ij** and **Ik**. Data provided by Dr. Yulia Getmanenko – Marder Group, Georgia Tech.
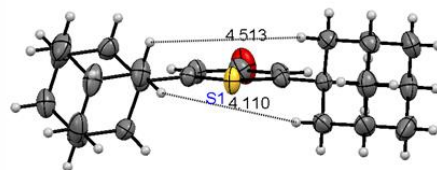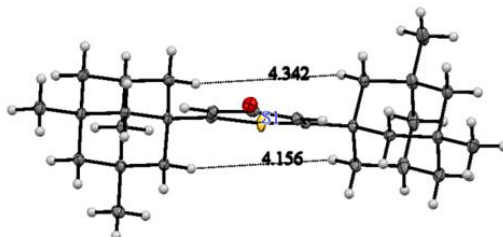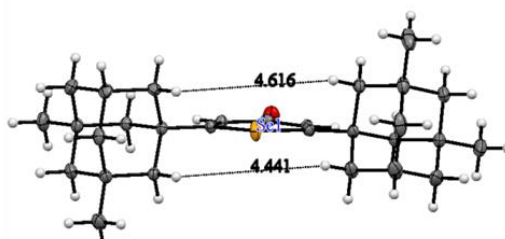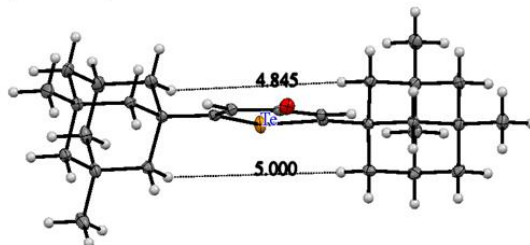
Figure 3.17. The shortest interadamantyl intramolecular H···H distances in (a) Thiopyranone **5a**; (b) Thiopyranone **5c**; (c) Selenopyranone **5d**; (d) Telluropyranone **5e**. Data provided by Dr. Yulia Getmanenko – Marder Group, Georgia Tech.

3.2.5   *Experimental Details*

3.2.5.1   <u>Polymer Purification</u>

Bisphenol A polycarbonate (Sigma Aldrich, 435120, Mw ca. 46 kDa) and PMMA (Sigma Aldrich 182230, Mw ca. 97kDa) were purified by making a 12% wt solution in 1,1,2-trichloroethane (TCE) at 60 °C and then precipitating in cold methanol, and then drying under vacuum suction. This process is repeated three total times to remove undesired surfactant from the commercially supplied pelletized polymers. PVC (Sigma Aldrich, 189588, Mw ca. 62 kDa) and PS (Polysciences, 00574, Mw 250-300 kDa) were used as received.

3.2.5.2   <u>Film Preparation</u>

All dyes were provided by Dr. Yulia Getmanenko (Marder group, GT) and used as-received (synthesis detailed in reference [197]). Films were cast using Laurell Technologies WS-650-23 spin coater operated at 750 rpm for 4 min. Thin films, both neat and polymer blends, used in linear absorption measurements were cast from 1 wt% dye solutions in spectroscopy grade 1,1,2-trichloroethane (TCE) (97% from Sigma-Aldrich), with the exception of PVC blends which were spun from spectroscopy grade cyclopentanone (≥99% Sigma-Aldrich) due to its low solubility in TCE. The solutions for spin coating thicker films used for linear loss and nonlinear optical measurements from TCE were made by mixing equal masses of 6 wt% dye solution and 6 wt% polymer solution and stirring vigorously to ensure mixing. PVC blend films from cyclopentanone were made in a similar manner but starting dye and polymer solutions were both 8 wt% to increase viscosity to achieve film thicknesses comparable to those from TCE. All solutions were

filtered through 0.2 μm PTFE syringe filter prior to spin casting to remove large impurities and undissolved particulates. The substrates for the thinner films were 1.0 mm thick microscope slides, while the thicker films were cast on 0.5 mm thick fused silica glass wafers, cut to ca. 1 × 2.5~4 cm in size to allow enough length of light propagation for accurate loss measurements. The thicknesses of the films were determined using Dektak 6M profilometer; the thicknesses of the thinner and thicker films were ca. 80-400 nm, and ca. 0.9–2.6 μm, respectively.

3.2.5.3 Characterization of Linear Absorption, Refractive Indices, and Propagation Loss

Absorption spectra were recorded using a dual-beam Shimadzu UV-3101PC UV-Vis-NIR scanning spectrophotometer. For all spectroscopic measurements (both linear and nonlinear) on solutions, spectrophotometric grade chloroform (Sigma-Aldrich) was used. Linear absorption measurements were performed on 6 μM solutions in 1 cm pathlength quartz cuvettes. The absorption spectra of the thin films were taken using a 1.0 mm thick microscope slide or 0.5 mm thick fused silica substrate as the reference, to match the substrate on which the films were coated.

The refractive indices and linear losses of the films were determined using a Metricon 2010 prism coupler. The light source was a Melles-Griot Diode laser 57STL051 using ca. 1.2 mW of CW light at 1550 nm. The incident laser light strikes a highly refractive gadolinium gallium garnet prism with $n_0 = 1.934$ at 1550 nm mounted on a rotary table. The film to be measured is brought into contact with the prism using a pneumatically-operated coupling piston. At angles of incidence where the criterion for total internal reflection is violated, called critical coupling mode angles, the photons tunnel from the

base of the prism across the air gap into the film, and propagate along the length of the film, causing a sharp drop in the intensity of light striking the photodetector near the exit surface of the prism. At these angles of maximum light coupling, the complex transcendental mode equations that govern the reciprocity become a system of linear equations with common solution for the film index, n_0. [203]

For linear loss measurements, the prism is set to the mode angle furthest away from the substrate, the light being guided by the film is measured using a movable fiber detector that scans across the length of the film. The plot of the intensity with respect to distance traveled by the fiber detector produces an exponential decay profile, from which the linear loss is calculated. For Metricon 2010, the detectable range for this loss-based measurement is 0.5–20 dB cm^{-1}. The error associated with the technique depends on the length of the film and the quality of the exponential fit. For typical films (ca. 3.5 cm in length), the error is estimated to be ca. ±20%. It should be noted that these losses include not only the linear absorption by the chromophores but also optical scattering. The latter is most likely responsible for the loss of 1.9 dB cm^{-1} measured in a pure APC film.

3.2.5.4 <u>Nonlinear Optical Characterization</u>

The light source used for all nonlinear optical measurements was a regeneratively amplified Ti:Sapphire system (Solstice, Spectra-Physics) that produces sub- 90 fs (HW1/e) pulses at 800 nm with a repetition rate of 1 kHz. This, in turn, pumps an optical parametric amplifier of white-light continuum (TOPAS-C, Spectra-Physics) that provides output pulses of <100 fs (HW1/e) in the appropriate spectral bands. Using this light source, Z-scans were performed to determine the real and imaginary components of the third-order

nonlinearity of the samples. The operation principle and standard layout for the Z-scan technique are well understood, and accepted. [204, 205] The details of data processing methods are discussed in the reference. [195]

The spatial and temporal properties of the pulse are given by the following; the HW1/e^2 radius of the beam was ca. 60 µm, its Rayleigh range was 3.5–5.1 mm, the pulse widths ranged from 48~65 fs (HW1/e), and the beam shape was found to be Gaussian with an M value of 1~1.08. The experimental setup was calibrated using well-established nonlinearities for samples of fused silica [143], ZnS [144], and ZnSe [206]. The repetition rate of the system was reduced to 50 Hz for γ measurements to avoid effects of thermal lensing. The resulting open- and closed-aperture scans were then corrected by subtracting their respective background contributions: the solvent, CHCl$_3$, in the cases of solution measurements, and the spot to be measured at a low enough irradiance as to not observe NLO behavior in the case of film measurements. To ensure that the extracted apparent values of Re($\chi^{(3)}$) and Im($\chi^{(3)}$) do indeed represent third-order nonlinearities, the Z-scans on each sample were performed at various excitation irradiances ranging from 30–250 GW cm^{-2}. Both Re($\chi^{(3)}$) and Im($\chi^{(3)}$) values for the heptamethine solutions and films showed a negligible level of irradiance dependence, as expected for purely third-order nonlinearities. From the error propagation analysis using the standard deviations in the experimental parameters, the experimental uncertainties were estimated to be ±8% for Re(γ), ±11% for |Re(γ)/Im(γ)|, ±13% Re($\chi^{(3)}$) and ±18% for |Re($\chi^{(3)}$)/Im($\chi^{(3)}$)|.

3.3 Linear and Nonlinear Optical Properties of Benzoindole-Terminated Heptamethines with Cl- and Bulky Pd(PPh₃)₂Cl Groups in Solution and Amorphous Polycarbonate Blend Films

3.3.1 *Background and Experimental Approach*

Previous reports, as well as results from section 3.2, on the substitution of chalcogenopyrylium-terminated heptamethine dyes with rigid, bulky organic groups demonstrated that one can effectively reduce interactions in the solid state and thus improve 2PA-FOMs in neat and APC blend films by selectively rendering the conjugated backbone of the dye inaccessible via strategic molecular design. [25, 195] Building on this work, Davydenko et al. [183] recently discovered that, while attempting to use Pd-catalyzed cross-couplings to attach bulky aryl groups to central *meso* position on polymethine chains, *meso*-Cl-substituted heptamethines readily underwent oxidative addition with $Pd(PPh_3)_4$ to form stable compounds. It was found that *meso*-Cl-substituted benzoindole-terminated heptamethines reacted cleanly with one molar equivalents of $Pd(PPh_3)_4$ to yield compounds **1-5'Cl**, **Pd** in Figure 3.18, of interest in this investigation, and other compounds such as perylene diimides, merocyanines, and **6'Pd** from Figure 3.23.
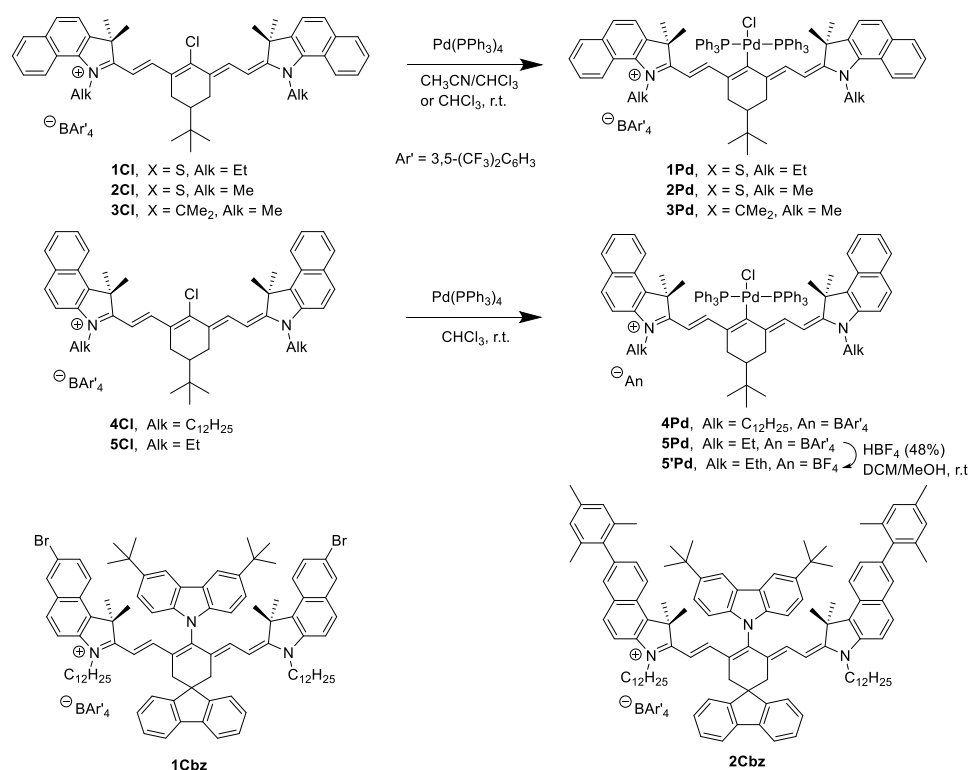
Figure 3.18. Benzoindole-terminated heptamethine compounds and reaction diagrams used for NLO solution and film measurements. Partially reproduced from Davydenko *et al.* [183] with permission. Copyright 2016 Journal of the American Chemical Society.

In combination with ^tBu "back" groups, $Pd(PPh_3)_2Cl$-substituted dyes, or more simply referred to as Pd-dyes, are expected to possess significant, rigid, out-of-plane bulk to prevent aggregation between dyes in the high number density solid state. Indeed, crystal structures of these compounds (Figure 3.19) show that, compared to their Cl-substituted counterparts, Pd-dyes offer no evidence of interchain interactions because of the massive Pd-group. Further, due to a lack of steric hinderance around the benzoindole end groups, one can observe some planar interactions between two adjacent end groups, as seen for **1Pd** (Figure 3.19c-d) and **5'Pd** (Figure 3.19g-h). Interestingly, substantial overlap is observed between the phenyl rings of neighboring **1Pd** compounds possessing

128

benzo[g]indole groups compared to the much-reduced overlap seen between two compounds with benzo[e]indole groups, such as **5'Pd**.
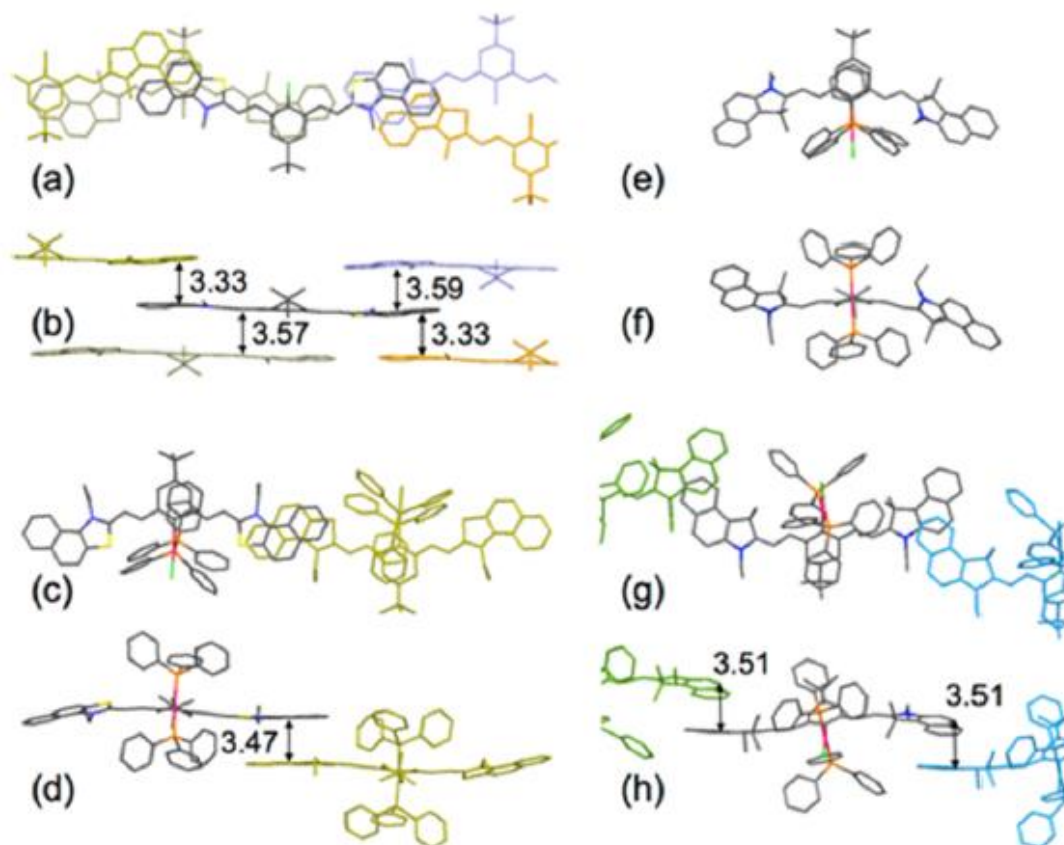
Figure 3.19. Crystal structures of (a-b) **2Cl**, (c-d) **1Pd**, (e-f) **5Pd**, and (g-h) **5'Pd**, showing for each interactions of the π system of one polymethine cation (colored by element) with that of its neighbors (uniform colors). Selected interplanar and atom-plane distances in are indicated. H atoms, counterions, solvent molecules, and disorder have been omitted for clarity. Reproduced from Davydenko et al. [183] with permission. Copyright 2016 Journal of the American Chemical Society.

Since end-on-end group interactions are possible, absorption spectra in concentrated solutions and thin films must be monitored carefully to verify that J-like aggregates are avoided during linear and NLO measurements. With regards to film processing, preliminary solubility tests show that **4Pd** is sparingly soluble in 1,1,2-trichloroethane (TCE) and therefore a new film processing method needed to be developed.

Additionally, given the tendency for APC blend films from TCE to form ripples that cause significant thickness fluctuations (ca. ±15%), optimizing the spinning/drying conditions is of interest and will be discussed in terms of films quality for Z-scan. [207] As such, Z-scan measurements in solution and high number density blend films (50% wt) with APC at 1300 and 1550 nm will be conducted to gauge the dispersion of $Re(\gamma)$, $Re(\chi^{(3)})$, and the 2PA-FOMs for the compounds in question and to characterize the influence of this Pd-substituent on the NLO properties of benzoindole-terminated heptamethines in reference to chalcogenopyrylium-dyes previously discussed. [195] Specifically, data at 1550 nm will be compared to values obtained for chalcogenopyrylium-dyes in previous sections (3.2) as well as benchmark NLO materials Si and GaAs. [33] To complement NLO measurements, linear loss data at 1550 nm is presented to further gauge the effectiveness of Pd-substituents in reducing linear optical losses in the solid state, which is critical for assessing device relevance for these materials.

3.3.2   *Results and Discussion*

3.3.2.1   Linear Absorption Data and NLO Measurements in Solution

Linear absorption spectra for the palladium-bearing, benzoindole-terminated dyes (Figure 3.18) in solution with chloroform and in 50% wt amorphous polycarbonate (APC) blend films are shown in Figure 3.20. Solution spectra show that the addition of the Pd group resulted in a blue shift compared to Cl-dyes, which is attributed to the Pd group being a stronger π donor and/or weaker σ acceptor than Cl. [183] The subtle change in the solution spectral position upon Pd-substitution is also met with a small change in the vibrational fine structure of the high energy shoulder of the cyanine-like band where Pd-

dyes show slightly reduced absorbance. [208, 209] The full width at half maximum (FWHM) for the normalized absorption spectra for both Cl- and Pd-substituted dyes were comparable (**3Cl**: 49 nm, **3Pd**: 45 nm, **4Cl**: 42 nm, and **4Pd**: 41 nm), further corroborating the limited impact that the bulky Pd group has on the electronic transitions among this series of dyes.
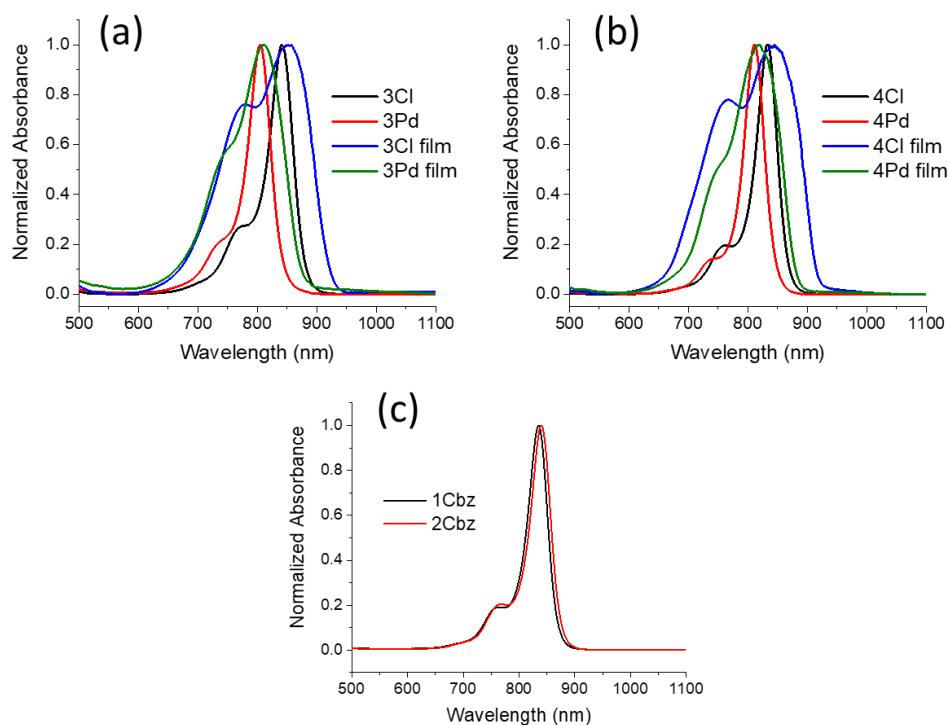
Figure 3.20. Absorption spectra for (a) **3Cl** and **3Pd** in chloroform solutions and 50% wt thin films with APC, (b) **4Cl** and **4Pd** in chloroform solutions and 50% wt thin films with APC, (c) **1Cbz** and **2Cbz** in chloroform solutions.

Absorption spectra in 50% wt APC thin films (Figure 3.20) show broadened peaks compared to their corresponding solution spectra and red-shifting that is more profound for less bulky substituted Cl-dyes than the Pd-analogue. From these spectra, Pd-dyes maintained solution-like spectra with no evidence of J-like aggregation and minimal spectral broadening compared to Cl-dyes; where less steric bulk resulted in significant

broadening and a dramatic increase in the high-energy shoulders that could be associated with a multitude of intermolecular interactions between the heptamethine backbone and other dyes or the host polymer. This difference is seen clearly when examining the FWHM of the blend film spectra where **3Cl** and **4Cl** spectra gave FWHM values of 161 nm and 172 nm, respectively, compared to 118 nm and 112 nm for **3Pd** and **4Pd**, respectively. These trends were consistent with similar spectra reported for neat films of the same set of dyes, in addition to others, by Davydenko *et al.* [183] and highlights the success of the bulky palladium groups with regards to preventing strong polarizing interactions with the heptamethine backbone in the solid state.

Table 3.7. Average NLO data from Z-scan measurements in chloroform solution at 1550 nm for Cl-, Pd-, and Cbz-substituted heptamethine dyes.

Cmpd	λ_{max} (nm)[a]	λ_{max} (nm)[b]	$Re(\gamma)$ 10^{-33} (esu)	$Im(\gamma)$ 10^{-33} (esu)	$|Re(\gamma)/Im(\gamma)|$ [c]
3Cl	841	852	-1.4 [c]	1.5 [c]	0.9 [c]
3Pd	805	812	-2.4 [c]	4.6 [c]	0.5 [c]
4Cl	833	844	-8.4 [c]	9.2 [c]	0.9 [c]
4Pd	811	818	-3.2 [c]	4.1 [c]	0.8 [c]
1Cbz	835	d	-30 [e]	6.8 [e]	4.4 [e]
2Cbz	840	d	-31 [e]	1.0 [e]	3.0 [e]

a) In solution, b) In 50% wt APC blend films, c) Irradiance ca. 90 GW/cm^2, d) Because only thick films (ca. 1 µm) were made, absorption data in film was outside the detection range of the absorption spectrometer (i.e. >>2.5 OD) and thus was not quantifiable, and e) irradiance ca. 57 GW/cm^2.

Nonlinearities at 1550 nm in chloroform solutions of benzoindole-terminated dyes (Figure 3.18) are presented in Table 3.7. Compared to the nonlinearities obtained for chalcogenopyrylium dyes in section 3.2 and reference [195], $Re(\gamma)$ for both Cl- and Pd-dyes were generally an order of magnitude lower and gave figures of merit ($|Re(\gamma)/Im(\gamma)|$, 2PA-FOM) in the range of 0.5-0.9 at an irradiance of 90 GW/cm^2; much lower than the

FOM $\geq$ 12 desired for AOSP. This trend is clearly rationalized by examining the maximum absorption wavelength, which is ca. 170 nm blue-shifted relative to even the shortest wavelength absorbing thiopyrylium dye (**Im** – Table 3.1) and means that, comparatively, benzoindole-dyes are less polarizable and are not able to benefit as greatly from resonance enhancement when measuring the telecommunications window. Additionally, significant irradiance dependence was observed for scans of all benzoindole dyes, regardless of substitution. As seen in Figure 3.21b, Z-scans at increasingly large pulse energies (proportional to irradiance), show that there was a concomitant increase in the $Re(\gamma)$ (note: these are negative n_2 materials, so values will thus become increasingly negative), with $Im(\gamma)$ remaining relatively constant over the measured range of energies. This resulted in an apparent increase in 2PA-FOM with increasing irradiance that was attributed to excited state refraction (ESR), an effective NLO process likely resulting from the population of a low-lying, two-photon state close to the primary one-photon transition (ca. 775 nm – half the wavelength of the 1550 nm beam). This phenomenon is thought to occur via vibronic-coupling associated with C-C stretching modes along the conjugated backbone, similar to what was seen by Ohira *et al.* [210] for squaraine dyes with indolinylidenemethyl end groups. [208, 209] This photophysical mechanism is illustrated in Figure 3.21a, where the vibronic coupling makes possible an appreciably strong transition between the singlet ground state (g) and a low lying, two-photon-allowed state (e') just above the lowest 1PA state (e).
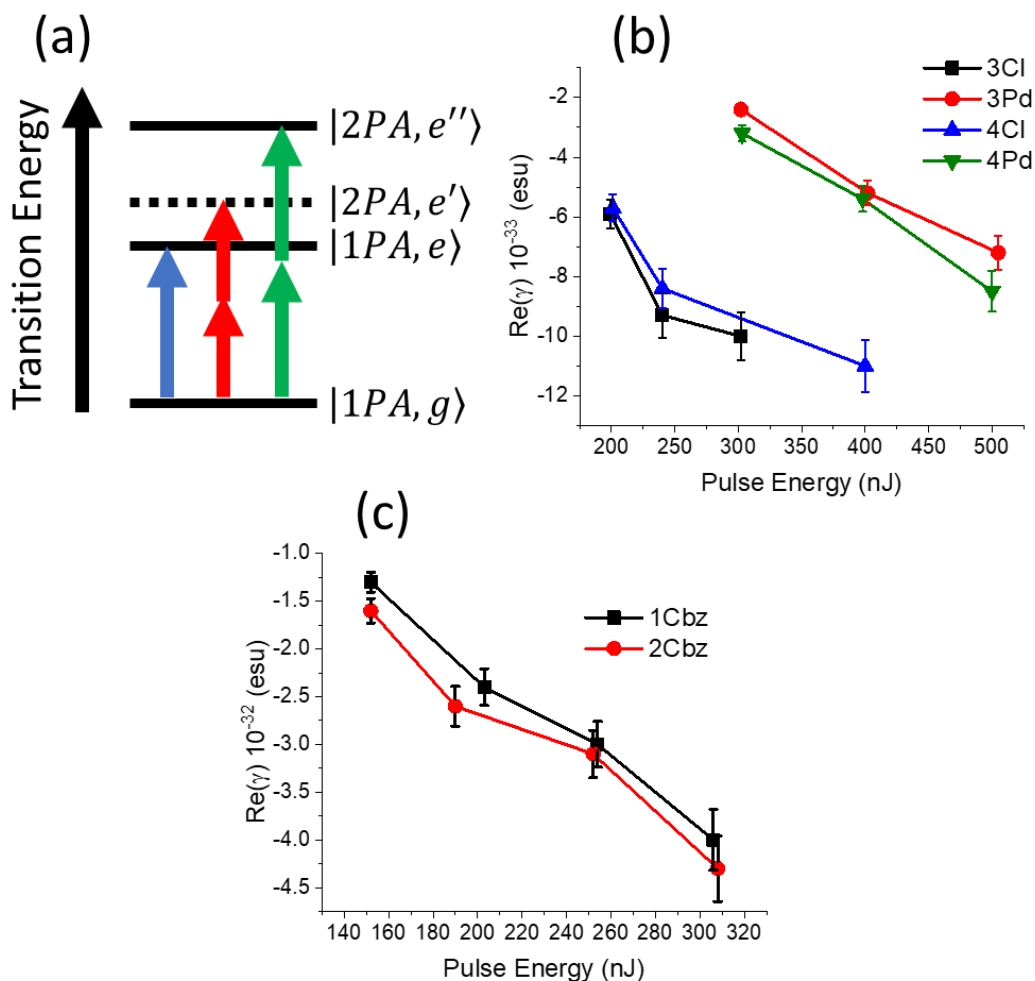
Figure 3.21. (a) Jablonksi diagram showing possible 1PA and 2PA transitions, where solid lines represent purely electronic transitions and the dotted line represents the vibronic-coupled state (e'). Additionally, the singlet ground state (g), the first real 1PA state (e), and the first hypothetical, purely electronic 2PA state (e'') are shown. The blue arrow represents the photon energy required to linearly excite the g → e transition, the red arrows illustrate the degenerate excitation of the vibronic 2PA transition g → e' (the case for Z-scan measurements for this set of materials at 1550 nm), and the green arrows are even higher energy photons needed to excite the hypothetical purely electronic 2PA state (e''). Plots showing dependence of average Re(γ) on pulse energy (E) (proportional to irradiance (I) according to eq. 2.11) at 1550 nm from Z-scan in chloroform solutions for (b) Cl- and Pd-dyes and (c) **1Cbz** and **2Cbz**.

Under non-resonant conditions, the low-lying vibronic 2PA state could benefit AOSP by providing a means to control the dispersion of Re(γ) in the telecommunication window. [210] However, the behavior of the benzoindole-terminated compounds is undesirable for AOSP because a real 2PA excited state is accessed degenerately by 1550 nm photons and likely has a lifetime orders of magnitude longer than the femtosecond pulses used to achieve ultrafast AOSP, which fundamentally limits the switching speed as well as phase modulation efficiency. To rule out any Cl- and Pd-specific phenomena contributing to the observed irradiance dependence, Z-scan measurements on benzoindole-terminated cyanines with carbazole "front" substitution (**1Cbz** and **2Cbz** from Figure 3.18) were performed and demonstrated a similar trend with regards to irradiance dependence (as seen in Figure 3.21c); affording nonlinearities that were approximately an order of magnitude larger than those for the Cl- and Pd-dyes. It is noted that no irradiance dependence has been reported for 4,5,5-trimethyl-3-cyano-2(5H)-furanylidenepropane-, or "TCF-", terminated, anionic heptamethines with Cl- in the "front" position, ᵗBu in the "back", with bulky counterions, and similar red-shifted absorption maxima to benzoindole dyes presented here. [29]

To better understand the dispersion of this effect on the high energy side of the telecommunications window, Z-scan measurements were performed at 1300 nm for Cl-, Pd-, and Cbz-substituted dyes in chloroform solutions. Results are plotted in Figure 3.22 and show generally larger nonlinearities for Cl- and Pd-dyes at 1300 than 1550 nm, which is primarily attributed to greater resonance enhancement that comes from shifting the measurement wavelength toward the resonance of the closely-spaced 1PA/vibronic-2PA states. Additionally, the magnitude of the change in |Re(γ)| with increasing irradiance was

comparable to that observed at 1550 nm. Compared to Cl- and Pd-dyes, the Cbz-substituted compounds exhibited less dispersion and, interestingly, the trend is opposite that for Cl- and Pd-dyes where $|Re(\gamma)|$ at 1550 nm is consistently larger than that at 1300 nm. Although the exact cause is unclear, this phenomenon could be related to the position of the vibronic-2PA band being red-shifted relative to those in the Cl- and Pd-compounds and thus is being excited more favorably at 1550 nm than at 1300 nm. Assuming the spectral position of the higher-energy fine structure bands from 1PA reflects that of the vibronic 2PA state (e'), this could be explained by the e' state being situated closer to 775 nm, equivalent to the total transition wavelength when pumping degenerately at 1550 nm, than it is to the total transition wavelength at 1300 nm (650 nm).
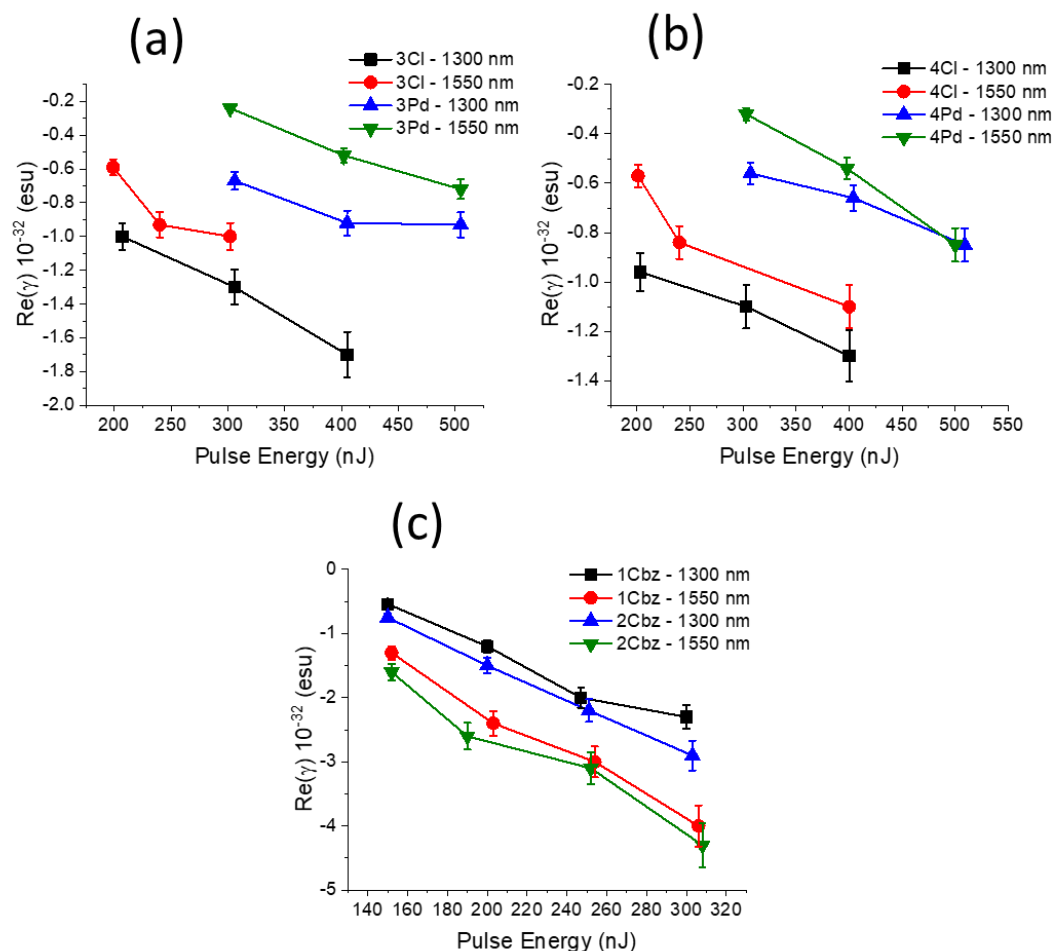
Figure 3.22. Plots comparing the dependence of average Re(γ) on pulse energy (proportional to irradiance) at 1300 and 1550 nm from Z-scan in chloroform solutions for a) **3Cl** and **3Pd**, b) **4Cl** and **4Pd**, c) **1Cbz** and **2Cbz**.

It was noted that, over several hours, chloroform solutions of **3Cl**, **3Pd**, **4Pd**, and **4Cl** would noticeably change color from a dark green to a red/brown, likely due to decomposition. This breakdown mechanism was investigated in further detail in the supplementary information by Davydenko *et al.* [183]. To avoid complications with degradation, solutions of Cl- and Pd-dyes in chloroform were made fresh shortly before measurements and measured immediately. Although more rigorous quantum chemical calculations and NLO measurements are needed as confirmation, the analysis presented in

this section indicates that the molecular geometry of benzoindole-terminated heptamethines results in significant vibronic coupling that makes possible a 2PA-allowed transition with appreciable degenerate cross section in the 1300-1550 nm wavelength range. [211]

3.3.2.2   Linear and NLO Measurements of 50% wt Dye:APC Blend Films

Film preparation for 50% wt blend films with APC for Cl-, Pd-, and Cbz-dyes was initially attempted with 1,1,2-trichloroethane (TCE) as the spinning solvent (as described in 3.2.5.2), in which 4Pd demonstrated little-to-no solubility. To maximize consistency between blend films within this set of compounds, an alternative recipe was found with a solvent (1,2-dichloroethane – DCE) in which all dyes from this series were soluble. [207] Compared to the longer spinning speeds needed to fully dry films spun from TCE, optical-quality films are obtained from DCE by flooding the substrate with well-mixed, filtered blend solution and then adjusting the acceleration speed to spread the blend solution evenly over the entire substrate surface over a short period of time and then drying the film quickly under vacuum. It was noted that higher concentrations of individual dye and polymer solutions prior to blending were necessary to increase the viscosity of total solution to compensate for lower viscosity of DCE relative to TCE. [212] This straightforward method (details in section 3.3.4.2) results in films of sufficient thickness for Z-scan (ca. 1 µm) with reduced thickness variations relative to those seen in APC films spun from TCE. Indeed, this film processing method has been successful in making 50% wt blend films of APC with **6'Pd** (Figure 3.23) to yield acceptable quality Z-scans for the analysis of aggregation mitigation for anionic heptamethine dyes enabled by the same bulky Pd-substitution method reported in reference [183]. The degree of spectral broadening for thin films made

by this method relative to spectra in chloroform solutions of Cl- and Pd-substituted dyes were discussed previously in section 3.3.2.1.
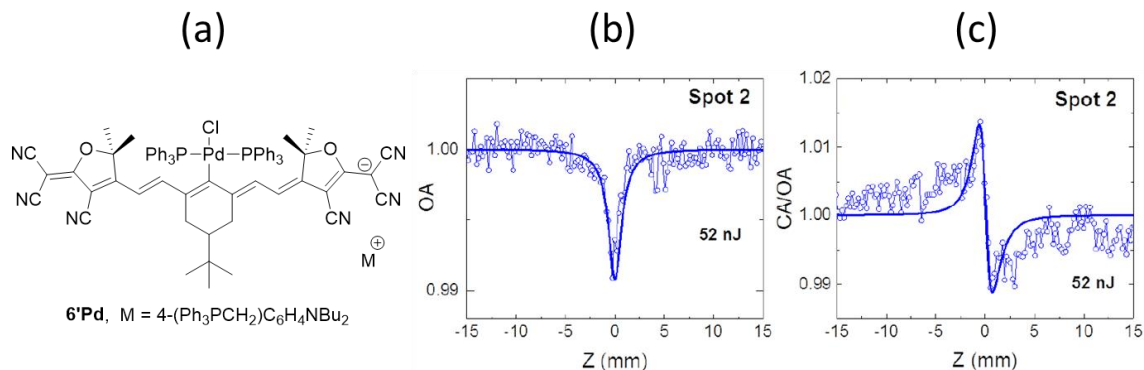
Figure 3.23. (a) Structure of **6'Pd**, (b) open aperture and (c) closed/open aperture scan of a 50% wt blend film with **6'Pd** and APC. Parts b and c reproduced from Davydenko et al. [183] with permission. Copyright 2016 Journal of the American Chemical Society.

Z-scan data from 50% wt APC films (Table 3.8) gave values of $Re(\chi^{(3)})$ at an irradiance of 90 GW/cm^2 comparable to the benchmark NLO materials Si and GaAs (Table 3.5) at 1550 nm. As such, at lower irradiances, the NLO properties of these materials were generally lower than that for Si and GaAs. Relative to the macroscopic extrapolated values $(Re(\chi^{(3)})_{extr})$ calculated from solution data, $Re(\chi^{(3)})$ at a similar irradiance (90 GW/cm^2) for most samples (with **4Cl** as the exception) was approximately an order of magnitude larger, which also facilitated macroscopic FOMs that were greater by at least a factor of 4.4 (the case of **4Cl**) and, in the largest case (**3Pd**), by a factor of 16.6. However, it should be stressed that, because these materials exhibit irradiance-dependent $Re(\chi^{(3)})$, quantitative comparisons cannot be drawn in a straightforward way and care must be taken to avoid speculation when discussing molecular trends.

Table 3.8. NLO and linear loss data at 1550 nm for 50% wt APC blend films with Cl- and Pd-dyes.

Compound	$Re(\chi^{(3)})\ 10^{-11}$ (esu) [a]	FOM [a]	$Re(\chi^{(3)})_{extr}\ 10^{-11}$ (esu)	FOM_{extr}	Linear Loss (dB cm^{-1})
3Cl	-4.9	4.1	-0.20	0.9	5.8
3Pd	-2.0	8.3	-0.24	0.5	3.6
4Cl	-1.5	4.0	-0.99	0.9	5.6
4Pd	-2.2	11	-0.25	0.8	3.3

a) Irradiance ca. 90 GW/cm^2 and b) Extrapolated from solution NLO data at irradiance of ca. 90 GW/cm^2.

Although **3Pd** and **4Pd** gave similar $|Re(\chi^{(3)})|$ values at the same irradiance, **3Cl** and **4Cl** were markedly different. **4Cl** was found to break the trend established in solution measurements where Cl-substituted dyes typically gave larger values of $|Re(\gamma)|$, presumably due to red-shifted absorption maxima (relative to Pd-dyes) enabling substantially greater benefit from resonance enhancement. Since **4Cl** showed the largest $|Re(\gamma)|$ from this series but gave the smallest $|Re(\chi^{(3)})|$, one must consider the possibility that, in the high number density solid-state, this dye could be participating in deleterious interactions with other dyes or the polymer host that alter its electronic properties. Typically, such interactions result in an increase in $Im(\chi^{(3)})$ and result in lower 2PA-FOM. However, this was not observed for **4Cl** in 50% wt APC blends, as evidenced by the similar FOM between the Cl-substituted compounds suggesting that, with a reduction in $|Re(\chi^{(3)})|$, also came a equal reduction in $Im(\chi^{(3)})$. This observation appears more like a dilution effect, which could suggest that the solubility of **4Cl** in DCE blend solutions is slightly less than the other dyes reported here and results in some dye being lost during filtering.
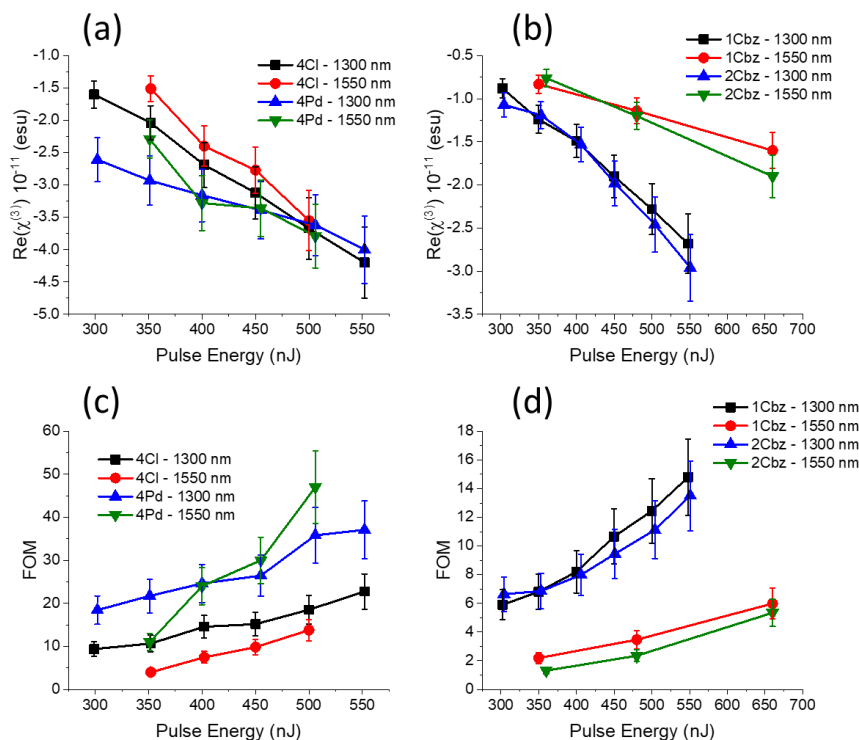
Figure 3.24. Plots of a) Irradiance-dependent $Re(\chi^{(3)})$ for **4Cl** and **4Pd**, (b) irradiance-deppendent $Re(\chi^{(3)})$ for **1Cbz** and **2Cbz**, (c) FOM for **4Cl** and **4Pd**, and (d) FOM for **1Cbz** and **2Cbz** in 50% wt APC blend films. Values for **3Cl** and **3Pd** could not be obtained due to uncertainty in $Im(\chi^{(3)})$, possibly related to film damage.

Regardless of anomalously low and irradiance-dependent nonlinearities, the 2PA-FOM for Pd-bearing dyes in APC blends are appreciably larger than their Cl-analogues (Table 3.8 and Figure 3.24c) at a given irradiance, which supports the hypothesis of bulky Pd-substitution as an effective means for preventing aggregation in the solid state. Further, the trend in linear loss for these films at 1550 nm corroborates this argument, given that Cl-substituted films showed moderate loss values (5.6-5.8 dB cm^{-1}) and Pd-dyes gave lower values (3.3-3.6 dB cm^{-1}), which are attributed to minimizing polarizing interactions between the dye and its environment in the solid-state. Further, this is corroborated by the similarity in loss values for these compounds to heavily substituted thiopyrylium-dyes **7** and **8** (3.5 and 3.4 dB cm^{-1}, respectively) in reference [195]. Although **4Pd** (FOM = 11)

141

approaches the requirements for AOSP (FOM $\geq$ 12) at moderate irradiances, it is again stressed that the role of excited states in this process present significant limitations to the application of these materials as an active NLO material. This can be seen in Figure 3.24, where Re($\chi^{(3)}$) and FOM are plotted against pulse energy at 1300 and 1550 nm. Unlike Re(γ) from solution, Re($\chi^{(3)}$) obtained for the pair **4Cl** and **4Pd** showed no significant dispersion between data collected at 1300 versus 1550 nm. However, FOM for **4Pd** blends are distinctly higher than **4Cl**, which is likely associated with reduced Im($\chi^{(3)}$) as a result of the bulky group mitigating electronic changes in the excited state. From Figure 3.24c, one can also see that the irradiance dependence in the FOM for **4Pd** are greater than the rest of the set. The somewhat sharply rising FOM was originally thought to be a function of film damage where, at high irradiances (ca. 200 GW/cm^2, close to 550 nJ in pulse energy at 1300 and 1550 nm with beam waist ca. 40 µm), ablation of the polymer blend can occur and result in the appearance of increased transparency, i.e. decreased Im($\chi^{(3)}$). However, nonlinear transmission values obtained via Z-scan did not increase with increases in pulse energy for this sample, which suggests that ablation-induced transparency did not occur. Although cause for a small degree of irradiance dependence in Im($\chi^{(3)}$) is unclear, another possible explanation is local heating while the sample is translated through the focus of the beam, which might induced morphology changes in the film during scans at higher irradiance. On this topic, degradation issues discussed in the previous section were also of concern in blend films, where fresh, green films containing Pd-dyes would turn red in color after prolonged exposure to ambient light and/or oxygen conditions. This, however, is avoided over the timescale of the measurement by preparing fresh films prior to

measurement, storing films under vacuum protected from ambient light conditions, and measuring in a dark room.

Compared to the dispersion behavior for **1Cbz** and **2Cbz** in 50% wt APC blends, the relative similarity of values obtained for $Re(\chi^{(3)})$ and FOM for the Cl- and Pd-dyes is somewhat surprising given the stratification of the $Re(\gamma)$ data seen in Figure 3.22. However, considering the relatively small spectral shift between these compounds and the substantial degree of broadening observed in Cl-dye films, it is possible that the even moderate broadening of the vibronic 2PA band (g → e') from Pd-dyes in the solid state could overlap significantly with the, hypothetically, more greatly broadened Cl-dye vibronic band and thus possess similar transition strengths in the telecommunications window, which may flatten dispersion in this wavelength range. This, of course, assumes that the broadening of 1PA spectra (Figure 3.20a-b) is reflective of that within the vibronically-assisted 2PA transitions and that the TDMs are similar in magnitude. Although it is unclear whether this is the exact cause for this observation, this could also mean that the broadening experienced by **1Cbz** and **2Cbz** in the solid state is less than that experienced by **4Cl** and **4Pd**. An alternative hypothesis for this phenomenon, that is yet to be tested, is that the vibronic structure changes significantly in **1Cbz** and **2Cbz**, such that the vibronic 2PA band is destabilized relative to the 1PA state, resulting in greater transition strength when pumped by shorter wavelengths (i.e. 1300 nm).

3.3.3 *Summary and Conclusions*

In this section, evidence was presented to quantify the impact of $Pd(PPh_3)_2Cl$-substitution on the meso-position for the backbone of benzoindole-terminated

heptamethine dyes with regards to mitigating aggregation interactions in 50% wt APC blend films to preserve solution-like NLO properties. Successful deaggregation was evident from the observed differences in the 2PA-FOM at 1550 nm, where Cl-substituted dyes demonstrated smaller values at the same irradiance than their Pd-analogues. Additionally, the reduced linear loss at 1550 nm for Pd-substituted compounds in APC blends relative to Cl-dyes in the same matrix were attributed to the protection of the heptamethine backbone from deleterious electronic changes in highly concentrated films. Analysis of the NLO performance for these compounds was somewhat complicated by irradiance dependent $Re(\gamma)$ and $Re(\chi^{(3)})$, which were attributed to ESR. This was thought to occur because of 2PA made possible by the vibronic coupling of C-C stretching modes of the conjugated heptamethine chain with electronic states of the molecule. With careful control of irradiance, one can still deduce some molecular information, however, because of the role of real excited states in these processes, the dyes examined in this section are not suitable for AOSP applications as the lifetime of the excited state fundamentally limits the switching speeds and device efficiency one could obtain in the telecommunications wavelength window.

3.3.4 *Experimental Details*

3.3.4.1 Polymer Purification

Poly(bisphenol A carbonate) (APC) (Sigma Aldrich, 435120, Mw ca. 46 kDa) pellets were dis-solved in *N*-methyl-2-pyrrolidone (NMP) to make a 12% w/w solution at 75 °C. The warm solution was then slowly poured into cold methanol while stirring, which yielded white clumps of precipitated APC. The precipitate was filtered and dried on a

vacuum suction filter. The process of dissolving in NMP, precipitating in methanol, and drying under vacuum suction was repeated twice more. After three cycles of precipitation, APC was dried under vacuum in an oven overnight at 80 °C.

3.3.4.2 Preparation of 50% wt APC:Dye Blend Films

Double side polished fused silica substrates were cleaned first by soaking in piranha solution (3:1 H_2SO_4:30% H_2O_2 by volume) with stirring for 12 hours. After washing thoroughly with water and drying with a stream of nitrogen, the substrates were then sonicated in acetone for 10 min and then blown dry with nitrogen. Thereafter, substrates were sonicated in isopropanol for 10 min and blown dry with nitrogen. Sonication in isopropanol was repeated twice more, making sure to dry between each step.

Dyes were provided by Dr. Iryna Davydenko (Marder group, GT) and used as-received. To properly flood the 15×25 mm^2 substrate when spin coating, 300 μL of blend film solution (dye + APC) was required. An 8% w/w solution of APC in 1,2-dichloroethane (DCE) (Sigma-Aldrich, 99+% spectrophotometric grade) with a total volume of 1 mL and an 8% w/w solution of dye in DCE with a total volume of 150 μL were prepared and stirred separately to complete dissolution. 150 μL of the APC solution was combined with the 150 μL dye solution and stirred well to ensure mixing. With the substrate placed in position on the chuck of the spin coater, the blend solution was filtered using a 13 mm VWR Nonsterile 0.2 μm PTFE Membrane Syringe Filter with Polypropylene Housing directly onto the substrate, taking care to evenly flood the entire substrate surface. Films were spun by accelerating at 500 RPM/s to 1000 RPM over 2 s. After spinning, films were quickly transferred to a desiccator to be dried under vacuum overnight and protected from any light exposure.

3.3.4.3 Linear Characterization and Thickness Measurements

Absorption spectra, prism coupling measurements (refractive index and linear loss), and thickness measurements were performed as described in section 3.2.5.3.

3.3.4.4 Z-scan Measurements in Solution and 50% wt APC Blend Films

The laser source, general Z-scan method, and error propagation are described in section 3.2.5.4. The spatial and temporal properties of the pulse are given by the following; the HW1/e^2 radius of the beam was ca. 40-50 µm, its Rayleigh range was 2.9-4.0 mm, the pulse width was 55 fs (HW1/e), and the beam shape was found to be Gaussian with an M value of 1-1.09. Open- and closed-aperture scans were then corrected by subtracting their respective background contributions: the solvent, $CHCl_3$, in the cases of solution measurements, and the spot to be measured at a low enough irradiance as to not observe NLO behavior in the case of film measurements. To ensure that the extracted apparent values of $Re(\chi^{(3)})$ and $Im(\chi^{(3)})$ do indeed represent third-order nonlinearities, the Z-scans on each sample were performed at various excitation irradiances ranging from 40–250 GW cm^{-2}. For solutions measurements, concentrations were in the 1-2 mM range.

3.4 Materials Processing for Optical-Quality Films of Polymethine-Polymer Blends for Nonlinear Optical Measurements and Photonic Device Applications

3.4.1 *Background and Experimental Approach*

Amorphous polycarbonate (APC) and its copolymers have been some of the preferred polymer matrices for NLO and photonic applications making use of spun coated films because of its: low cost, optical transmission in the near IR, ease of processability

given its appreciable solubility in a variety of organic solvents, and miscibility with various types of chromophores (i.e. neutral, polar, ionic) in the solid-state. [29, 183, 184, 195, 207] Despite these desirable properties, blend films from APC frequently suffer from film thickness variations even when spin coating from good solvents (i.e. high solubility) with reasonably viscosity and moderate-to-slow drying rates such as 1,1,2-trichloroethane (TCE) which, normally, give uniform films due to controlled wetting and evaporation. These thickness variations typically come in the form of ripples and can introduce significant errors in spectroscopic measurements sensitive to path length differences within a sample, such as Z-scan, or even make data interpretation from these techniques impossible due to overwhelming noise. [207] Additionally, due to its amorphous nature, APC lacks the mechanical strength necessary for the fabrication of photonic devices using APC blends as cladding layers, which typically requires additional processing such as dicing or solution coating of encapsulation layers that can cause the underlying APC film to delaminate or deform severely. [25] This set of issues is largely associated with poor surface adhesion to silica- and silicon-based substrates and film stretching, which can lead to delamination or leave material hanging over the edge of the substrate. As a result, this can obstruct views in optical microscopes, SEMs, and preclude the option of edge-on coupling light into photonic structures, like waveguides such as the one depicted from an edge-on view in Figure 3.25a-b.
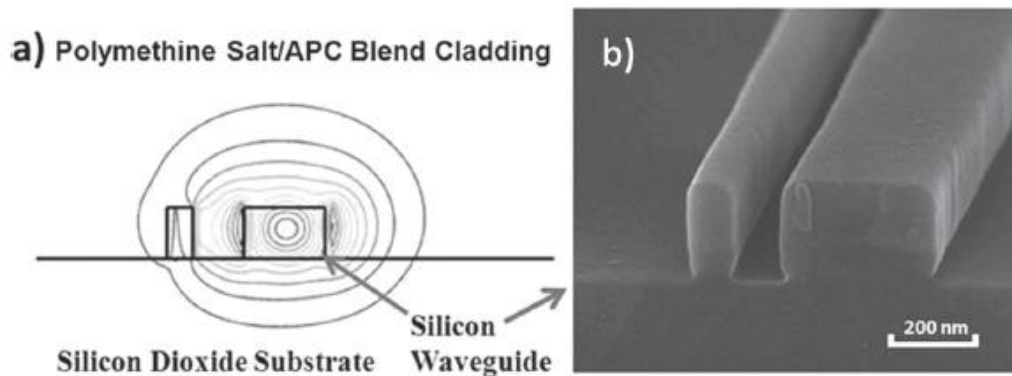
Figure 3.25. (a) Calculated optical mode pattern for the TE_0 mode of an asymmetric slotted waveguide, (b) SEM micrograph of the cross-section of a fabricated slotted waveguide with with 100 nm and 310 nm width silicon rails, 180 nm slot width and 200 nm rail thickness. Reproduced from Li *et al*. [29] with permission. Copyright 2012 Advanced Materials.

The limitations of APC call for the use of different processing methods or different polymer materials to improve the mechanical aspects of the film while maintaining sufficient optical-quality and high dye concentrations needed for NLO applications. To systematically test the variables that most significantly impact film quality without changing the identity of the polymer from well-characterized APC, the approach to optimizing film quality will began by investigating the impact of surface modification chemistries and changes in wetting on film formation. The poor adhesion of APC is likely related to a mismatch in intermolecular forces between the chemical functionalities along the backbone and the substrate surface which govern the strength of adhesion. One such approach to achieve attractive interactions is surface modification via silanization.
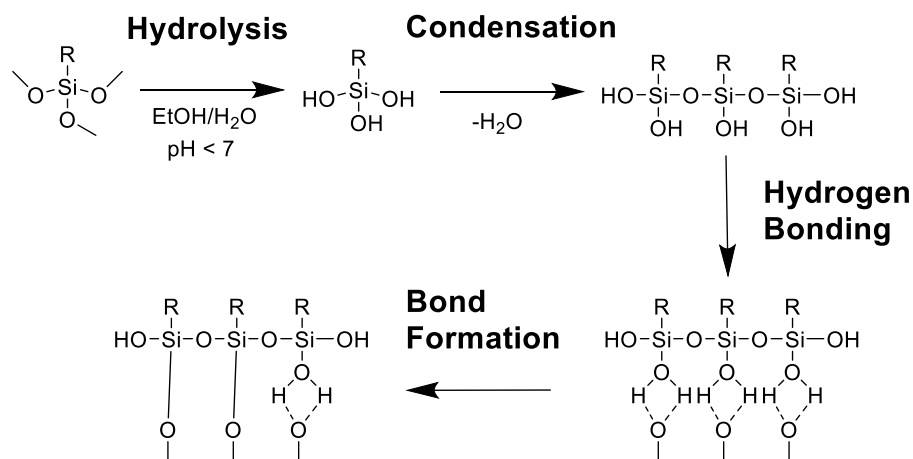
Figure 3.26. Reaction diagram showing steps of the silanization process.

Salinization is a well-known surface modification method with somewhat standardized procedures available via Gelest for common silanes but also a multitude of customized procedures in the literature for more exotic structures with widely varied reactivity and surface chemistries. [213] The generic method for silanization is illustrated in Figure 3.26, which is started by making a dilute solution of alkoxysilane solution in an ethanol-water mixture with the option of adding weak acid to lower the pH to facilitate hydrolysis. Once the hydroxylated silane is formed, it undergoes a reaction with the hydroxyl groups on the substrate, eventually forming a covalent bond with the surface. Assuming dense, uniform coverage, the modified surface now takes on the character of the terminal groups attached to the silane (R) changing the surface energy and, thus, the way materials wet and adhere to the surface. Additionally, carefully chosen silanes with reactive end groups can be synthetically modified further to obtain terminal groups that one might not find in commercially available products, which can afford more flexibility and customizability. In this work, one such method involving a Michael addition reaction is utilized and will be discussed in detail. The success of modification will be tested by

149

tracking changes in surface energy of modified substrates with contact angle goniometry and improvements in film uniformity and adhesion will be verified with stylus profilometry and tape pull tests, respectively.

The rest of the work reported in this section will investigate the impact of polymer host identity on film quality. As such, polymethylmethacrylate (PMMA), polyvinvylchloride (PVC), and a cyclohexyl-bearing APC copolymer (APCC) were chosen as alternate hosts (Figure 3.37) because, like APC, they are inexpensive, optically transparent in the IR and can make optical-quality thin films from a variety of solvents but potentially offer more in terms of mechanical strength given that PMMA and PVC, in particular, have a higher degree of crystallinity than APC and potentially greater adhesion with hydrophilic surfaces compared to the relatively non-polar APC. Film thickness uniformity and adhesion will be characterized by stylus profilometry and tape-pull tests, respectively.

3.4.2 *Results and Discussion*

3.4.2.1 Effects of Surface Chemistry on APC Films

Previous attempts to coat fused silica waveguides on non-modified fused silica substrates (also referred to as hydroxylated (OH) silica, given that oxygen cleaning or piranha treatment is used for cleaning, which hydroxylates the silica surface) with a 50% wt APC:**Ib** (structure for **Ib** in Figure 3.4 from section 3.2) resulted in poor wetting around features (Figure 3.27). Since neat APC forms a film with good waveguide infiltration and surface coverage (as seen in Figure 3.27b-c, albeit with some thickness variations), the poor film quality then likely due to a mismatch in interactions between the blend solution

and the waveguide surface, which suggests that, at 50% loading, the dye-substrate interaction becomes significant and the wetting behavior of the polymer no longer dominates. To make the interface amenable to blend film formation, the surface of the waveguide was modified by 3-mercaptopropyl trimethoxysilane (MPTMS) to create a moderately hydrophilic surface (compared to hydroxylated surface of a "bare" fused silica surface) over which APC and the dye is expected to wet evenly (work done by Dr. Hyeongeu Kim). Indeed, films were obtained with good quality, coverage, and feature infiltration (Figure 3.27d-e). Despite the good quality of this film, this sample ultimately failed in the device preparation stage where mechanical dicing was necessarily applied to smooth the film/waveguide edge and the film delaminated. This was attributed to poor adhesion which, again, points to a mismatch in interactions between the blend film/substrate interface.
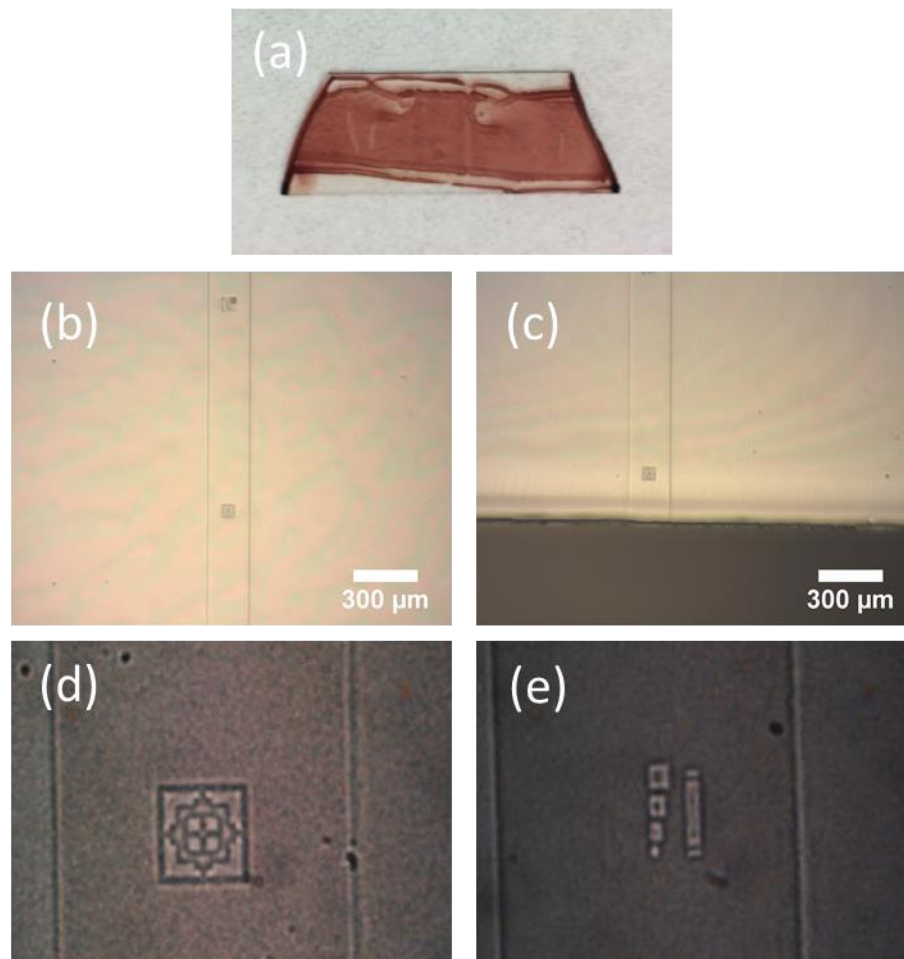
Figure 3.27. (a) Image of waveguide-bearing fused silica substrate with poor quality 50% wt **Ib**:APC blend on unmodified fused silica (b) Micrograph (4x) of fused silica waveguide covered and infiltrated well by a neat APC film (c) Micrograph (4x) of same waveguide from image "b" near the edge, showing good surface coverage of APC over entire substrate, including the edge (d-e) High magnification micrographs of **Ib**:APC blends covering and infiltrating fused silica waveguides surface modified by 3-mercaptopropyltrimethoxysilane. Micrographs "d-e" courtesy of Dr. Hyeongeu Kim – Perry group, Georgia Tech.

Poor adhesion of APC is unsurprising, given that even high-quality, neat APC films with thicknesses in the range of 1-2 µm made by the author have been found to totally delaminate during tape pull tests (see 3.4.4.3 for details) regardless of spin conditions or spinning solvent on unmodified silica-based substrates. However, despite dramatic improvements in wetting and waveguide infiltration upon surface modification with MPTMS, the observed delamination suggests that interactions between the thiolated surface and blend film were not strong enough to promote sufficient adhesion. As such, it was salient to find alternative surface modifiers that could maintain satisfactory film quality and coverage while improving adhesion. For this purpose, two silanes known to be compatible with APC, 3-aminopropyl triethoxysilane (APTES) and benzoyloxypropyl trimethoxysilane (BPTMS) – see sections 3.4.4.4 and 3.4.4.5, respectively, for surface modification procedure and Figure 3.28a-c for structures – were selected to achieve moderately hydrophobic surfaces relative to hydroxylated silica that bear organic terminal groups, which are thought to provide more favorable surface in terms of dye and polymer interface interactions. The success of modification was confirmed by comparing the contact angle (see 3.4.4.6 for experimental details) of these surfaces with water droplets in comparison with a clean (see 3.4.4.1 for methods), hydroxylated silica surface. [214] As expected, the contact angle of the modified surfaces followed the trend OH<ATPES<BPTMS, in agreement with the expected increase in hydrophobicity based on the identity of the terminal group for each silane (Figure 3.28d-f).
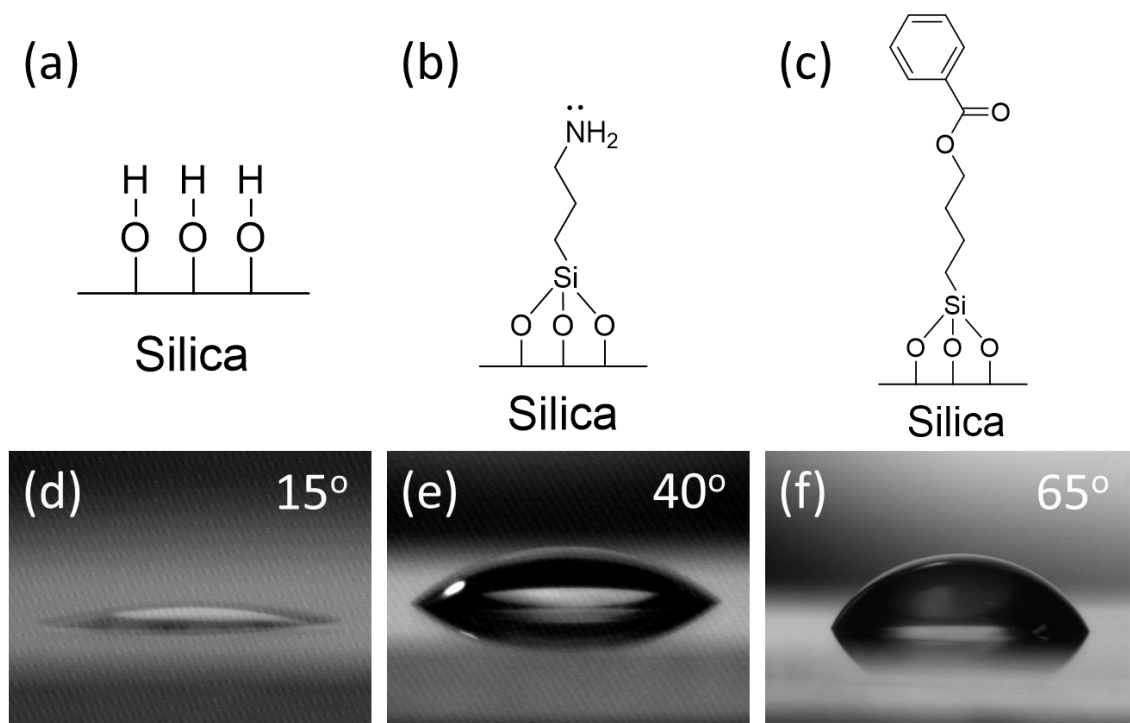
Figure 3.28. Surface structure of a silica surface bearing: (a) Hydroxyl groups; (b) APTES; and (c) BPTMS. Contact angle of water on: (d) Unmodified, hydroxylated fused silica (e) ATPES-modified fused silica in agreement with reference [215]; and (f) BPTMS-modified fused silica.

When attempting to coat a 50% wt **Ib**:APC film from TCE onto APTES-modified substrates, the wetting was so poor that hardly any of the blend solution remained on the substrate after spin coating. Given that there was some wetting with a hydroxylated surface and that APC is known to wet well on APTES, this indicates that the primary amine terminal group of APTES may participate in unfavorable interactions with **Ib** to cause dewetting. Although this hypothesis is untested, when considering the Lewis basicity of primary alkyl amines, it may be possible that the APTES electronically polarizes dyes attempting to solidify at the interface which could drastically change the solvation and wetting dynamics while spinning. Clearly, more extensive study is needed to confirm this trend with other terminal groups of appreciable Lewis basicity and with other dyes with

154

similar bulky substitution and varied chalcogen identity. The same blend films spun from dibromomethane (DBM, used to compensate for losses in thickness typically observed for APC films spun from TCE on BPTMS substrates. Wetting of DBM is anticipated to be similar to TCE, given similar contact angles obtained from goniometry) on BPTMS-modified surfaces produced films comparable in wetting and coverage to the samples with hydroxylated surfaces (comparing Figure 3.27a with micrographs from Figure 3.29). Although better in quality than ATPES, BPTMS surfaces still did not afford improvements in coverage and wetting which may also be due to unfavorable interactions with the dye and relatively nonpolar, hydrophobic surface. Considering the ionic nature of the dye, **Ib** may only interact weakly with the phenyl-bearing surface via dispersion forces which may explain the marginal film quality.
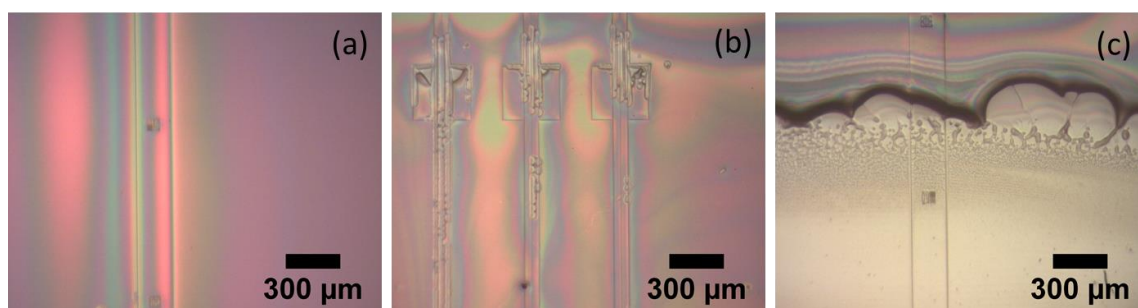
Figure 3.29. Micrographs (4x) of 50% wt **Ib**:APC film from DBM on BPTMS-modifed, waveguide-bearing fused silica substrate showing: (a) Decent infiltration for a small section of a waveguide feature (b) Poor wetting around a set of waveguide features and (c) Poor wetting near the edge of a fused silica substrate/waveguide.

Although the investigation involving APTES and BPTMS, in comparison with MPTMS, presents a limited study of the dependence of blend solution wetting on fused silica, one can deduce that the dye interactions at the interface are indeed significant but cannot be easily described given the multitude of intermolecular forces simultaneously

occurring during spinning/drying, which could induce electronic changes in the dye and dramatically affect the wetting dynamics. Without a clear understanding of the surface/blend solution interactions, the selection of alternative silanes becomes complicated due to the large spectrum of silanes that could be used to create more or less hydrophilic surfaces bearing more or less basic terminal functionalities in reference to those of APTES and BPTMS. However, given that the miscibility of **Ib** in APC seems reasonable regardless of the film processing method tried to this stage, a more convenient and selective approach would be to tailor the surface to be more APC-like such that both dye and polymer will interact favorably.

To accomplish this, a Michael addition reaction, similar to a method for making hyperbranched thin films from reference [215], was used to covalently link APC-like surface groups, i.e. bisphenol A dimethacrylate (BDA) and bisphenol A ethoxylate (BEDA), to fused silica. This simple process begins by modifying the silica surface with ATPES and then reacting the amine-bearing surface with acrylate-terminated BDA or BEDA to covalently bind them to the silica surface, as illustrated in Figure 3.30c. The full experimental procedure for this modification process is given in section 3.4.4.7.
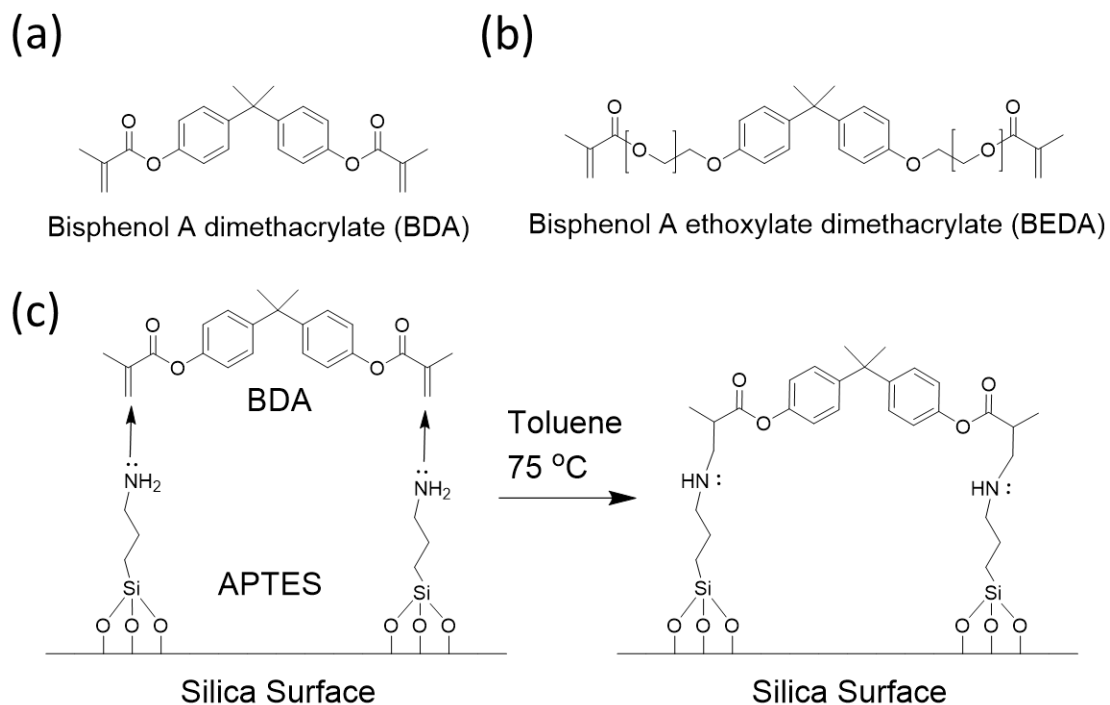
Figure 3.30. (a) Chemical structure of BDA, (b) Chemical structure of BEDA and (c) Illustration of michael addition reaction between APTES and BDA to covalently link BDA to APTES and thus the silica substrate.

Successfully modified BDA and BEDA surfaces gave an average contact angle of ca. 55° for both compounds, which was 15° greater than APTES and 10° lower than the BPTMS-modified substrate. Initial attempts to coat non-waveguide-bearing fused silica substrates modified with BDA and BEDA, separately, with 50% wt **Ib**:APC blend films from TCE yielded appreciably thick films (ca. 2 µm) with improved surface coverage compared to hydroxylated, APTES-, and BPTMS-modified samples, although some defects were present in the films (Figure 3.31a). The defects, primarily pinholes, could be caused by nonuniform surface coverage of the APC-like surface modifiers, resulting in non-uniform wetting and thus possibly drying during spin coating. Tape tests on these films showed improvements in adhesion in that total delamination did not occur, however, some film material did peel off with the tape and continued to peel with multiple tape pulls.

157

Stylus profilometry measurements on samples before and after tape pulls revealed that ca. 100-200 nm of film material could be removed with a single tape pull. This is reflected in the absorption spectra taken of peeled off films on Scotch® tape, where significant optical density from dye absorption can be seen for two consecutive tape pulls in Figure 3.31b from a film coated on a BEDA-modified substrate. Although the exact cause for this phenomenon is unclear, the marginal mechanical strength and pinhole defects seen in these films may signify phase separation, resulting in segregated dye- and polymer-rich regions that reduce long-range mechanical strength over the entire film.
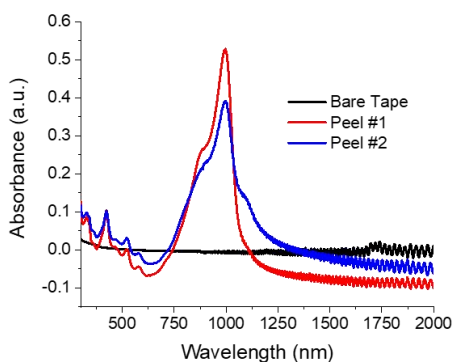
Figure 3.31. (a) Image of two 50% wt **Ib**:APC films from TCE on BEDA-modified fused silica substrates after a tape test showing some peeling but not total delamination and (b) Absorption spectra of bare tape and two consecutive peels with significant absorption from **Ib** contained with peeled-off layers stuck to tape.

Despite this limitation, the film adhesion for the BDA- and BEDA-modified samples was deemed satisfactory for the purposes of prototyping NLO waveguide

measurements assuming the probability of total delamination during dicing is fairly low based on the performance of the films during tape tests. From this assumption, blend films were spun on BDA- and BEDA-modified, waveguide-bearing fused silica substrates. Much like the waveguide-less samples, coverage and thickness of the films obtained were substantially better, but the infiltration around features was poor. Micrographs of waveguide features showed many defects. primarily in the form of bubbles, particularly around more complex feature shapes (similar wetting issues were seen with BPTMS-modified substrates, Figure 3.29b). This is evident when comparing the infiltration around a simpler circular or straight line waveguide feature (Figure 3.32a-b) to that of a set of rectangular shapes directly next to smaller waveguide features (Figure 3.32c). These uniformity issues could be the result of a complex set of processing variables, namely surface coverage of the BDA and BEDA modifiers around complex features and change in drying dynamics upon the significant change in surface chemistry. From the work discussed thus far, the lack of success that surface modification has had in improving film quality and adhesion prompted further investigations into other polymer hosts to determine if APC is particularly incompatible in this material system. Results for this work are discussed in the next section.
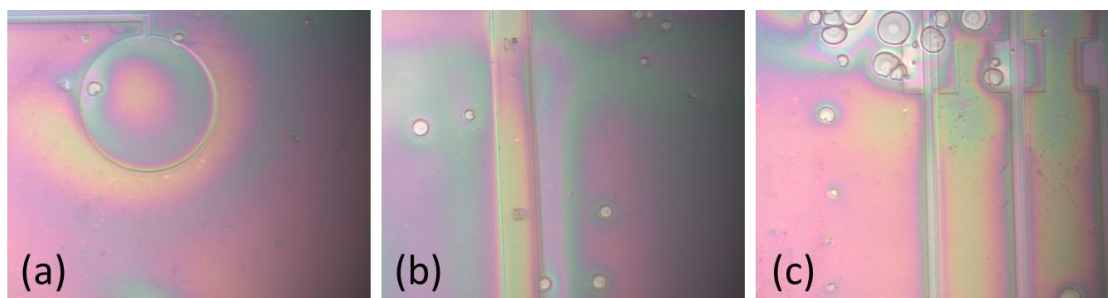
Figure 3.32. Micrographs (4x) of a 50% wt **Ib**:APC film from TCE on waveguide-bearing, BDA-modified fused silica substrate showing: (a) Film quality and infiltration in and around a circular waveguide feature (b) Film quality and infiltration in and around a straight waveguide feature and (c) Bubbles and pinhole defects around rectangular features close to smaller waveguides.

3.4.2.2   Blend Films with APC Copolymer, PMMA, and PVC

With various attempts at surface modification (section 3.4.2.1), giving only marginal improvements in adhesion between APC and fused silica substrates, exploratory experiments were conducted to determine the impact that changing the polymer host identity has on adhesion in blend films. For this test, it was necessary to obtain a series of polymers that, like APC, are optically transparent in the NIR, capable of forming glassy films, inexpensive and, to some degree, are miscible with polymethine dyes (particularly **Ib**) in the solid state. Considering these criteria, a cyclohexyl-bearing APC copolymer (referred to as APCC), polymethylmethacrylate (PMMA), and polyvinylchloride (PVC) were chosen – see Figure 3.37 for structures. Examples of 50% wt **Ib**:polymer blend films spun from TCE can be seen in for APC, APCC, and PMMA on unmodified fused silica substrates in Figure 3.33a-c, respectively. Due to the limited solubility of PVC in TCE, the PVC blend film (Figure 3.33d) was spun from cyclopentanone (CP). Similar wetting behavior was seen for films spun from TCE, regardless of polymer identity, where the center of the film appeared somewhat uniform in composition and thickness but significant

160

dewetting was observed at the edge. This was not seen in the PVC film from CP, which gave a reasonably thick (ca. 1.4 μm) and uniform film with good coverage over the entire substrate. Tape tests for the APC, APCC and PVC films resulted in total delamination after one pull, indicative of poor adhesion. On the other hand, the blend film with PMMA survived multiple tape pulls in nearly pristine condition, with only adhesive and other surface contaminants left on its surface. From this observation, it appears that the adhesion forces between PMMA and the substrate, even the in presence of high concentration of dye, are much greater than APC and are potentially due to stronger hydrogen bonding and/or dipole interactions between the hydroxylated surface and the methacrylate functionalities of PMMA. Due to the excellent adhesion for the PMMA blend, film processing optimization was pursued and is detailed in the following section (3.4.2.3).

(a)	(b)	(c)	(d)
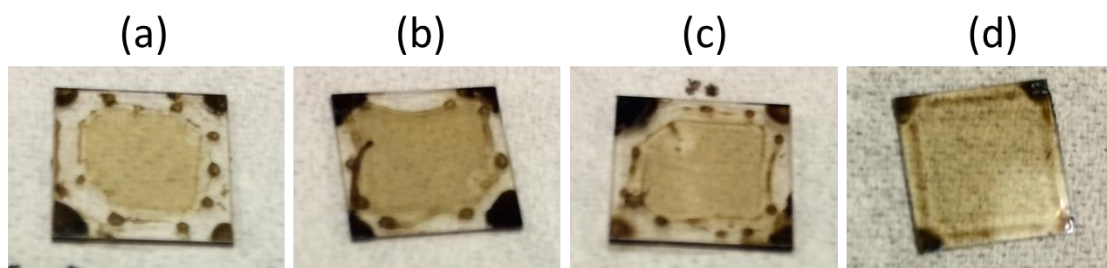
Figure 3.33. 50% wt **Ib**:polymer films on unmodified fused silica blended with (a) APC, (b) APCC, (c) PMMA and (d) PVC. Each substrate is 1x1 cm^2.

3.4.2.3   Successes and Challenges of Device Films from Dye:PMMA Blends

In light of the excellent adhesion observed via tape tests on 50% wt **Ib**:PMMA film from TCE, further optimization is warranted; however, the PMMA film seen in Figure 3.33c was thinner (ca. 1 μm) than what is desired for device applications (ca. 2 μm) and wetting at the edge was poor. These issues were corrected by changing the spinning solvent

161

to DBM which, at the same weight percentage as a TCE solution, will provide a more concentrated solution due to its much higher density (ca. 2.5 g/mL) and will increase viscosity and thus improve film thickness and also increase the drying rate because of its lower boiling point. Indeed, initial tests of neat 8% wt PMMA films from DBM gave glassy, uniform films with excellent surface coverage, substantial thickness (5 µm), and good adhesion. This excellent film quality was translated to a 50% wt blend solution of **Ib**, yielding a 3.3 µm thick film on an unmodified 1x1 cm^2 fused silica test substrate (Figure 3.34a) that showed excellent durability during tape tests, as evidenced by the similarity in surface roughness/thickness profiles before and after the tape tests (Figure 3.34b-c). When testing how this processing method would work for APC blends under the same conditions, higher quality films were obtained with improved wetting compared to those from TCE. However, these films were still poorer in quality than the PMMA films and, similar to those on BDA/BEDA-modified surfaces, showed some partial delamination (Figure 3.34d-e).
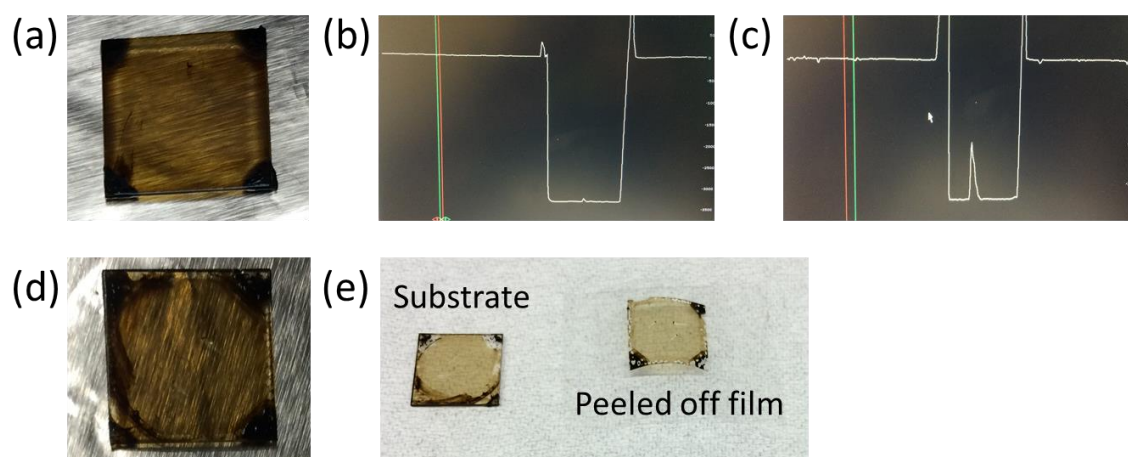
Figure 3.34. (a) 50% wt **Ib**:PMMA blend from DBM on unmodified fused silica, (b) Surface and thickness profile from stylus profilometry before tape test, (c) Surface and thickness profile after tape test – additional surface roughness confirmed by microscopy to be residual adhesive from Scotch® tape, (d) 50% wt **Ib**:PMMA blend from TCE on

unmodified fused silica, and (e) Tape test of blend film spun from TCE showing partial delamination.

Due to the success of PMMA blends from DBM on smaller scales, this blend was applied to unmodified waveguide-bearing fused silica substrates. The resulting films were glassy films with excellent coverage and were optically dark, suggesting high concentrations of dye in the solid state were obtained (Figure 3.35a). As such, unambiguous optical micrographs could not be obtained to directly image the waveguide filling. However, little-to-no defects were found over the entire substrate or near any waveguide features and the film was found to support a slab mode, demonstrating its high optical quality. Waveguide measurements were precluded by high optical loss due to wear and roughening that the waveguides had sustained over many coating and measurement trials. However, this sample was found to have strong saturable absorption in the NIR and was successfully implemented as a saturable absorption element to demonstrate a nonlinear all-optical probabilistic graphical model as described in reference [216] and Figure 3.35b.
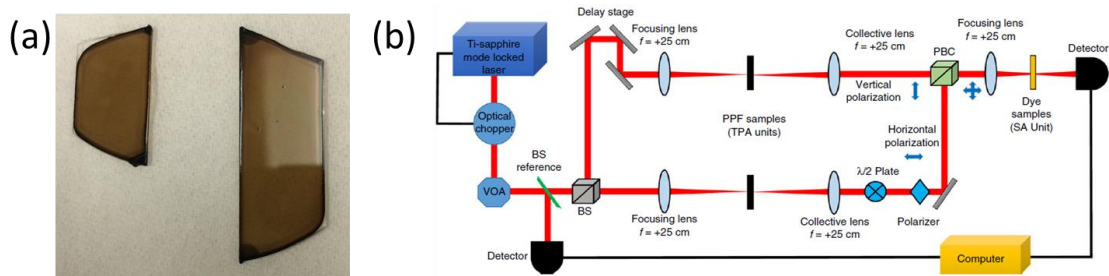
Figure 3.35. (a) Two unmodified, waveguide-bearing fused silica substrates with high-quality 50% wt **Ib**:PMMA films from DBM that were used to demonstrate (b) Setup used to demonstrate multiplicative optical elements, using films from "a". "b" reproduced from Babaeian *et al*. [216] with permission. Copyright 2018 Nature Communications.

The successful implementation of PMMA blends from DBM in an optics application warranted further study as a cladding layer for small silicon waveguides with

tight mode confinement and thus high electric fields with which nonlinear optical waveguide measurements can be performed. In doing so, initial micrographs (Figure 3.36a) of waveguide features showed macroscopic-level coverage and filling comparable with that seen from the fused silica samples. However, closer inspection of the infiltration of small (ca. <100 nm) silicon slot waveguides via cross sectional SEM (Figure 3.36b) revealed that air bubbles had formed at the base of the slot, resulting in nonuniform filling of the waveguide. Additionally, from this SEM image one can see an inhomogeneous film interior, which may signify phase separation. Some evidence for this is presented in Figure 3.36c, where dark field microscopic images show strong scattering of an area of the film next to ring resonators, suggesting that dye crystals or particles of aggregates precipitated while drying. It should be noted that, at this concentration, the film thickness (ca. 2.6 µm) would have been satisfactory for device operation, had the films been of acceptable quality.
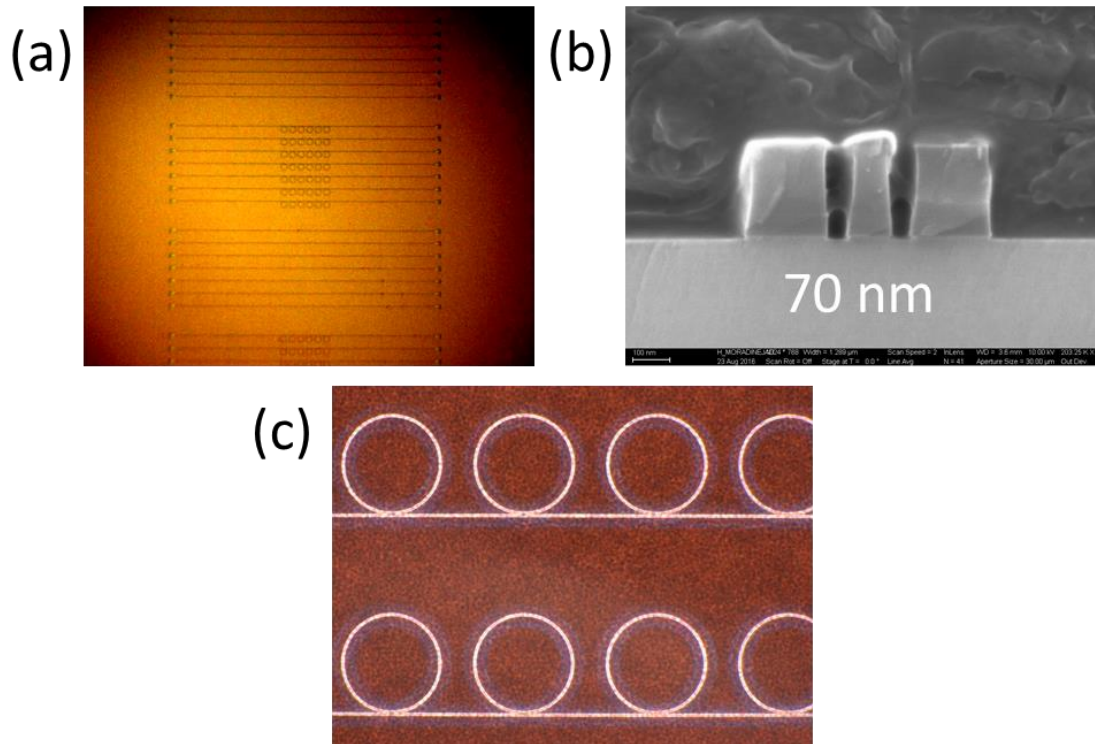
Figure 3.36. (a) Micrograph (10x) showing 50% wt **Ib**:PMMA film from DMB covering and infiltrating silicon waveguides – image adjusted in brightness and contrast using ImageJ, (b) Cross sectional SEM image of silicon slot waveguides with 70 nm slot widths showing bubbles at the base of the slot, and (c) Darkfield micrographs showing scattering form the film covering a set of ring resonators. Images "b-c" courtesy of Dr. Hesam Moradinejad – Adibi group, Georgia Tech.

The issues of phase separation and nonuniform filling are both issues of concentration. To rectify these issues, the concentration of dye and PMMA was decreased to half the concentration (4% wt) of the first coating attempts (8% wt) with the intent to reduce precipitation while spinning and reduce viscosity to promote more uniform filling of slotted waveguides. Despite this, nonuniform slot infiltration was observed for both neat PMMA and blend films at lower concentrations for slot widths of 50-80 nm. Naturally, the decrease in concentration gave a concomitant reduction in film thickness to 1.3-1.8 µm, below the desired thickness of 2 µm. At this stage in the investigation, alternative strategies

165

to obtain a high-chromophore density organic cladding layer on silicon waveguides were no longer pursued. Although the 50% **Ib**:PMMA blends are promising for NLO waveguide applications, more optimization is needed to achieve infiltration of ultra-small slot waveguides.

3.4.3 *Summary and Conclusions*

In section 3.4 of this dissertation, evidence was presented to highlight the challenges (i.e. wetting, adhesion, and film uniformity) that face the successful integration of organic NLO cladding layers on inorganic photonic structures and film optimization chemistries to rectify them. For 50% wt **Ib**:APC blends, poor adhesion on unmodified and modified substrates precluded waveguide characterization due to partial or total delamination. Although some improvements in adhesion were made when selectively modifying fused silica surfaces with APC-like terminal groups (BDA and BEDA), partial delamination and nonuniform wetting prevented these films from being achieving the quality necessary for waveguide measurements. Given that changes in surface chemistries did not resolve the adhesion problems associated with APC films, blends from PMMA were investigated and found to give excellent adhesion, thickness, and film quality when spun from DBM. These films were used as a saturable absorption element to successfully demonstrate a nonlinear all-optical probabilistic graphical model. This same blend was then used to coat much smaller (ca. 50-80 nm) silicon slot waveguides but encountered phase separation and infiltration issues even at lower film concentrations, that were not present in the larger fused silica waveguides.

3.4.4 *Experimental Details*

3.4.4.1   Substrate Cleaning

Substrates were cleaned by sonicating in acetone for 10 minutes, drying with a stream of nitrogen and then sonicating three times in isopropanol for 10 minutes each, making sure to dry between each step with a stream of nitrogen. The sonication-cleaned substrates were then subjected to 3 minutes of O_2 plasma to produce a heavily hydroxylated surface. An alternative method to sonication and plasma etching is to immerse substrates in piranha solution (3:1 v/v H_2SO_4: 30% H_2O_2) for one hour; making sure to wash well with DI water and then methanol after immersion and drying with a stream of nitrogen in between rinses.

3.4.4.2   Film Preparation of 50% wt **Ib**:APC Blends from TCE and DBM

Dye was provided by Dr. Yulia Getmanekno and Janos Simon (Marder group, GT). 8% wt solutions of APC (Sigma Aldrich, 435120, Mw ca. 46 kDa) and **Ib** (synthesis described previously in [195]) were prepared in TCE (97%, Sigma Aldrich), separately, ensuring to stir well so both samples are well-dissolved prior to mixing. The individual solutions were then mixed in equal masses and stirred well to make the 50% wt blend solution. Solutions were filtered with a 0.2 µm PTFE membrane filter (13 mm syringe filter VWR No. 28145-491) directly unto fused silica substrates cleaned via the sonication-plasma method described in 3.4.4.1. The following spin coating parameters were used to obtain the film: 1) Ramp 100 RPM/s to 500 RPM in 5 s and 2) Accelerate 250 RPM/s to 750 RPM then hold for 5 minutes. Films were immediately moved from the spin coater into a vacuum desiccator to dry for at least one hours, protected from ambient light. Thicknesses were determined by a Dektak 6M stylus profilometer.

3.4.4.3   Tape Pull Tests

A tape pull test is a simple and qualitative experiment to gauge the adhesion of a film to a substrate by bringing the entire film of interest into contact with the adhesive-coated side of low-to-moderate adhesive tape, such as Scotch® Tape, and then pulling the tape of the film with moderate force to see if the film stays attached to its substrate or delaminates. For the purposes of this thesis, films that stay attached to their respective substrates are characterized as having sufficient adhesion to survive device processing steps prior to waveguide measurements. Absorption spectra of delaminated films were measure using a dual-beam Shimadzu UV-3101PC UV-Vis-NIR scanning spectrophotometer. For absorption spectrum of the tape, an air reference was used with a single piece of Scotch® tape in the sample holder spot. For delaminated samples, a single piece of Sotch® tape was used as the reference, while the sample was a single piece of tape and delaminated film.

3.4.4.4   Surface Modification Procedure for 3-Aminopropyltrimethoxysilane (APTES)

A 2% v/v solution of APTES (Gelest SIA0610.0, used as received) in 95% v/v ethanol/water was prepared and stirred for 5-10 minutes to allow time for hydrolysis to occur prior to submerging substrates. Substrates were cleaned with the sonication-plasma method described in 3.4.4.1. Immediately after plasma treatment, the hydroxylated substrates were submerged in the 2% v/v ATPES-modifier solution for 5 minutes, with stirring. The substrates were then removed, washed with ethanol and then dried with a stream of nitrogen prior to being re-submerged for another 5 minutes. The process of submersion and rinsing was repeated 3 total times. After the final rinse and drying stage,

substrates were baked under the protection of a glass petri dish to avoid surface contaminants at 110 ºC for 5-10 minutes. After baking, substrates were used as quickly as possible to avoid degradation of the surface in ambient conditions. Average contact angle for these samples was found to be 40º, in agreement with literature. [215]

3.4.4.5 Surface Modification Procedure for benzoyloxypropyltrimethoxysilane (BPTMS)

A 2% v/v solution of BPTMS (Gelest SIB0959, used as received) in toluene was prepared and stirred for 5-10 minutes to allow time for hydrolysis to occur prior to submerging substrates. Substrates were cleaned with the sonication-plasma method described in 3.4.4.1. Immediately after plasma treatment, the hydroxylated substrates were submerged in the 2% v/v BPTMS-modifier solution for 2 hours, with stirring. After submersion, the substrates were then rinsed with toluene and baked under the protection of a glass petri dish to avoid surface contaminants at 110 ºC for 5-10 minutes. After baking, substrates were used as quickly as possible to avoid degradation of the surface in ambient conditions. Average contact angle for these sample was found to be 65º.

3.4.4.6 Contact Angle Goniometry

Contact angle goniometry was performed using a SEO Phoenix300 with DI water as the solvent droplet. Drops of ca. 40 µL in volume were dropped onto the substrate and then the image was taken at a slightly downward angle looking edge-on to capture the profile of the droplet with a camera. 8-bit grayscale images of the droplet profile were then imported into ImageJ© where the contact angle was quantified by fitting the droplet profile with a polynomial function using the open-source drop_snake plugin. [214] The was

accomplished by specifying 5-10 points along the top surface of the droplet, starting from the left edge of the droplet at the liquid-substrate interface and ending at the right liquid-substrate interface. Reported contact angles are averages over five samples.

3.4.4.7 Michael Addition Reaction for Modification of Silica Surfaces by BDA and BEDA

APTES surface modification was performed as described in section 3.4.4.4. For bisphenol A dimethacrylate (BDA, Sigma Aldrich 156329, used as received) modification, APTES-modified substrates were immersed in 2% wt BDA solution in toluene immediately after baking and were heated at 75 °C for one hour to complete the Michael addition reaction. Following the Michael addition, substrates were sonicated in toluene for 5 minutes, dried with nitrogen, and then sonicated in methanol for 5 minutes. The methanol sonicated substrates were then dried with nitrogen and used immediately to avoid surface degradation. For bisphenol A ethoxylate diacrylate (BEDA, Sigma Aldrich 412090, used as received), the same procedure was applied, but the modification solution was 5% v/v BEDA in toluene.

3.4.4.8 Film Preparation for Comparing 50% wt **Ib** Blend Films in APC, APCC, PMMA, and PVC

8% wt solutions of APC (Sigma Aldrich, 435120, Mw ca. 46 kDa) and **Ib** (synthesis described previously in [195]) were prepared in TCE, separately, ensuring to stir well so both samples are well-dissolved prior to mixing. The individual solutions were then mixed in equal masses and stirred well to make the 50% wt blend solution. Solutions were filtered with a 0.2 µm PTFE membrane filter (13 mm syringe filter VWR No. 28145-491) directly

unto fused silica substrates cleaned via the sonication-plasma method described in 3.4.4.1.

The following spin coating parameters were used to obtain the film: 1) Ramp 100 RPM/s

to 500 RPM in 5 s and 2) accelerate 250 RPM/s to 750 RPM then hold for 5 minutes. Films

were immediately move from the spin coater into a vacuum desiccator to dry for at least

one hours, protected from ambient light. For films spun from DBM, a similar procedure to

the one for TCE was followed, except the starting solutions were made 6% wt prior to

mixing to form the blend solution.

(a)
Bishphenol A polycarbonate (APC)

(b)
Poly[bisphenol A carbonate-co-4,4'-(3,3,5-trimethylcyclohexylidene)diphenol carbonate]
(APCC)

(c)
Polymethylmethacrylate (PMMA)

(d)
Polyvinylchloride (PVC)
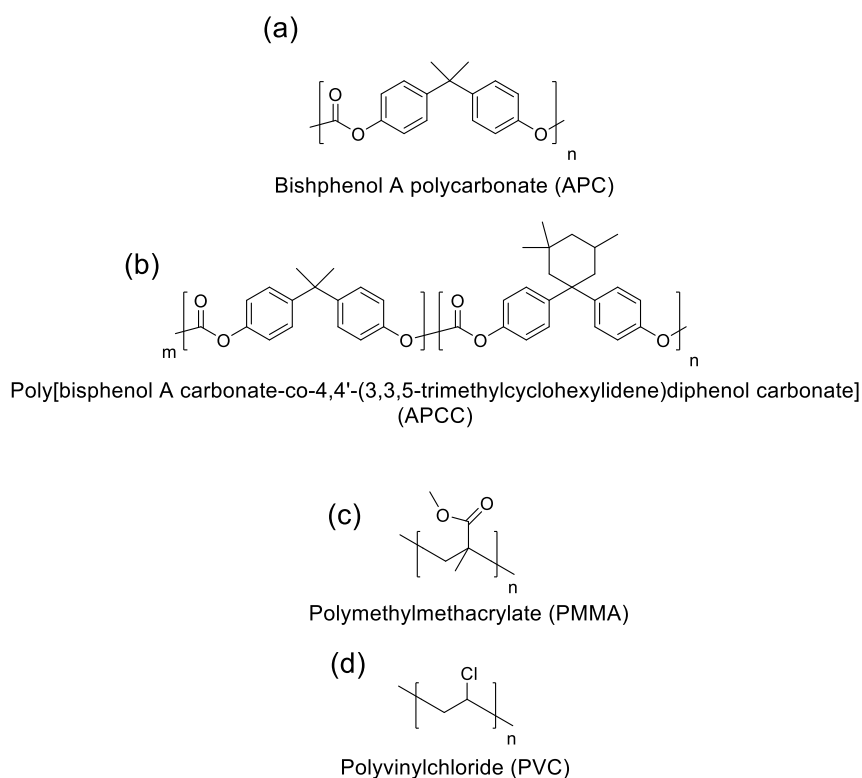
Figure 3.37. Chemical structures of (a) APC, (b) APCC, (c) PMMA, and (d) PVC.

3.5   Chapter Summary

This chapter presented advances in understanding the solution and solid state NLO

properties of high-conjugated polymethine dyes of interest for AOSP in the

telecommunications windows (1.3-1.6 µm) and the impact that solution processing and surface chemistry can have on the fabrication of optical-quality, high number density polymethine-polymer blend films. In section 3.2, judicious substitution of high $|Re(\gamma)|$ chalcogenopyrylium-terminated heptamethine dyes with bulky, rigid, out-of-plane groups in the "front", "back", and "end" positions allowed for the preservation of solution-like NLO properties in the solid state due to effective deaggregation; where several dyes demonstrated 2PA-FOM suitable for AOSP. This bulky substitution method, however, was not as totally effective in preventing deleterious interactions in blend films for a telluropyrylium dye (**Ip** – Figure 3.4), which showed significant saturable absorption at 1550 nm, likely due to aggregation-induced spectral broadening and thus linear absorption during NLO measurements. Despite this, APC blends with the Te-dye gave 1PA-FOM greater than that for DDMEBT, a vacuum-processed organic compound used to successfully demonstrate all-optical switching [23], although the presence of saturable absorption ultimately precludes the utility for this Te blend for AOSP. Additionally, it was largely found that linear loss in the solid state improved appreciably in increasing bulky substitution, which was attributed to the successful mitigation of aggregation and other polarizing interactions between the dye and other dyes and host matrix in blend films. NLO measurements of a Se-dye (**Ij**) in multiple polymer hosts (APC, PS, and PVC) showed no signs of host dependence despite dramatically different polymer environments, further corroborating the bulky groups' ability to isolate the dye in high number density films and facilitate miscibility. This was not found for the Te-dye (**Ip**) which, in addition to the aforementioned saturable absorption issue, showed significant dependence of $|Re(\chi^{(3)})|$ on the identity of the polymer host.

In section 3.3, a study was presented that quantified the degree to which an inorganic-based bulky group, Pd(PPh$_3$)$_2$Cl – introduced via a straightforward synthetic procedure [183] – could preserve solution-like nonlinearities for a benzoindole-terminated heptamethine dyes in 50% wt APC blends was presented. Compared to chalcogenopyrylium dyes of the same chain length, the |Re(γ)| for benzoindole dyes were generally an order of magnitude smaller, due to inherently smaller polarizabilities, as evidenced by relatively blue-shifted 1PA maxima, which was exacerbated slightly upon the addition of the Pd-group. This, in turn, reduced the degree to which benzoindole dyes could participate in resonance enhancement when measured at 1550 nm. In solution and films, both Cl- and Pd-substituted dyes exhibited irradiance-dependent |Re(γ)| and |Re($\chi^{(3)}$)|, respectively, when measured at 1300 and 1550 nm, which was attributed to ESR due to a vibronically-coupled 2PA state close to the primary 1PA transition. [210] This trend was also found in Cbz-substituted benzoindole dyes of the same chain length. Although the nonlinearities for Cl- and Pd-dyes were found to be comparable to benchmark NLO materials Si and GaAs [33] at moderate irradiances (ca. 90 GW/cm^2), achieving resonance with a real excited state in the telecommunications window inherently limits the maximum achievable switching speed and modulation efficiency of potential devices made from these material, which is dictated by the lifetime for that state.

Lastly, section 3.4 detailed film processing approaches to achieve thick ($\geq$ 1 µm), uniform high number density films of a chalcogenopyrylium dye with APC that demonstrated sufficient surface adhesion and mechanical strength to survive device processing while retaining excellent optical-quality. Despite the use of silane-modified surfaces to make fused silica substrate surfaces more APC- and dye-compatible, it was

found that APC still lacked the mechanical strength, wetting, and surface adhesion to be suitable for proof-of-concept device demonstrations. Subsequent studies testing these properties in different polymer hosts found that PMMA provided optical quality films with excellent uniformity, thickness, and adhesion. As a result, a 50% wt thiopyrylium dye (**Ib**) and PMMA blend film was successfully used to demonstrate an all-optical probabilistic model by taking advantage of its saturable absorption properties in the NIR.

3.6   References

23.   Koos, C., Vorreau, P., Vallaitis, T., Dumon, P., Bogaerts, W., Baets, R., Esembeson, B., Biaggio, I., Michinobu, T., Diederich, F., Freude, W., and Leuthold, J., *All-optical high-speed signal processing with silicon–organic hybrid slot waveguides.* Nature Photonics, 2009. **3**: p. 216.

25.   Hales, J.M., Barlow, S., Kim, H., Mukhopadhyay, S., Brédas, J.-L., Perry, J.W., and Marder, S.R., *Design of Organic Chromophores for All-Optical Signal Processing Applications.* Chemistry of Materials, 2014. **26**(1): p. 549-560.

29.   Li, Z.a., Liu, Y., Kim, H., Hales, J.M., Jang, S.-H., Luo, J., Baehr-Jones, T., Hochberg, M., Marder, S.R., Perry, J.W., and Jen, A.K.-Y., *High-Optical-Quality Blends of Anionic Polymethine Salts and Polycarbonate with Enhanced Third-Order Non-linearities for Silicon-Organic Hybrid Devices.* Advanced Materials, 2012. **24**(44): p. OP326-OP330.

30.   Hales, J.M., Matichak, J., Barlow, S., Ohira, S., Yesudas, K., Brédas, J.L., Perry, J.W., and Marder, S.R., *Design of Polymethine Dyes with Large Third-Order Optical Nonlinearities and Loss Figures of Merit.* Science, 2010. **327**(5972): p. 1485-1488.

33.   Dinu, M., Quochi, F., and Garcia, H., *Third-order nonlinearities in silicon at telecom wavelengths.* Applied Physics Letters, 2003. **82**(18): p. 2954-2956.

38.   Meyers, F., Marder, S.R., Pierce, B.M., and Bredas, J.L., *Electric Field Modulated Nonlinear Optical Properties of Donor-Acceptor Polyenes: Sum-Over-States Investigation of the Relationship between Molecular Polarizabilities (.alpha., .beta., and .gamma.) and Bond Length Alternation.* Journal of the American Chemical Society, 1994. **116**(23): p. 10703-10714.

40.   Mukhopadhyay, S., Risko, C., Marder, S.R., and Brédas, J.-L., *Polymethine dyes for all-optical switching applications: a quantum-chemical characterization of*

counter-ion and aggregation effects on the third-order nonlinear optical response. Chemical Science, 2012. **3**(10): p. 3103-3112.

47.   Scarpaci, A., Nantalaksakul, A., Hales, J.M., Matichak, J.D., Barlow, S., Rumi, M., Perry, J.W., and Marder, S.R., *Effects of Dendronization on the Linear and Third-Order Nonlinear Optical Properties of Bis(thiopyrylium) Polymethine Dyes in Solution and the Solid State.* Chemistry of Materials, 2012. **24**(9): p. 1606-1618.

49.   Bouit, P.-A., Aronica, C., Toupet, L., Le Guennic, B., Andraud, C., and Maury, O., *Continuous Symmetry Breaking Induced by Ion Pairing Effect in Heptamethine Cyanine Dyes: Beyond the Cyanine Limit.* Journal of the American Chemical Society, 2010. **132**(12): p. 4328-4335.

61.   Tolbert, L.M. and Zhao, X., *Beyond the Cyanine Limit: Peierls Distortion and Symmetry Collapse in a Polymethine Dye.* Journal of the American Chemical Society, 1997. **119**(14): p. 3253-3258.

136.   Barlow, S., Brédas, J.-L., Getmanenko, Y.A., Gieseking, R.L., Hales, J.M., Kim, H., Marder, S.R., Perry, J.W., Risko, C., and Zhang, Y., *Polymethine Materials with Solid-State Third Order Susceptibilities Suitable for All-Optical Signal-Processing Applications.* Mater. Horiz., 2014. **1**: p. 577-581.

143.   Milam, D., *Review and assessment of measured values of the nonlinear refractive-index coefficient of fused silica.* Applied Optics, 1998. **37**(3): p. 546-550.

144.   Krauss, T.D. and Wise, F.W., *Femtosecond measurement of nonlinear absorption and refraction in CdS, ZnSe, and ZnS.* Applied physics letters, 1994. **65**(14): p. 1739-1741.

182.   Covey, J., Finke, A.D., Xu, X., Wu, W., Wang, Y., Diederich, F., and Chen, R.T., *All-optical switching with 1-ps response time in a DDMEBT enabled silicon grating coupler/resonator hybrid device.* Optics Express, 2014. **22**(20): p. 24530-24544.

183.   Davydenko, I., Barlow, S., Sharma, R., Benis, S., Simon, J., Allen, T.G., Cooper, M.W., Khrustalev, V., Jucov, E.V., Castañeda, R., Ordonez, C., Li, Z.a., Chi, S.-H., Jang, S.-H., Parker, T.C., Timofeeva, T.V., Perry, J.W., Jen, A.K.Y., Hagan, D.J., Van Stryland, E.W., and Marder, S.R., *Facile Incorporation of Pd(PPh₃)₂Hal Substituents into Polymethines, Merocyanines, and Perylene Diimides as a Means of Suppressing Intermolecular Interactions.* Journal of the American Chemical Society, 2016. **138**(32): p. 10112-10115.

184.   Davydenko, I., Benis, S., Shiring, S.B., Simon, J., Sharma, R., Allen, T.G., Chi, S.-H., Zhang, Q., Getmanenko, Y.A., Parker, T.C., Perry, J.W., Brédas, J.-L., Hagan, D.J., Van Stryland, E.W., Barlow, S., and Marder, S.R., *Effects of meso-M(PPh₃)₂Cl (M = Pd, Ni) substituents on the linear and third-order nonlinear*

optical properties of chalcogenopyrylium-terminated heptamethines in solution and solid states. Journal of Materials Chemistry C, 2018. **6**(14): p. 3613-3620.

185. May, J.C., Lim, J.H., Biaggio, I., Moonen, N.N.P., Michinobu, T., and Diederich, F., *Highly efficient third-order optical nonlinearities in donor-substituted cyanoethynylethene molecules.* Optics Letters, 2005. **30**(22): p. 3057-3059.

186. Lepkowicz, R.S., Przhonska, O.V., Hales, J.M., Fu, J., Hagan, D.J., Van Stryland, E.W., Bondar, M.V., Slominsky, Y.L., and Kachkovski, A.D., *Nature of the electronic transitions in thiacarbocyanines with a long polymethine chain.* Chemical Physics, 2004. **305**(1): p. 259-270.

187. Bredas, J.L., Silbey, R., Boudreaux, D.S., and Chance, R.R., *Chain-length dependence of electronic and electrochemical properties of conjugated systems: polyacetylene, polyphenylene, polythiophene, and polypyrrole.* Journal of the American Chemical Society, 1983. **105**(22): p. 6555-6559.

188. Belfield, K.D., Bondar, M.V., Hernandez, F.E., Przhonska, O.V., and Yao, S., *Two-photon absorption of a supramolecular pseudoisocyanine J-aggregate assembly.* Chemical Physics, 2006. **320**(2): p. 118-124.

189. Busse, G., Frederichs, B., Petrov, N.K., and Techert, S., *Structure determination of thiacyanine dye J-aggregates in thin films: Comparison between spectroscopy and wide angle X-ray scattering.* Physical Chemistry Chemical Physics, 2004. **6**(13): p. 3309-3314.

190. Kemnitz, K., Yoshihara, K., and Tani, T., *Short and excitation-independent fluorescence lifetimes of J-aggregates adsorbed on silver(I) bromide and silica.* The Journal of Physical Chemistry, 1990. **94**(7): p. 3099-3104.

191. Tani, K., Ito, C., Hanawa, Y., Uchida, M., Otaguro, K., Horiuchi, H., and Hiratsuka, H., *Photophysical Property and Photostability of J-Aggregate Thin Films of Thiacyanine Dyes Prepared by the Spin-Coating Method.* The Journal of Physical Chemistry B, 2008. **112**(3): p. 836-844.

192. Baraldi, I., Caselli, M., Momicchioli, F., Ponterini, G., and Vanossi, D., *Dimerization of green sensitizing cyanines in solution. A spectroscopic and theoretical study of the bonding nature.* Chemical Physics, 2002. **275**(1): p. 149-165.

193. Caselli, M., Latterini, L., and Ponterini, G., *Consequences of H-dimerization on the photophysics and photochemistry of oxacarbocyanines.* Physical Chemistry Chemical Physics, 2004. **6**(14): p. 3857-3863.

194. Gadde, S., Batchelor, E.K., Weiss, J.P., Ling, Y., and Kaifer, A.E., *Control of H- and J-Aggregate Formation via Host−Guest Complexation using Cucurbituril Hosts.* Journal of the American Chemical Society, 2008. **130**(50): p. 17114-17119.

195. Barlow, S., Brédas, J.-L., Getmanenko, Y.A., Gieseking, R.L., Hales, J.M., Kim, H., Marder, S.R., Perry, J.W., Risko, C., and Zhang, Y., *Polymethine materials with solid-state third-order optical susceptibilities suitable for all-optical signal-processing applications.* Materials Horizons, 2014. **1**(6): p. 577-581.

196. Gieseking, R.L., Mukhopadhyay, S., Risko, C., Marder, S.R., and Brédas, J.-L., *Effect of Bulky Substituents on Thiopyrylium Polymethine Aggregation in the Solid State: A Theoretical Evaluation of the Implications for All-Optical Switching Applications.* Chemistry of Materials, 2014. **26**(22): p. 6439-6447.

197. Getmanenko, Y.A., Allen, T.G., Kim, H., Hales, J.M., Sandhu, B., Fonari, M.S., Suponitsky, K.Y., Zhang, Y., Khrustalev, V.N., Matichak, J.D., Timofeeva, T.V., Barlow, S., Chi, S.-H., Perry, J.W., and Marder, S.R., *Linear and Third-Order Nonlinear Optical Properties of Chalcogenopyrylium-Terminated Heptamethine Dyes with Rigid, Bulky Substituents.* Advanced Functional Materials, 2018. **0**(0): p. 1804073.

198. Panda, J., Virkler, P.R., and Detty, M.R., *A Comparison of Linear Optical Properties and Redox Properties in Chalcogenopyrylium Dyes Bearing Ortho-Substituted Aryl Substituents and tert-Butyl Substituents.* The Journal of Organic Chemistry, 2003. **68**(5): p. 1804-1809.

199. Detty, M.R. and Murray, B.J., *Telluropyrylium dyes. 1. 2,6-Diphenyltelluropyrylium dyes.* The Journal of Organic Chemistry, 1982. **47**(27): p. 5235-5239.

200. Simard, T.P., Yu, J.H., Zebrowski-Young, J.M., Haley, N.F., and Detty, M.R., *Soluble, Infrared-Absorbing Croconate Dyes from 2,6-Di-tert-butyl-4-methylchalcogenopyrylium Salts.* The Journal of Organic Chemistry, 2000. **65**(7): p. 2236-2238.

201. Marder, S.R., Perry, J.W., Bourhill, G., Gorman, C.B., Tiemann, B.G., and Mansour, K., *Relation between Bond-Length Alternation and 2nd Electronic Hyperpolarizability of Conjugated Organic-Molecules.* Science, 1993. **261**(5118): p. 186-189.

202. Fu, J., Padilha, L.A., Hagan, D.J., Van Stryland, E.W., Przhonska, O.V., Bondar, M.V., Slominsky, Y.L., and Kachkovski, A.D., *Experimental and theoretical approaches to understanding two-photon absorption spectra in polymethine and squaraine molecules.* Journal of the Optical Society of America B, 2007. **24**(1): p. 67-76.

203. Tien, P.K. and Ulrich, R., *Theory of Prism–Film Coupler and Thin-Film Light Guides.* Journal of the Optical Society of America, 1970. **60**(10): p. 1325-1337.

204. Sheik-Bahae, M., Said, A.A., and Van Stryland, E.W., *High-sensitivity, single-beam n 2 measurements.* Optics letters, 1989. **14**(17): p. 955-957.

205.	Sheik-Bahae, M., Said, A., Wei, T.-H., Hagan, D.J., and Van Stryland, E.W., *Sensitive measurement of optical nonlinearities using a single beam.* Quantum Electronics, IEEE Journal of, 1990. **26**(4): p. 760-769.

206.	Major, A., Yoshino, F., Aitchison, J.S., Smith, P.W., Sorokin, E., and Sorokina, I.T., *Ultrafast nonresonant third-order optical nonlinearities in ZnSe for photonic switching at telecom wavelengths.* Applied physics letters, 2004. **85**(20): p. 4606-4608.

207.	Zhang, C., Dalton, L.R., Oh, M.-C., Zhang, H., and Steier, W.H., *Low Vπ Electrooptic Modulators from CLD-1: Chromophore Design and Synthesis, Material Processing, and Characterization.* Chemistry of Materials, 2001. **13**(9): p. 3043-3050.

208.	Mustroph, H., Reiner, K., Mistol, J., Ernst, S., Keil, D., and Hennig, L., *Relationship between the Molecular Structure of Cyanine Dyes and the Vibrational Fine Structure of their Electronic Absorption Spectra.* Chemical Physics and Physical Chemistry, 2009. **10**(5): p. 835-840.

209.	Mustroph, H. and Towns, A., *Fine Structure in Electronic Spectra of Cyanine Dyes: Are Sub-Bands Largely Determined by a Dominant Vibration or a Collection of Singly Excited Vibrations?* Chemical Physics and Physical Chemistry, 2018. **19**(9): p. 1016-1023.

210.	Ohira, S., Rudra, I., Schmidt, K., Barlow, S., Chung, S.-J., Zhang, Q., Matichak, J., Marder, S.R., and Brédas, J.-L., *Electronic and Vibronic Contributions to Two-Photon Absorption in Donor–Acceptor–Donor Squaraine Chromophores.* Chemistry – A European Journal, 2008. **14**(35): p. 11082-11091.

211.	Andrews, J.H., Khaydarov, J.D.V., Singer, K.D., Hull, D.L., and Chuang, K.C., *Characterization of excited states of centrosymmetric and noncentrosymmetric squaraines by third-harmonic spectral dispersion.* Journal of the Optical Society of America B, 1995. **12**(12): p. 2360-2371.

212.	Lide, D.R., *Handbook of Organic Solvents.* 1995, Boca Raton, FL: CRC Press, Inc.

213.	Arkles, B., *Silane Coupling Agents: Connecting Across Boundaries*, I. Gelest, Editor. 2014: Morrisville, PA.

214.	Stalder, A.F., Kulik, G., Sage, D., Barbieri, L., and Hoffmann, P., *A Snake-Based Approach to Accurate Determination of Both Contact Points and Contact Angles.* Colloids and Surfaces A: Physiochemical and Engineering Aspects, 2006. **286**(1-3): p. 92-103.

215.	Wang, G., Fang, Y., Kim, P., Hayek, A., Weatherspoon, M.R., Perry, J.W., Sandhage, K.H., Marder, S.R., and Jones, S.C., *Layer-By-Layer Dendritic Growth of Hyperbranched Thin Films for Surface Sol–Gel Syntheses of Conformal,*

Functional, Nanocrystalline Oxide Coatings on Complex 3D (Bio)silica Templates. Advanced Functional Materials, 2009. **19**(17): p. 2768-2776.

216.   Babaeian, M., Blanche, P.-A., Norwood, R.A., Kaplas, T., Keiffer, P., Svirko, Y., Allen, T.G., Chen, V.W., Chi, S.-H., Perry, J.W., Marder, S.R., Neifeld, M.A., and Peyghambarian, N., *Nonlinear optical components for all-optical probabilistic graphical model.* Nature Communications, 2018. **9**(1): p. 2128.

CHAPTER 4. TWO-PHOTON ABSORPTION AND PHOTOSTABILITY OF ORGANIC, HIGHLY CONJUGATED, FUSED-RING COMPOUNDS

4.1   Chapter Introduction

This chapter details a systematic spectroscopic investigation into the structure-property relationships that influence the 2PA behavior of organic, highly-conjugated, fused-ring compounds (quadrupolar type A-π-D-π-A) of interest for optical limiting applications in the NIR. Results from ND2PA measurements will be discussed in detail for two series of compounds that elucidate the impact that core structure (section 4.2.2.1) and end group acceptor strength (section 4.2.2.2) have on 2PA spectral characteristics and maximum 2PA cross sections (δ_{max}) for these dyes in chloroform solutions. Analysis will be provided to describe the molecular origin of these phenomena and will be compared with other known organic and organometallic compounds with large 2PA responses from the literature to assess the potential for these materials as optical limiters. Further, a brief photostability study is presented to gauge the degree of photobleaching for the fused-ring compounds in PMMA blend films relative to better-characterized fullerenes (C_{71} and PCBM), also in PMMA blends.

4.2   2PA Spectra, Cross Sections, and Photostability Measurements of Organic, Highly Conjugated, Fused-Ring Compounds

4.2.1   *Background and Experimental Approach*

The synthetic pathways with which the structures of organic and organometallic chromophores can be tuned to achieve large 2PA has been explored extensively for a

variety of small molecules and polymers. [96-98, 101, 217] From various structure-property studies on π-conjugated quadrupolar dyes, the structural variables that were found to most strongly influence the 2PA behavior for a given molecule were:

1) Core (a.k.a. bridge) structure: A complex mixture of interdependent structural variables that includes:

    a. Length of the π conjugated system

    b. Conformation / flexibility

    c. Electron donating or accepting character

    d. Nature of the linkers connecting the core to its end groups

2) End groups: That is, whether the molecule is terminated by an electron donating or electron accepting group and how the molecular orbitals of these groups contribute to the π electron delocalization of the molecule.

As such, numerous studies have shown that, in addition to increasing delocalization and thus polarizability, the transition dipole moments (TDMs, M_{ge}, $M_{ee'}$) for compounds with greater numbers of electrons (Nπ) are enhanced, which are related to the distance over which charge is displaced upon excitation to real, higher-lying excited states. [101, 218, 219] The importance of this is clearly shown by the relation of the TDMs to the 2PA cross section (δ in units of GM)

$$\delta \propto \frac{M_{ge}{}^2 M_{ee'}{}^2}{\left(E_{ge} - \hbar\omega\right)^2 \Gamma_{ge'}} = \frac{M_{ge}{}^2 M_{ee'}{}^2}{\Delta^2 \Gamma_{ge'}} \tag{4.1}$$

where M_{ge} is the TDM between the ground (g) and first excited singlet state (e), $M_{ee'}$ is the TDM between the first (e) and second (e') excited singlet states, $\Gamma_{ge'}$ is a damping term associated with the FWHM of the 2PA band, and Δ is the detuning term that describes the energy difference between the two-photon excitation wavelength and the 1PA energy gap (E_{ge}). [85, 97]

This approach, however, has its limits, as even conjugated molecules lose conformational planarity at long chain lengths that disrupts the coherence of the wavefunction and thus isolates π electrons to segments along the chain. Indeed, several studies have shown the effects of planarity on δ, where more rigid, planar systems have systematically demonstrated stronger 2PA than their less planar analogues by maximizing π-orbital overlap. [98, 101, 220] Naturally, synthetic strategies were developed to counteract this issue, such as the utilization of a fused-ring, planar core structures over more flexible biphenyl bridges. [83, 221]

Beyond length and planarity, synthetic chemistries can change the character of the core in terms of its electron donating or accepting strength. As stated earlier, inherent to the success of quadrupolar structures is large charge transfer upon excitation, which can be accomplished, for example, by judiciously substituting an electron acceptor (A) group in the center of the core and coupling it with strongly donating (D) end groups (quadrupole type: D-A-D) such that significant charge transfer takes place upon excitation from the periphery of the molecule toward the center. This strategy has proven effective in the pursuit of stronger 2PA by adding additional D/A functionalities to the core to alter the character of an otherwise neutral moiety or by changing the components of the core entirely. [105, 217, 222]

Further, the way in which cores are connected to their end groups can have a profound impact on the 2PA response since, particularly for D-π-A-π-D and A-π-D-π-A quadrupoles, this connection can strongly impact the overall delocalization and magnitude of TDMs. This was exemplified by several studies comparing 2PA between analogous molecules with vinylene (sp^2) and ethynylene (sp) linkers, which in general, showed that vinylene linkers facilitate greater conjugation, although in most cases the increase in δ relative to ethynylenes was not profound. [101, 221] However, for systems where poor planarity is an issue, ethylene linkers can have substantial impacts. One such case was found for Zn-porphyrin dimers which, when linked by a vinylene group, adopted a twisted confirmation due to greater rotational degrees of freedom that dramatically reduced δ relative to a dimer with an ethynylene linker that was forced into planarity due to the restricted rotational movement about the triple bond. [223-225]

The aim of this section is to apply these molecular design strategies to a new set of A-π-D-π-A chromophores that could demonstrate large 2PA responses but also demonstrate additional qualities, such as photostability and the ability to bare side-groups that do not contribute to the conjugation but can enhance solubility in various solvents for film processing and device purposes. The structures of interest in this chapter are shown in Figure 4.1 and are characterized by large, highly π-conjugated, fused-ring cores that possess electron rich thiophene groups, which are coupled with a variety of electron acceptors as terminal groups.
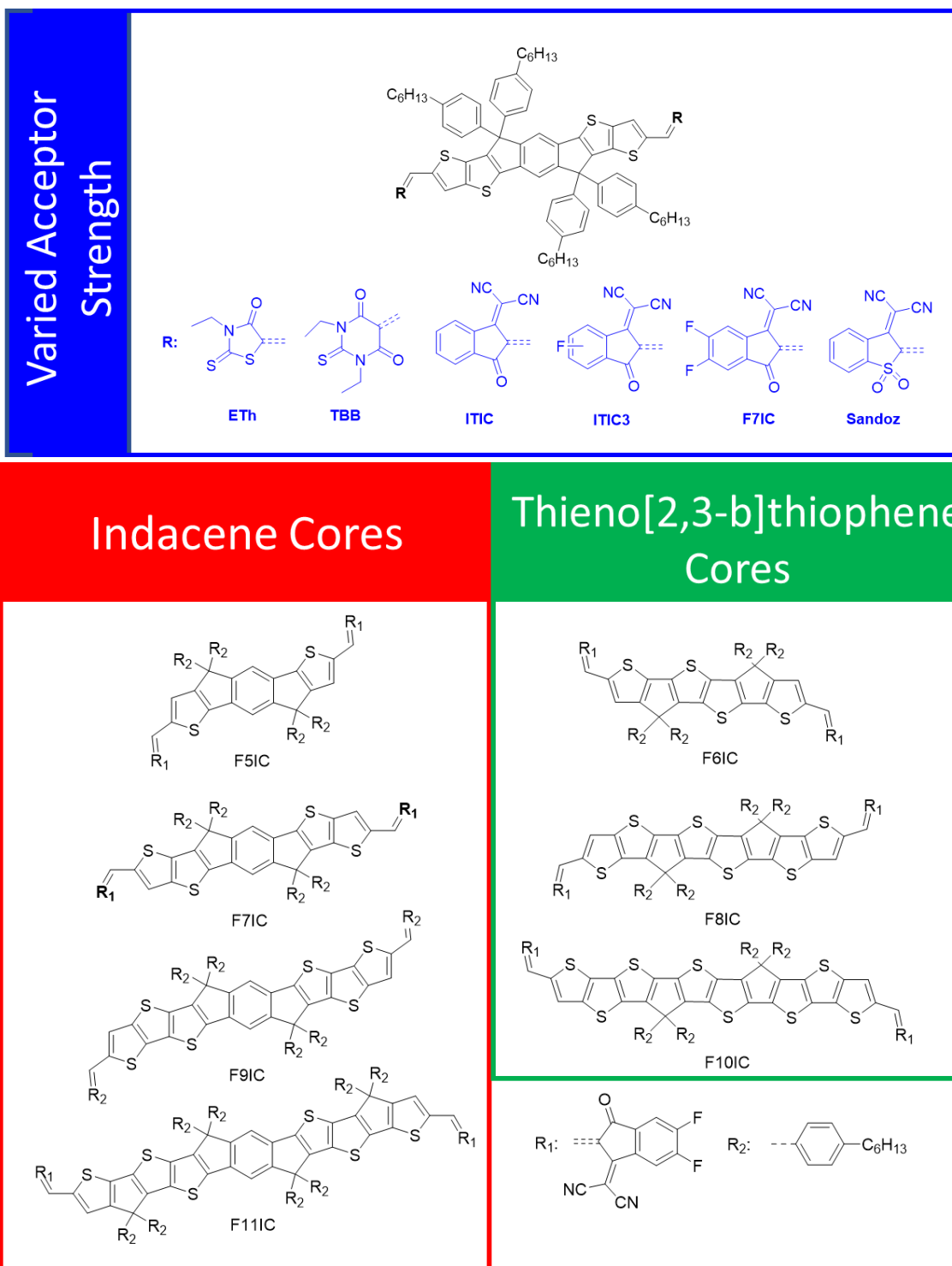
Figure 4.1. Fused-ring compound structures divided into the three categories under investigation: (Blue) Varied acceptor strength, (Red) Varied indacene-based cores, and (Green) Varied Thieno[2,3-b]thiophene-based core.

Although 2PA of some fused-ring structures have been studied previously, the work described here presents a systematic investigation of a set of chromophores ranging from 5-11 rings and four different acceptor end groups which, to the best of the author's knowledge, is the most extensive investigation into A-π-D-π-A quadrupolar, fused-ring, small molecules for which 2PA has been characterized. [101, 222, 226, 227] The dyes of interest for this study are hypothesized to demonstrated large 2PA due to the high degree of planarity, extensive π-conjugation, and may also provide enhanced photostability, when compared to less rigid, planar structures. [228-230] Additionally, because of the electron-donor character and reduced aromaticity of the thiophenes in the core, large electron transfer is expected upon excitation, where delocalized π-electrons from the core are anticipated to be pulled strongly toward the accepting end groups. [231]

As such, the structure-property relationships in this investigation will follow two themes: 1) How the length of the core, i.e. the number of fused rings, influences with magnitude and spectra 2PA response while holding the acceptor strength of the end group constant, and 2) How the same properties are influenced by varying acceptor strength while keeping core size the same. Regarding the size of the cores, two series of dyes will be measured, where one set is comprised of a s-indacene (referred to simply as indacene from here on) moiety and the other set is centered around a thieno[2,3-b]thiophene (TT) moiety. In the following section, linear and NLO measurements on these compounds in chloroform solution will be presented, and the impact these structural variables have on the observed 2PA properties will be discussed.

4.2.2   *Results and Discussion*

4.2.2.1   Influence of the Core

Linear absorption spectra in dilute chloroform solutions (ca. 6-10 µM) are plotted in Figure 4.2 showing the changes in linear absorption as a function of ring count. For the indacene- and TT-based series, the incremental increase in ring count concomitantly red-shifted 1PA λ_{max}, which was generally ascribed to a substantially upshifted HOMO with a much smaller upshifted LUMO for larger cores. [231, 232] For indacene compounds (Figure 4.2a), absorption maxima were found to steadily increase ca. 20 nm in the order of F5IC<F7IC<F9IC but then dramatically increase by 64 nm between F9IC and F11IC. Further, the spectral broadness increases with the number of rings in the series F5IC-F9IC (FWHM = 154, 226, 234 meV, respectively), with F11IC being an exception (176 meV). This was clearly due to the reduction in the high energy shoulder adjacent to the primary absorption band for F11IC compared to compounds with fewer rings, which is likely related to changes in the vibrational fine structure that is unique to F11IC. [233] Absorption spectra for the TT series (Figure 4.2b) gave a similar trend, however, all dyes from this set absorbed at longer wavelengths compared to the indacene compounds. As was seen in similar compounds, this was attributed to destabilized HOMO and slightly stabilized LUMO for TT dyes compared to those for indacene dyes. [234, 235] Similar degrees of spectral broadening were found for F6IC, F8IC, and F10IC (FWHM = 159, 240, and 270 meV, respectively). Additional linear absorption data such as the TDMs between the ground and first excited singlet state (M_{ge}) are summarized in Table 4.1. No evidence of aggregation was found, even at high concentrations (ca. 1 mM).
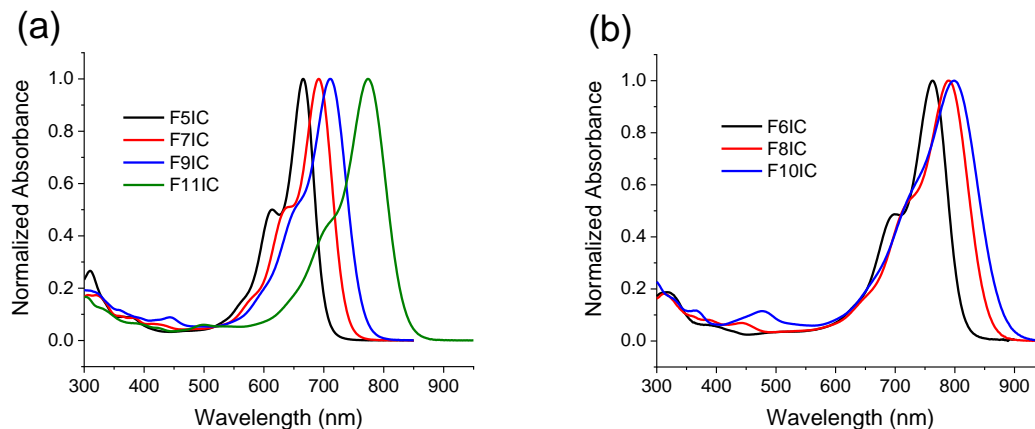
Figure 4.2. Normalized absorption spectra in dilute chloroform solutions for the series of (a) indacene- and (b) TT-based cores.

2PA spectra in ca. 1 mM chloroform solutions obtained via ND2PA (see section 4.2.4.1 for details) are plotted in Figure 4.3a-b. From the collective spectra, indacene- and TT-based compounds showed strong 2PA in the total transition wavelength range 500-750 nm, which corresponded to a large range of degenerate laser wavelengths in the NIR (ca. 1000-1500 nm). Like 1PA spectra, red-shifted 2PA bands were found with an increasing number of rings as well as an increase in the degenerate 2PA cross section (δ), which are summarized in Table 4.1. [83, 101] Further, the 2PA maxima for TT-based compounds were shifted to slightly longer wavelengths even when compared individually to indacene dyes with one additional ring. Regarding the red-shifted 2PA maxima, this trend was attributed to the stabilization of the lowest-lying 2PA singlet state with increasing numbers of rings, as shown in Figure 4.4a-b. [83, 85, 101] Interestingly, F11IC showed two strong 2PA maxima (Figure 4.3a) within this range of wavelengths, with one peak at the somewhat expected (relative to that of F9IC) laser wavelength 1344 nm and a higher energy band at 1122 nm. The 1122 nm band for F11IC was ascribed to a nearby, higher-lying 2PA state (e'' from Figure 4.4a). The greater δ for the 1122 nm band is ascribed to

the smaller detuning term Δ (equation 4.1) compared to the 1344 nm band. A second peak was not seen for F10IC, whose spectral position (1346 nm) was nearly identical to the lower energy band of F11IC. For more blue-shifted compounds, it is unclear whether they also have a second local maximum because this spectral region is likely outside the measurable range.
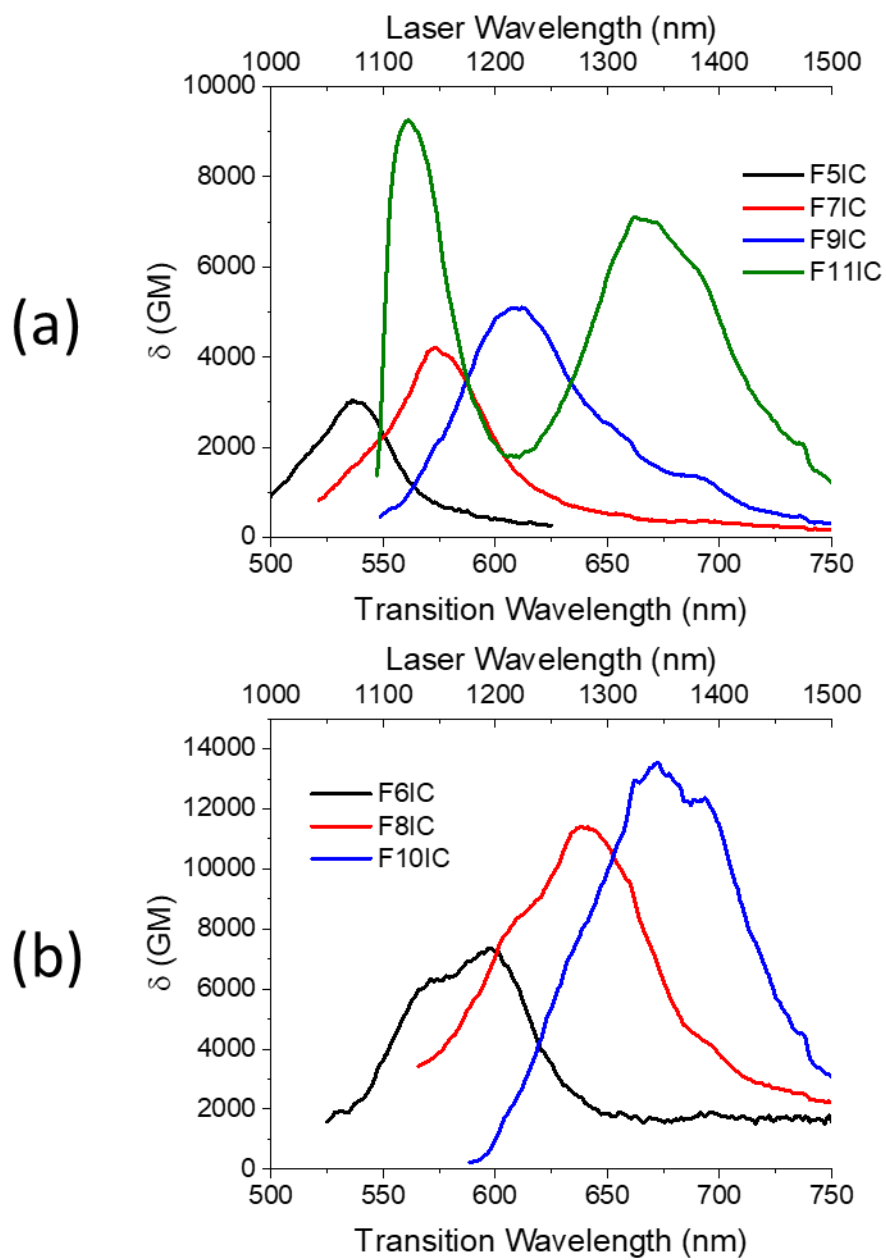
Figure 4.3. Degenerate 2PA spectra from ca. 1 mM chloroform solutions for (a) indacene- and (b) TT-based cores.
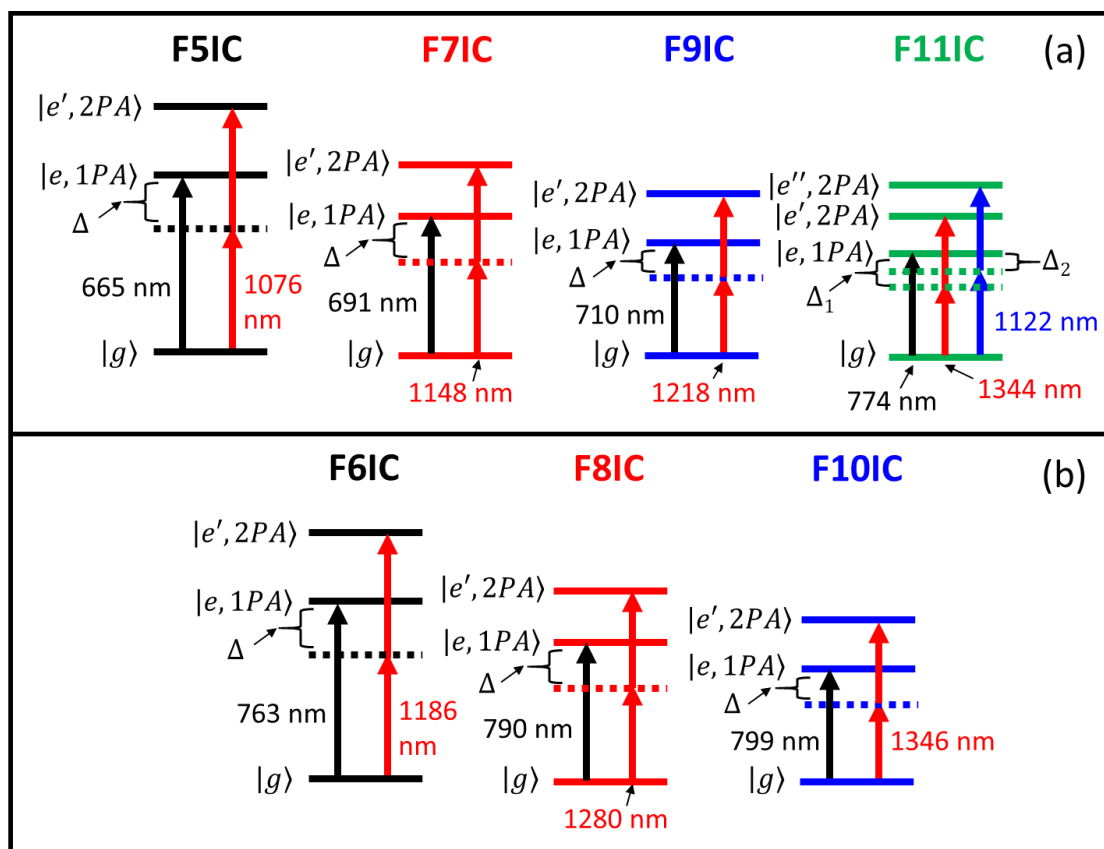
Figure 4.4. Jablonksi diagrams with 3-4 singlet states describing 1PA and 2PA transitions for (a) the indacene series and (b) the TT series. Labels correspond to ground state (g), first 1PA excited state (e), first 2PA excited state (e') and, for F11IC, second 2PA excited state (e''). Black and non-black arrows represent 1PA and 2PA transitions, respectively. Δ is the detuning energy defined as $\Delta = E_{ge} - \hbar\omega$, where E_{ge} is the optical energy gap for g $\rightarrow$ e and ω is the angular frequency of photons driving 2PA transitions. Drawings not to scale.

Focusing on the 2PA maxima for each compound, an increase in δ is found for both sets of compounds as a function of the number of rings in the core (Table 4.1); with values in the range of 3100 – 13600 GM, covering a sizeable part of NIR (1076-1346 nm). This trend can be generally rationalized by the larger values of M_{ge} and $M_{ee'}$ and smaller Δ values for cores with more rings. It was noted that δ values of for TT-based compounds were significantly larger than their indacene counterparts, with F10IC having the largest overall δ (13600 GM); even larger than that for the higher-energy 2PA peak of F11C (9300

190

GM). This markedly different response for TT dyes is the result of substantially smaller values of Δ and larger M_{ge} and $M_{ee'}$ values that cooperatively increase δ over indacene dyes. The generality of this trend breaks down when comparing F10IC and F11IC since the values of M_{ge} and Δ are comparable for these compounds and thus the stronger 2PA response of F10IC is attributed to substantially larger $M_{ee'}$ (30.9 D) relative to F11IC (20.3-23.0 D). This is indicative of larger charge transfer to the periphery of F10IC upon excitation to higher energy states (e') compared to the longer core of F11IC. Considering the enhanced delocalization (apparent from red-shifted 1PA) and lower aromaticity of the TT centers (as well as the additional thiophenes for progressively larger cores), this combination could feasibly facilitate large charge transfer of the π electrons from the thiophenes toward the strongly electron accepting end groups and justify these observations. [231]

Table 4.1. Linear and 2PA data for the indacene- and TT-based core series in chloroform solutions.

Dye	1PA (nm)	2PA Laser λ (nm)[a]	δ (10^3 GM)[a]	$\delta/N\pi$ (GM)	M_{ge} (D)[b]	$M_{ee'}$ (D)[c]	Δ (eV)
F5IC	665	1076	3.1	62	22.5	21.1	1.83
F7IC	691	1148	4.2	72	26.0	22.2	1.77
F9IC	710	1218	5.1	77	28.5	23.4	1.72
F11IC	774	1122	9.3	133	34.6	20.3	1.57
	774	1344	7.0	100		23.0	1.58
F6IC	763	1186	7.4	137	26.7	26.0	1.60
F8IC	790	1280	11.4	184	32.4	28.4	1.54
F10IC	799	1346	13.6	194	34.3	30.9	1.53

(a) Values from 2PA maxima obtained by ND2PA, upper limit of error $\pm$ 20%; (b) Calculated according to $M_{ge} = 0.09584 \times (\int \varepsilon \, dv/v_{max})^{0.5}$, (c) Calculated according to $M_{ee'} = \frac{nc(E_{ge}-\hbar\omega)}{4\pi\omega L^4 M_{ge}}\left(\frac{5\Gamma_{ge'}\delta_{max}}{\hbar}\right)^{0.5}$ assuming $\Gamma_{ge'} = 100$ meV for all samples [85].

A common metric used to normalize δ in terms of molecular size (measured by number of π electrons, Nπ) such that 2PA molecules of different sizes can be compared more directly is the ratio δ/Nπ (Table 4.1). Using the compounds here (type A-π-D-π-A) as an example, because the effective conjugation spreads to the accepting end groups (A), this effectively lengthens the molecule and must be accounted for when comparing to other structures, like D-π-A-π-D, where the donors (D) participate in conjugation but do not lengthen the molecule to the extent seen in A-π-D-π-A compounds. In doing so, the counting method used for this thesis assumes 2 π electrons come from every double bond along the core and from parts of the end groups that participate in the overall conjugation. For example, the molecule ITIC is taken to have 58 total π electrons, with 30 coming from the core and 28 from the end groups where the C=O, C≡N, and C=C doubles bonds within the phenyl rings are in-plane with the core and thus likely contribute to the conjugation. For the series of cores discussed here, δ/Nπ values were found to increase appreciably with longer core size, indicating that increasing the length of the fused-ring π system provides 2PA enhancements, similar to what has been seen for bis(styryl)benzenes. [85] Further analysis will be provided in section 4.2.3, regarding how the indacene and TT dyes compare to compounds the literature with 2PA responses in the same wavelength range.

4.2.2.2   Influence of End Groups

Linear absorption spectra in dilute chloroform solutions (ca. 1-10 µM) for 7-ring, indacene-based compounds ITIC, ITIC3, F7IC, and Sandoz with varying acceptor strengths are plotted in Figure 4.5. As anticipated, compounds with increasing acceptor strength gave increasingly red-shifted spectra and concomitant increases in M_{ge}, as summarized in Table 4.2. The spectra presented here did not cover as wide of a wavelength

range as was seen with varying core length (section 4.2.2.1). However, this was done purposefully so that the 2PA responses of this set will be readily measurable by ND2PA in the NIR. Varying acceptor identity did not appear to induce dramatic changes in spectral broadening given the comparable FWHM values obtained for this series (ITIC, ITIC3, F7IC, and Sandoz were 251, 253, 226, and 258 meV, respectively). Further, no evidence of aggregates could be found, even at high concentrations (ca. 1 mM).
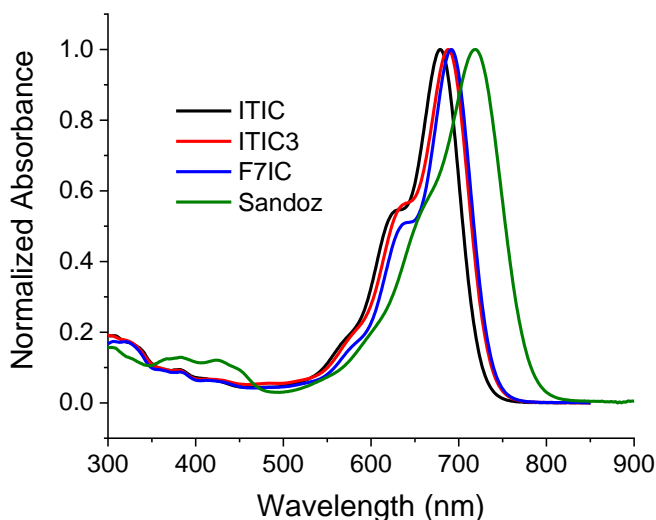
Figure 4.5. Normalized absorption for ITIC, ITIC3, F7IC, and Sandoz.

The 2PA spectra in ca. 1 mM chloroform solutions for this series were measured by ND2PA in the 500-750 nm total transition wavelength range (1000-1500 nm in terms of laser wavelength, see section 4.2.4.1 for details). In agreement with the literature, increasing end-group acceptor strength resulted in gradually red-shifted 2PA bands, which was attributed largely to substantial LUMO stabilization. [83, 101] Since ITIC, ITIC3, and F7IC only differ by incremental Fluorine-substitutions on the phenyl ring of the end group, small red-shifts were expectedly obtained that mirror the 1PA shifts. Similarly, the much

stronger Sandoz acceptor resulted in a significantly longer wavelength-absorbing 2PA band, compared to the rest of this series. Unlike the trend from different core lengths, spectral broadness did not vary significantly for these compounds (FWHM 202, 195, 192, and 206 meV for ITIC, ITIC3, F7IC, and Sandoz, respectively).
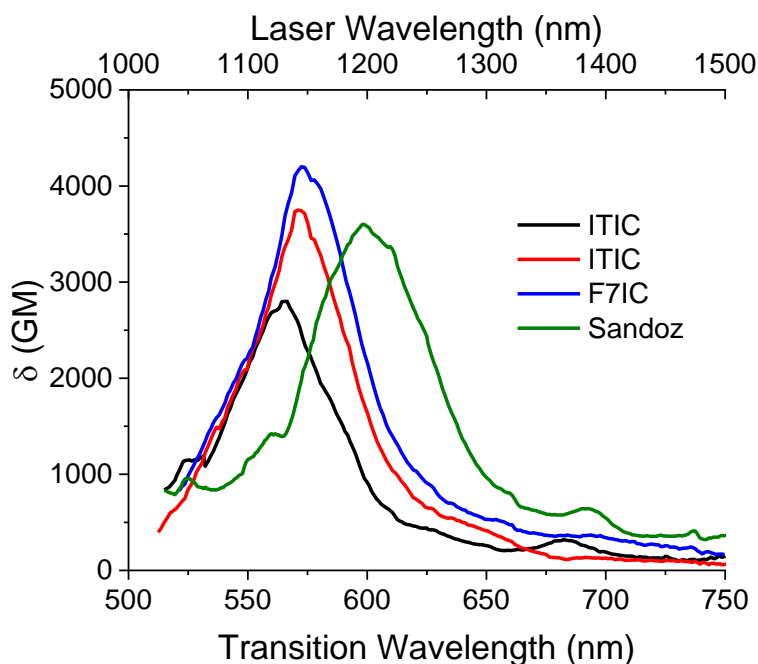
Figure 4.6. Degenerate 2PA spectra from ca. 1 mM chloroform solutions for ITIC, ITIC3, F7IC, and Sandoz.

The impact of acceptor strength on the maximum δ from ND2PA was not as profound as that seen for different core lengths, as evidenced by the narrow range (3600-4200 GM) of values obtained (data summarized in Table 4.2). Since these compounds have the same number of π electrons, this was also reflected in the similarity of their $\delta/N\pi$ values. In the series ITIC, ITIC3, and F7IC, δ was found to increase slightly as expected, however, this trend did not continue for Sandoz, despite substantially greater delocalization that was evident from red-shifted 1PA and 2PA spectra. [83, 232, 236] This is surprising given that

its M_{ge} was the highest of the compounds in this series (albeit slightly) and the 1PA

detuning term (Δ), was lower by at least 70 meV relative to other compounds. This exact

cause for this is unclear, however, it is possible that this value is underestimated due to

uncertainties in the concentration, measured irradiances, and/or beam waists during

ND2PA. If Sandoz was underestimated, one might also expect a larger value of $M_{ee'}$,

relative to the rest of the dyes with weaker acceptors in this series. Additional comparisons

between these dyes, the varied cores series, and literature compounds will be presented in

section 4.2.3.

Table 4.2. Linear and 2PA data for different end groups in 1 mM chloroform solutions.

Dye	1PA (nm)	2PA Laser λ (nm)	δ (10^3 GM)[a]	$\delta/N\pi$ (GM)	M_{ge} (D)[b]	$M_{ee'}$ (D)[c]	Δ (eV)
ITIC	679	1130	3.7	64	24.8	21.8	1.80
ITIC3	688	1142	3.8	66	25.6	21.3	1.77
F7IC	691	1148	4.2	72	26.0	22.2	1.77
Sandoz	719	1192	3.6	62	26.4	20.2	1.70

(a) Values from 2PA maxima obtained by ND2PA, upper limit of error $\pm$ 20%; (b) Calculated according to $M_{ge} = 0.09584 \times (\int \varepsilon \, d\nu / \nu_{max})^{0.5}$, (c) Calculated according to $M_{ee'} = \frac{nc(E_{ge} - \hbar\omega)]}{4\pi\omega L^4 M_{ge}} \left(\frac{5\Gamma_{ge'}\delta_{max}}{\hbar}\right)^{0.5}$ assuming $\Gamma_{ge'} = 100$ meV for all samples [85].

4.2.2.3 Photostability in PMMA Blend Films

Photostability under intense illumination (100 mW/cm^2 incoherent, white light)

was measured by monitoring the linear transmission at the primary absorption band

maximum for each blend film over time (see section 4.2.4.3 for details). To obtain optical-

quality, thin films for these measurements, fused-ring materials were blended (50% wt)

with polymethylmethacrylate (PMMA). Further, C$_{71}$ and PCBM:PMMA blends were made

to serve as references, given the abundance of literature available for the photochemistry

of these systems. [237-239] The results from these measurements were plotted in terms of the normalized change in absorbance over time for compounds with varied acceptor strength and core sizes, as seen in Figure 4.7 and Table 4.3. Focusing first on the series with increasing acceptor strength (in the order of Eth<TBB<ITIC<Sandoz), no trends were apparent based on end group identity, but Sandoz was found to be the least stable of this group with a 56% reduction in absorbance over 3 hours of constant exposure. Similar absorbance changes were found for Eth (51% reduction) which, like Sandoz, gave an exponential-like decay within the same amount of time. ITIC and TBB were the second-most and most photostable, respectively, in this series, although both compounds still showed appreciable decreases in absorbance at 25% and 23%, respectively. However, it was noted that ITIC gave an exponential-like decay but TBB showed a linear decay which suggests that, should the measurements have continued, TBB would likely have a greater reduction in absorbance at longer times than ITIC.

Turning attention to variations in core size (F5IC-F11IC), it was found that photostability was generally better for compounds with red-shifted absorption maxima (see Table 4.1 and Table 4.2 for 1PA λ_{max} data). Indeed, the shortest wavelength-absorbing compound (F5IC) in this series showed the greatest reduction in absorbance (44%) and the longest (F10IC) showed the least ($\leq$ 1%). The exception to this trend was F11IC, which experienced a greater absorbance decrease (16%) than the nearest blue-shifted indacene dye, F9IC, that only showed a 5% reduction. The exact cause for this deviation is unclear. It was noted that, of all the fused-ring compounds examined here, F10IC was the only compound to show no significant degradation over a 3 hour exposure period for which no

photobleaching could be quantifiably detected given the baseline stability fluctuations (±

1%) over the acquisition period.
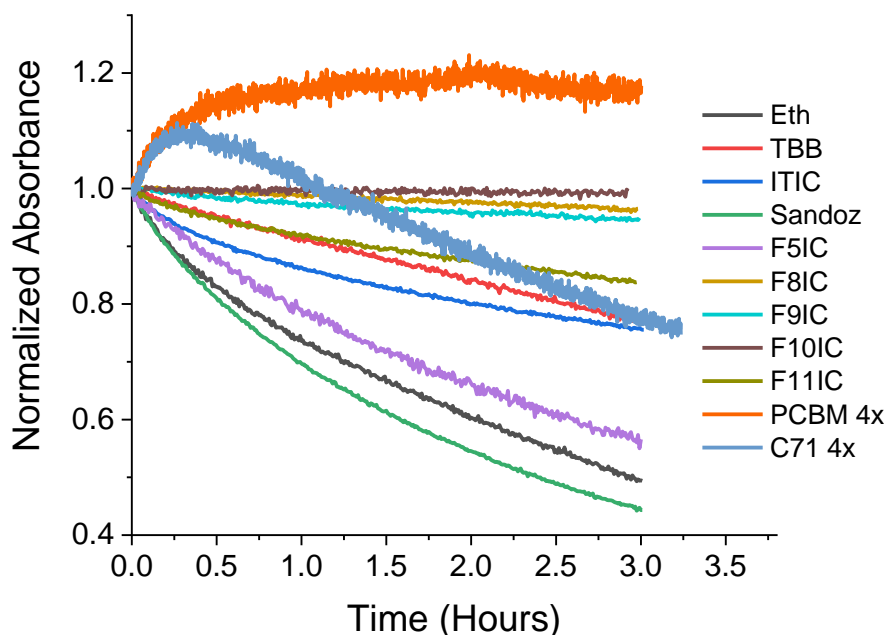
Figure 4.7. Plot showing the change in normalized absorbance overtime for PMMA:dye
blend films with varying acceptor strength (Eth, TBB, ITIC, Sandoz), core structure (F5IC-
F11IC), and reference fullerenes (PCBM and C_{71}).

Regarding the photostability of the fullerene-based blends (C_{71} and PCBM), a

complex absorption profile was observed where, for both fullerenes, the absorbance

initially increased over a period of a few hours and then either leveled off (case for PCBM)

or photobleached gradually (case for C_{71}) over a 12 hour exposure period. These trends are

plotted in Figure 4.7 where the time axis was scaled from 12 to 3 hours for ease of viewing

with fused-ring data. Such phenomena from fullerenes have been documented before and

are associated with photodimerization that results in a stronger absorbing species in the

violet-UV region associated with fullerene absorption. [237, 240] PCBM appeared to be

very photostable under continuous illumination over a 12 hour period, when considering

the lack of change in absorbance after the initial increase. On the other hand, C_{71} showed a 25% reduction in absorbance over the same timescale. Thus, one can see that, overall, the fullerenes were more stable than most fused-ring compounds under the same illumination conditions. However, given the limited change in absorbance for longer wavelength-absorbing compounds (F8IC, F9IC, and F10IC) over a 3 hour period, there exists the potential for these materials to be more photostable than at least C_{71}, although further experiments are needed to confirm.

The trends found from varying core size (and thus red-shifted) are somewhat surprising given that, generally, extended organic π systems are prone to photo-induced redox reactions, for which a multitude examples have been shown. [241-245] In examining some dyes of interest, increasingly negative reduction potentials were found for the series F5IC<F7IC<F9IC, which suggests that larger cores may more readily participate in photo-oxidative reactions compared to their smaller counterparts that may involve energy transfer with triplet oxygen in the solid state to initiate a decomposition reaction. [232, 241, 245] However, this trend is not found in the current analysis, which may suggest that oxygen-based degradation pathways are not the dominant contributor to the photobleaching seen here. To test the impact that ambient oxygen has had on measurements to-date, photostability measurements were done on a select series of PMMA:dye and fullerene blend samples that were encapsulated by parylene-C (structure in Figure 4.12), a vapor-deposited organic polymer with excellent visible-to-NIR transmission ($> 95\%$) and known oxygen and moisture barrier (see section 4.2.4.4 for deposition details). [246-248] Results from these measurements are compared with the films from Figure 4.7 exposed to ambient conditions, as shown in Figure 4.8 (fused-rings) and (C_{71} and PCBM).
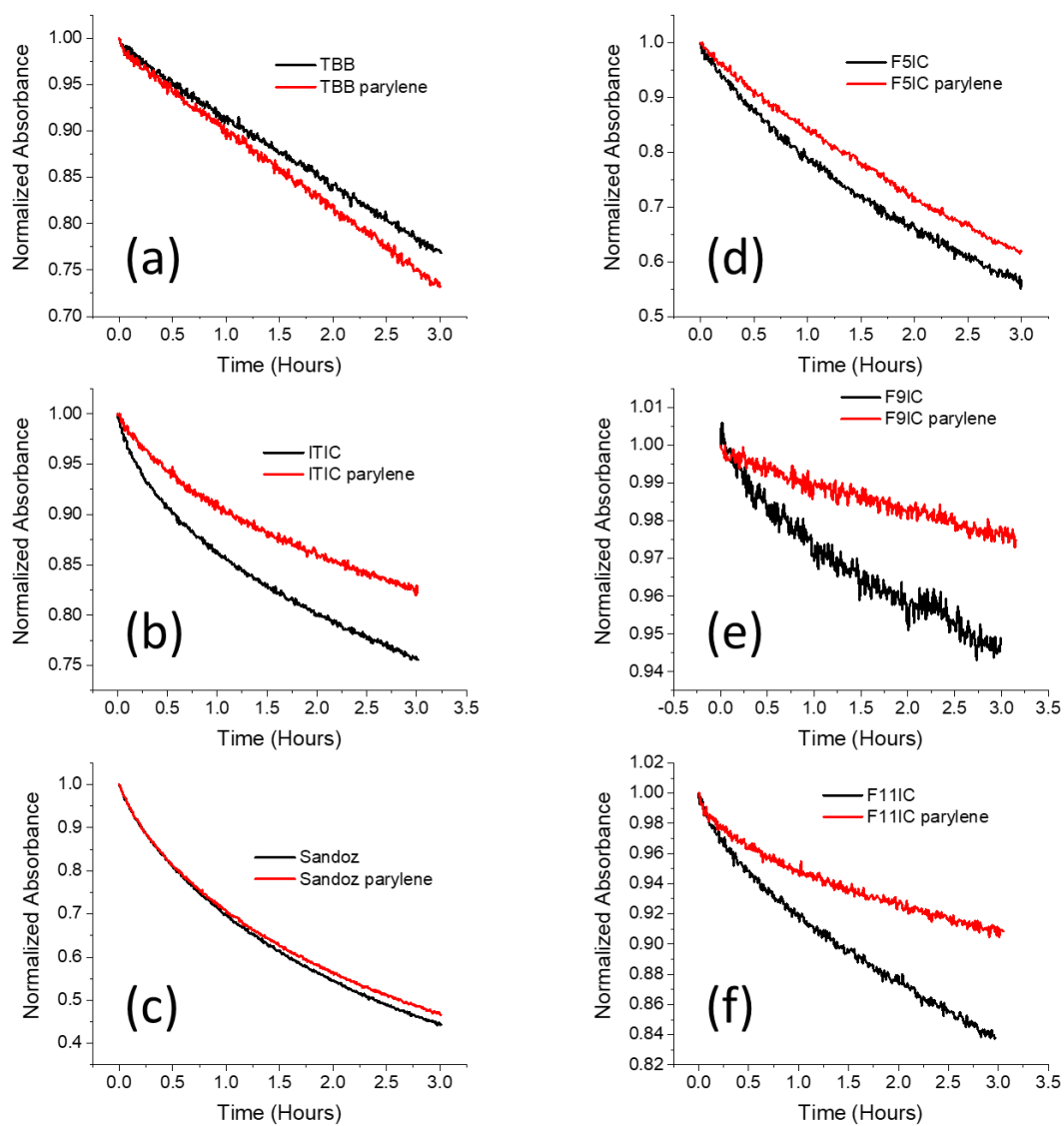
Figure 4.8. Plots comparing the normalized change in absorbance over time for as-spun and parylene-C encapsulated 50% wt PMMA blend films with (a) TBB, (b) ITIC, (c) Sandoz, (d) F5IC, (e) F9IC, and (f) F11IC.

Measurements on encapsulated samples found that, generally, ca.700 nm thick parylene-C coatings (see section 4.2.4.4 for details) were enough to reduce the photobleaching rate for a given fused-ring compound, with TBB being the only exception. Overall, this was attributed to the exclusion of oxygen and moisture by the perylene-C film and not reductions in irradiance due to the high transparency of parylene-C in the visible and NIR. For the series of different cores (F5IC, F9IC, and F11IC), small increases in photostability were seen (Table 4.3) that did not provide substantial evidence to determine whether larger cores fared better in the absence of oxygen than smaller ones. The same is likely true for the marginal increases in absorbance observed for ITIC and Sandoz, which were suspected of behaving similarly regarding the potential for photo-oxidation, as evidenced by red-shifted 1PA absorption.
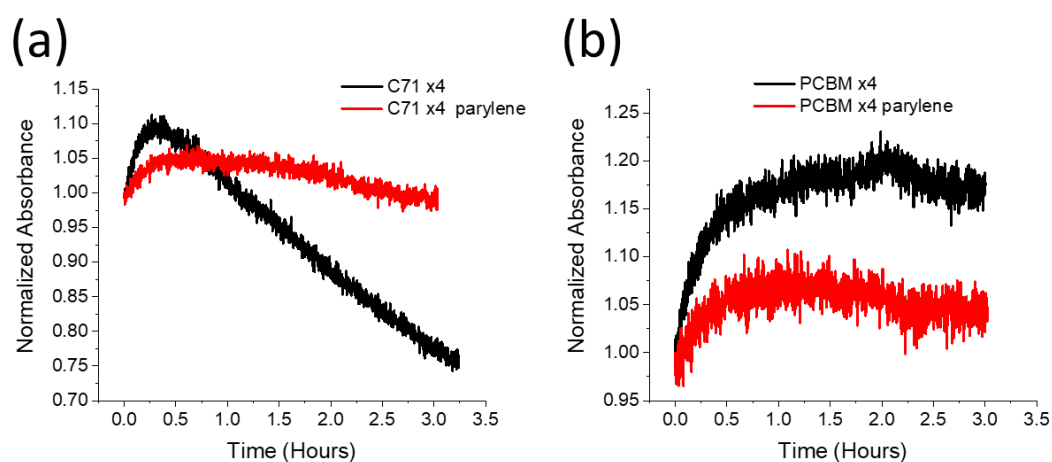
Figure 4.9. Plots comparing the normalized change in absorbance over time for as-spun and parylene-C encapsulated 78% wt PMMA blend films with (a) C_{71} and (b) PCBM.

Furthermore, encapsulated PMMA:C_{71} blends showed significant improvements in the photobleaching rate (Figure 4.9a) and resulted in a smaller initial increase in absorbance compared to samples exposed to ambient conditions. Of the samples analyzed so far,

oxygen appears to be a major factor controlling the kinetics of the C_{71} photoproduct responsible for these observations. However, without further experimentation, this mechanism has not been confirmed. A similar reduction in the initial absorbance increase was found for PCBM, however, not significant changes were observed toward longer times, thus confirming the excellent photostability of PCBM.

Table 4.3. Tabulated values for the wavelength (λ) measurement range over which spectra were average and percent decrease in absorbance for ambient-exposed and parylene-C coated films.

Compound	λ Range Averaged (nm)	Absorbance Decrease (%)	Absorbance Decrease – Parylene (%)
Eth	565-575	51	
TBB	605-615	23	27
ITIC	685-695	24	18
Sandoz	680-690	56	54
F5IC	645-655	43	38
F8IC	810-820	3	
F9IC	735-745	5	3
F10IC	840-850	< 1	
F11IC	770-780	16	9
C_{71}	460-470	25	0
PCBM	460-470	-	-

4.2.3 *Summary and Conclusions*

A spectroscopic study regarding the influence of core length and acceptor group strength on the 1PA and 2PA spectral shifts, and δ_{max} for a series of highly-conjugated, acceptor-terminated, fused rings was presented. Like trends seen by 1PA, 2PA spectra obtained by ND2PA showed that, generally, increasing core size and acceptor strength resulted in greater π electron delocalization and red-shifted absorption maxima. Overall, an increase in δ_{max} was found with cores possessing more fused rings and for compounds with increasing acceptor strength. This agreed with similar trends from studies on highly-

conjugated, non-fused-ring bis(styryl)benzene compounds. [83, 85] By exchanging the indacene moiety with TT, a substantial red shift in the 1PA and 2PA bands were observed, even compared to indacene cores with one additional total number of rings, which was attributed to less aromatic, electron-rich thiophenes causing substantial HOMO upshifts that narrow the optical gap that thus reduce Δ. [231, 235] Further, TT compounds consistently gave the higher δ_{max} values than even the longest indacene dyes, which is likely associated with more mobile π electrons along the core that facilitate large transfer (i.e. maximize M_{ge} and $M_{ee'}$) toward the molecule's periphery upon excitation, relative to indacene dyes.
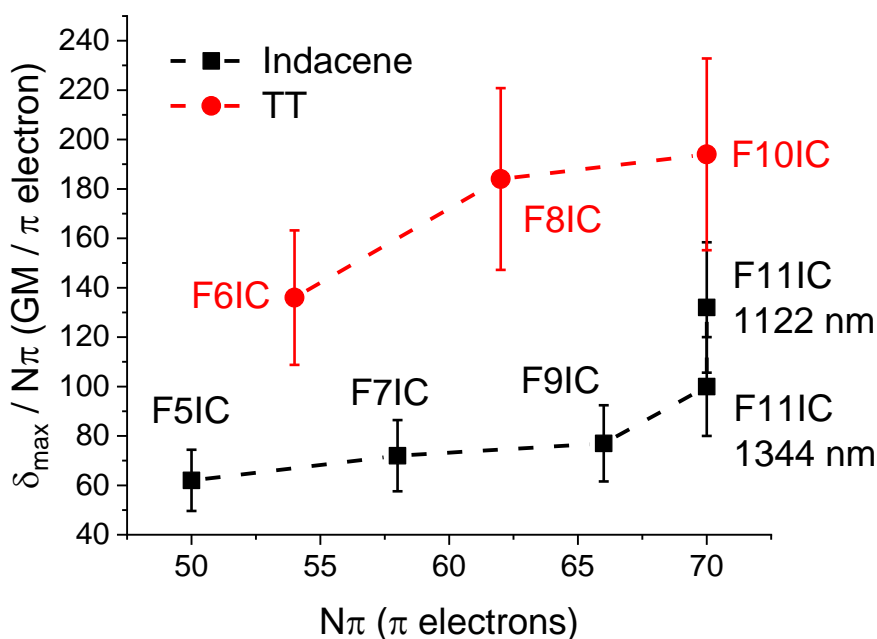
Figure 4.10. Plot showing δ_{max} .vs. $N\pi$ for fused-ring compounds with different core sizes.

This trend is illustrated in Figure 4.10, where plotting δ_{max} divided by the number of π electrons ($N\pi$) in each compound against $N\pi$ shows that the increase in core size does

not outweigh the gain in δ_{max} and highlights the differences in $\delta_{max}/N\pi$ between indacene- and TT-based compounds, as evidenced by the stratification of these data sets. A somewhat linear trend is found for the series F5IC<F7IC<F9IC that ends with sharp increase associated with the relatively larger cross sections from F11IC. On the other hand, the group trend for F6IC<F8IC<F10IC rises more sharply with increasing core size and shows that $\delta_{max}/N\pi$ for F6IC was comparable to the even strongest band (1122 nm) from F11IC. For the series with varied acceptor strength, based on the counting method used here (see Pawlicki *et al*. [101]), all compounds possessed the same number of electrons and generally showed an increased $\delta_{max}/N\pi$ with greater acceptor strengths.

Compared to well-known quadrupolar bis(styryl)benzene, oligophenylenevinylene, and squaraine compounds, the 2PA bands for the fused-ring structures studied here absorbed at comparably long wavelengths (ca. 1100-1400 nm). [83, 85, 103, 105, 249-251]. In identifying compounds with 2PA responses in a similar wavelength range for comparative purposes, a sizeable body of work has been done on porphyrin-based extended π systems, oligomers, and polymers. [98, 101, 249] In some cases, dyes with larger cores, such as F8IC and F10IC, were found to have larger 2PA responses (11,400-13,600 GM) compared to Ni-porphyrin (7200 GM, [226]), non-metal-containing hexaphyrin (9900 GM, [252]), and small (n = 2) oligomeric Ni-porphyrin compounds (8000 GM, [227]) that absorbed in a similar wavelength range. However, when compared to larger, more delocalized Zn-porphyrin oligomers [253], δ_{max} for even the molecules with the strongest 2PA here (F10IC) are substantially smaller in magnitude, although slightly more red-shifted spectrally. While the δ_{max} presented here are clearly less than those obtained for some squaraine compounds, fused-ring dyes do largely show enhanced 2PA relative to

bis(styryl)benzenes, particularly for molecules with larger cores (F78C-F11IC), and some long-chain A-π-A polymethine dyes longer wavelengths (>1350 nm). [83, 85, 251]

4.2.4 *Experimental Details*

4.2.4.1 ND2PA Measurements in Chloroform Solutions

The light source used for all nonlinear optical measurements was a regeneratively amplified Ti:Sapphire system (Solstice, Spectra-Physics) that produces sub- 90 fs (HW1/e) pulses at 800 nm with a repetition rate of 1 kHz. This, in turn, pumps an optical parametric amplifier of white-light continuum (TOPAS-C, Spectra-Physics) that provides output pulses of <100 fs (HW1/e) in the appropriate spectral bands. The measurement system used for ND2PA was a Helios transient absorption spectrometer (Spectraphysics). As shown in Figure 2.6, a part of the 800 nm beam was picked and used to generate the NIR white light probe using a nonlinear crystal (proprietary, material unknown – supplied by SpectraPhysics) with stable output in the ca. 850-1400 nm wavelength range. The pump beam is delivered by the TOPAS-C and is chopped at 500 Hz prior to being focused into the sample.

All samples were ca. 1 mM made in spectrophotometric grade chloroform (Sigma Aldrich 366919). Typical beam sizes (1/e diameter) used for measurements were 350-460 μm for the pump and 220-280 μm for the probe to ensure substantial overlap. Maximum overlap was found by adjusting the beam positions at the sample to maximize the excited state absorption (ESA) response from a Pb-porphyrin in ca. 1 mM chloroform solution. [87] Once optimal overlap was found, time zero was found for all samples, which depends on wavelength and the compound being measured but generally in the range of 13-30 ps

absolute delay. The typical 2PA transition for fused-ring systems was found to occur within a 0.1-0.12 ps time window. Given that the 2PA transitions are so short-lived, it was desired to capture the baseline prior to excitation and also the ESA at longer times so that the time delay at which the maximum response occurs could be easily identified. Starting 1.5 ps before time zero, scans were acquired over an absolute time delay of 3 ps, with 0.02 ps steps and a 1 second integration time per scan. Typical pulse energies delivered to the sample were in the 2-20 μJ range, depending on the response of the material and the available energy for a specific pump wavelength.

Since probe absorption will shift based on the material identity and the wavelength of the probe (see section 2.3.2 for explanation), measurements were typically done at multiple wavelengths per compound and the resulting spectra were then stitched to produce a single ND2PA spectrum. Table 4.4 lists the pump wavelengths used for stitching of ND2PA for each sample. Using the ratio of pump-to-probe size, pulse energy, and sample concentrations, the δ_{ND} was estimated by iteratively solving for the value of δ_{ND} that matched closest with the ΔOD given by the sample, taking an over three energies for each sample. δ_{ND} values reported in this section were divided by 2, to be put in terms of a degenerate δ. Estimated error for these values is $\pm$ 20%.

Table 4.4. Tabulated pump wavelengths used to obtain stitched ND2PA spectra.

Compound	Pump Wavelengths (nm)
ITIC	1050, 1300, 1550
ITIC3	1300, 1550
Sandoz	1300, 1550
F5IC	1200, 1300, 1550
F7IC	1300, 1550
F9IC	1300, 1550
F11IC	1300, 1550
F6IC	1300, 1550
F8IC	1550
F10IC	1550

4.2.4.2 <u>PMMA Blend Film Preparation</u>

Compounds ITIC, ITIC3, and F5IC-F11IC were synthesized as described previously in references [231-234, 236]. Eth, TBB, and Sandoz were synthesized by Dr. Junxiang Zhang, Marder Group, GT. 50% wt dye:PMMA blend films were made by first making separate 1% wt PMMA and fused-ring solutions in spectrophotometric grade chloroform (Sigma Aldrich 366919). The same was done for C71 and PCBM, except these precursor solutions were made ca. 3.5% wt in chloroform and mixed with 1% wt PMMA. Once the individual solutions were dissolved, equal volumes (250 µL each for 500 µL total volume) are mixed and stirred thoroughly to make the 50% blend solutions (78% wt for fullerene blends). The blend solutions are then filtered prior to spin coating with a 0.2 µm PTFE membrane filter (13 mm syringe filter VWR No. 28145-491) to remove undissolved dye or polymer particulate. 15x25x1 mm^3. Microscope glass slide substrates were cleaned according to the procedure listed in section 3.4.4.1. All films were cast using Laurell Technologies WS-650-23 spin coater operated at with an initial ramp step of 100 RPM/s for 5 s and then spinning at 1000 RPM for 30 s. 150 µL of 50% wt blend solution prior was

used to flood the substrate prior to spinning. Film thicknesses were determined using Dektak 6M profilometer to be ca. 200 nm. Typical films were 50% transmissive at their respective 1PA maxima at this concentration and thickness.

4.2.4.3 Photostability Measurements in PMMA Blend Films

Light source was a 250 W tungsten halogen projector lamp (Ushio EHJ 24V) whose output was curtailed by a ca. 5 mm-wide circular aperture to reduce incident intensity. As seen in Figure 4.11, the divergent beam was collimated by a slightly positive lens (C) and then focused more tightly by a higher-power lens (L1) onto the sample. The beam area was adjusted to be a 1 cm^2 diameter circle and neutral density filters were used to deliver 100 mW of lamp power at the sample, such that an illumination intensity is achieved that is comparable to that from a commercial solar simulator (100 mW/cm^2). This slightly divergent beam is then collected by a high-power lens (L2) and is focused into an optical fiber (OP400-2-UV-VIS Ocean Optics) coupled to a Linear Si CCD USB-650 Red Tide (Ocean Optics) detector, which is controlled by SpectraSuite. Backgrounds are taken with clean, non-film-bearing microscope glass slides. To obtain the average transmittance at the primary absorption peak for a material over time, SpectraSuite was programmed to average over a 10 nm spectral region covering the center of the primary absorption band, taking data points every 30 seconds. Since most fused-ring systems showed some level of photobleaching over 3 hours, this was chosen to be the illumination period for these samples. Due to the slower photokinetics of fullerene blends, they were collected for 12 hours. Curves shown in Figure 4.7-Figure 4.9 are averages of at least two blend films for each material.
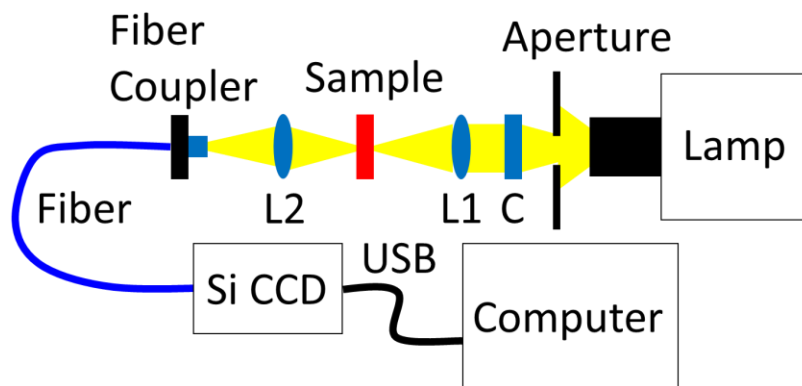
Figure 4.11. Illustration of photostability measurement setup showing the white light lamp output relayed to the sample via a collimating lens (C) and a focusing lens (L1), and then collected by a focusing lens (L2) and an optical fiber coupled with to the Si CCD spectrometer.

4.2.4.4   Parylene-C Encapsulation

Conformal vapor-deposited parylene-C coatings were obtained using a SCS Labcoter PDS 2010 system. The mass of parylene-C dimer (1.640 g) used was chosen based on calibration curve established by the instrument owners at the following deposition settings: Furnace temperature = 690 ℃, chamber gauge = 135 ℃, vaporizer = 175 ℃, system vacuum level = 40 mTorr. All samples were coated at the same time, which yielded a 671 nm conformal film (confirmed by a Dektak 6M profilometer).
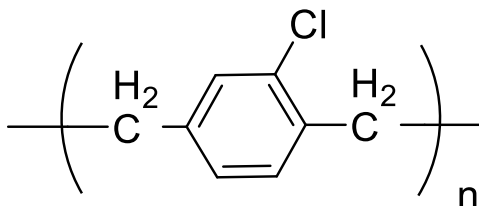
Figure 4.12. Chemical structure of parylene-C.

4.3   Chapter Summary

The work presented in this chapter involved a systematic, structure-property study with the aim of determining the influence of core identity and the strength of electron-accepting end groups on the 2PA response for a series of organic, highly-conjugated, fused-ring quadrupolar compounds of type A-π-D-π-A. Regarding core structure, a series of indacene-based molecules with an odd number of rings and a series of thienothiophene (TT)-based compounds with an even number of rings were investigated. ND2PA measurements were used to obtain the 2PA spectra and quantify the maximum 2PA cross sections (δ_{max}) in the NIR (1100-1500 nm) for these compounds in chloroform solutions and found that larger cores result in red-shifted 1PA and 2PA maxima and greater δ_{max}. This finding was attributed to a substantial upshifted HOMO, which was particularly large for TT-based dyes and resulted in these compounds possessing the most red-shifted 1PA and 2PA responses and largest values of δ_{max}, when compared to indacene compounds. [231, 232]

Similar measurements were performed on a set of fused-7-ring compounds bearing different acceptor groups and, generally, showed concomitant increases in 1PA and 2PA absorption wavelength and δ_{max} with larger acceptor strengths. Regarding δ_{max} values for this series, the only exception to this trend was Sandoz, which may have been underestimated due to uncertainties in the measured pulse energy and ratio of beam sizes between the pump and probe beams during ND2PA. This trend resulted from a significantly down-shifted LUMO and small down-shifted HOMO with increasing acceptor strength, thus lowering the optical energy gap for one- and two-photon transitions

and facilitating larger charge transfer from the electron rich core center to the acceptor-terminated edges of the molecule upon excitation. [83, 85, 101]

This set of materials presented a significant advance in the effort to extend 2PA responses for organic, fused-ring, quadrupolar A-π-D-π-A chromophores into the NIR for optical limiting applications, and demonstrated the effectiveness in doing so by selectively varying the core size and acceptor strength. Compared to well-known quadrupolar molecules with strong 2PA such as squaraines and bis(styryl)benzenes, several of the fused ring compounds studied here possessed significantly red-shifted 2PA maxima relative to the longest absorbing compounds from the literature as well as generally larger values of δ_{max} for compounds of comparable conjugation length. Although some chromophores from this investigation show larger 2PA responses than some porphyrin-based systems with large cross sections at similar NIR wavelengths, highly-conjugated, large oligomers from porphyrin-compounds still show greater 2PA than even F10IC, the dye with the largest δ_{max} obtained in this work. [226, 227, 253, 254] Further, while some A-π-A cyanines poses larger values δ_{max} of in the shorter wavelength range of the NIR (compared to dyes with smaller cores), these bands can drop rather sharply toward longer wavelengths where the larger-core compounds studied here possess stronger 2PA. [251]

Additionally, the photostability for select fused-ring compounds was characterized by monitoring the transmission of the primary absorption band in 50% wt dye:PMMA blend films and compared to reference films made from 78% wt fullerene:PMMA blends (fullerene = C_{71}, PCBM). While no specific trend was found for dyes with the same core but varied acceptor strength (Eth<TBB<ITIC<Sandoz, in order of acceptor strength), all of these compounds demonstrate significantly faster photobleaching over a continuous, 3

hour exposure period to incoherent white light than both fullerene blends over 12 hours of exposure. For the series with different cores sizes, larger cores were found to be more photostable over 3 hours of exposure than shorter cores, although an exception was found with F9IC and F11IC, and showed that F8IC and F10IC had potential to be more stable than C_{71} in PMMA blends but still not to the photostability level of PCBM. Further, select films encapsulated by a thin parylene-C oxygen barrier, generally, showed slight improvements in fused-ring photostability, which indicates that, while oxygen may have a role in this photobleaching process, other degradation mechanisms cannot be ruled out and could be the dominant contributors. A significant improvement was observed for encapsulated C_{71} films, indicative of an oxygen-dependent photobleaching pathway, but no marked differences were seen between encapsulated and ambient-exposed PCBM.

4.4   References

83.   Albota, M., Beljonne, D., Brédas, J.-L., Ehrlich, J.E., Fu, J.-Y., Heikal, A.A., Hess, S.E., Kogej, T., Levin, M.D., Marder, S.R., McCord-Maughon, D., Perry, J.W., Röckel, H., Rumi, M., Subramaniam, G., Webb, W.W., Wu, X.-L., and Xu, C., *Design of Organic Molecules with Large Two-Photon Absorption Cross Sections.* Science, 1998. **281**(5383): p. 1653.

85.   Rumi, M., Ehrlich, J.E., Heikal, A.A., Perry, J.W., Barlow, S., Hu, Z., McCord-Maughon, D., Parker, T.C., Röckel, H., Thayumanavan, S., Marder, S.R., Beljonne, D., and Brédas, J.-L., *Structure−Property Relationships for Two-Photon Absorbing Chromophores: Bis-Donor Diphenylpolyene and Bis(styryl)benzene Derivatives.* Journal of the American Chemical Society, 2000. **122**(39): p. 9500-9510.

87.   Hales, J.M., Cozzuol, M., Screen, T.E.O., Anderson, H.L., and Perry, J.W., *Metalloporphyrin polymer with temporally agile, broadband nonlinear absorption for optical limiting in the near infrared.* Optics Express, 2009. **17**(21): p. 18478-18488.

96.   Terenziani, F., Katan, C., Badaeva, E., Tretiak, S., and Blanchard-Desce, M., *Enhanced Two-Photon Absorption of Organic Chromophores: Theoretical and Experimental Assessments.* Advanced Materials, 2008. **20**(24): p. 4641-4678.

97.   Rumi, M., Barlow, S., Wang, J., Perry, J.W., and Marder, S.R., *Two-Photon Absorbing Materials and Two-Photon-Induced Chemistry*, in *Photoresponsive Polymers I*, S.R. Marder and K.-S. Lee, Editors. 2008, Springer Berlin Heidelberg: Berlin, Heidelberg. p. 1-95.

98.   He, G.S., Tan, L.-S., Zheng, Q., and Prasad, P.N., *Multiphoton Absorbing Materials: Molecular Designs, Characterizations, and Applications*. Chemical Reviews, 2008. **108**(4): p. 1245-1330.

101.   Pawlicki, M., Collins, H.A., Denning, R.G., and Anderson, H.L., *Two-Photon Absorption and the Design of Two-Photon Dyes.* Angewandte Chemie International Edition, 2009. **48**(18): p. 3244-3266.

103.   Chung, S.-J., Zheng, S., Odani, T., Beverina, L., Fu, J., Padilha, L.A., Biesso, A., Hales, J.M., Zhan, X., Schmidt, K., Ye, A., Zojer, E., Barlow, S., Hagan, D.J., Van Stryland, E.W., Yi, Y., Shuai, Z., Pagani, G.A., Brédas, J.-L., Perry, J.W., and Marder, S.R., *Extended Squaraine Dyes with Large Two-Photon Absorption Cross-Sections.* Journal of the American Chemical Society, 2006. **128**(45): p. 14444-14445.

105.   Pond, S.J.K., Rumi, M., Levin, M.D., Parker, T.C., Beljonne, D., Day, M.W., Brédas, J.-L., Marder, S.R., and Perry, J.W., *One- and Two-Photon Spectroscopy of Donor−Acceptor−Donor Distyrylbenzene Derivatives: Effect of Cyano Substitution and Distortion from Planarity.* The Journal of Physical Chemistry A, 2002. **106**(47): p. 11470-11480.

217.   Myung Kim, H. and Rae Cho, B., *Two-photon materials with large two-photon cross sections. Structure–property relationship.* Chemical Communications, 2009(2): p. 153-164.

218.   Ventelon, L., Charier, S., Moreaux, L., Mertz, J., and Blanchard-Desce, M., *Nanoscale Push–Push Dihydrophenanthrene Derivatives as Novel Fluorophores for Two-Photon-Excited Fluorescence.* Angewandte Chemie International Edition, 2001. **40**(11): p. 2098-2101.

219.   Makarov, N.S., Drobizhev, M., and Rebane, A., *Two-photon absorption standards in the 550–1600 nm excitation wavelength range.* Optics Express, 2008. **16**(6): p. 4029-4047.

220.   Ahn, T.K., Kim, K.S., Kim, D.Y., Noh, S.B., Aratani, N., Ikeda, C., Osuka, A., and Kim, D., *Relationship between Two-Photon Absorption and the π-Conjugation Pathway in Porphyrin Arrays through Dihedral Angle Control.* Journal of the American Chemical Society, 2006. **128**(5): p. 1700-1704.

221.   Mongin, O., Porrès, L., Charlot, M., Katan, C., and Blanchard-Desce, M., *Synthesis, Fluorescence, and Two-Photon Absorption of a Series of Elongated Rodlike and Banana-Shaped Quadrupolar Fluorophores: A Comprehensive Study*

of Structure–Property Relationships. Chemistry – A European Journal, 2007. **13**(5): p. 1481-1498.

222.   Lee, S.K., Yang, W.J., Choi, J.J., Kim, C.H., Jeon, S.-J., and Cho, B.R., *2,6-Bis[4-(p-dihexylaminostyryl)styryl]anthracene Derivatives with Large Two-Photon Cross Sections.* Organic Letters, 2005. **7**(2): p. 323-326.

223.   Drobizhev, M., Stepanenko, Y., Dzenis, Y., Karotki, A., Rebane, A., Taylor, P.N., and Anderson, H.L., *Understanding Strong Two-Photon Absorption in π-Conjugated Porphyrin Dimers via Double-Resonance Enhancement in a Three-Level Model.* Journal of the American Chemical Society, 2004. **126**(47): p. 15352-15353.

224.   Drobizhev, M., Stepanenko, Y., Dzenis, Y., Karotki, A., Rebane, A., Taylor, P.N., and Anderson, H.L., *Extremely Strong Near-IR Two-Photon Absorption in Conjugated Porphyrin Dimers: Quantitative Description with Three-Essential-States Model.* The Journal of Physical Chemistry B, 2005. **109**(15): p. 7223-7236.

225.   Frampton, M.J., Akdas, H., Cowley, A.R., Rogers, J.E., Slagle, J.E., Fleitz, P.A., Drobizhev, M., Rebane, A., and Anderson, H.L., *Synthesis, Crystal Structure, and Nonlinear Optical Behavior of β-Unsubstituted meso−meso E-Vinylene-Linked Porphyrin Dimers.* Organic Letters, 2005. **7**(24): p. 5365-5368.

226.   Kurotobi, K., Kim, K.S., Noh, S.B., Kim, D., and Osuka, A., *A Quadruply Azulene-Fused Porphyrin with Intense Near-IR Absorption and a Large Two-Photon Absorption Cross Section.* Angewandte Chemie, 2006. **118**(24): p. 4048-4051.

227.   Yoon, M.-C., Noh, S.B., Tsuda, A., Nakamura, Y., Osuka, A., and Kim, D., *Photophysics of meso-β Doubly Linked Ni(II) Porphyrin Arrays: Large Two-Photon Absorption Cross-Section and Fast Energy Relaxation Dynamics.* Journal of the American Chemical Society, 2007. **129**(33): p. 10080-10081.

228.   Jiao, C., Huang, K.-W., and Wu, J., *Perylene-Fused BODIPY Dye with Near-IR Absorption/Emission and High Photostability.* Organic Letters, 2011. **13**(4): p. 632-635.

229.   Gao, J.H., Li, R.J., Li, L.Q., Meng, Q., Jiang, H., Li, H.X., and Hu, W.P., *High-Performance Field-Effect Transistor Based on Dibenzo[d,d']thieno[3,2-b;4,5-b']dithiophene, an Easily Synthesized Semiconductor with High Ionization Potential.* Advanced Materials, 2007. **19**(19): p. 3008-3011.

230.   Nagai, A. and Chujo, Y., *Aromatic Ring-Fused BODIPY-Based Conjugated Polymers Exhibiting Narrow Near-Infrared Emission Bands.* Macromolecules, 2010. **43**(1): p. 193-200.

231.   Dai, S., Li, T., Wang, W., Xiao, Y., Lau, T.-K., Li, Z., Liu, K., Lu, X., and Zhan, X., *Enhancing the Performance of Polymer Solar Cells via Core Engineering of*

NIR-Absorbing Electron Acceptors. Advanced Materials, 2018. **30**(15): p. 1706571.

232.   Dai, S., Xiao, Y., Xue, P., James Rech, J., Liu, K., Li, Z., Lu, X., You, W., and Zhan, X., *Effect of Core Size on Performance of Fused-Ring Electron Acceptors.* Chemistry of Materials, 2018. **30**(15): p. 5390-5396.

233.   Jia, B., Dai, S., Ke, Z., Yan, C., Ma, W., and Zhan, X., *Breaking 10% Efficiency in Semitransparent Solar Cells with Fused-Undecacyclic Electron Acceptor.* Chemistry of Materials, 2018. **30**(1): p. 239-245.

234.   Li, T., Dai, S., Ke, Z., Yang, L., Wang, J., Yan, C., Ma, W., and Zhan, X., *Fused Tris(thienothiophene)-Based Electron Acceptor with Strong Near-Infrared Absorption for High-Performance As-Cast Solar Cells.* Advanced Materials, 2018. **30**(10): p. 1705969.

235.   Wang, J., Zhang, J., Xiao, Y., Xiao, T., Zhu, R., Yan, C., Fu, Y., Lu, G., Lu, X., Marder, S.R., and Zhan, X., *Effect of Isomerization on High-Performance Nonfullerene Electron Acceptors.* Journal of the American Chemical Society, 2018. **140**(29): p. 9140-9147.

236.   Lin, Y., Wang, J., Zhang, Z.-G., Bai, H., Li, Y., Zhu, D., and Zhan, X., *An Electron Acceptor Challenging Fullerenes for Efficient Polymer Solar Cells.* Advanced Materials, 2015. **27**(7): p. 1170-1174.

237.   Pont, S., Foglia, F., Higgins, A.M., Durrant, J.R., and Cabral, J.T., *Stability of Polymer:PCBM Thin Films under Competitive Illumination and Thermal Stress.* Advanced Functional Materials, 2018. **0**(0): p. 1802520.

238.   Distler, A., Sauermann, T., Egelhaaf, H.-J., Rodman, S., Waller, D., Cheon, K.-S., Lee, M., and Guldi, D.M., *The Effect of PCBM Dimerization on the Performance of Bulk Heterojunction Solar Cells.* Advanced Energy Materials, 2014. **4**(1): p. 1300693.

239.   Heumueller, T., Mateker, W.R., Distler, A., Fritze, U.F., Cheacharoen, R., Nguyen, W.H., Biele, M., Salvador, M., von Delius, M., Egelhaaf, H.-J., McGehee, M.D., and Brabec, C.J., *Morphological and electrical control of fullerene dimerization determines organic photovoltaic stability.* Energy & Environmental Science, 2016. **9**(1): p. 247-256.

240.   Wong, H.C., Higgins, A.M., Wildes, A.R., Douglas, J.F., and Cabral, J.T., *Patterning Polymer–Fullerene Nanocomposite Thin Films with Light.* Advanced Materials, 2013. **25**(7): p. 985-991.

241.   Song, L., Hennink, E.J., Young, I.T., and Tanke, H.J., *Photobleaching kinetics of fluorescein in quantitative fluorescence microscopy.* Biophysical Journal, 1995. **68**(6): p. 2588-2600.

242.   Song, B., Zhang, Q., Ma, W.-H., Peng, X.-J., Fu, X.-M., and Wang, B.-S., *The synthesis and photostability of novel squarylium indocyanine dyes.* Dyes and Pigments, 2009. **82**(3): p. 396-400.

243.   Chen, P., Li, J., Qian, Z., Zheng, D., Okasaki, T., and Hayami, M., *Study on the photooxidation of a near-infrared-absorbing benzothiazolone cyanine dye.* Dyes and Pigments, 1998. **37**(3): p. 213-222.

244.   Wu, T., Lin, T., Zhao, J., Hidaka, H., and Serpone, N., *TiO$_2$-Assisted Photodegradation of Dyes. 9. Photooxidation of a Squarylium Cyanine Dye in Aqueous Dispersions under Visible Light Irradiation.* Environmental Science & Technology, 1999. **33**(9): p. 1379-1387.

245.   Kanony, C., Åkerman, B., and Tuite, E., *Photobleaching of Asymmetric Cyanines Used for Fluorescence Imaging of Single DNA Molecules.* Journal of the American Chemical Society, 2001. **123**(33): p. 7985-7995.

246.   Chen, T.-N., Wuu, D.-S., Wu, C.-C., Chiang, C.-C., Chen, Y.-P., and Horng, R.-H., *Improvements of Permeation Barrier Coatings Using Encapsulated Parylene Interlayers for Flexible Electronic Applications.* Plasma Processes and Polymers, 2007. **4**(2): p. 180-185.

247.   Humphrey, B.J., *The application of parylene conformal coating technology to archival and artifact conservation.* Studies in Conservation, 1984. **29**(3): p. 117-123.

248.   Cieślik, M., Engvall, K., Pan, J., and Kotarba, A., *Silane–parylene coating for improving corrosion resistance of stainless steel 316L implant material.* Corrosion Science, 2011. **53**(1): p. 296-301.

249.   Odom, S.A., Webster, S., Padilha, L.A., Peceli, D., Hu, H., Nootz, G., Chung, S.-J., Ohira, S., Matichak, J.D., Przhonska, O.V., Kachkovski, A.D., Barlow, S., Brédas, J.-L., Anderson, H.L., Hagan, D.J., Van Stryland, E.W., and Marder, S.R., *Synthesis and Two-Photon Spectrum of a Bis(Porphyrin)-Substituted Squaraine.* Journal of the American Chemical Society, 2009. **131**(22): p. 7510-7511.

250.   Chung, S.-J., Rumi, M., Alain, V., Barlow, S., Perry, J.W., and Marder, S.R., *Strong, Low-Energy Two-Photon Absorption in Extended Amine-Terminated Cyano-Substituted Phenylenevinylene Oligomers.* Journal of the American Chemical Society, 2005. **127**(31): p. 10844-10845.

251.   Padilha, L.A., Webster, S., Przhonska, O.V., Hu, H., Peceli, D., Ensley, T.R., Bondar, M.V., Gerasov, A.O., Kovtun, Y.P., Shandura, M.P., Kachkovski, A.D., Hagan, D.J., and Stryland, E.W.V., *Efficient Two-Photon Absorbing Acceptor-π-Acceptor Polymethine Dyes.* The Journal of Physical Chemistry A, 2010. **114**(23): p. 6493-6501.

252. Ahn, T.K., Kwon, J.H., Kim, D.Y., Cho, D.W., Jeong, D.H., Kim, S.K., Suzuki, M., Shimizu, S., Osuka, A., and Kim, D., *Comparative Photophysics of [26]- and [28]Hexaphyrins(1.1.1.1.1.1): Large Two-Photon Absorption Cross Section of Aromatic [26]Hexaphyrins(1.1.1.1.1.1).* Journal of the American Chemical Society, 2005. **127**(37): p. 12856-12861.

253. Drobizhev, M., Stepanenko, Y., Rebane, A., Wilson, C.J., Screen, T.E.O., and Anderson, H.L., *Strong Cooperative Enhancement of Two-Photon Absorption in Double-Strand Conjugated Porphyrin Ladder Arrays.* Journal of the American Chemical Society, 2006. **128**(38): p. 12432-12433.

254. Kim, D.Y., Ahn, T.K., Kwon, J.H., Kim, D., Ikeue, T., Aratani, N., Osuka, A., Shigeiwa, M., and Maeda, S., *Large Two-Photon Absorption (TPA) Cross-Section of Directly Linked Fused Diporphyrins.* The Journal of Physical Chemistry A, 2005. **109**(13): p. 2996-2999.

CHAPTER 5. SIMULATIONS AND ELLIPSOMETRY MEASUREMENTS TO ENABLE THEORETICAL UNDERSTANDING AND STATISTICAL ANALYSIS OF DIATOM PORE PATTERNS

5.1 Chapter Introduction

5.1.1 *Structure of C. Wailessii Diatom Frustules and High Index Replicas*

The entire structure of a complete *C. wailessii* diatom, depicted in Figure 5.1f, is characterized by two valves (a.k.a frustules) that are held together by a girdle band. Although porous structures are found on all parts of the diatom, the photonic-crystal-like patterns of the valves make them the component of interest for this dissertation and are thus isolated from other structural. Within the valve itself, multiple porous layers are found with holes of varying sizes depending on the layer in which they exist. The outermost layer of the diatom (i.e. the top and bottom most surface from Figure 5.1f), called the cribellum (not pictured), is located closely to the internal layer (cribrum) and possesses very fine holes (ca. 50 nm in diameter) spread seemingly ubiquitously over the entire layer surface. The inner cribrum layer, pictured in Figure 5.1h, contains a network of 200-300 nm diameter holes that are typically aligned vertically within the center of the large holes (ca. 1 µm diameter) in the inner-most layer, the foramen (pictured in Figure 5.1j – looking from the foramen side of the valve).
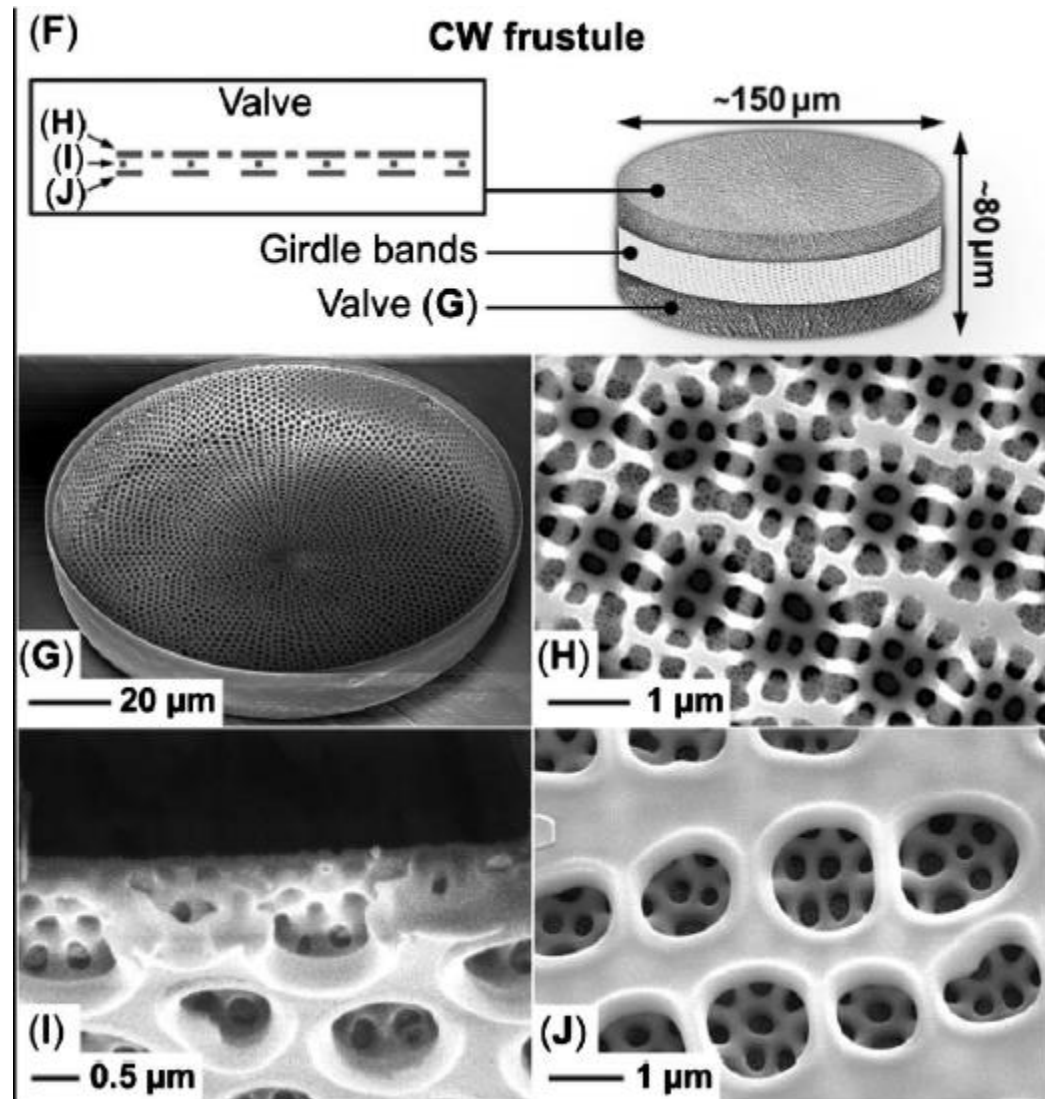
Figure 5.1. (f) Illustration of entire *C. wailessii* structure of for a fully intact valve; (g) SEM image of a single valve; (h) High magnification SEM of cribrum hole pattern; (i) Cross sectional SEM showing the cribrum, areola, and foramen layers; and (j) High magnification SEM of foramen hole pattern. Adapted from Romann *et al*. [126] with permission. Copyright 2015 Optics Letters.

The cribrum and foramen are separated by a support layer (Figure 5.1i), called the areola, which creates an air gap between the two hole-bearing layers. Although the thickness of each layer can vary frustule-to-frustule, even within the same growth batch, cross sectional SEM analysis of *C. wailessii* diatoms from this study were found to give typical cribrum and foramen layer thicknesses of 500 and 900 nm, respectively, with a 400 nm airgap that is the areola layer. Cribellum thickness is estimated to be ca. 50-100 nm, although this is difficult to quantify given the close proximity to the cribrum layer and the lack of index contrast when imaging with SEM.

As seen in Figure 5.1g, *C. wailessii* frustules are characterized by having a relatively flat surface in the center of the valve and then sharply curving upward at the edge, making a petri dish-like shape. The degree of curvature is also varies valve-to-valve. As will be discussed in this chapter, the variability in hole pattern structure is related to the entropy associated with their growth, which is determined by a multitude of factors. [255] Additionally, because experimental evidence suggests that the focusing effect is only observed when light enters the cribellum side and leaves the foramen side, all simulations and experiments will be conducted in this geometry. The majority of analyses in this chapter will assume that high index replicas of these structures perfectly preserve the layer and hole structure, unless otherwise noted.

5.1.2 *Hypothetical Framework for Beam Propagation and Diffraction at Through C. Wailessii Diatom Frustules*

Since there are multiple layers bearing high densities of holes in each frustule, an optical beam will undergo several light-matter interactions while propagating through this

structure. Since the focusing behavior of these valves is strongly suspected to be associated with the diffraction from the hole patterns from these layers, the description of optical waves propagating through the structure will be discussed in this context. However, it is noted that the transmission of light waves, particularly in transparent materials like silica, will also contribute to the interference pattern in the plane behind the frustule. As such, the thickness variations along the frustule valve can also result in a transmission phase grating-like effect. In terms of diffraction, the model is simplified by only considering the diffraction from the cribrum and foramen holes, for the sake of discussion (Figure 5.2).

Figure 5.2. Illustration of the propagation of diffracted waves through the cribrum and foramen layers of a model diatom frustule. The blue, red, and green wavelets from the cribrum represent the Fraunhofer diffraction happening from three different holes, whose wavefronts flatten into a plane wave prior to being diffracted again by the foramen.

Starting with the diffraction coming from the cribrum layer (bottom Figure 5.2), the ca. 300 nm diameter holes strongly diffract the visible-NIR wavelengths of interest (550-1050 nm) resulting in multiple wavelets generated by the closely clustered holes in

this layer. Remembering the rule of thumb for Fraunhofer diffraction ($R > a^2 / \lambda$), where R here is the distance between the cribrum and the foramen layer (ca. 400 nm) and a is the diameter of the foramen holes (ca. 300 nm), indeed, Fraunhofer diffraction is expected in the distance between the cribrum and the foramen given the calculated values of a^2 / λ were in the range of 86-163 nm. Under this assumption, by the time the waves reach the foramen layer, the wavefronts have become plane waves and can be likened to an unimpeded beam coming from a far away, coherent point source. Based on this assumption, the diffraction contributions from the cribrum layer are ignored as the memory of this diffraction event is thought to be lost when the broadened plane waves are diffracted again by the foramen holes. Further, this assumes minimal destructive interference and phase preservation by the wavelets from the cribrum such that the superposition of plane waves reaching the foramen layer is reasonably uniform in amplitude and phase.

Although the argument presented above is based on a high degree of approximation, it is done with the intent was to reduce the relevant structural variables of the diatom to a more manageable number for the ease of analysis while maintaining physical consistency. As such, the hypothetical picture of the frustule now considers only the diffraction from the hole pattern of the foramen layer. In terms of simulations and measurements, this approximation dramatically simplifies the structural components needed for simulations that improves computational efficiency, while simplifying the analysis for interference effects. In this chapter, analysis will be presented for the theoretical aspects of diatom focusing behavior working under the structural assumptions discussed here. Additionally, these simplifications will enable the parameterization of hole patterns that is crucial for

quantitatively understanding the influence of hole arrangements on the observed optical properties.

5.2   Image Processing and Statistical Analysis of Foramen Hole Patterns

5.2.1   *Background and Experimental Approach*

Since diatoms are naturally-derived structures from a living organism, frustule-to-frustule variations in the photonic crystal-like hole patterns are inevitable. In terms of their optical properties, this presents complications that preclude one's ability to straightforwardly compare these interference phenomena with man-made photonic crystals that are experimentally and theoretically understood. Additionally, this appreciable variability makes comparisons difficult even between diatoms of the same growth culture, which raises questions about the generality of the observed focusing seen from diatom frustules to-date. For *C. wailesii* diatoms, regions in the center of the foramen layer for a given frustule appear to have pseudo-hexagonal hole patterns (Figure 5.1g,j) with a significant density of holes over the entire surface (on the order of 1000 total holes). [127] However, to the best of the author's knowledge, there is no clear mathematical relationship describing this pattern which, fundamentally, is the origin for the ambiguity in their optical behavior. Therefore, to better understand these biophotonic systems, it is necessary to parameterize the hole patterns so that a numerical quantity can be obtained and used to compare the hole pattern structure of diatoms to each other and other photonic systems. In this way, one can potentially determine how structural changes might affect the interference behavior of these diatoms quantitatively and also obtain a sense of how these frustules compare to state of the art metalenses. [107, 115]
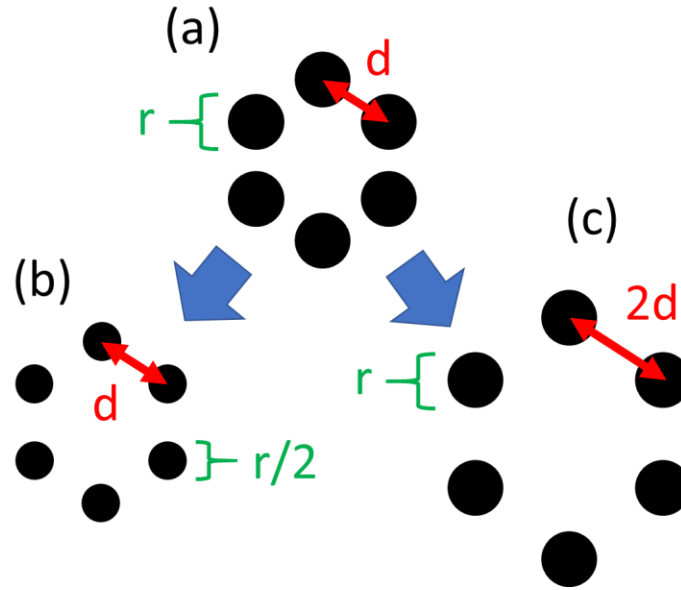
Figure 5.3. (a) Hexagonal array with hole-to-hole spacing (d) and hold size (r); (b) Hexagonal array with same d as part "a" but holes are half the size; and (c) Hexagonal array where d is twice as long but r is the same as "a".

The first step in this parameterization process is to define a limited number of physically-relevant quantities that are strongly tied to the interference pattern from a given frustule. This assumes the hole pattern itself is the governing factor for this behavior. To get a sense of the meaningful structural variables, one can consider the case of a small hexagonal array with six holes at each vertex that is illuminated by laser beam at an optical frequency (Figure 5.3). Recalling Young's double slit experiment (section 2.4.1), the distance between the slits of the diffracting screen determined the spacing between constructive orders of interference and thus determine how the secondary wavelets interfere in the far field behind the screen. An analogous situation can be found with hexagonal arrays (and thus pseudo-hexagonal hole patterns from frustules) with circular holes (apertures), where the spacing between holes (d from Figure 5.3) will ultimately

determine the distance at which the secondary wavelets achieve maximum constructive interference and produce a local intensity maximum, reminiscent of a focal spot.

The second parameter for consideration is the size of each hole (aperture) which, as shown in the discussion of Fraunhofer diffraction (section 2.4.2), heavily impacts the curvature of the secondary wavelet diffracted by a hole and thus how quickly wavefronts flatten and interfere in the far field behind the frustule. To simplify the analysis related to this parameter, all holes in the foramen layer are considered perfectly circular, which allows for one to directly correlate hole size with a radius. It is noted that, clearly, not all holes from the foramen layer are perfectly circular. However, inspection of the diatom structures of interest for this study show that the vast majority of holes are, indeed, circular enough to justify this assumption. Referring to Figure 5.3, one can anticipate that the circularity of secondary wavelets will be greater for smaller holes than large ones, suggesting that wavefronts will flatten less rapidly for pattern "b" than "a" and thus influence the spatial overlap in the somewhat near field.

Although the suggested parameters (radius and hole-to-hole distance) are straightforward conceptually, the calculation of these parameters is considerably difficult because of the variability in each structure and because these values must be determined experimentally based on images of the frustules. Additionally, due to the large numbers of holes, finding the center of each hole and then calculating the distance between them manually becomes prohibitively time-consuming. Therefore, it is desirable to rapidly calculate these quantities computationally; preferably using the information available from a hole pattern image to do so. The literature on such methods is sparse, however, in a report by Cohoon *et al.* [256], the computational mapping of diatom hole patterns was presented.

As seen in Figure 5.4, judicious image processing and analysis allowed for the extraction of hole-to-hole distances for multiple diatom species using a Delaunay triangulation algorithm to find the nearest neighbor connectivity between holes and build histograms of the distributions of edge lengths. Although the method of locating the centres of each hole was not specified in that study (assumed to be done manually), it is the rate limiting step for this pursuit since the center locations must be obtained prior to triangulation. Additionally, only limited results were provided to discuss the fitting of statistical distributions to the obtained data and whether these statistics could enable a descriptive or possibly even inferential understanding of these systems. Further, obtaining a distribution of radii is also of interest because of the wealth of information they could provide in terms of how hole size varies diatom-to-diatom and between native frustules and higher index replicas.
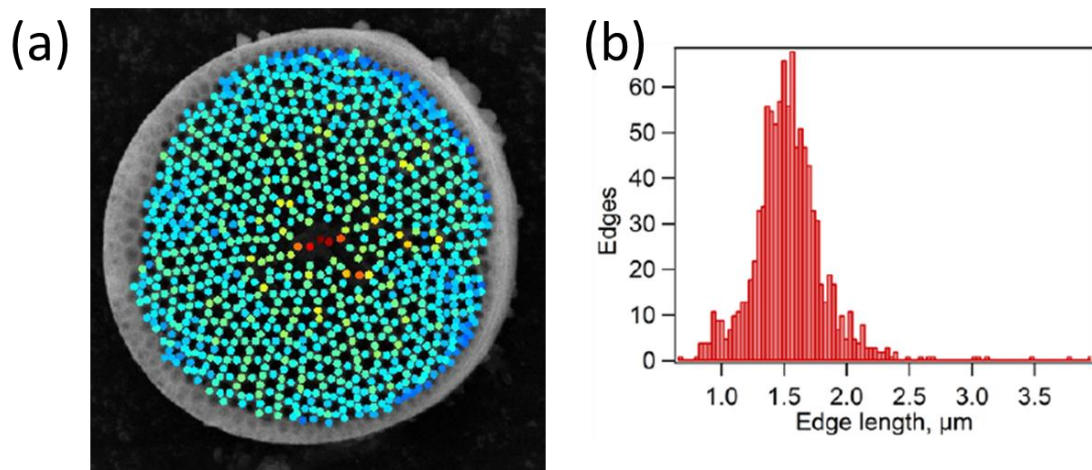
Figure 5.4. (a) Point heat map overlaid with the original *C. radiatus* diatom image, where each point corresponds to an edge and the color corresponds to the distance between each hole center; (b) Histogram of edge lengths obtained from Delaunay triangulation on diatom image "a". Reproduced from Cohoon *et al.* [256] with permission. Copyright 2015 Proceedings of SPIE.

In the following sections, the development and implementation of a program for rapid hole center location and hole-to-hole distance calculation is discussed in detail. The utility of Circular Hough Transforms for circle detection from SEM images of hole patterns will be explored, as well as the success with which the data it yields can be used for triangulation for determining hole-to-hole distances. Although further elaboration on the success of these methods will come after experimentation, compared to other approaches like image cross-correlation, this method provides inherently provides a more direct method to extracting the two physical quantities of interest (radius and hole-to-hole distance) due to the availability of straightforward functions in Matlab to perform these operations.

5.2.2   *Results and Discussion*

5.2.2.1   Hole Identification and Radius Estimation via Circle Hough Transforms

The foundation for rapid, programmatic identification of diatom holes (assumed perfect circles for the sake of this discussion) with foramen patterns is contained within a feature detection algorithm called a Circle Hough Transform (CHT). [257, 258] This algorithm is one of a variety of specialized Hough Transforms, which focuses solely on detecting circles, even among images containing other shapes and noise. CHTs are not rigorously specified algorithms and can be implemented in a number of ways. For this study, the phase-coding CHT built into the "imfindcircles" function in Matlab2017b was used. [259] Edge detection is a critical part of this function, which uses the pixels at the edge of a given circle to solve for the center location and the radius of each circle. This algorithm works best when circle edge pixels are step edges, that is, there is a large

226

difference (high gradient) between the brightness of the foreground in the immediate area around the circle and the circle edge itself. With regards to diatom images, this is achieved by optimizing the contrast of SEM images such that the foreground (the foramen) material is bright and the holes are as dark as possible. Prior to hole detection, it is necessary to binarize the grayscale image obtained from SEM to create this step function, this is illustrated in Figure 5.5a-b showing a high-quality grayscale SEM image of a section of foramen holes and the resulting binary image. [258, 259]
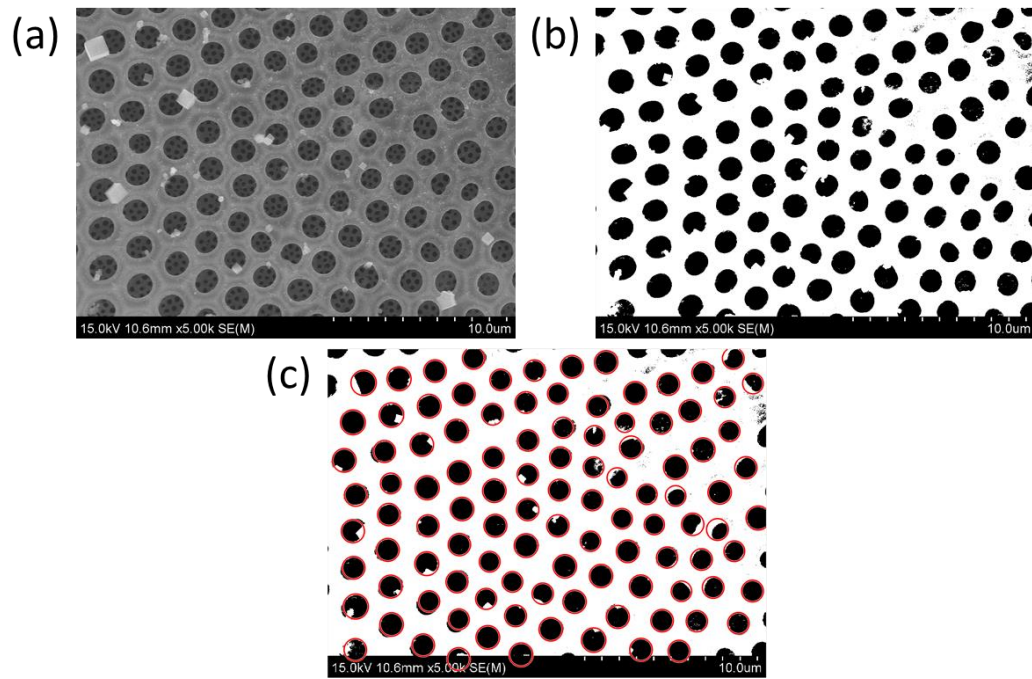
Figure 5.5. (a) Gray scale SEM image of MgO/Si replica foramen holes; (b) Binarized image of "a"; and (c) Estimated circle sizes and locations (red circles) overlaid on real, binarized holes.

For this variant of the CHT method, there are three main steps involved in the computation of hole locations and radius estimation. In the first step, foreground pixels with high contrast are chosen as candidate pixels that are allowed to cast "votes" in the accumulator array. This process is illustrated in Figure 5.6a, where a pixel along the edge

of a high-contrast circle (solid, black line) is used as the basis for a voting pattern (dashed line) with "votes" (red dots) cast at specific points along its perimeter that are compiled into an accumulator array, which records the votes at specific locations in the image. [259] For the second step, when this voting system is repeated for multiple pixels around the edge of a real circle, one obtains an accumulator array with a local maximum (green dot in Figure 5.6b) resulting from overlapping "votes" that are used to determine the center location of the circle. For the phase-coding method, complex values are used in the accumulator array with radius information encoded in the phase of array entries, which means that "votes" cast by the edge pixels contain information not only about center locations but also the radii of the circle associated with the center locations. Therefore, the third step is decoding the phase information from the estimated center location in the accumulator array to obtain the radius data. [257] Programmatically, the radii of a collective set of holes are found by specifying a narrow range of radii within the "imfindcricles" function, which is then encoded into the phase information while the CHT operates on the data set. The length of time required to optimize this process depends greatly on image contrast and hole shape uniformity, however, a typical run takes approximately 10 minutes; enabling the detection of many holes over a short period of time. Indeed, results for a successful hole detection and location for ca. 100 foramen holes on a MgO/Si diatom replica are shown in Figure 5.5c, where the red circles symbolize the computed hole location and radius, and are overlaid on top of the real, binarized holes. It is noted that, to reduce ambiguity in data analysis, the definition for radius is the radius of the computed circle used to estimate the size and location of a real hole.

Once satisfactory hole detection parameters are found, the hole center locations and radii are stored in arrays can be used for additional calculations or the construction of histograms for statistical analysis. As will be discussed in the following chapters, hole center locations are fed into a Delaunay triangulation algorithm to obtain nearest-neighbor distances between holes. Additionally, statistical analysis of the radii distribution for a larger data sets will be used to quantify variations in hole size from diatom-to-diatom, between diatoms of different materials, and even different areas within the foramen layer of the same frustule.
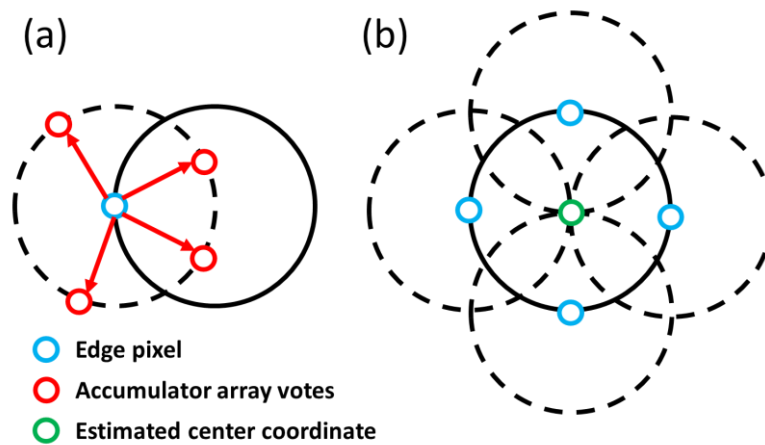
Figure 5.6. (a) Candidate edge pixel (blue dot) lying on an actual circle (solid line) and the voting pattern (dashed line) where, at points along the voting pattern, "votes" (red dots) are cast; and (b) Candidate pixels (blue dots) on the edge of a real circle whose collective voting patterns result in a maximum in the accumulator array at the center coordinate of the circle (green dot).

5.2.2.2   Obtaining Hole-to-Hole Distances via Delaunay Triangulations

With an array of hole center locations in-hand, these values are run through a 2D Delaunay triangulation (DT) algorithm to establish the connectivity pattern between holes from the SEM images and extract hole-to-hole distance information, requiring only

seconds of computing time from a moderately powerful laptop (Lenovo ideapad 750 with an Intel CORE i7 processor). DTs have been used extensively in scientific computing, primarily due to its ability to connect data points in a nearest-neighbor fashion. [260, 261] This is of interest for analysing diatom hole patterns, because the quantity of interest for this investigation is, indeed, the nearest-neighbor distances between holes in the foramen pattern. For 2D data, this method operates under the Delaunay criterion, otherwise known as the empty circumcircle criterion, which demands that a circle overlapping with three vertices in a triangle cannot contain additional vertices from adjacent triangles within its interior. [261] An example of samples that follow this criterion are illustrated in Figure 5.7a-b, where in "a" the triangle T1 is shown to obey this criterion as vertex V2 is left out of the circle interior. The same is true of "b", where vertex V1 is left out and thus triangle T2 follows the criterion. Further, examples of non-DTs are presented in Figure 5.7c-d.
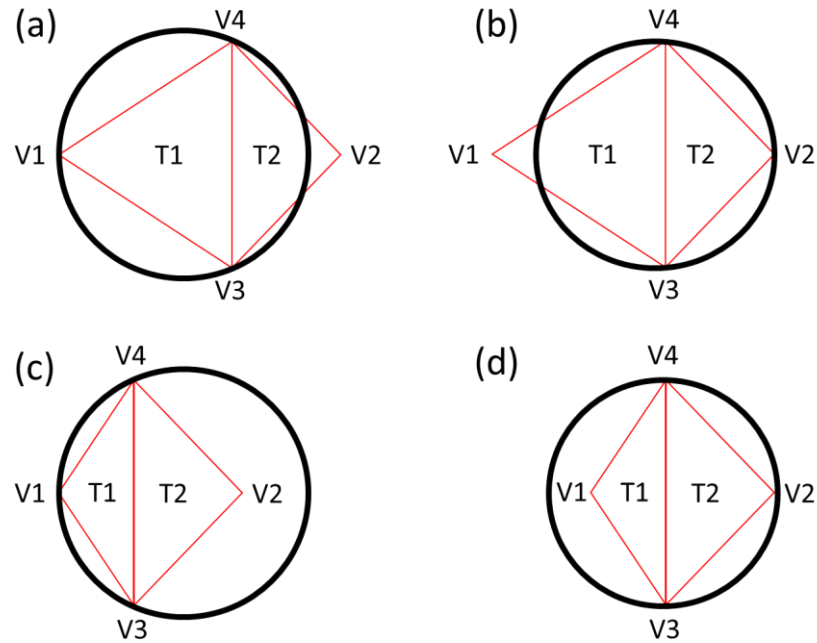
Figure 5.7. Illustration of (a) T1 obeying the Delaunay criterion; (b) T2 obeying the Delaunay criterion; (c) T1 not obeying the Delaunay criterion and; (d) T2 not obeying the Delaunay criterion.

By applying the triangulation to an array of holes, one can visualize the nearest-neighbor connectivity between closely-spaced foramen holes. This is depicted in preliminary results from Figure 5.8a-b, where the edges (red lines) connecting the center points (green dots) of adjacent holes are overlaid with the binary and original SEM images, respectively. From those overlays, it is evident that the good quality binarization enabled accurate estimates of hole center locations and thus the clear connectivity between holes in the center of the image with pseudo-hexagonal periodicity. It was noted that a few instances of holes that were partially covered by debris (primarily MgO crystals left over from reaction) still yielded accurate hole location and thus were able to participate normally in triangulation. This was attributed to the quality of the part of the edge that was cleanly imaged; allowing a critical mass of "votes" to build a reliable accumulator array. This

observation demonstrates the usefulness in this method utilizing the edge pixels of holes to determine center locations for imperfect holes, and thus the eventual connectivity obtained via triangulation. There are limits to this, however, as seen by small sections of holes that are largely out-of-frame that went undetected. Additionally, because a radius range must be specified for identification, extremely small and large holes (relative to average hole size) will not be detected.

It was noted that the connections between holes close to the edge of the image were not always between nearest-neighbors, which resulted in inflated edge lengths without physical significance in these regions. These non-physical edges, as well as the physically-relevant ones in the center of the image, were stored in an array containing the edge length information for each connection from a given sample. As will be discussed in the following section (5.2.2.3), and in further detail in sections 5.2.2.3-5.2.2.21, careful analysis of the distributions obtained from these data sets will be used to statistically quantify the meaningful structural parameters (i.e. hole radius and edge length) for a given diatom frustule or high index replica.
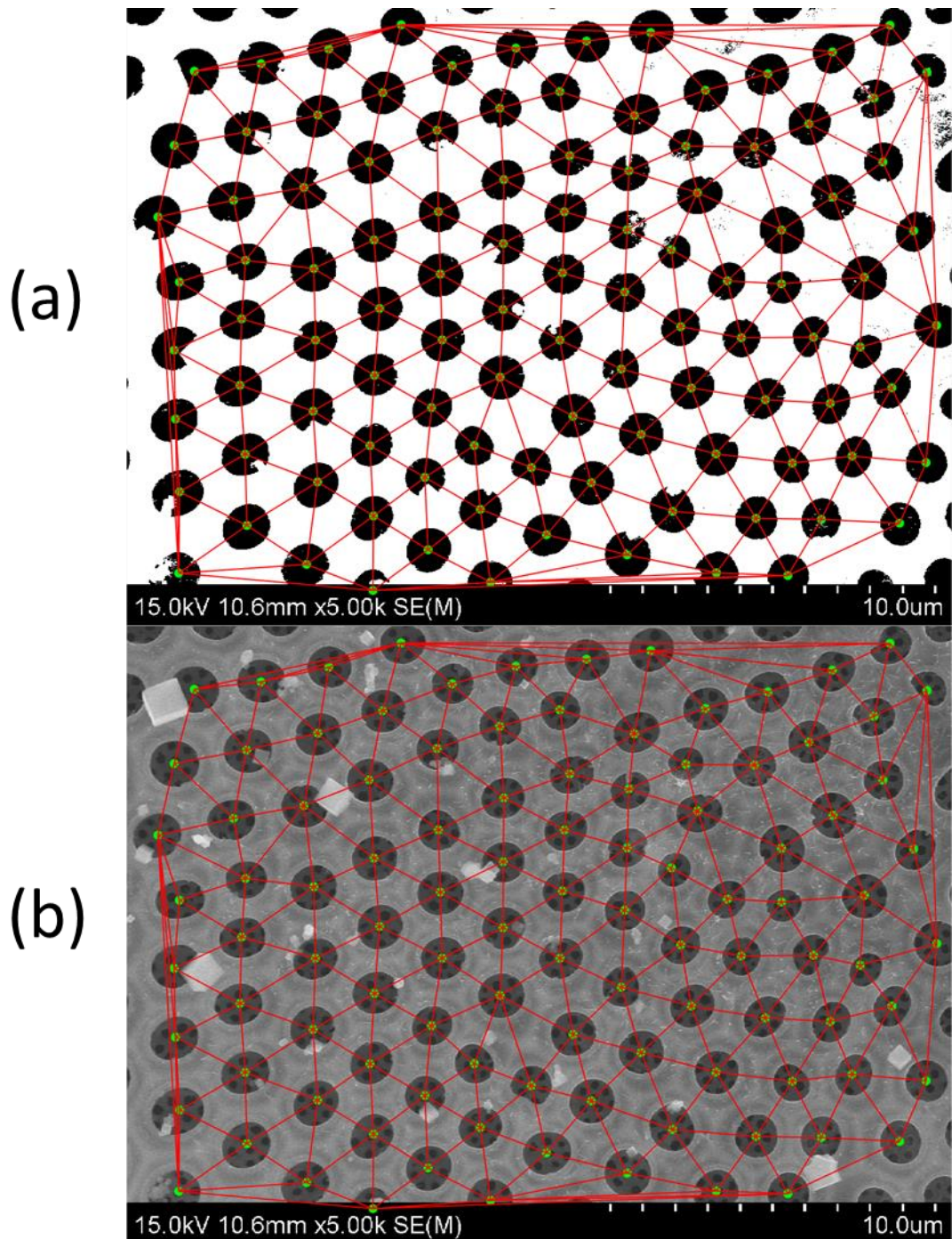
Figure 5.8. (a) Binary image with no additional processing of a MgO/Si foramen pore pattern overlaid with edge lengths (red lines) and hole center locations (green dots) derived from CHT hole detection and Delaunay triangulation; and (b) The same overlay as in "a" but with the original SEM image showing reasonably accurate estimations of hole centres and connectivity between adjacent holes.

233

5.2.2.3   <u>Statistical Analysis of Diatom Hole Radii and Edge Lengths</u>

Since diatoms have many foramen holes (ca. 700-900), the approach to statistically analysing these patterns is focused on obtaining large sample sizes, thus taking advantage of this naturally occurring phenomenon. As demonstrated in previous sections, the CHT and DT methods allowed for rapid radius and edge length quantification for a moderately large number of holes (ca. 100) within an imaging area of limited size. Although this can provide substantial preliminary data, the goal of this study is to obtain as much information as possible about the entire hole pattern of the foramen layer for a given diatom frustule or replica. This, however, presents a challenge from a hole detection point of view given that, for large area images, the resolution of the image is lower than what is required to accurately determine hole centre coordinates and estimate radii. To circumvent this issue, diatoms were divided into four quadrants, as illustrated in Figure 5.9, at an imaging resolution (ca. 20-40 nm/pixel) that is sufficiently accurate for use of CHT and DT that simultaneously allows for a larger number of holes to be analyzed in a single image.

After analysis, the results from each quadrant are then combined in a single array from which a population is built that is characteristic of the pore pattern that encompasses the entire foramen layer. Practically, the mapping of the entire pattern can be complicated by image quality, primarily as a function of illumination uniformity. This is particularly problematic for holes near the edge of the frustule where *C. Wailessii* diatoms, no matter the material, have significant curvature and typically exhibit excessive and/or nonuniform brightness relative to the rest of the frustule when imaged by SEM (e.g. Figure 5.9). Thus, upon binarization, these holes are typically lost to the foreground. Despite the loss of edge holes, a typical CHT run will yield 700-800 holes, although some exceptions exist (see

section 5.2.2.20 for details). Although it is difficult to quantify the percentage of holes lost due to these issues, visually (Figure 5.9), one can see that the vast majority of holes closer to the frustule interior have sufficient contrast to be successfully located by CHT.
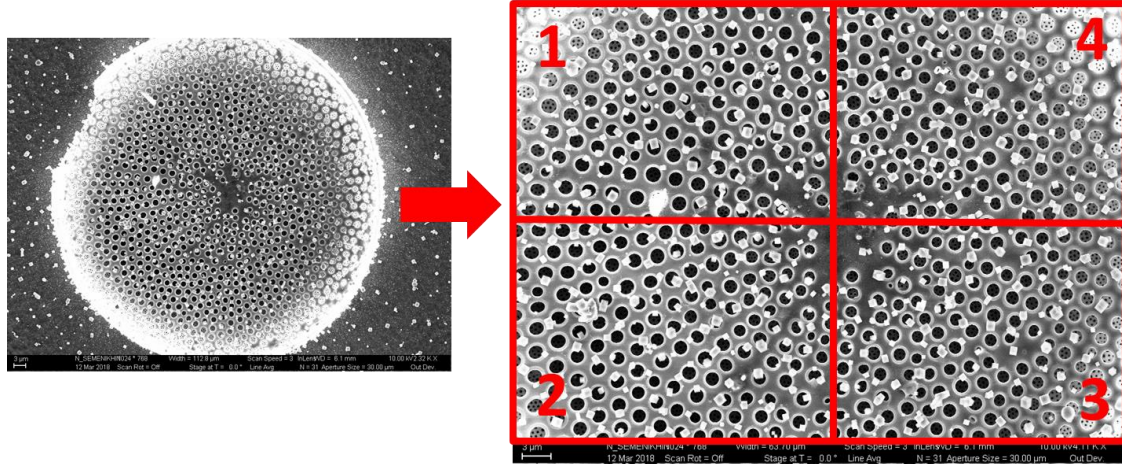
Figure 5.9. Diagram depicting the sectioning of the foramen layer from an MgO/Si replica into four quadrants with higher magnification/resolution than a larger area image.

Since distributions of data tend toward normality with large sample sizes, preliminary statistical analysis for radii and edge length data sets will be fitted with a normal distribution, the parameters for which are described by [262]

$$f(x, \mu, \sigma) = \frac{1}{\sqrt{2 \pi \sigma^2}} \, exp\left(\frac{-(x - \mu)^2}{2 \, \sigma^2}\right) \tag{5.1}$$

where μ is the mean of the sample, σ is the standard deviation, and x is the value of a random sample. Further, the higher order moments of the normal distribution, such as skewness and kurtosis, provide measures of data asymmetry about the mean and "tailedness", respectively. An univariate, perfectly-symmetric, normally distributed data set will give a skewness of 0 and a kurtosis of 3, which allows one to use any deviations

from these values to quantify how far the distributions stray from normality. [262] If the distributions approach normal for all samples, the mean and standard deviation from this analysis will yield parameters that can be used to compare the dimensions of the pore patterns between diatoms.

Looking ahead, one can anticipate that edge lengths obtained via triangulation may give asymmetric distributions that cannot necessarily be assumed to adhere to a specific parametric distribution. Although the nonphysical edges will likely be a significant contributor to this, other structural factors such as vacancies (i.e. a missing hole with a dense pattern of holes) can also induce asymmetry by locally increasing the hole-to-hole distance of edge lengths associated with that groups of holes. Likewise, if severe asymmetries are present in the radii data, it is better to accurately fit this data and obtain an empirical estimate of the most probable radius value based on the entire distribution that can be obtained independent of symmetry rather than relying on values extracted from a poorly fitting normal probably density function (PDF). This issue can be overcome using a Kernel Density Estimator (KDE), which for a univariate random sample $(X_1, \ldots, X_n)$ is described by [263, 264]

$$g(x, h) = \frac{1}{nh} \sum_{i=1}^{n} K\left(\frac{x - X_i}{h}\right) \tag{5.2}$$

where the kernel (K) is defined as

$$K = \frac{(1 - x^2)^p}{2^{2p+1} B(p + 1, p + 1)} \{|x| < 1\} \tag{5.3}$$

and B is comprised of gamma functions, e.g. $\Gamma(a)$:

$$B(a, b) = \frac{\Gamma(a)\Gamma(b)}{\Gamma(a+b)} \tag{5.4}$$

$$\Gamma(a) = (a-1)! \tag{5.5}$$

In equation 5.2, h, called the bandwidth, is parameter that controls the degree of smoothing applied to obtain a continuous PDF. The power of this method is that it is non-parametric and solves for the PDF taking local features in a histogram into account such that asymmetry or even subtle changes in the data set can be fit accurately. Although various kernels exist, the Epanechnikov kernel (i.e. $p = 1$) is the most efficient due to its ability to minimize asymptotic mean integrated square error (AMISE) and was therefore used in this investigation. [263] Substituting $p = 1$ into equation 5.2, the Epanechnikov kernel (K_{Ep}) is expressed as:

$$K_{Ep} = \frac{3}{4}(1-x^2)\,\{|x| < 1\} \tag{5.6}$$

The application of the KDE method to radius and edge length distributions obtained via CHT-DT is discussed in detail in sections 5.2.2.5-5.2.2.20 and Chapter 6. Analysis will be provided about the accuracy, precision, and trends found in the data, and whether these statistics are descriptive or can be used inferentially.

5.2.2.4 Metallization of Silica Diatoms for High Contrast Imaging

As mentioned previously, achieving high-quality binarized images of the foramen hole patterns are crucial to the success of hole identification and triangulation procedure.

Since MgO/Si and Mg_2Si replicas contain higher atomic mass Mg, the backscattering is substantial and thus obtaining high contrast SEMs, i.e. dark holes with bright surface of the foramen, can be accomplished with relative ease. Naturally, this is not the case with the native silica valves making high-contrast imaging difficult. Initial attempts to image native silica valves were done necessarily at high accelerating voltages and were plagued by charging that significantly distorted images. More importantly, because silica is not as conductive as the higher index replicas, charging can result in significant movement of the frustule about the substrate. In extreme cases, the frustule can move off the substrate entirely and is lost. To combat the charging effects, silica valves were coated with thin layers of Au/Pd (60/40 composition ratio) to enhance backscattering and conductivity (see experimental detail in section 6.6 for specifics of the deposition procedure). Since the sputtered film only deposits vertically onto the sample, holes of the foramen and inner layers visible through the foramen holes do not vary in size because of coating. The hole identification and triangulation results of these coated silica frustules and their non-coated high index replicas are presented in the following sections.

5.2.2.5   Silica Frustule 1

Visual inspection of the foramen hole pattern of silica frustule 1 (silica 1) in Figure 5.10 shows that the overall pattern within the inner half of the valve is semi-regular with reasonably circular-shaped holes. Towards the edge there were an appreciable number of defects, primarily missing holes, resulting in a much lower hole density toward the edge of the valve. However, despite the missing holes, the holes next to edge were regular in shape and provided good contrast for binarization and thus were located accurately. Although there seemed to be more significant curvature at the top right edge of the frustule,

appreciable curvature was generally not seen until just before reaching the edge. In addition to the even illumination of most of the foramen, these observations suggest that this valve was relatively flat, which allowed for successful hole location and triangulation with only a few instances of missed holes and one instance of overcounting an oblong hole.

Figure 5.10. Large area image of entire foramen hole pattern for silica 1 made from stitching all four individual quadrants. SEM images by Nikolay Semenikhin, Sandhage Group, Georgia Tech.

The radius distribution from this analysis (Figure 5.11) gave a symmetric histogram that was fit well by a normal PDF with the mean and standard deviation (0.64 ± 0.05 µm) comparable to that of Silica 1. Further, this fit is justified by the calculated kurtosis of 3.59, somewhat close to the ideal value of 3 for normally distributed data sets. Unsurprisingly, the most probable radius obtained from the KDE is only slightly higher than the normal

mean, consistent with the slightly positive skew (0.18) for this sample. However, given that the resolution of the image was ca. 40 nm, radius values are rounded to the hundredths place and thus the results from the normal fit and KDE are identical.

Figure 5.11. Histograms of (a) hole radius distribution (blue) fit by a normal PDF (b) hole radius distribution (green) fit by Kernel PDF (c) edge length distribution (red) fit by Kernel PDF for Silica 1.

Turning to the edge length distribution (Figure 5.11c), a sharp peak followed by a slowly decaying tail toward longer edge lengths was found. Although the histogram is plotted to 6 µm, there were edges obtained from triangulation at greater lengths. This is partially due to non-nearest neighbor edges between holes at the edges whose actual neighbors are washed out of the image by poor contrast, cannot be seen due to curvature,

or are misshapen and cannot be identified. Since the triangulation algorithm will establish connections between all data points, these edges are obtained and present a set of non-physical edge lengths that are far separated from the physically meaningful edge lengths plotted in Figure 5.11c. Inflated edge lengths can also be found in the center of the frustule where nearly all frustules have significantly less hole density and thus greater separation between holes that are typically located easily during circle finding. Accounting for this separation, it was determined that any two holes that are separated by a distance greater than 10 µm cannot be considered nearest-neighbors. This constraint was applied when making the histogram where edge lengths >10 µm were omitted from the distribution. A bin size of 133 nm (75 bins) was chosen to yield a smoothly evolving histogram. This plotting method was applied to all subsequent samples, as will be shown in the following sections.

Since the edge length distribution is asymmetric – the long tail of which is ascribed to an appreciable number of slightly longer edges caused by missing holes and other real structural defects – and it is not clear that the data gives two clear modes that could be fit individually, it cannot be assumed that it adheres to any particular symmetric, parametric statistical distribution, such as the normal distribution. Although there are parametric distributions that could be applied to reasonably fit an asymmetric data set, such as a skew normal, beta or gamma distribution [265], the quantity of most interest is the most probable edge length that one can extract from any continuous distribution that well fits the data set. This was achieved by a KDE function in Matlab2017b©, which estimates the PDF of the distribution using a small number of parameters (see section 5.5.1.2 for discussion on KDE) with computational ease. Using the suggested bandwidth parameter within the

Matlab2017b© algorithm, a smooth, nicely fitting PDF is obtained that fits well to all parts of the edge length distribution plotted in Figure 5.11c. It is stressed again that the statistics obtained for this diatom and others will be more descriptive than intuitive as the goal of this algorithm is to obtain a semi-quantitative estimation of whether there are significant differences (i.e. differences beyond the resolution of the images) between frustules of the same material and replicas of different materials. However, from these Kernel-estimated PDFs it is possible for one to obtain relative information about the edge lengths in the event that tails become pronounced or other modes appear in the distribution. In this regard, the asymmetry of the distribution will be closely monitored in subsequent diatom samples to determine the relative population of hole pairs resulting in larger edge lengths that may be the result of missing holes or structural defects.

5.2.2.6 Silica Frustule 2

Compared to Silica 1, this frustule (Figure 5.12) did not provide the same level of contrast, which required careful tuning of the binarization threshold. Due to the similar grayscale value between holes and the foreground of the foramen, it was necessary to keep the threshold of the binarization low to not remove too many edge pixels from holes. As anticipated, with such a low threshold comes noise from the uneven illumination of the foramen surface. Before going through the trouble of attempting to subtract this noise from the image, the hole detection routine performed to determine how accurately it could find and locate holes with significant background. Surprisingly, hole detection was largely successful, although several holes were missed due to poor circularity or covered by debris rather than lacking contrast from the foreground or not being distinguishable from

background nose. There were also seven instances of overcounting holes between the top

right and bottom right quadrant due to large oval-shaped or conjoined holes.

Figure 5.12. Large area image of entire foramen hole pattern for silica 2 made from stitching all four individual quadrants. SEM images by Nikolay Semenikhin, Sandhage Group, Georgia Tech.

Despite the lack of contrast and presence of misshapen holes, the radius distribution

yielded a somewhat symmetric histogram (Figure 5.13a) that was reasonably fitted by a

normal distribution (0.66 ± 0.07 µm) which is also reflected by the approximately

Gaussian-shaped PDF estimated by the Kernel method. The edge length distribution

obtained from triangulation appears to be bimodal, with the primary peak centred 2.02 µm

as it was in Silica 1 (1.95 µm) and a pronounced shoulder centred at 3.4 µm rather than a

gradually tapering tail. The longer mode is clearly reflective of the many voids between

various groups of holes over the entirety of the foramen surface. Unsurprisingly, the peak height ratio of the short and long mode is ca. 2:1 given the number of vacancies and separated groups of holes on the frustule.

Figure 5.13. Histograms of (a) hole radius distribution (blue) fit by a normal PDF (b) hole radius distribution (green) fit by Kernel PDF (c) edge length distribution (red) fit by Kernel PDF for Silica 2.

5.2.2.7   Silica Frustule 3

Silica 3 was a good quality diatom (Figure 5.14) with relatively few vacancies compared to Silica 1-2 and maintained reasonable hole pattern uniformity even close to the edge. This pattern gave substantial contrast and even illumination, which made hole detection quick and accurate for all holes that were not misshapen or too small to fit

reasonably within the radius estimation range. The radius distribution (Figure 5.15a) obtained from this frustule gave a somewhat symmetric-looking histogram that that tended toward higher values. Despite this slight asymmetry, the mean obtained (0.62 ± 0.05 µm) assuming normality was only slight lower than the most probable radius estimated by the Kernel method (m), which is consistent with the small skew of -0.07 and kurtosis close to 3 (2.56). The edge length distribution for this frustule was similar to Silica 1 in that a smoothly varying band gave way to a slowly decreasing tail at larger values. However, the most probable edge length for this frustule (2.29 µm) was slightly higher than that than estimated for Silica 1-2.

Figure 5.14. Large area image of entire foramen hole pattern for silica 3 made from stitching all four individual quadrants. SEM images by Nikolay Semenikhin, Sandhage Group, Georgia Tech.

Figure 5.15. Histograms of (a) hole radius distribution (blue) fit by a normal PDF (b) hole radius distribution (green) fit by Kernel PDF (c) edge length distribution (red) fit by Kernel PDF for Silica 3.

5.2.2.8   Silica Frustule 4

Silica 4 (Figure 5.16) showed significant curvature at the edge as well as many misshapen holes at and approaching the edge. As such, the imaging method was modified to image a slightly smaller area in the center of the frustule with better illumination. Although the number of holes imaged was slightly lower than, e.g. Silica 1 and 3, this approach still allowed for the detection of 420 holes from which a reliable approximation of the radius and edge length distributions could be made. Since many holes were oval-shaped but still had decent contrast, there were 3 instances of overcounting with this frustule and several instances of missed holes, particularly ones near or at the edge) that

were misshapen. However, edge connectivity and circle finding in the center of the frustule
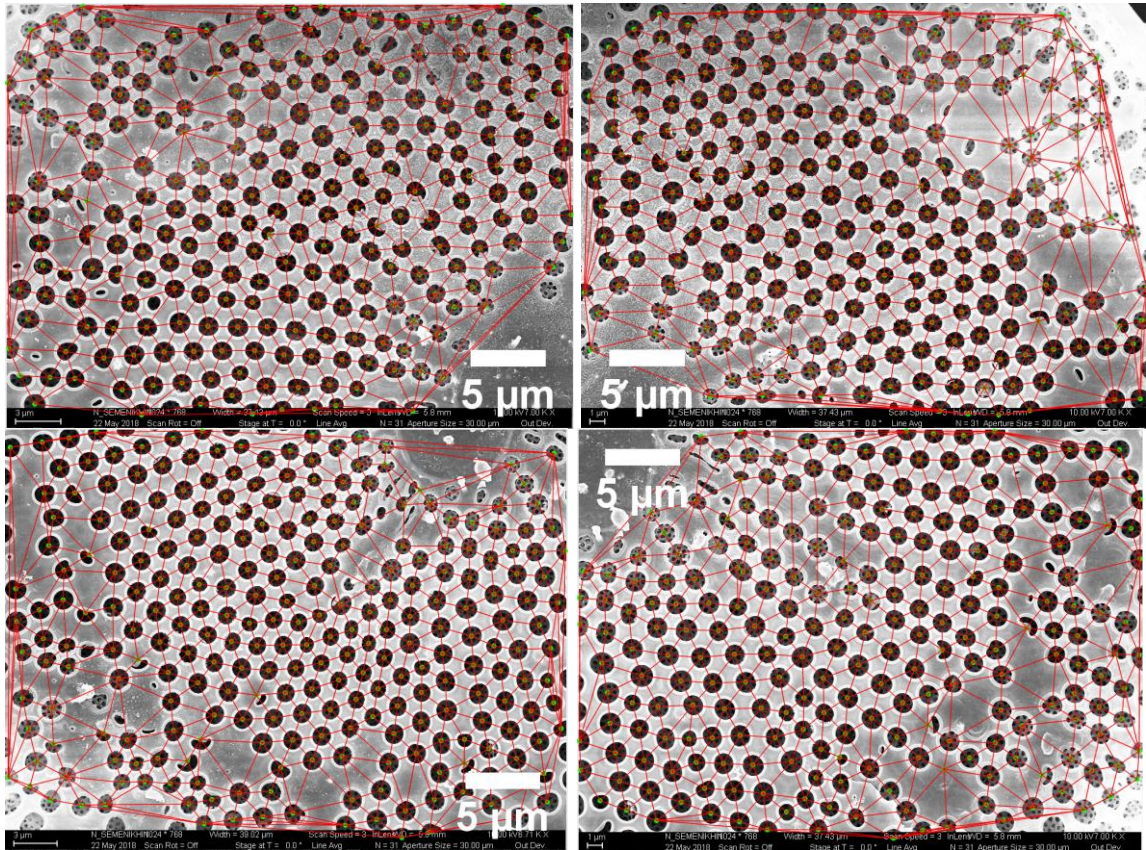
was comparable to Silica 1-3.

Figure 5.16. Large area image of entire foramen hole pattern for silica 4 made from stitching all four individual quadrants. SEM images by Nikolay Semenikhin, Sandhage Group, Georgia Tech.

Histograms depicting the radius distribution give a somewhat symmetric looking

histrogram that is fit well by a normal distribution (mean = 0.64 ± 0.06 µm and kurtosis =

3.29) with comparable mean radius to all silica frustules examined thus far. In terms of the

edge length distribution, Figure 5.17c shows, similar to Silica 2, a pronounced tail at larger

edge lengths is representative of the appreciable number of vacancies and holes with poor

contrast near the edge. Despite the many defects of this frustule the most probable edge

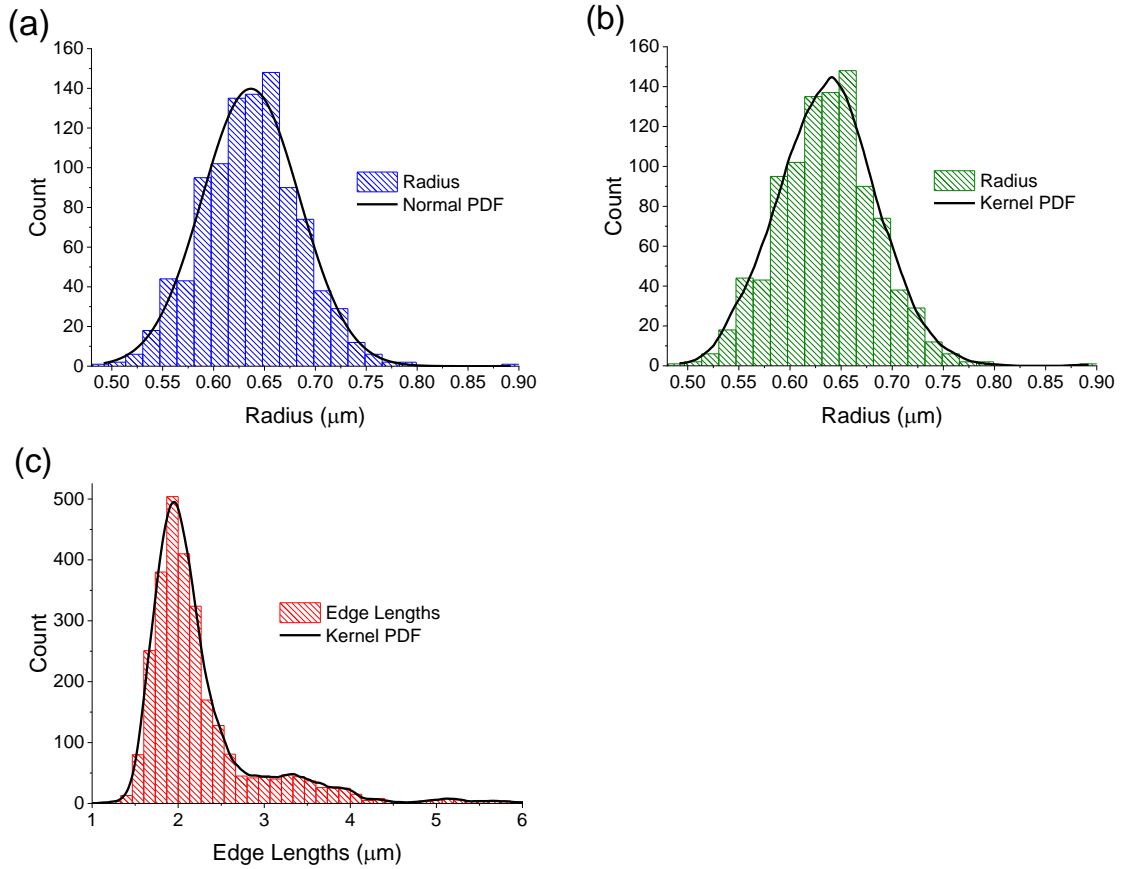length (1.91 µm) is comparable with values obtained for Silica 1-3.

Figure 5.17. Histograms of (a) hole radius distribution (blue) fit by a normal PDF (b) hole radius distribution (green) fit by Kernel PDF (c) edge length distribution (red) fit by Kernel PDF for Silica 4.

5.2.2.9   Silica Frustule 5

Overall, silica 5 (Figure 5.18) was a good quality frustule with a moderate number of vacancies and minimal surface debris, excluding the large chunk found in the lower left quadrant. The relative flatness of the diatom allowed for high contrast between the holes and foramen even close to the perimeter of the frustule. This facilitated the success of hole detection and location to where only a few instances of very small or irregular holes were missed with no overcounting. Analysis of the radius distribution (Figure 5.19a) gave a narrow, symmetric histogram with mean 0.67 ± 0.06 µm, which matches closely with the

most probable radius estimated by the Kernel method (0.68 µm). Further, the edge length

distribution was quite similar to previous frustules.

Figure 5.18. Large area image of entire foramen hole pattern for silica 5 made from stitching all four individual quadrants. SEM images by Nikolay Semenikhin, Sandhage Group, Georgia Tech.

Figure 5.19. Histograms of (a) hole radius distribution (blue) fit by a normal PDF (b) hole radius distribution (green) fit by Kernel PDF (c) edge length distribution (red) fit by Kernel PDF for Silica 5.

5.2.2.10 MgO/Si Replica 1

The first of the samples for a higher index replica, MgO/Si 1 (Figure 5.20) gave very dark holes but overall not substantial contrast between holes and the foreground. Additionally, there was some asymmetry in the curvature around the perimeter of the frustule which required some quadrants (lower left and right) to be taken at higher magnification to remove edge effects but still image a large number of holes. However, with careful thresholding during binarization, one can obtain binary images with sufficient contrast so that hole detection resulted in only a few instances of missed holes due to small

size or highly irregular shape. The radius distribution for this replica gave a symmetric distribution that was fit well by a normal PDF (kurtosis = 3.33) to yield a mean radius of 0.62 ± 0.05 µm, matching exactly with Kernel estimated radius and comparable to the average mean radius from Silica 1-5 (0.65 ± 0.02 µm).
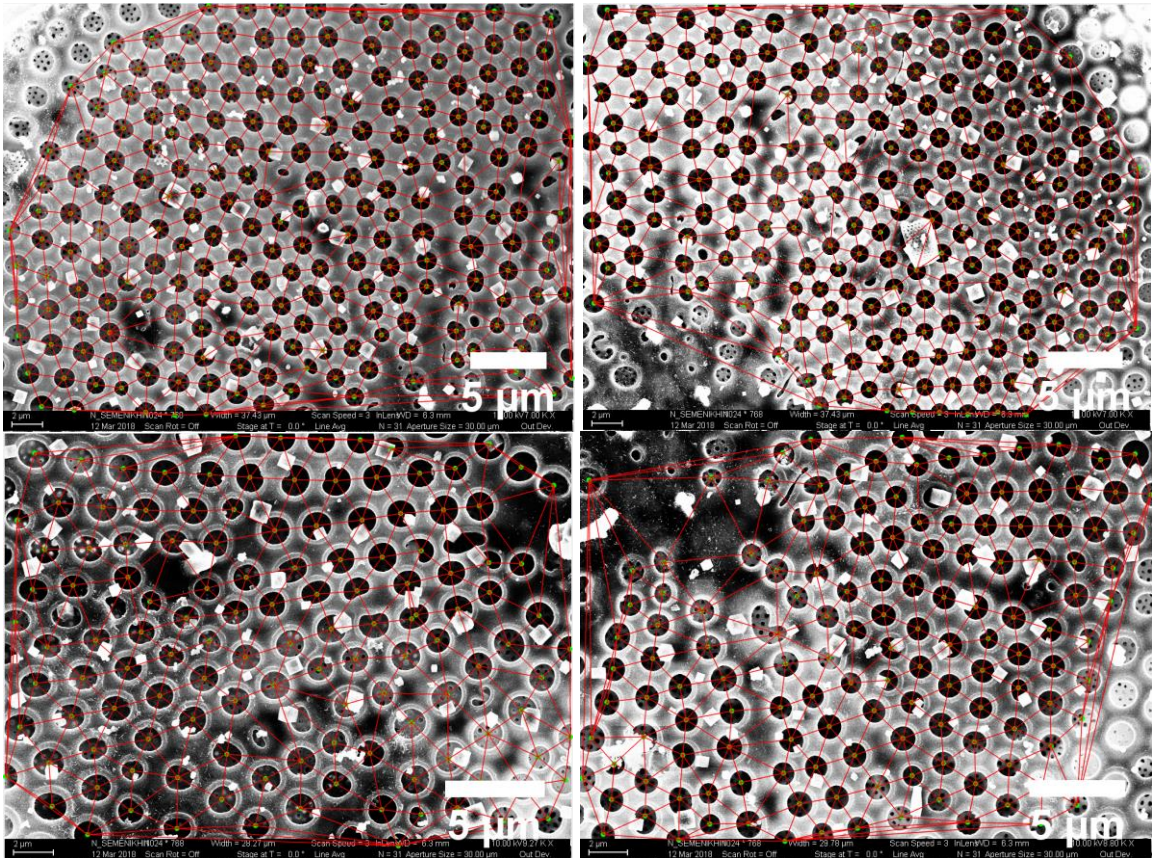
Figure 5.20. Large area image of entire foramen hole pattern for MgO/Si 1 made from stitching all four individual quadrants. SEM images by Nikolay Semenikhin, Sandhage Group, Georgia Tech.

The edge length distribution (Figure 5.21c) for this replica gave a smoothly-evolving asymmetric histogram, typical in shape to what was seen for silica frustules were a large, somewhat narrow peak centred at 2.07 µm gives way to a slowly decreasing tail at longer distances. This initial result shows that, so far, a good-quality MgO/Si replica has a similar mean radius and most probable hole-to-hole distances compared to silica frustules

251

(2.06 ± 0.14 µm). This trend will be further evaluated for the MgO/Si replicas in the following sections and later compared to the even higher index Mg$_2$Si replicas.

Figure 5.21. Histograms of (a) hole radius distribution (blue) fit by a normal PDF (b) hole radius distribution (green) fit by Kernel PDF (c) edge length distribution (red) fit by Kernel PDF for MgO/Si 1.

5.2.2.11 MgO/Si Replica 2

MgO/Si 2 (Figure 5.22) provided excellent contrast between holes and the foramen foreground, facilitating hole detection and providing good quality location with only 3 instances of overcounting when encountering oval-shaped holes and a few missed holes near the edge due to small size, poor contrast from curvature or misshapenness. This translated into symmetric radius histograms (Figure 5.23a) that were well fit by a normal

distribution (kurtosis = 3.01) to give a mean radius of 0.62 ± 0.05 µm. Further, the edge

length distribution showed a very minimal tail and gave a most probable edge length (2.05
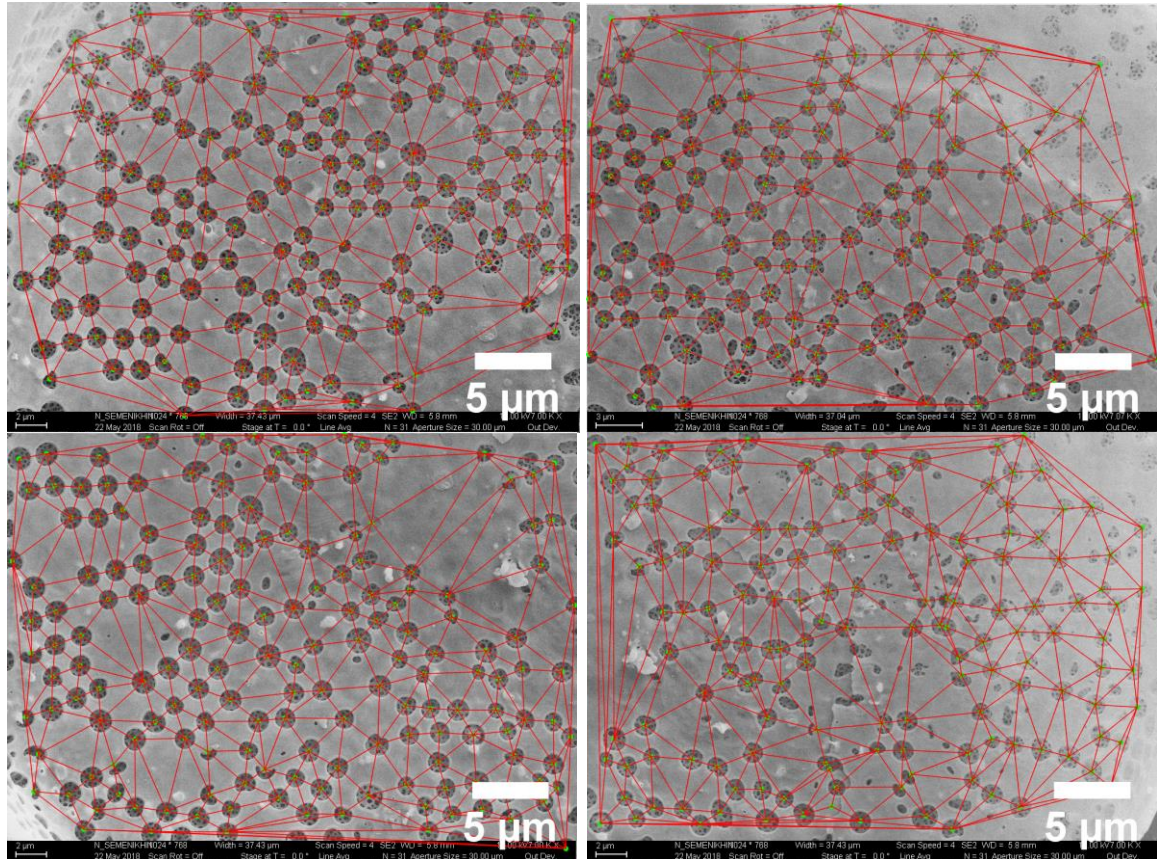
µm) comparable to MgO/Si 1 and the silica frustules.

Figure 5.22. Large area image of entire foramen hole pattern for MgO/Si 2 made from stitching all four individual quadrants. SEM images by Nikolay Semenikhin, Sandhage Group, Georgia Tech.

Figure 5.23. Histograms of (a) hole radius distribution (blue) fit by a normal PDF (b) hole radius distribution (green) fit by Kernel PDF (c) edge length distribution (red) fit by Kernel PDF for MgO/Si 2.

5.2.2.12 MgO/Si Replica 3

Similar to MgO/Si 2, MgO/Si 3 (Figure 5.24) gave images with nice contrast but

had significantly more curvature and thus less contrast toward the edge of the frustule. In

this case the smaller holes from the cribrum layer were still visible and with decent contrast,

which had the potential to complicate hole detection and skew the distribution. This was

avoided by carefully raising the binarization threshold so that only the darkest holes toward

the center of the frustule remained. Although this method worked well for this replica, one

must be careful not to raise the threshold so much that pixels at the edge of the holes closer

to the valve centre. If improperly adjusted, this could artificially make the holes appear small during hole detection and thus bias the radii toward smaller values. To make sure that the binarization was not biasing the radii, images of gradually increasing binarization thresholds were analyzed and their mean radii were compared to verify what threshold level was removing too many edge pixels from high contrast holes. This analysis yielded a somewhat symmetric histogram (Figure 5.25a-b) that appears to tend toward higher values. A mean radius of 0.61 ± 0.05 µm was obtained by fitting with a normal distribution (kurtosis = 2.78), which matched closely with the Kernel-estimated radius of 0.61 µm. Examination of the edge length histogram shows, much like MgO/Si 2, a smoothly-evolving peak (centred at 2.22) that gives way to a small but gradually decreasing tail.

Figure 5.24. Large area image of entire foramen hole pattern for MgO/Si 3 made from stitching all four individual quadrants. SEM images by Nikolay Semenikhin, Sandhage Group, Georgia Tech.
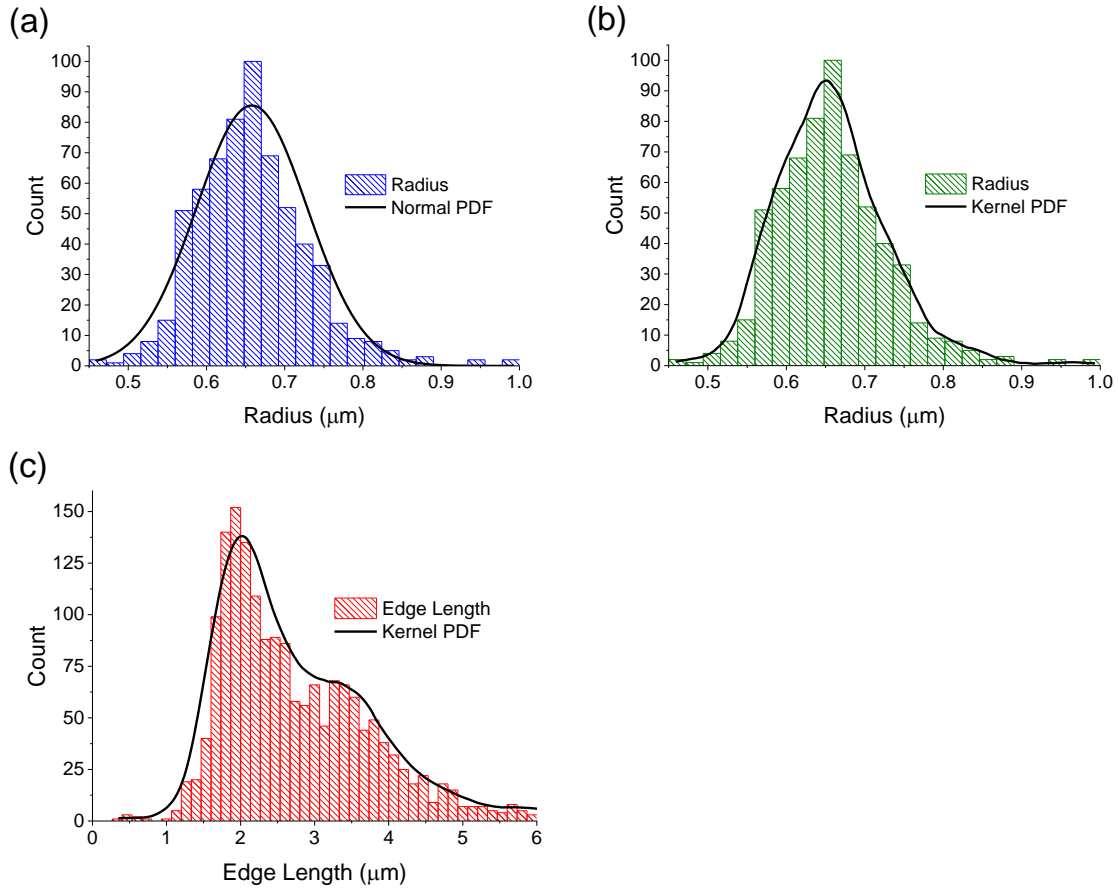
Figure 5.25. Histograms of (a) hole radius distribution (blue) fit by a normal PDF (b) hole radius distribution (green) fit by Kernel PDF (c) edge length distribution (red) fit by Kernel PDF for MgO/Si 3.

5.2.2.13 MgO/Si Replica 4

Overall, MgO/Si 4 (Figure 5.26) was a good quality replica with substantial contrast between hole and the foreground but suffered from inhomogeneous curvature that resulted in poor contrast for many holes imaged in the top right quadrant. Unlike MgO/Si 3, the cribrum holes in this quadrant did not have appreciable contrast and were largely removed during binarization. Additionally, most of these smaller holes had poor contrast and were not seen by the hole detection algorithm, minimising false positives. Despite this, the optimized hole detection parameters gave one false positive due to a grouping of dark

foreground pixels in the top left quadrant close to the center of the frustule. Outside of this false positive, hole detection was generally successful only missing seven irregularly large or small holes, most of which were toward lower contrast regions close to the edge.
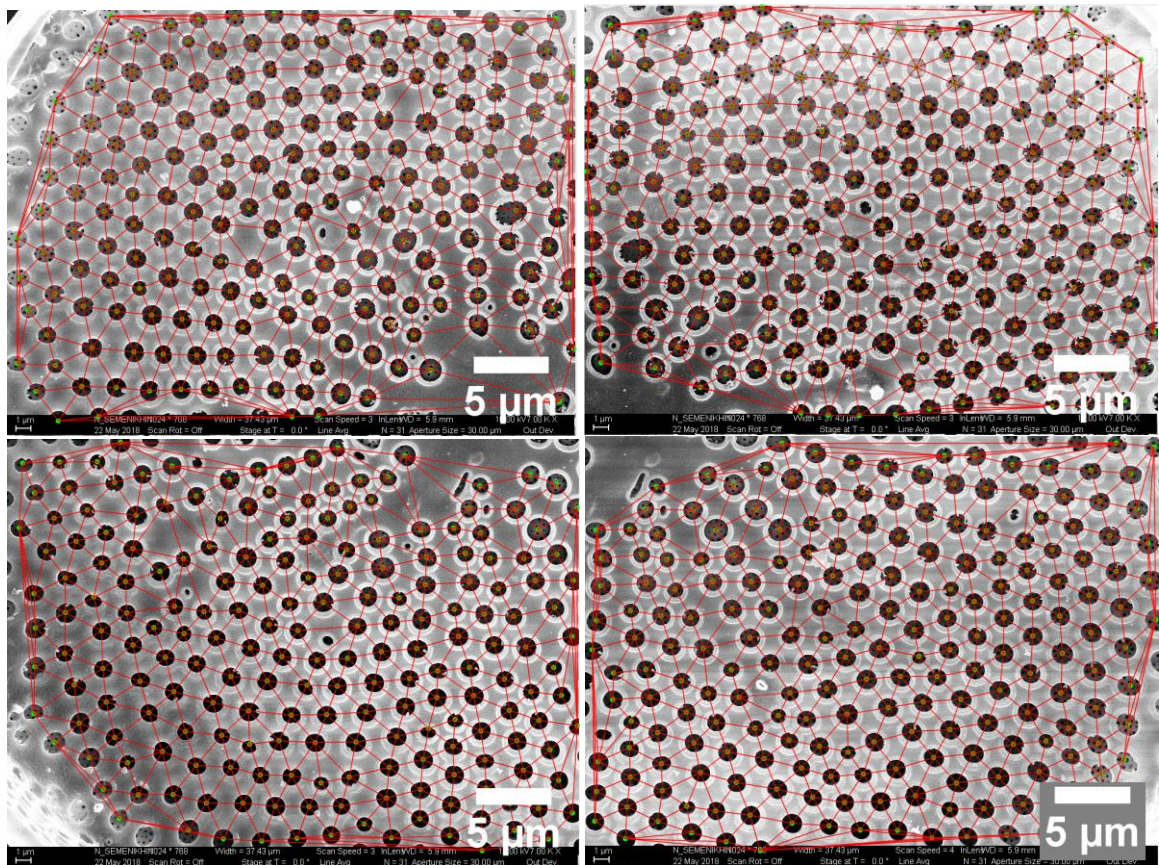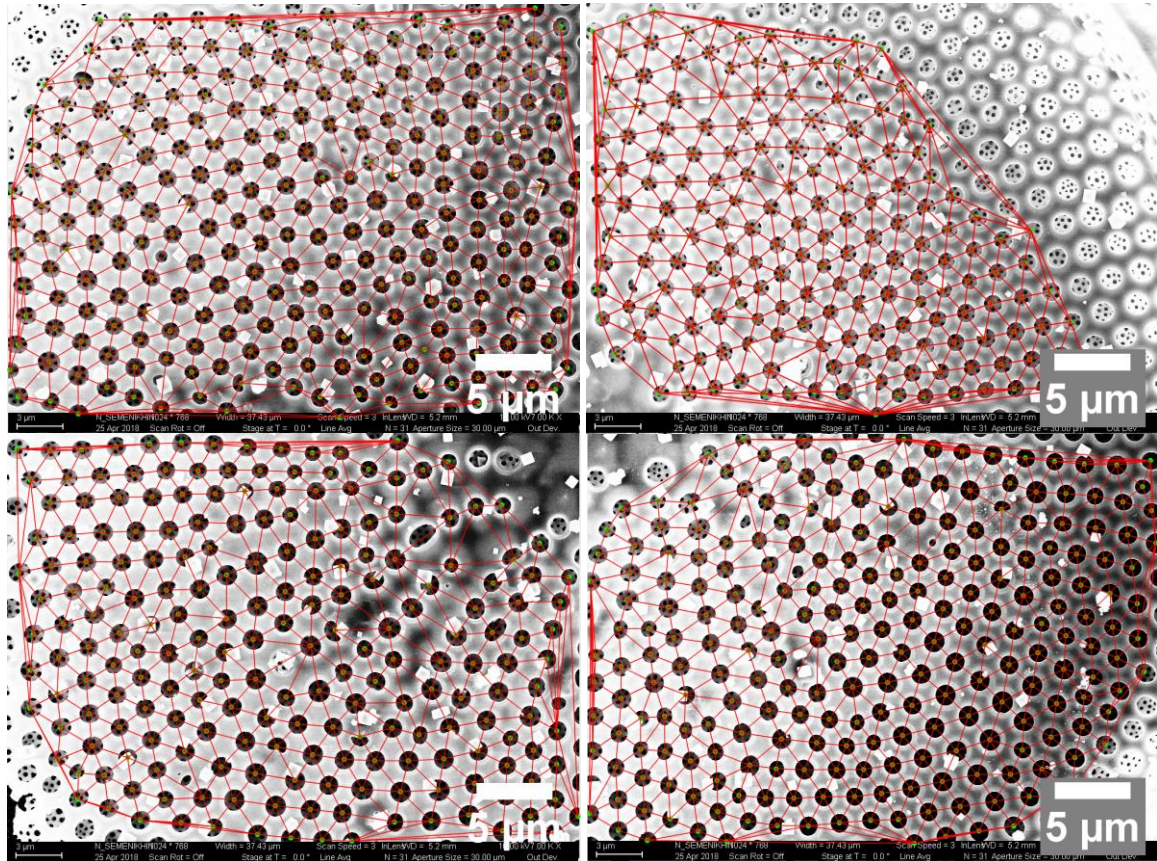

Figure 5.26. Large area image of entire foramen hole pattern for MgO/Si 4 made from stitching all four individual quadrants. SEM images by Nikolay Semenikhin, Sandhage Group, Georgia Tech.

Consistent with the MgO/Si replicas analyzed thus far, MgO/Si 4 gave a radius data set (Figure 5.27a) fit nicely by a normal distribution (kurtosis = 3.43) to give a mean radius of 0.59 ± 0.05 µm, matching closely with the kernel estimated radius of 0.58 µm. Continuing the trend of the MgO/Si replicas examined thus far, MgO/Si 4 gives a fair narrow edge length distribution centred at 2.04 µm with a minimal tail at longer lengths.

This suggests that the MgO/Si replicas picked for this analysis likely possess fewer vacancies than the group of silica frustules.
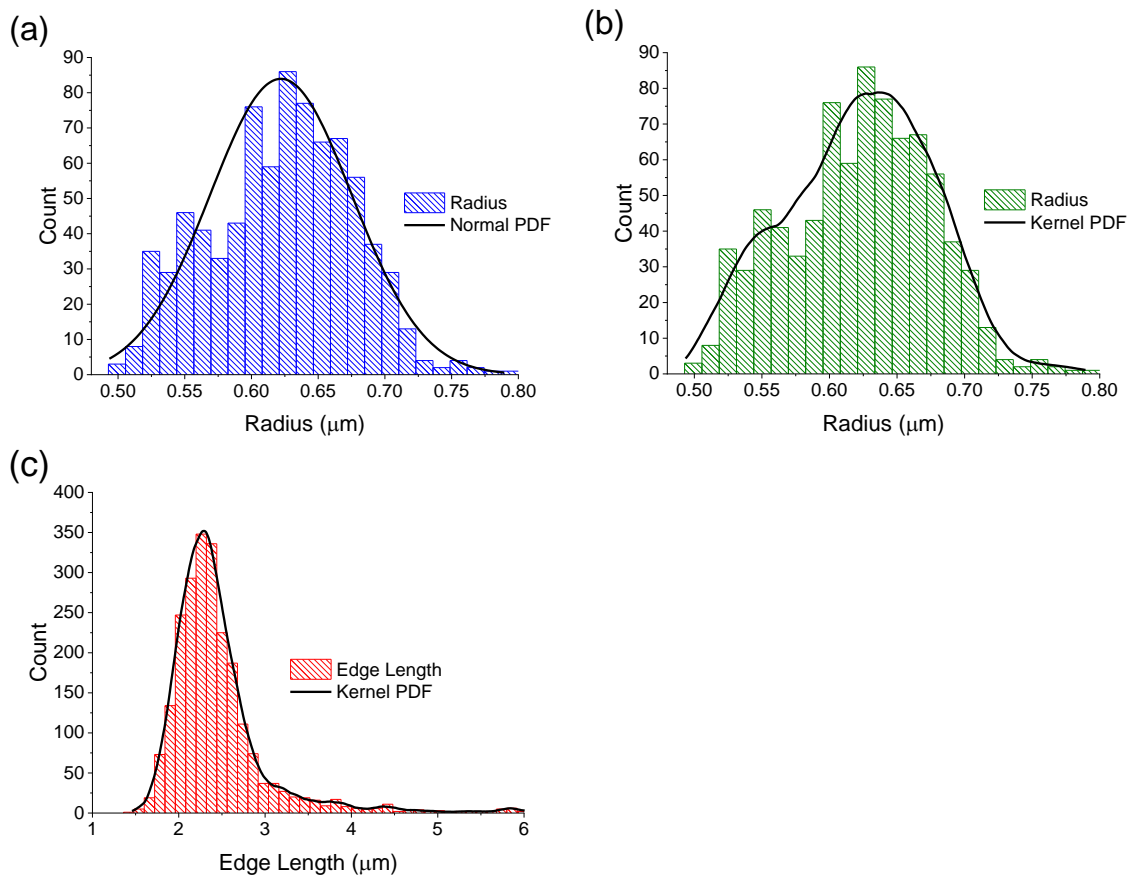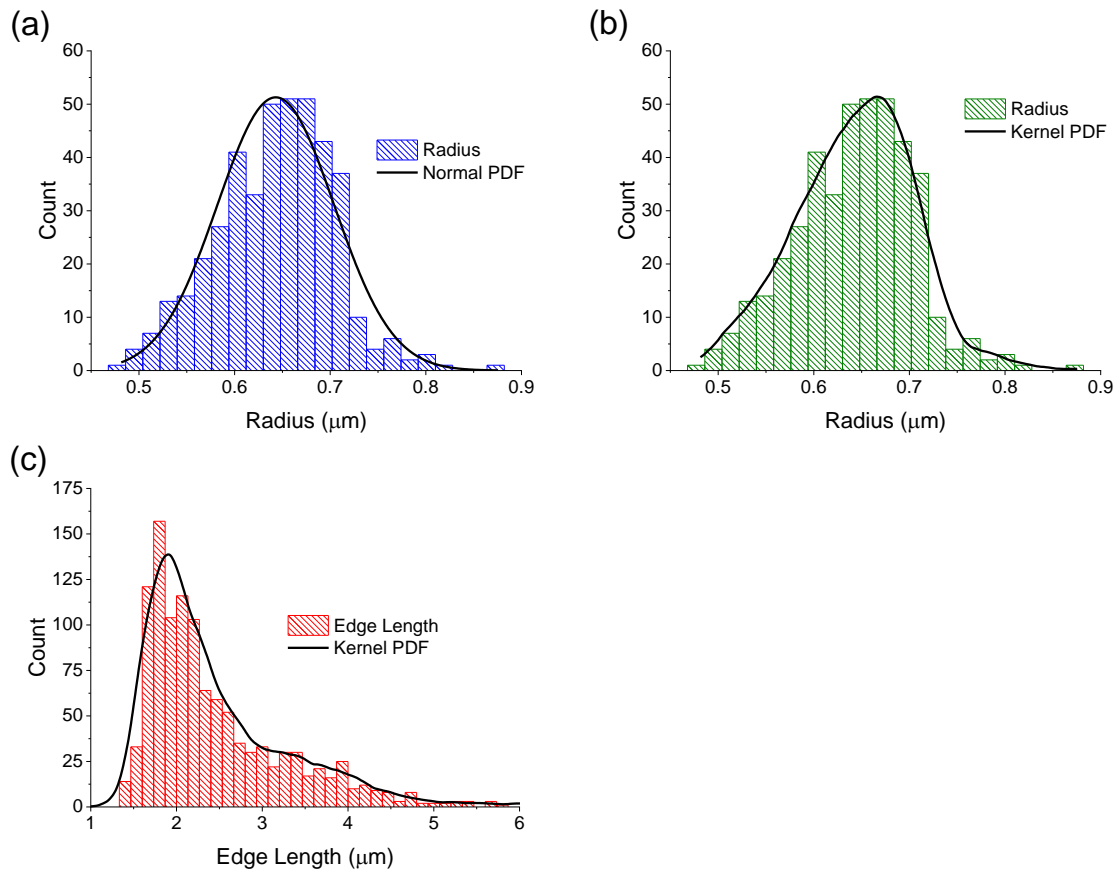

Figure 5.27. Histograms of (a) hole radius distribution (blue) fit by a normal PDF (b) hole radius distribution (green) fit by Kernel PDF (c) edge length distribution (red) fit by Kernel PDF for MgO/Si 4.

5.2.2.14 MgO/Si Replica 5

Overall, the MgO/Si 5 (Figure 5.28) replica gave a nice quality frustule with a uniform hole pattern. However, like MgO/Si 3, nonuniform curvature at the edge of the frustule resulted in significant loss of contrast for holes that approach the edge. In this case, the cribrum holes had enough contrast to survive binarization, despite numerous attempts to remove via careful thresholding, to give small clusters of holes, which were found by

the hole detection algorithm and biased the radius data set. To avoid this issue, the image was manually edited in ImageJ FIJI© using the drawing tools to erase the cribrum holes at the edge. Other aspects of the image were manually cleaned up in this stage, such as salt and pepper noise and other dark pixels associated with the foreground that survived binarization. It is stressed that at no point in this manual cleaning process were any pixels associated with high index holes edited in any way. The manually edited image was then saved as its own unique image and run through the hole detection algorithm once more. During the editing process the pixel/distance ratio of the image was left unchanged to maximize agreement with other quadrants in this frustule as well as other frustules and replicas. Outside of the manually removed holes, the hole detection algorithm on missed 2 holes among all quadrants due to extremely small size and misshapenness.
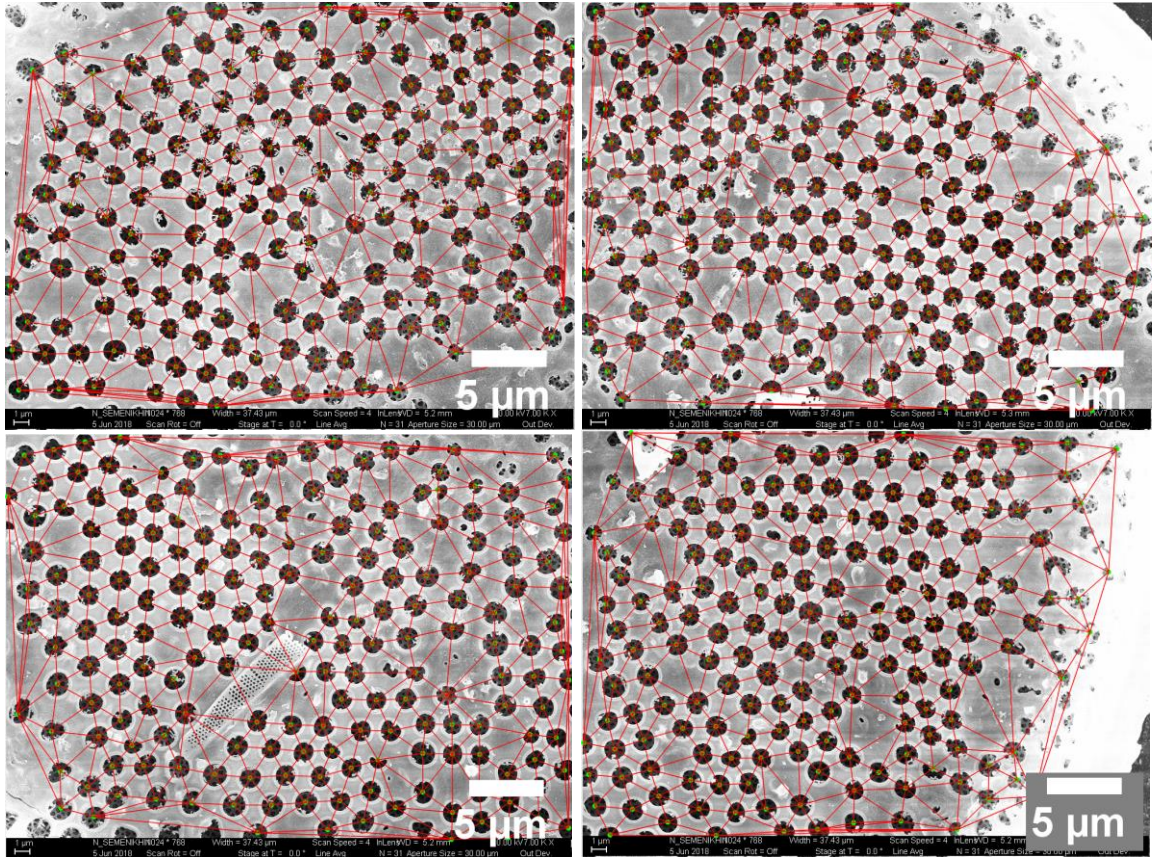
Figure 5.28. Large area image of entire foramen hole pattern for MgO/Si 5 made from stitching all four individual quadrants. SEM images by Nikolay Semenikhin, Sandhage Group, Georgia Tech.

The radius distribution or MgO/Si 5 gave a somewhat symmetric histogram (Figure 5.29) that was fit reasonably by a normal distribution (mean $= 0.56 \pm 0.04$ µm and kurtosis $= 4.54$), but not as well compared to previous MgO/Si replicas. Further analysis showed that the mean radius matched well with most probable one estimated by the kernel method (0.55 µm), where the kernel PDF was noticeably normal in appearance with a slightly elongated tail toward higher radius values. Regarding the edge length distribution, MgO/Si 5 proved to be consistent with all MgO/Si replicas examined in this study giving a similar-looking histogram centred at 2.06 µm with minimal long-distance tail.
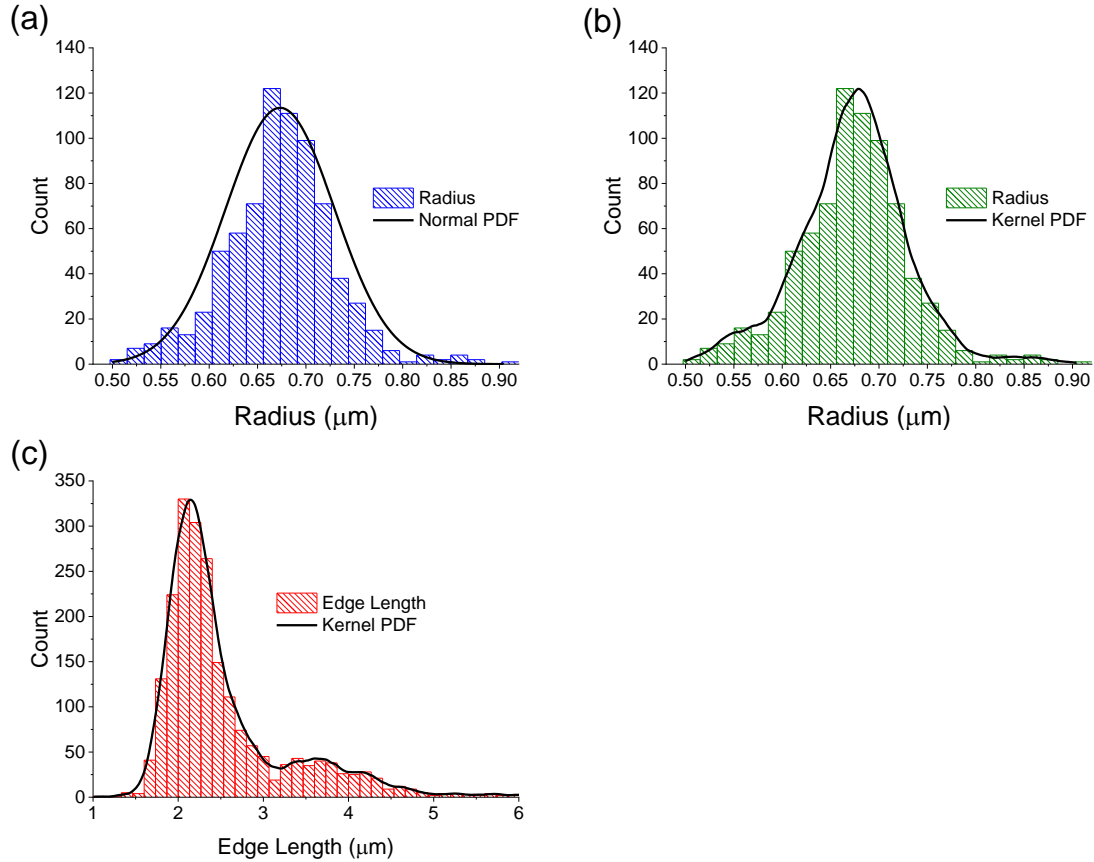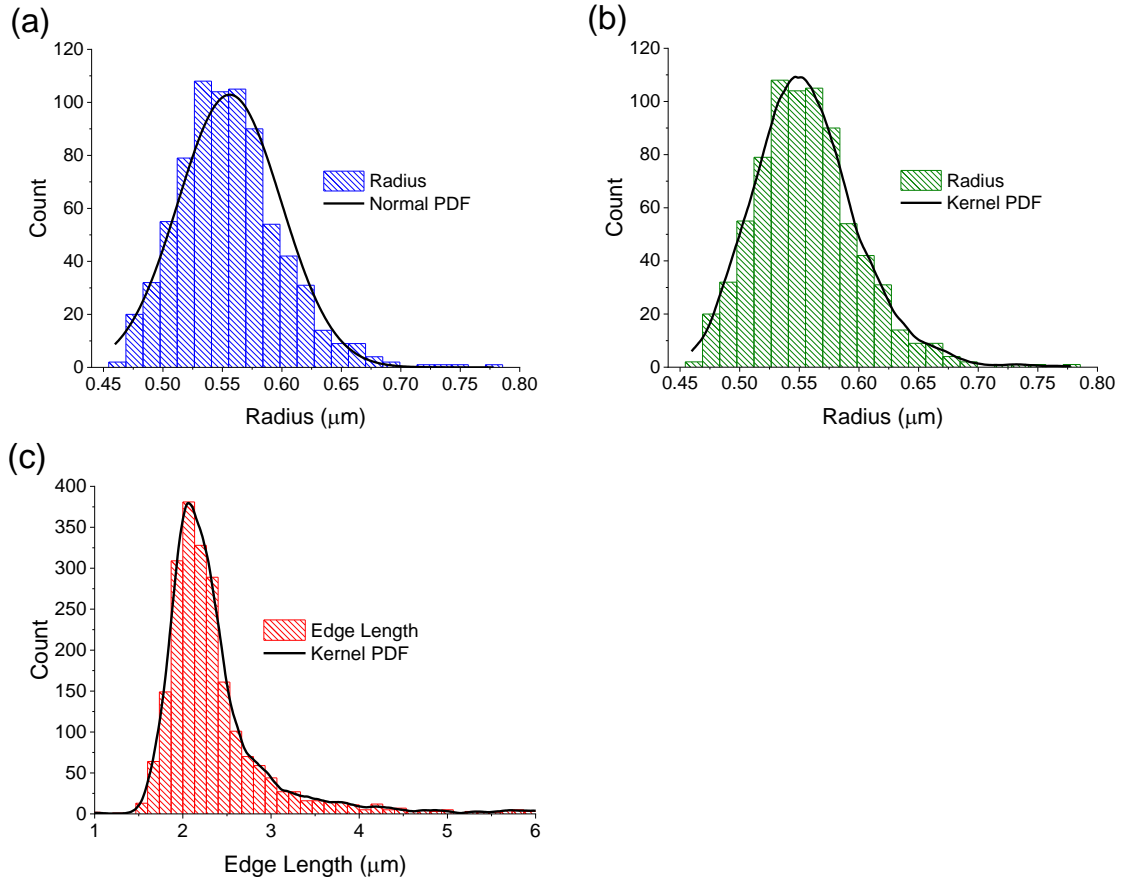
Figure 5.29. Histograms of (a) hole radius distribution (blue) fit by a normal PDF (b) hole radius distribution (green) fit by Kernel PDF (c) edge length distribution (red) fit by Kernel PDF for MgO/Si 5.

5.2.2.15 Mg₂Si Replica 1

The first of the Mg$_2$Si replicas (Figure 5.30) was a nice quality frustule with high hole density, even surface illumination, and good hole-foreground contrast leading up to the edges of the frustule. Aside from a large piece of debris between the top and bottom right quadrants, the surface debris was minimal and a nearly all holes were quite circular. As a result, all holes other than those cut off by the edge of the image were found. Analysis of the radius distribution gave a slightly asymmetric histogram tending toward larger radii which contributed to the data set bordering on normality (kurtosis = 4.13). The normal

mean obtained was $0.66 \pm 0.04\,\mu m$, close in value to the kernel estimated radius $(0.64\,\mu m)$. Despite the large debris fragment in the middle of the frustule, Figure 5.31c shows a fairly narrow edge length distribution centred at $2.04\,\mu m$ with a minimal tail at longer lengths. Such a narrow distribution and lack of a tail adequately describes the characteristics of the pore pattern of this replica in that, relative to the other frustules and replicas examined thus far, the limited number of vacancies and high degree of uniformity in hole size, spacing and density over a large area of the frustule surface minimizes the variance.
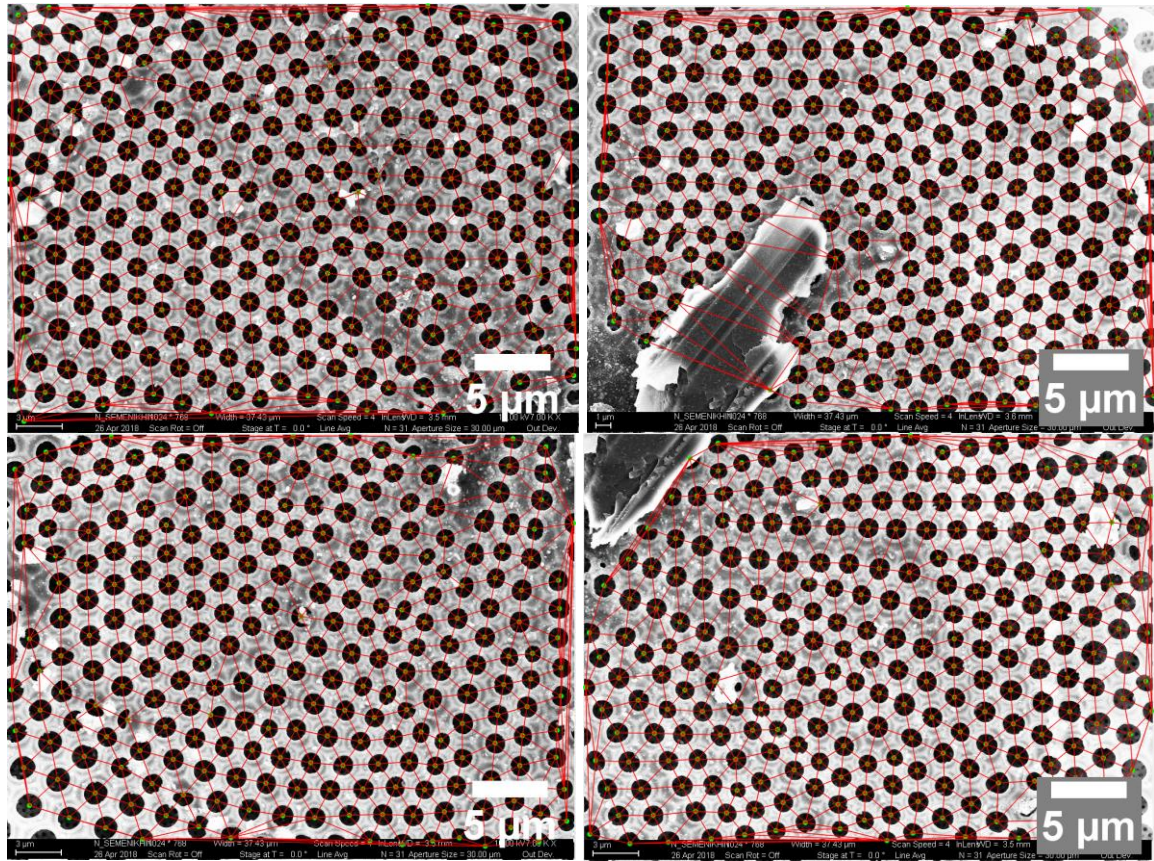
Figure 5.30. Large area image of entire foramen hole pattern for Mg_2Si 1 made from stitching all four individual quadrants. SEM images by Nikolay Semenikhin, Sandhage Group, Georgia Tech.
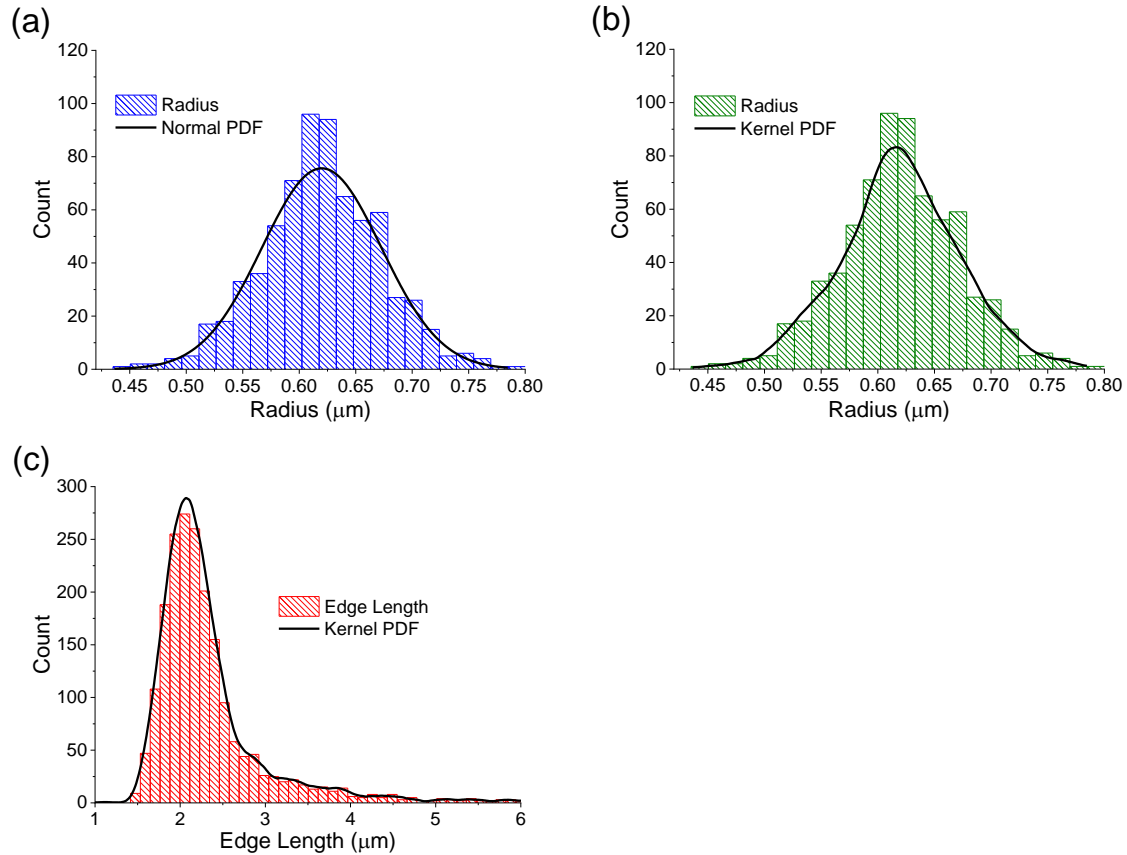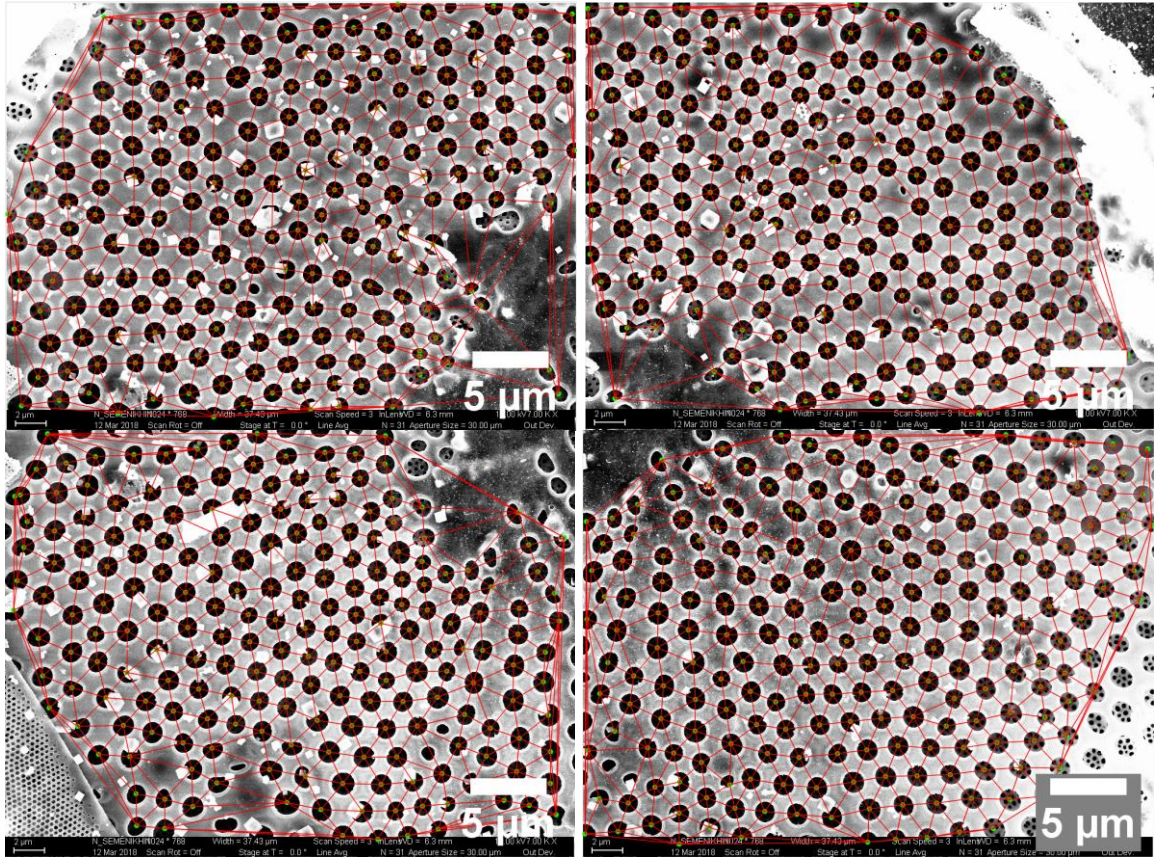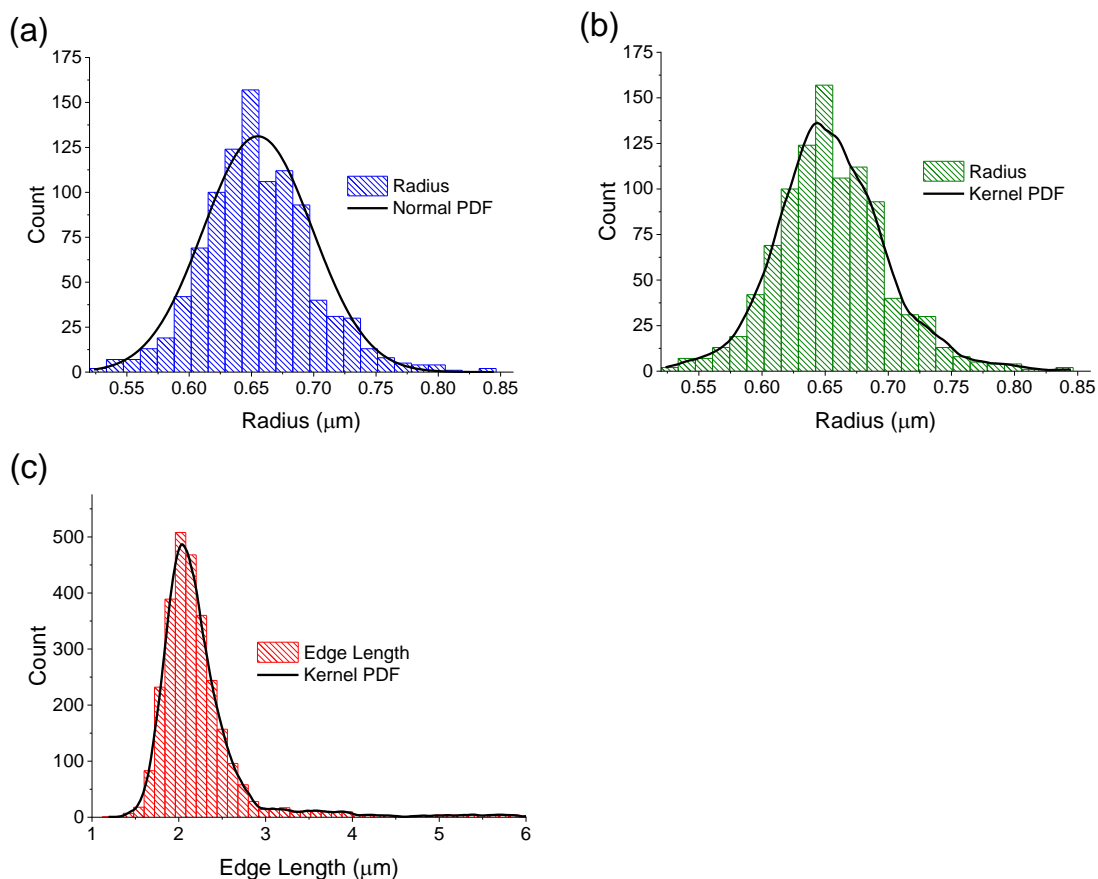
Figure 5.31. Histograms of (a) hole radius distribution (blue) fit by a normal PDF (b) hole radius distribution (green) fit by Kernel PDF (c) edge length distribution (red) fit by Kernel PDF for Mg_2Si 1.

5.2.2.16 <u>Mg_2Si Replica 2</u>

Compared to Mg_2Si 1, this replica (Figure 5.32) has noticeably more vacancies and more oval-shaped holes, although the hole pattern was still generally quite uniform and with good contrast between holes and the foramen layer. For the top left quadrant, a group of ca. 25 holes near the edge of frustule were consistently double counted during hole detection in a way that could significantly skew the distribution. Like MgO/Si 5, these holes were manually removed so that they would not interfere during hole detection and thus eventually bias the edge lengths toward shorter distances. Despite this, nearly all holes

that were reasonably captured within the frame of the image were detected. Together the data from all quadrants gave symmetric radius distribution (Figure 5.33a) that was fit well by a normal PDF (kurtosis = 3.73) to give a mean 0.67 ± 0.05 µm close to that of Mg_2Si 1 and the average for silica frustules (0.65 ± 0.02 µm) and MgO/Si replicas (0.60 ± 0.03 µm). Turning to the edge length histogram, as anticipated, this plot shows a more pronounced long-distance tail than that of Mg_2Si 1 and, when considering only the primary band, the variance is slightly greater. This comparison is notable because it is a clear example of two patterns that are largely similar but differ significantly in one aspect – the number of vacancies. Similar analysis was explored in Silica 2, but this example however this sample have significant bimodal character in its distribution. The difference highlighted here is subtler, giving an example of the triangulation methods sensitivity to relatively small number overall changes in a given structural parameter.
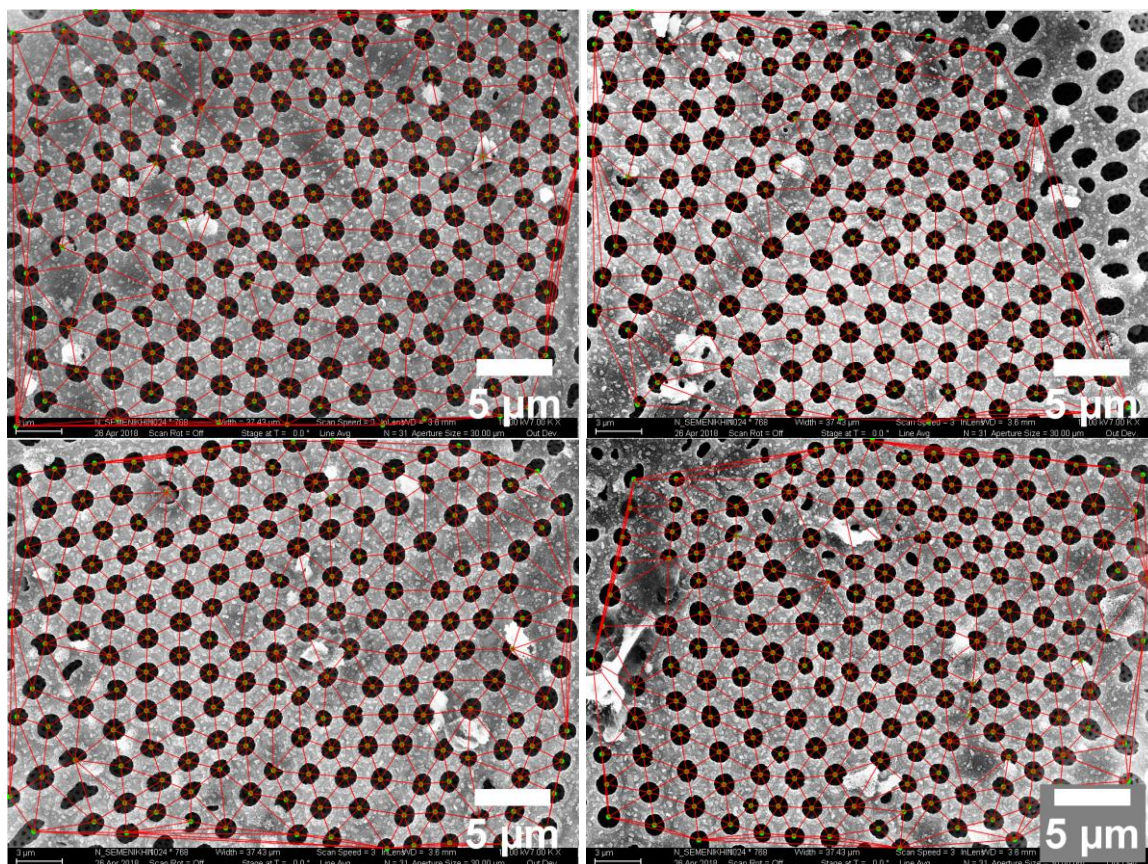
Figure 5.32. Large area image of entire foramen hole pattern for Mg$_2$Si 2 made from stitching all four individual quadrants. SEM images by Nikolay Semenikhin, Sandhage Group, Georgia Tech.
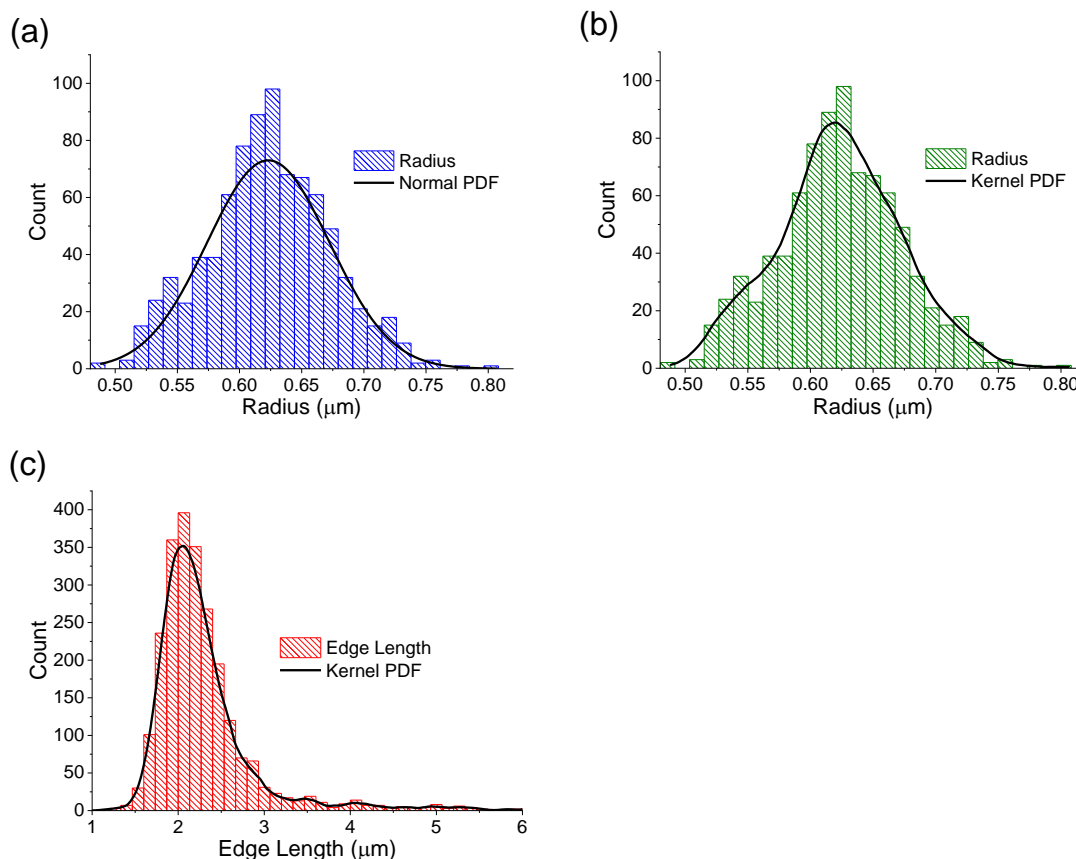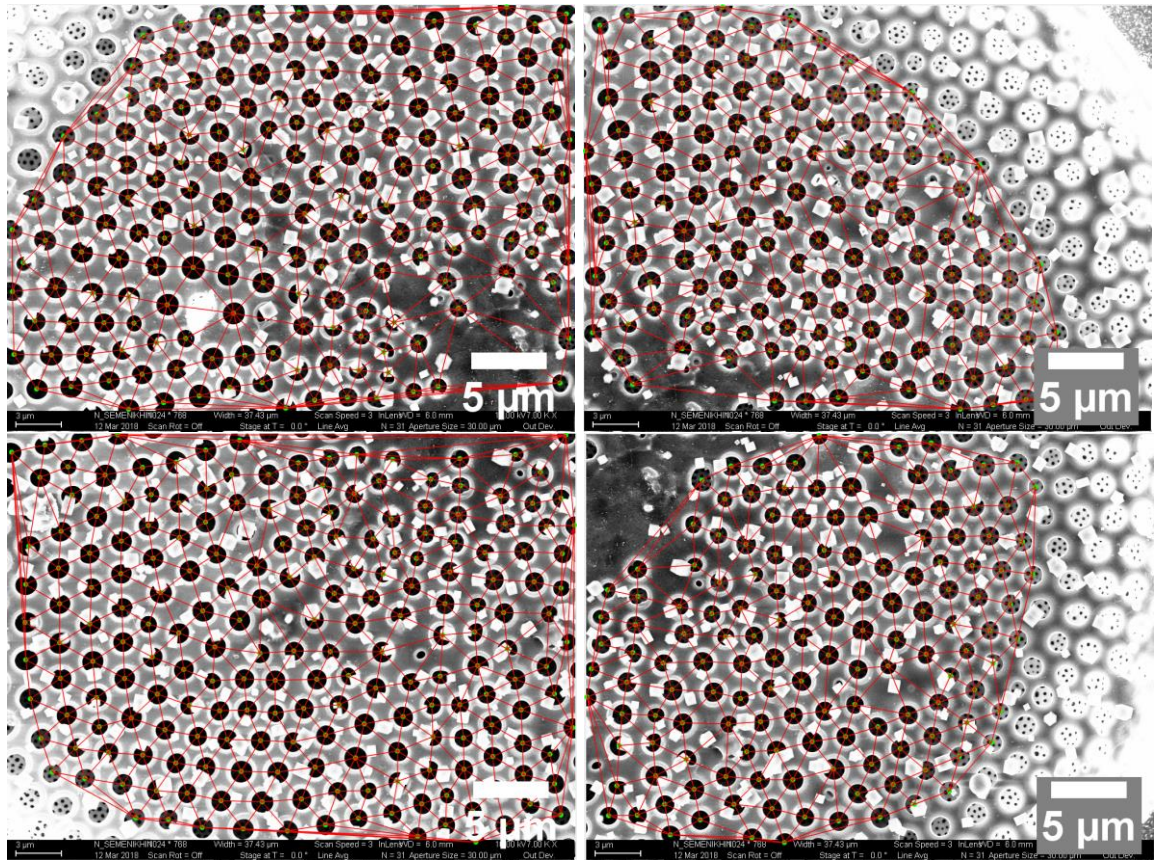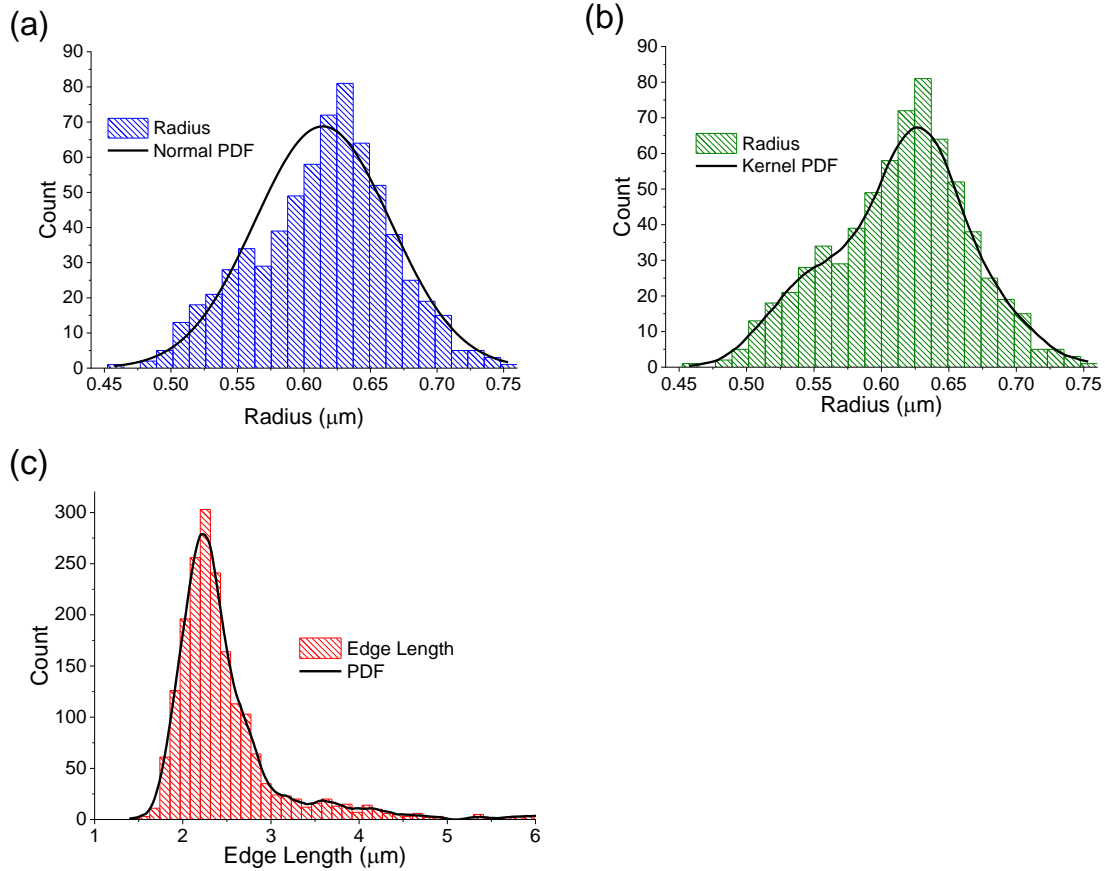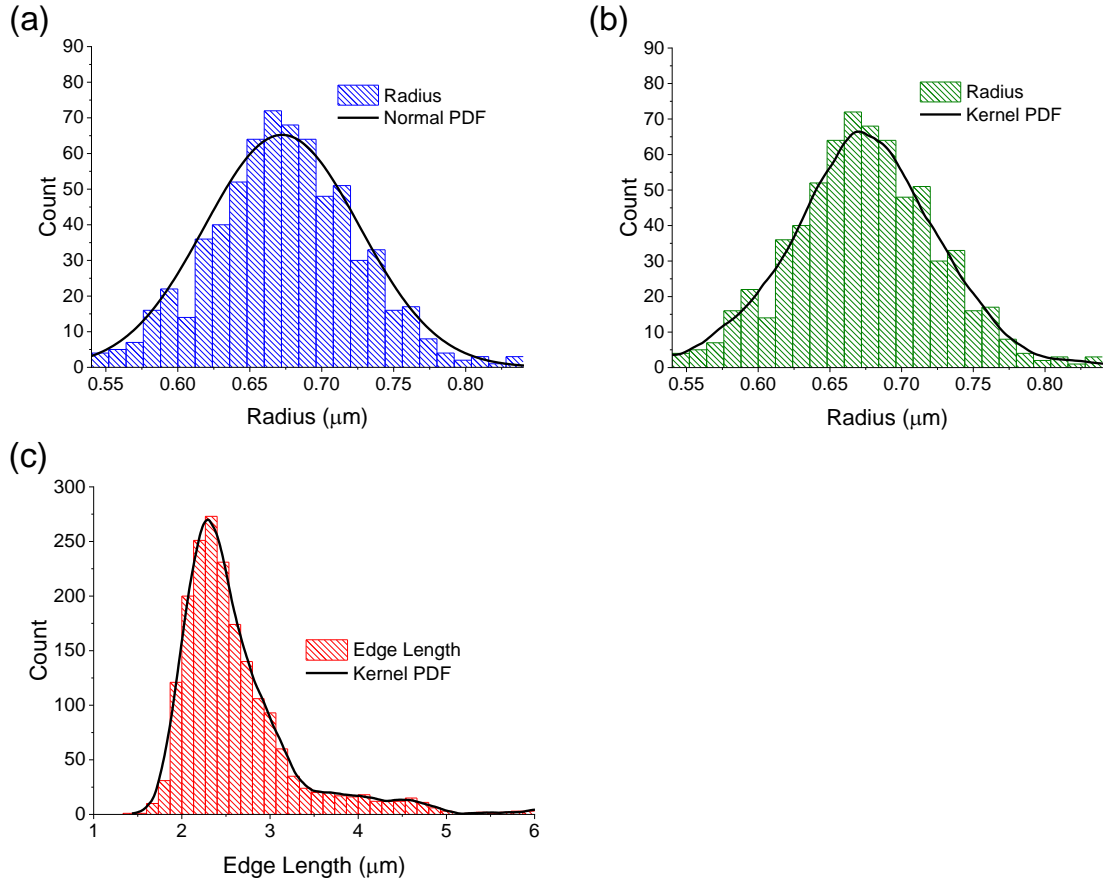
Figure 5.33. Histograms of (a) hole radius distribution (blue) fit by a normal PDF (b) hole radius distribution (green) fit by Kernel PDF (c) edge length distribution (red) fit by Kernel PDF for Mg$_2$Si 2.

5.2.2.17 Mg$_2$Si Replica 3

Mg$_2$Si 3 (Figure 5.34) shows comparable hole density and contrast to Mg$_2$Si 2 but has a greater degree of curvature, resulting in more holes at the edges having poor contrast. In intermediate cases like the top right quadrant, a small group (7-8) of misshapen holes with poor contrast were necessarily removed in a similar manner to MgO/Si 5 and Mg$_2$Si 2. Also, there is a noticeable crack in the top right corner of the bottom left quadrant that was not detected as a hole. The radius distribution (Figure 5.35a) from this set of images gave a symmetric histogram fit well by a normal distribution (kurtosis = 2.68) to yield a

mean radius of 0.68 ± 0.05 µm. The mean value is close to the kernel estimated value (0.67

µm) and the values seen in the two previous Mg_2Si replicas. The edge length distribution

gave a reasonable histogram, typical of the histograms seen thus far for frustules of similar

hole density and number of vacancies with a most probable edge length of 2.24 µm.

Figure 5.34. Large area image of entire foramen hole pattern for Mg_2Si 3 made from stitching all four individual quadrants. SEM images by Nikolay Semenikhin, Sandhage Group, Georgia Tech.

Figure 5.35. Histograms of (a) hole radius distribution (blue) fit by a normal PDF (b) hole radius distribution (green) fit by Kernel PDF (c) edge length distribution (red) fit by Kernel PDF for Mg_2Si 3.

5.2.2.18 $\underline{Mg_2Si\ Replica\ 4}$

Mg_2Si 4 (Figure 5.36) was a good quality replica with little surface debris and a uniform pore pattern with few vacancies. All quadrants gave a multitude of holes with good contrast despite some uneven curvature in the top and bottom right quadrants that caused poor contrast in holes close to the edges. With careful binarization, the cribrum holes beneath these foramen holes are removed from the to avoid detection while only missing two misshapen holes in the upper right quadrant. The radius histogram for this data set (a) gave a distribution somewhat asymmetric in appearance, tending toward larger radii. When

it with a normal PDF this data set fit reasonably well (kurtosis = 2.78) with a mean radius of 0.58 ± 0.05 µm, which was smaller than that of the other Mg_2Si replicas analyzed thus far. However, this mean radius was not significantly different than the most probable radius estimated by the Kernel method (0.59 µm). For the edge length distribution, Mg_2Si 4 gave smooth and narrow histogram centred at 2.50 µm with a small tail to longer distances. Similar to Mg_2Si 1, this is indicative of uniform hole density over a large area of the foramen surface and minimal vacancies.
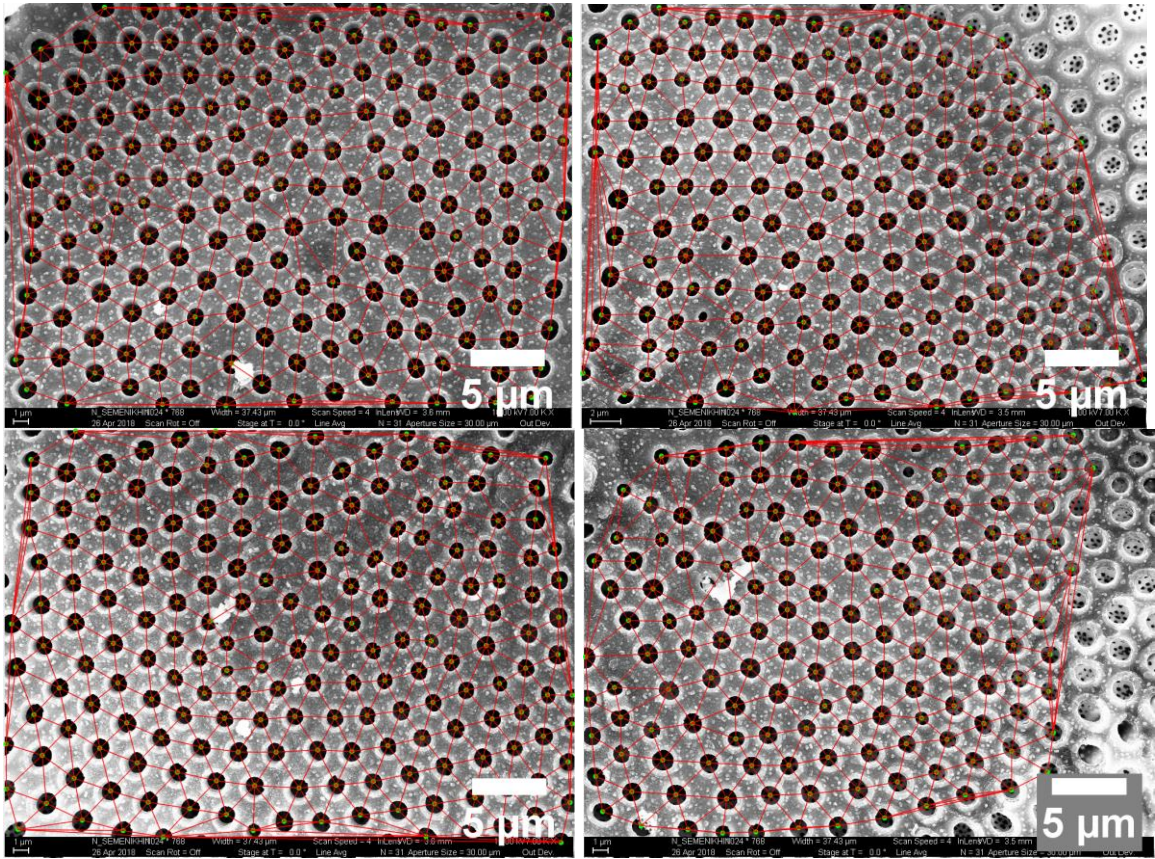
Figure 5.36. Large area image of entire foramen hole pattern for Mg_2Si 4 made from stitching all four individual quadrants. SEM images by Nikolay Semenikhin, Sandhage Group, Georgia Tech.
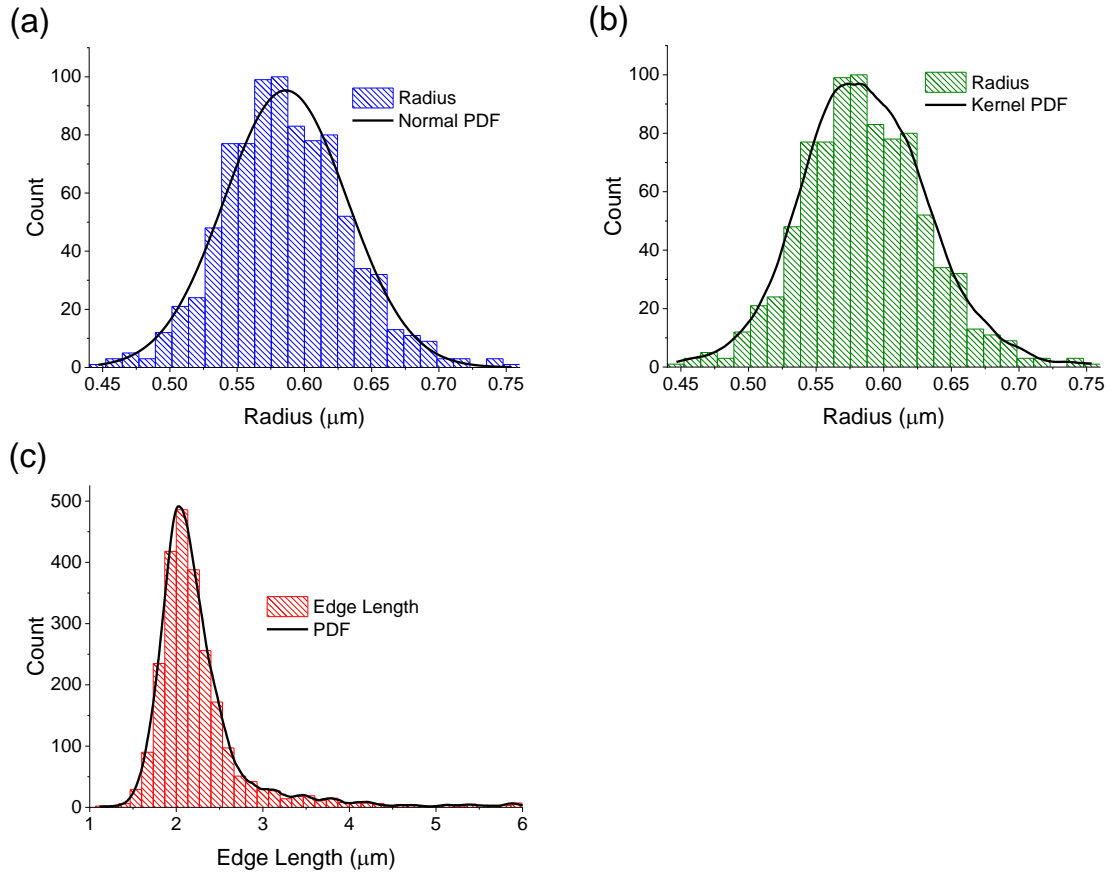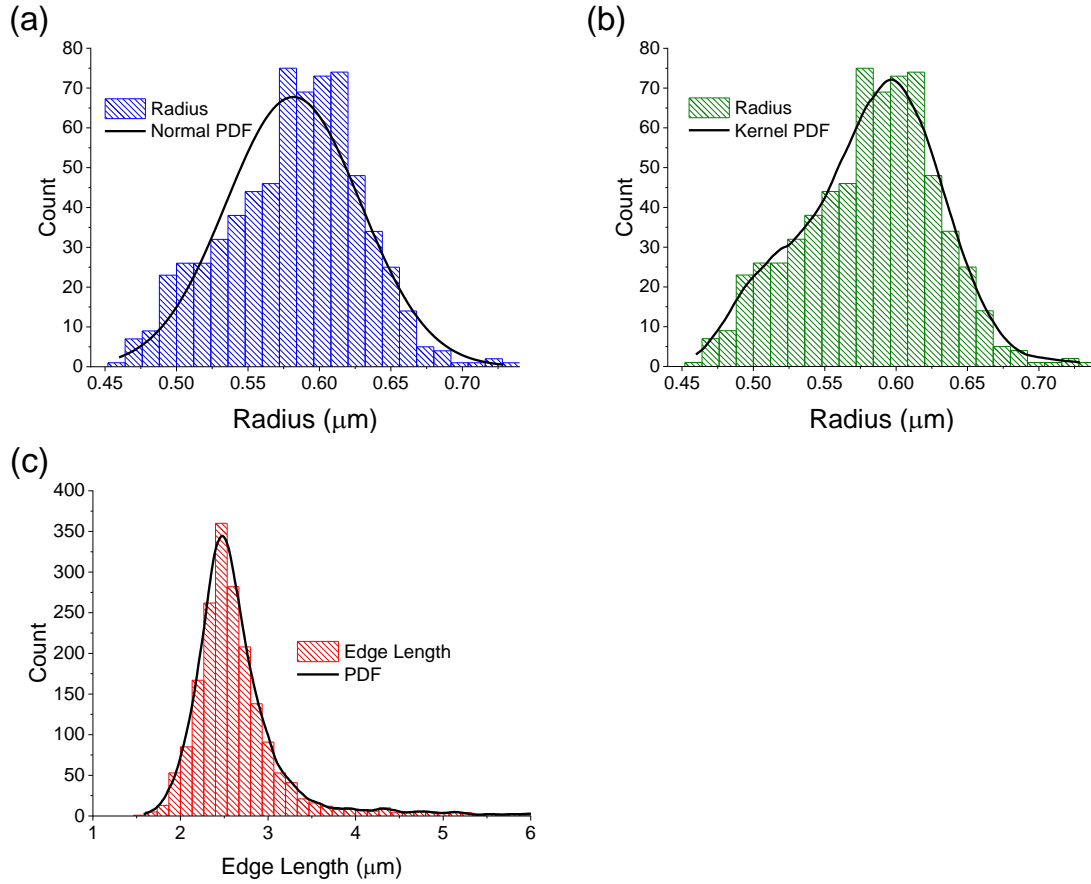
Figure 5.37. Histograms of (a) hole radius distribution (blue) fit by a normal PDF (b) hole radius distribution (green) fit by Kernel PDF (c) edge length distribution (red) fit by Kernel PDF for Mg$_2$Si 4.

5.2.2.19 Mg$_2$Si Replica 5

The last of the Mg$_2$Si replicas (Figure 5.38) was a good quality frustule having good hole-foreground contrast with minimal surface debris and even illumination. Except for 2-3 poor contrast holes in the lower left quadrant close to the curving edge, circle detection readily located all holes fully within the image frame and only missed two misshapen holes of small size between the top and bottom left quadrant. This yielded a symmetric radius distribution (Figure 5.39a) which, when fit by a normal PDF gave a mean radius of 0.60 ± 0.05 µm (kurtosis = 2.86) that was comparable to the most probable radius estimated by

271

the Kernel method (0.59 µm). Like the previous Mg$_2$Si replicas with uniform hole density, the edge length distribution for this frustule was quite narrow with a peak centre of 2.31 µm and minimal counts along faint tail of the PDF toward longer edge lengths.
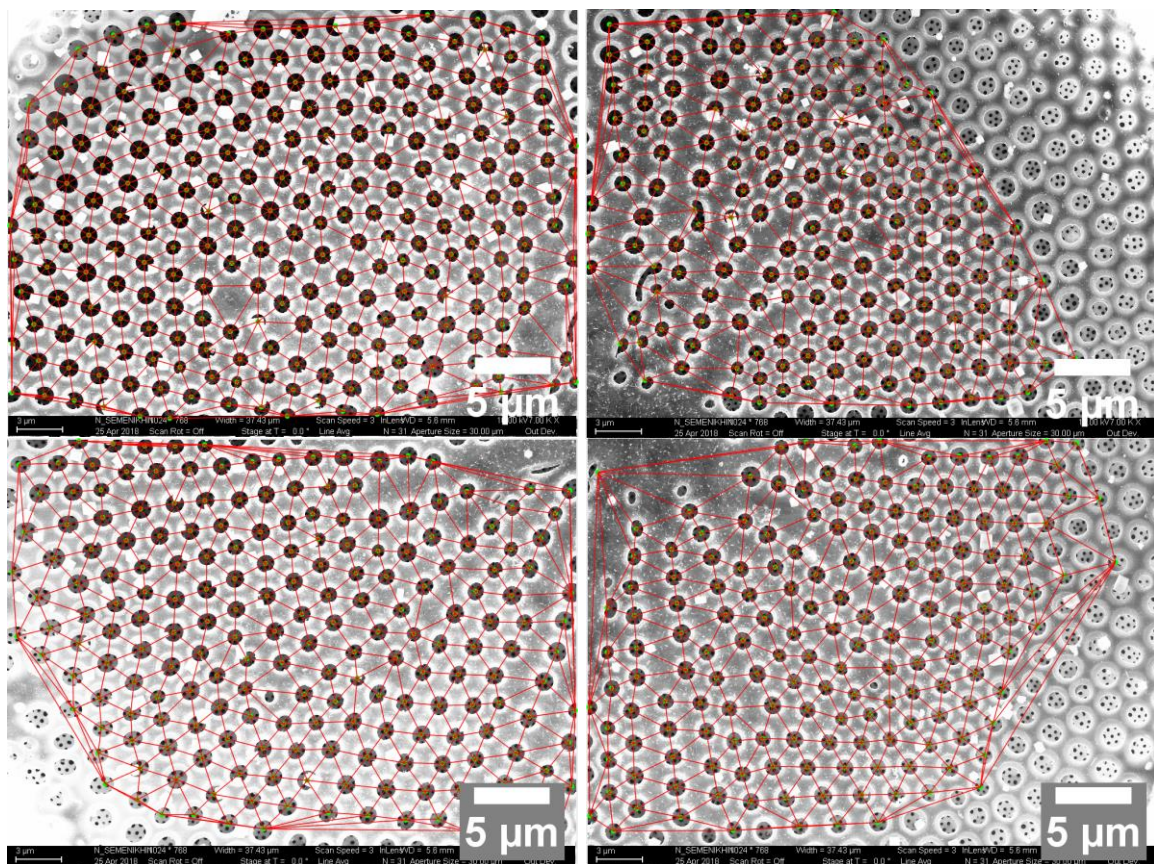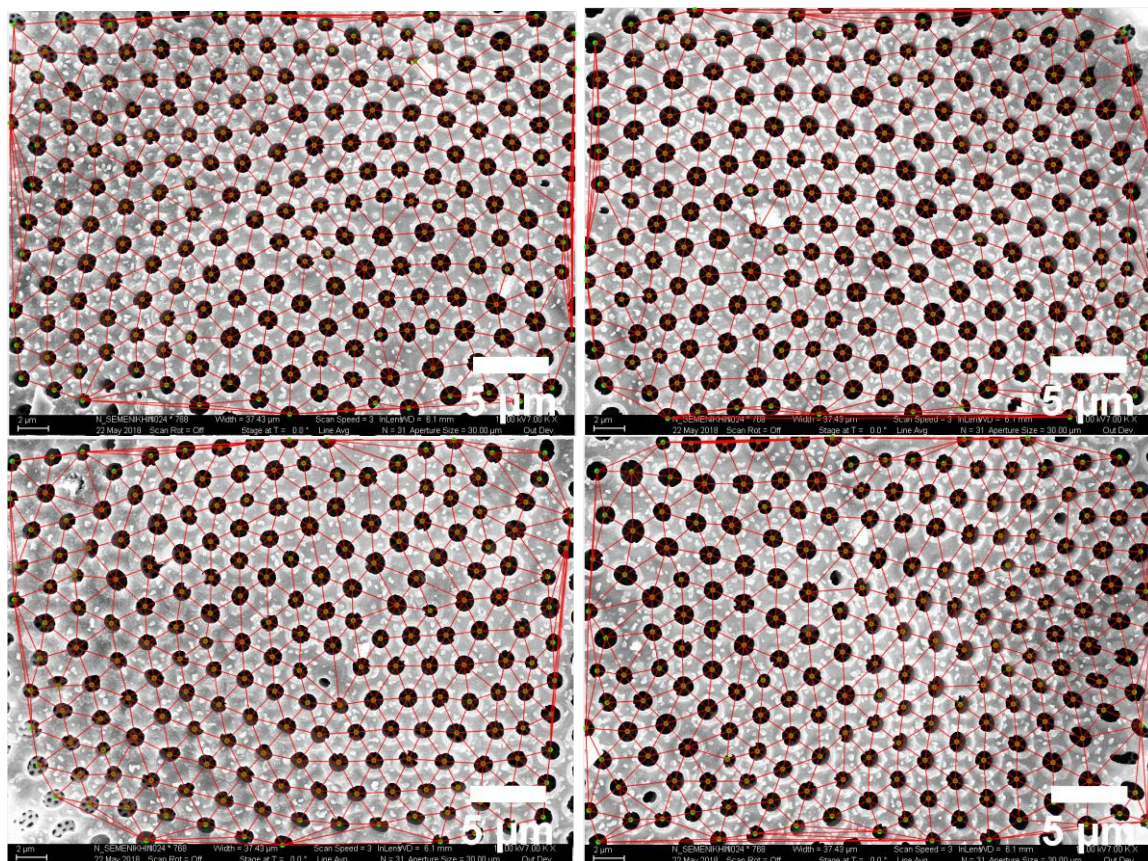

Figure 5.38. Large area image of entire foramen hole pattern for Mg$_2$Si 5 made from stitching all four individual quadrants. SEM images by Nikolay Semenikhin, Sandhage Group, Georgia Tech.
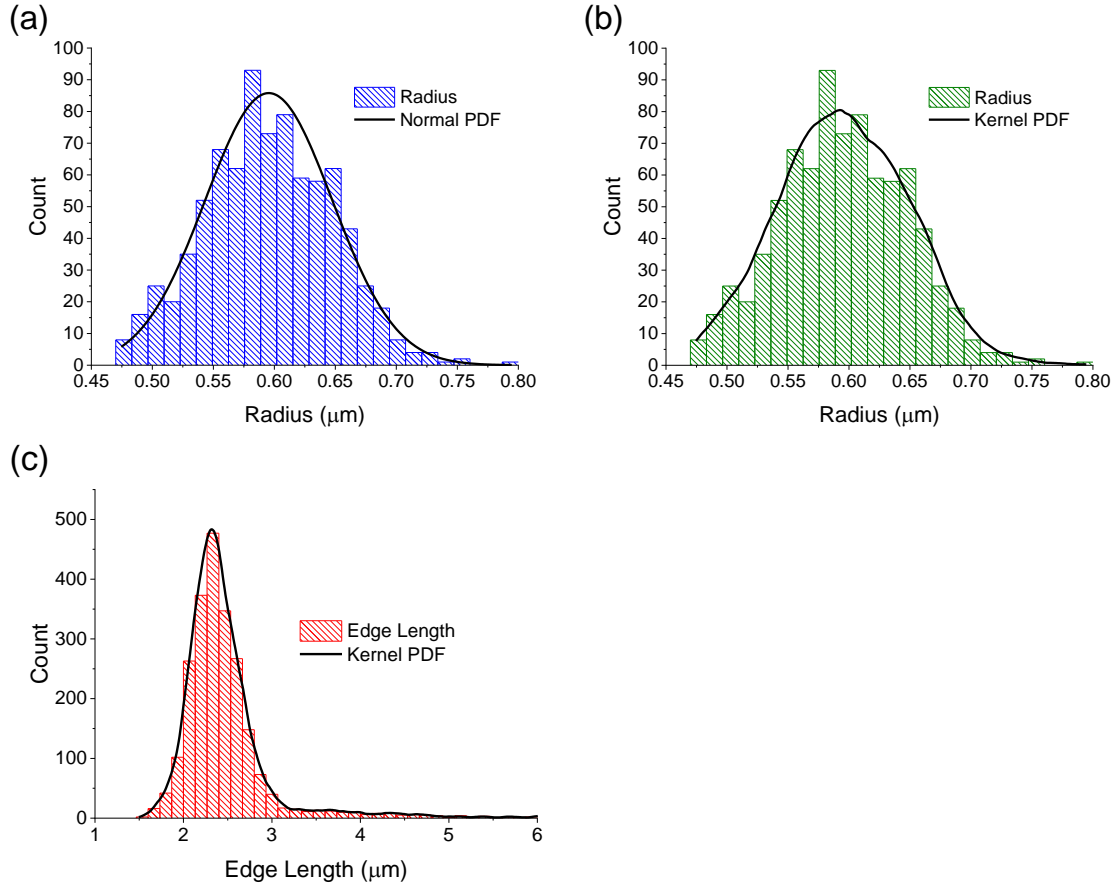
Figure 5.39. Histograms of (a) hole radius distribution (blue) fit by a normal PDF (b) hole radius distribution (green) fit by Kernel PDF (c) edge length distribution (red) fit by Kernel PDF for Mg_2Si 5.

5.2.2.20 <u>Assessment of Hole Pattern Images and Statistical Analysis Using the Quadrant</u>

<u>Method</u>

A summary of the results for the statistical pore pattern analysis of 5 frustules of each material (i.e. silica, MgO/Si, Mg_2Si) is provided in Table 5.1 and Table 5.2. Focusing first on hole size, there were no significant differences between native frustules or either of their higher index replica based on the similarity in the magnitude of the mean radius for each material. This finding is corroborated by nearly identical values found via KDE, which assumes no symmetry or parametric relationship and thus better account for

asymmetries in the data set. At first glance, the standard deviations for the mean radius of individual frustules and the average value reported for each material are surprisingly narrow. Considering that the typical resolution of the images analyzed with this hole detection-triangulation method was in the 26-37 nm/pixel range, the baseline uncertainty in estimated radii is ca. 4-6% assuming a typical hole radius of 0.63 µm derived from the data in Table 5.1.

Table 5.1. Radius data obtained from the quadrant image analysis method.

Sample	Mean Radius Normal (µm)*	Skew	Kurtosis	MP Radius Kernel (µm)**	No. Holes
SiO_2 1	0.64 ± 0.05	0.18	3.59	0.64	985
SiO_2 2	0.66 ± 0.07	0.77	4.94	0.65	627
SiO_2 3	0.62 ± 0.05	-0.07	2.56	0.64	818
SiO_2 4	0.64 ± 0.06	-0.04	3.26	0.67	420
SiO_2 5	0.67 ± 0.06	0.13	4.28	0.68	752
Average	0.65 ± 0.02		3.73 ± 0.82	0.65 ± 0.02	
MgO/Si 1	0.62 ± 0.05	-0.03	3.33	0.62	698
MgO/Si 2	0.62 ± 0.05	0.08	3.01	0.62	850
MgO/Si 3	0.61 ± 0.05	-0.20	2.78	0.61	677
MgO/Si 4	0.59 ± 0.05	0.22	3.43	0.58	872
MgO/Si 5	0.56 ± 0.04	0.75	4.54	0.55	764
Average	0.60 ± 0.03		3.42 ± 0.61	0.60 ± 0.03	
Mg_2Si 1	0.66 ± 0.04	0.42	4.13	0.64	989
Mg_2Si 2	0.67 ± 0.05	-0.10	3.73	0.67	691
Mg_2Si 3	0.68 ± 0.05	0.21	2.68	0.67	713
Mg_2Si 4	0.58 ± 0.05	-0.18	2.78	0.60	678
Mg_2Si 5	0.60 ± 0.05	0.12	2.86	0.59	816
Average	0.64 ± 0.03		3.24 ± 0.58	0.64 ± 0.04	

*95% Confidence   **MP stands for "Most Probable"

At this point in the analysis it is salient to discuss what this means in terms of the accuracy of the radii estimated by the hole detection and what physically meaningful information can be taken from these results. To quickly reiterate some previously mentioned points, due to the immense complexity of the frustule structure and the hundreds

or thousands of holes contained therein, assumptions were made to simplify the theoretical basis on which these calculations are based. Although potentially heuristic, the objective for this study was to obtain as close to a quantitative estimate of the mean hole size for each sample as possible while analysing larger area images with moderate resolution. It was hypothesized that sampling many holes from good-quality images with moderate resolution can overcome the lack of fine resolution which can only be achieved when imaging smaller sets of holes if one could carefully analyze the large data set statistically.

This began by defining a simple geometric quantity that would adequately describe the shape of each detected hole. To put this quantity in the simplest of terms, a critical assumption was made: that all holes detected were perfectly circular. From the diatom images shown in previous sections, there are always a small-to-moderate number oval-like or misshapen holes present on the diatom surface and possibly cracks that appear like holes to a computer. However, this computational limitation was accounted for considering that the vast majority of the holes that are detected by the algorithm are reasonably circular and will dominate the data set such that the sampling of even moderate numbers (potentially dozens) of non-circular features will not significantly skew the radius distribution. Although a ratio of "good"-to-"bad" holes is difficult to quantify, the collective observations of the individual frustules in previous sections show that, in the worst of cases where 20 holes out of total 750 holes are considered "bad" due to misshapenness, the ratio of "good":"bad" holes is approximately 37.5:1. For frustules with relatively uniform hole size and few structural defects or debris, like Mg_2Si 1, this ratio could increase by an order of magnitude.

The above assumption holds if there is sufficient resolution to capture small variations in hole radii and that image binarization is performed at the lowest possible threshold so little-to-no edge pixels are lost and one prevents the artificial shrinking holes. Returning briefly to the discussion of variance in the obtained data sets, the standard deviations for the radius of individual frustules, typically in the $\pm$ 40-70 nm range, are approximately 1.5-2 times that of the fundamental limit set by the typical resolution of the image (26-37 nm). Although it is difficult to define quantitatively, visually, one can observe that careful binarization allowed for the accurate preservation of holes size in binary images as is shown in Figure 5.40 with minimal foreground noise.
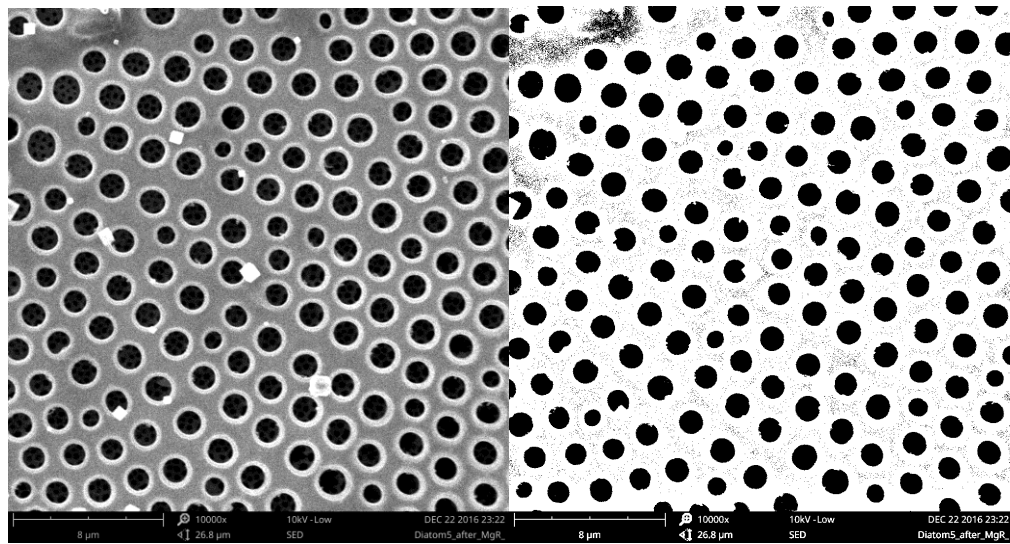
Figure 5.40. (Left) Grayscale image of holes in MgO/Si replica (Right) Binarized image of the same hole set. SEM images by Sunghwan Hwang, Sandhage Group, Purdue.

The uncertainty of hole size estimation is assumed to be limited by the resolution of the original grayscale image. This suggests that, although the standard deviations in the data sets are close to the resolution limit, they are likely large enough to be considered distinguishable from the baseline fluctuations in pixel density during the binarization

process, i.e. the possibility that two neighboring pixels with grayscale values just different enough for one to move to the foreground upon binarization and the other not. Based on this admittedly sizeable set of assumptions, the accuracy of the estimated radii and their corresponding standard deviations are considered consistent with the physical dimensions of a given frustule pore pattern but not a quantitative calculation of these values. The work presented here is considered a semiquantitative estimate that provides descriptive statistics about appreciable differences ($\pm$ 10% or greater) between the pore patterns of different diatoms and an approximate measure of hole pattern uniformity based on the spread of the data and features of the histogram, such as symmetry and normality. A simple solution to this is to increase magnification while imaging to increase the pixel/distance ratio, however, this comes at the cost of imaging less holes, requiring more post processing, binarization, and analysis time. Since the current data set gave a reasonable approximation to the hole size distribution, no further analysis was done with images of higher resolution.

Returning to the analysis of the radii data in Table 5.1, the percent difference in the average mean radius obtained from a normal distribution between any combination of materials was $\leq$ 8%. Given the care with which SEM images were taken to ensure that samples had comparable contrast and magnification, the agreement between values corroborates the quality of shape preservation and confirms that there are only subtle ($< \pm$ 10%)) between the mean radius of holes as a function of foramen material identity. The implications of this on focusing trends observed from imaging in the visible and NIR will be discussed further in section 6.2.2.2.

The analysis of most probable hole-to-hole distances obtained from the distribution of edge lengths are less straightforward to assess from an accuracy standpoint, considering

that the distances can change depending on the connectivity. However, given the success with which the CHT located hole center positions and the relatively comparable hole density among the frustules analyzed (estimated based on the number of holes sampled for diatoms of similar overall diameter from Table 5.1), the large numbers of edge lengths sampled will afford a semiquantitative estimate of the hole-to-hole distances for individual frustules that provides satisfactory evidence for whether there are gross differences ($\pm$ 10% or greater) between hole-to-hole distances of individual frustules. The most probable hole-to-hole distance for each frustule and the number of holes sampled are summarized in Table 5.2.

Table 5.2. Edge Length data obtained from quadrant analysis method.

	SiO_2 1	SiO_2 2	SiO_2 3	SiO_2 4	SiO_2 5	Average
MP H-H* Distance (μm)	1.95	2.02	2.29	1.91	2.14	2.06 $\pm$ 0.14
No. of Edges	2849	1790	2351	1180	2157	

	MgO/Si 1	MgO/Si 2	MgO/Si 3	MgO/Si 4	MgO/Si 5	Average
MP H-H* Distance (μm)	2.07	2.05	2.22	2.04	2.06	2.09 $\pm$ 0.06
No. of Edges	2003	2457	1938	2514	2201	

	Mg_2Si 1	Mg_2Si 2	Mg_2Si 3	Mg_2Si 4	Mg_2Si 5	Average
MP H-H* Distance (μm)	2.04	2.29	2.24	2.50	2.31	2.28 $\pm$ 0.15
No. of Edges	2861	1976	2043	1929	2343	

*MP H-H stands for "Most Probable Hole-to-Hole"

Generally, the arithmetic mean of the most probable hole-to-hole distance was comparable across all materials. Native silica frustules and MgO/Si replicas showed nearly identical (ca. 1% difference) average values. The greatest difference observed was between

the average value of Mg_2Si and Silica (10% difference). Based on this estimation, it appears that, while there are no gross differences (>10%) between frustules of different materials, there is a non-negligible difference between the lower index materials (silica and MgO/Si) and the highest index material, Mg_2Si. This may be related to a slight expansion in the diameter of the frustule related to a volume expansion upon the addition of a larger metal (Mg) once fully converted. Visually this can be seen in Figure 5.41 where the diameter of the Mg_2Si replica was found to be ca. 16% greater than that of the silica frustule. The significance of this on the focusing behavior of individual diatoms will be discussed in section 6.2.2.2.

5.2.2.21 Analysis of Same Hole Set Through Each Conversion Stage and Comparison to Quadrant Data

Initial analysis of hole shape preservation at different stages of conversion were performed by imaging smaller groups of holes (15) and measuring their radii manually in ImageJ©. This data, summarized in Table 5.3, provided a data set that passed a t-test (at the 0.05 level) to show there were no significant differences between the change in radius of the same 15 holes tracked through each step of the conversion. One critical assumption for the t-test validation method is that the sample data follows a normal distribution. This is corroborated by the radius distributions in previous sections consistently showing normal-like behavior and is a valid assumption. However, given that only 15 holes were sampled, a supporting investigation was done using the hole detection/triangulation approach to determine if this trend can be validated using a method that can sample a larger number of holes in a short amount of time (minutes) and if the two different methods would yield similar results. In doing so, images of a section with ca. 170 holes at each stage of

conversion en route to making Mg₂Si 5 (Figure 5.42) were analyzed with the hole

detection-triangulation algorithm describe in previous sections.

Table 5.3. Manually calculated change in hole size at different stages of diatom frustule conversion. Data provided by Sunghwan Hwang, Sandhage Group, Purdue.

	SiO_2	MgO/Si	Change from SiO_2 to MgO/Si	Si	Change from MgO/Si to Si	Mg_2Si	Change from Si to Mg_2Si
	1.39 µm	1.36 µm	-30 nm	1.42 µm	+60 nm	1.35 µm	-70 nm
	1.48 µm	1.48 µm	0 nm	1.50 µm	+20 nm	1.5 µm	0 nm
	1.51 µm	1.48 µm	-30 nm	1.53 µm	+50 nm	1.48 µm	-50 nm
	1.23 µm	1.23 µm	0 nm	1.24 µm	+10 nm	1.21 µm	-30 nm
	1.46 µm	1.39 µm	-70 nm	1.42 µm	+30 nm	1.4 µm	-20 nm
	1.42 µm	1.40 µm	-20 nm	1.40 µm	0 nm	1.41 µm	+10 nm
	1.15 µm	1.17 µm	+20 nm	1.13 µm	-40 nm	1.15 µm	+20 nm
	1.29 µm	1.30 µm	+10 nm	1.32 µm	+20 nm	1.32 µm	0 nm
	1.34 µm	1.32 µm	-20 nm	1.35 µm	+30 nm	1.34 µm	-10 nm
	1.25 µm	1.29 µm	+40 nm	1.26 µm	-30 nm	1.18 µm	-60 nm
	1.43 µm	1.44 µm	+10 nm	1.40 µm	-40 nm	1.47 µm	+70 nm
	1.46 µm	1.43 µm	-30 nm	1.42 µm	-10 nm	1.42 µm	0 nm
	1.15 µm	1.13 µm	-20 nm	1.11 µm	-20 nm	1.13 µm	+20 nm
	1.34 µm	1.29 µm	-50 nm	1.28 µm	-10 nm	1.25 µm	-30 nm
	1.46 µm	1.46 µm	0 nm	1.48 µm	+20 nm	1.46 µm	-20 nm
Average change* (nm)			-13 ± 16		+6 ± 17		-13 ± 21

Results for this analysis are summarized in Table 5.4. Upon calculating the change in radius at each stage of conversion, the magnitude of the change at each step was comparable to the resolution of the image (ca. 26 nm). Unlike the data analyzed in section 5.2.2.20, this difference is likely not distinguishable from pixel density fluctuations during binarization and thus one cannot assume that the values obtained are physically realistic. This was evident in the net change accounting for all conversion steps (-0.0009 µm) which, when rounded to the proper significant figure gives an ambiguous value of 0.00 µm. A similar value was predicted by the Kernel method.
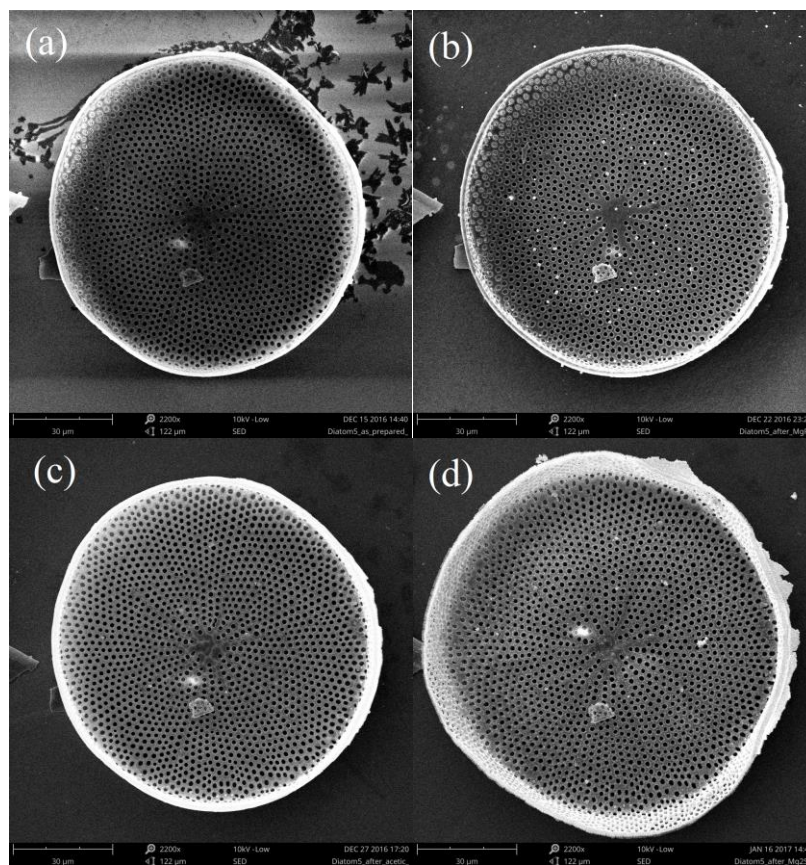
Figure 5.41. SEM images of (a) native silica valve (b) MgO/Si replica (c) porous silicon replica (d) Mg_2Si replica of Mg_2Si 5. SEM images by Sunghwan Hwang, Sandhage Group, Purdue.
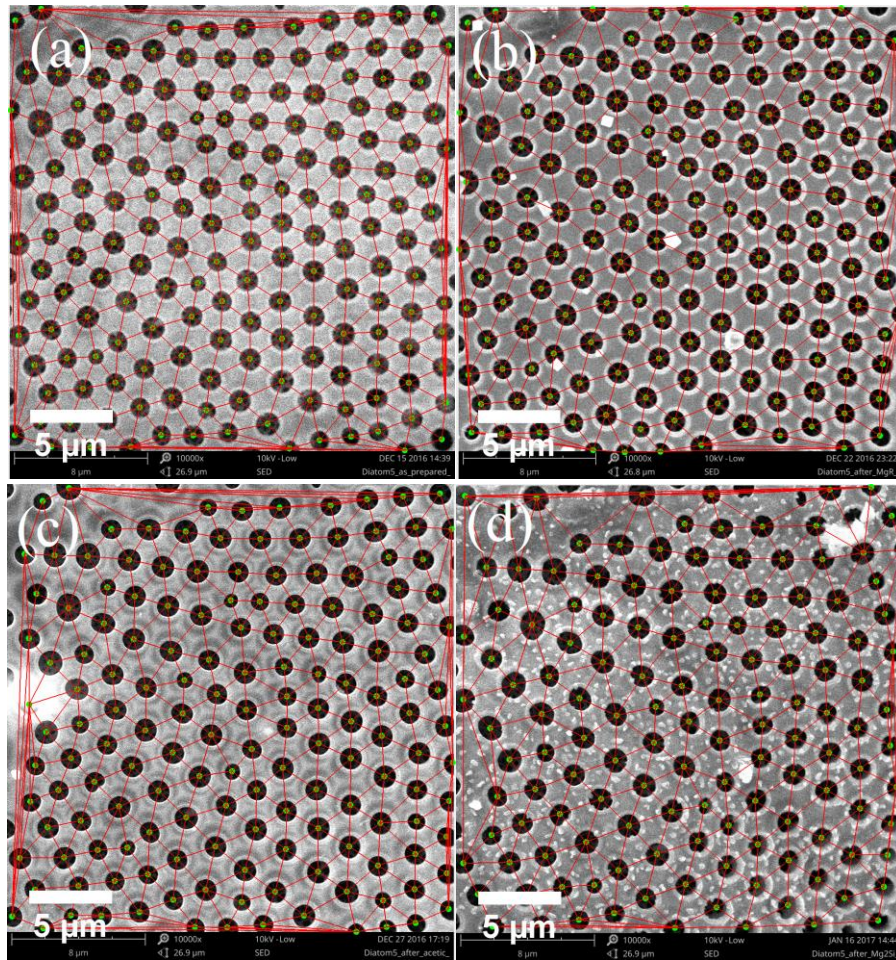
Figure 5.42. SEM images of the same section of holes on Mg_2Si 5 for (a) native silica (b) MgO/Si (c) porous silicon (d) Mg_2Si. SEM images by Sunghwan Hwang, Sandhage Group, Purdue.

While it is not surprising that the difference between conversion stages yielded small changes in radius, this also does not properly assess this method's ability to accurately quantify these results. This could be related to a smaller sample size, an important aspect of this method, where the number of holes sampled for this trial study was one-fourth the size of a normal data set. However, the nonphysical nature of the results

could also indicate that the resolution for this set of images was less than what was required to accurately capture small variations in hole sizes.

Table 5.4. Comparison of data from all stages of conversion for section of Mg_2Si 5.

	SiO$_2$	MgO/Si	Si	Mg$_2$Si	Net Change
Mean Radius Normal (μm)	0.63	0.60	0.62	0.63	
MP Radius Kernel (μm)	0.65	0.63	0.64	0.65	
MP H-H Distance (μm)	2.14	2.19	2.17	2.30	
No. Holes	168	164	158	137	
No. Edges	481	471	451	388	
Radius Normal* Difference (μm)		-0.0280	0.0135	0.0136	-0.0009
Radius Kernel* Difference (μm)		-0.0255	0.0110	0.0143	-0.0002
H-H Difference* (μm)		0.0520	-0.0221	0.1344	0.1643

*Values for these quantities are based on raw data given to four decimal places. Resolution for these images was ±26 nm, final reported values are rounded to the hundredths place.

5.2.3   *Summary and Conclusions*

The worked detailed in this section presented the development and application of an algorithm involving a circle locating program, made possible through CHTs, and a Delaunay triangulation method for the analysis of SEM images of diatom foramen pore patterns. For SEMs with high contrast between holes and the material of the foreground, it was found that the CHT can accurately locate circle centers of judiciously binarized images with minimal post processing, in the majority of cases after binarization, that allows one to obtain physically-consistent estimates of the radius for each hole and the connectivity between neighboring holes. Through careful analysis, pseudo-normal distributions of radii were obtained and were found not to differ considerably when compared against KDE fits

that assume no parametric distribution or symmetry constraints. This, however, was not true for distributions of edge lengths, which followed an asymmetric distribution characterized by having a slowly decaying tail toward longer edge lengths. These data sets were analyzed by a KDE and thus provide an empirical PDF from which the most probably edge length values for each frustules or replica could be obtained. From this, descriptive statistics were obtained regarding the average mean radii and most probable edge lengths and found that, for both quantities, there were no significant differences (i.e. $\geq 10\%$) between diatom frustules and replicas in reference to the differences seen in imaging measurements (section 6.2.2.2). This was attributed to high-quality shape preservation achieved by carefully controlling reaction conditions through the various stages of conversion for diatom frustule and their high index replicas.

5.2.4 *Experimental Details*

5.2.4.1 Scanning Electron Microscopy for Imaging and Hole Pattern Statistics

High resolution and high contrast imaging of diatom and replica frustules for hole pattern statistics was accomplished using a Zeiss Ultra 60 FE-SEM. For high contrast images, all samples were imaged with an accelerating voltage of 10kV. Typical magnification was 7000x for quadrant images and 2170-3170x for whole frustule images with an aperture size of 30.00 µm. Typical scan speed was 3-5.

5.2.4.2 Gold/Palladium Sputtering for Metallization of Silica Diatom Frustules

Metallization of silica diatom frustules was achieved by sputter coating of 60:40 Gold:Palladium thin film using a Hummer 6 Sputtering System. Successful deposition

conditions involved keeping vacuum pressure below 200 mTorr during sputtering with constant flow of Argon gas for plasma with and constant operating current of 25 A for 3 minutes. Since this process is manual, coating thickness will vary sample-to-sample. However, estimated coating thickness is 40-50 nm.

5.3 Ellipsometry Measurements and Modelling of Solution Processed Silica, MgO/Si, and Mg$_2$Si Films

5.3.1 *Background and Experimental Approach*

To accurately account for the effect of refractive index on the optical properties (theory discussed in section 2.4) of natural silica frustules and their high index replicas, ellipsometry measurements were conducted to determine the dispersion curves for these materials in the 500 – 1100 nm wavelength range. Since these films were made from fired TEOS films obtained via spin coating, experimentally confirming the wavelength dependence of these materials is important because: 1) Little-to-no experimental data exists for MgO/Si and Mg$_2$Si films made under similar reaction conditions and 2) The index of a material, particularly thin films, can vary appreciably depending on the processing or reaction conditions. As such, careful attention will be given to characterizing the dispersion curves for the lowest index material - silica, from which MgO/Si and Mg$_2$Si films are made – and gauging the agreement with literature. This is to ensure that, after firing, a uniform dense layer of amorphous silica is formed with reasonable surface roughness. To confirm this, multiple models will be applied in the 500-1100 nm wavelength range, including: a single layer (with regard to the layer on top of the sapphire substrate) fit by a Sellmeier

285

equation derived the literature [133], graded layer (testing density gradients), or multilayers (extreme and unlikely case of stratified layers).

Since information about the optical properties of MgO/Si is limited, obtaining a well-fitting model for this material over the range of 500-1100 nm will be pursued. For composite materials such as MgO/Si, a common model used to estimate the overall dielectric function, and real (n) and imaginary (k) components therein, is an effective medium approximation (EMA, discussed in section 2.3.4). To obtain index information, this analysis is done programmatically in the ellipsometry instrument software where one specifies the expected composition ratio in terms of percentage, as well as other parameters such as thickness, roughness, and absorption coefficient (if known). To match as closely to the composition of the film as possible, a mixture of 65% MgO and 35% Si will be assumed, which agrees well with the expected ratio of molar volumes and was confirmed previously by energy-dispersive X-ray spectroscopy (EDX). If this modelling method is unsuccessful, alternate models, such as those mentioned previously for silica, will be tested. Similar analysis will be carried out for even higher index films of Mg_2Si.

5.3.2 *Results and Discussion*

Initial ellipsometry measurements on silica and MgO/Si films yielded Ψ and Δ spectra with strong oscillations, which caused ambiguity in the modelling of the film layers. These oscillations likely come from the anisotropy of sapphire facilitating strong reflections (potentially coherent) from the back surface of the substrate, despite the accurate modelling of the double side polished sapphire substrate; i.e. index estimated within ±0.001 of literature. [266] Another possibility is that there are variations in the

density of silica and MgO/Si or nonuniform boundaries between the film and substrate that could cause some scattering or interference fringes. Working under the coherent back reflections hypothesis, the back surface of each substrate was roughened thoroughly with a diamond scribe, with the expectation that a roughened back surface will result in more diffuse reflections rather than specular ones and reduce or eliminate the oscillations. Although it did not completely eliminate the oscillations, roughening satisfactorily reduced the waviness in the scans allowing for an acceptable fit.

The dispersion curve for the silica thin film made by firing a spun coated tetraethyl orthosilicate (TEOS) film matched well with curves from the literature (within ±0.01) with a moderately low MSE (23) when modelled as a bilayer film with sapphire as the substrate and silica as the top layer and fit with a Sellmeier dispersion relation. [133, 267] Due to the high IR transparency for silica, more light reaches the back surface of the sapphire substrate and likely causes stronger oscillations when compared to the less IR-transmissive MgO/Si (Figure 5.43a). In addition to this, the discrepancy between the index of this film and the literature could also be ascribed to thickness variations, as evidenced by coloration in the film from interference fringes. Given the beam size is ca. 3 mm in diameter, it is feasible for a thickness gradient to be sampled during measurement. These issues could also be responsible for the slight difference in roughness estimated by ellipsometry (4 nm) and AFM (9 nm). For synthetic film focal imaging, the measurement area is small (ca. $100 \times 100 \ \mu m^2$) and thus thickness variations are less likely a factor. The literature curve was used for simulation purposes for better spectral resolution and consistency when comparing simulations to experimental data. [267]
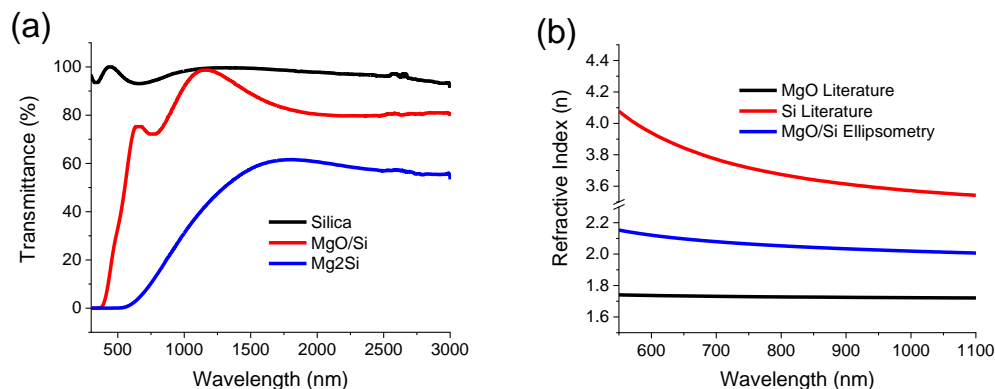
Figure 5.43. Plot of (a) transmittance spectra for thin films of silica, MgO/Si, and Mg$_2$Si (b) dispersion curves over 550-1100 nm for MgO from literature, MgO/Si from ellipsometry and Si from literature.

Ellipsometry measurements for the lesser-known MgO/Si material gave smoother-looking spectra than silica, which is attributed to greater reflectance because of the increased refractive index and optical density in the visible and NIR that removes much of the effects from the sapphire substrate (in addition to roughening). This layer was modelled using an effective medium approximation (EMA) assuming 65% MgO and 35% Si. [132, 163, 167, 168, 268] Thickness (263 nm) and roughness (20 nm) estimates obtained from this model for the MgO/Si layer were accurate within a few nanometres to the values obtained from cross section SEM and AFM (Figure 5.44), respectively. The MSE value (45) obtained from the fit was the lowest among the available methods (i.e. graded layer and multilayer stack) that could be considered physically consistent with the sample and gave a dispersion curve intermediate between that of neat MgO and Si, as seen in Figure 5.43b. [132, 268] Due to appreciable surface roughness and thickness variations, this MSE value was the lowest that could be obtained. As will be discussed later in Chapter 6, the estimated refractive index for MgO/Si matched well with the expected increase in focusing

distance for standardized hole patterns with known dimensions and hole size semi-quantitatively predicted by BPM simulations from section 5.4.
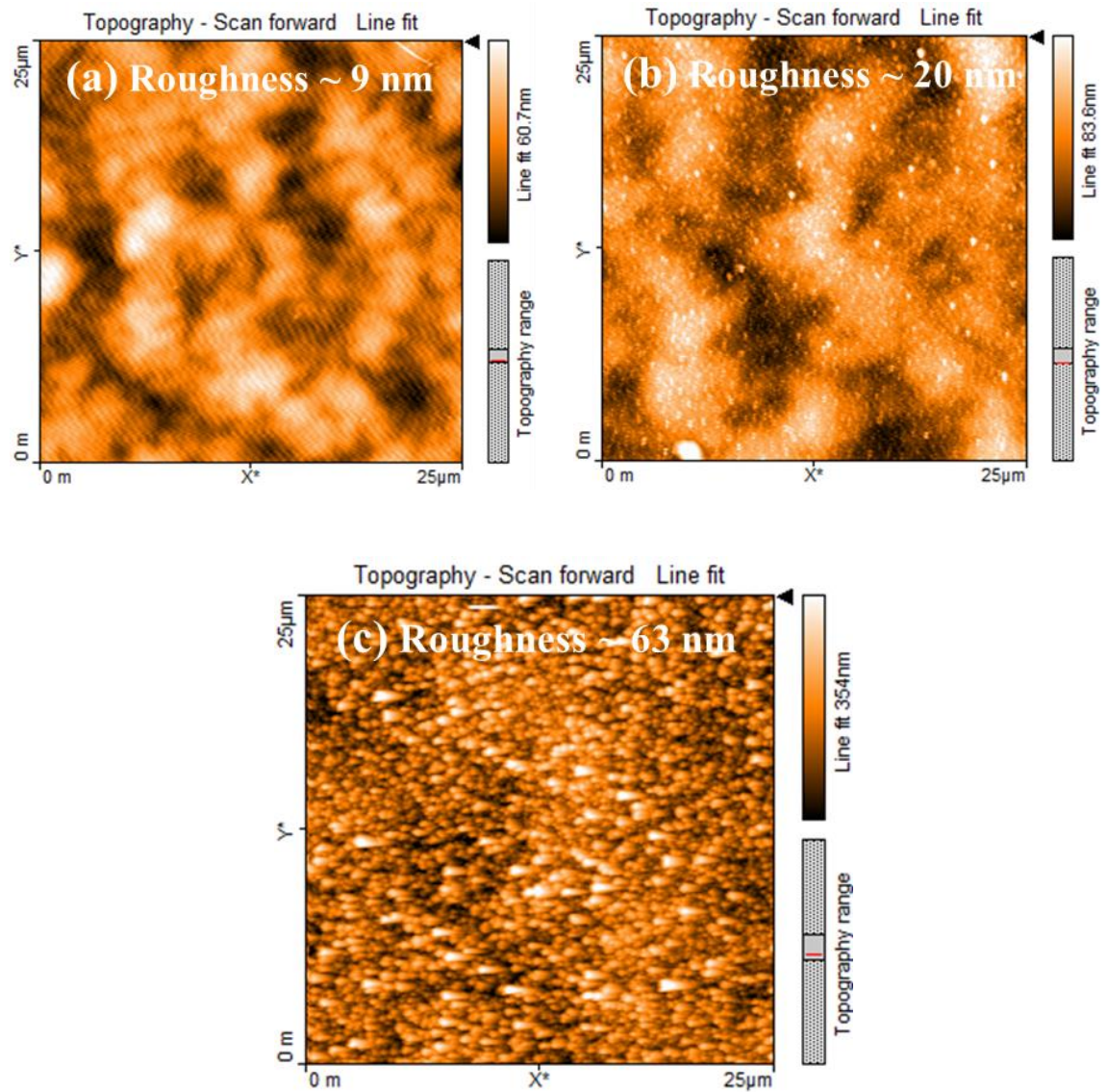
Figure 5.44. AFM images of (a) silica (b) MgO/Si thin film (c) Mg_2Si thin film measured via ellipsometry.

Measurements attempted on an Mg_2Si film did not yield spectra that could be reliably fit by any physically reasonable model (i.e. EMA, graded index, multilayer). Severe oscillations and noise are likely caused by significant surface roughness (ca. 63 nm

from AFM) resulting in significant scattering. Qualitatively, this was supported by ellipsometric measurements taken on Mg2Si samples after roughening the back surface of the sapphire showing equally poor scans. These observations were corroborated by high-resolution SEM of the same thin film (Figure 5.47). These issues are further complicated by strong, broad absorption bands in this spectral range that has been confirmed by absorption spectroscopy (Figure 5.43a). Indeed, one can see discontinuities at ca.700 and 1330 nm in the raw spectra, particularly for Delta, in Figure 5.45 that are likely indicative of two absorption resonances in this film. Although, this observation adds to the complexity of the current analysis, it presents interesting optical behavior considering that, generally, anomalous dispersion of a materials refractive index is observed near resonances. Such effects have been exploited for photonics applications such as controlling group velocity dispersion in fiber optics. [269] If single crystalline Mg$_2$Si films can be achieved or the roughness of polycrystalline films can be reduced, it might be possible to quantify the dispersion in this spectral region.
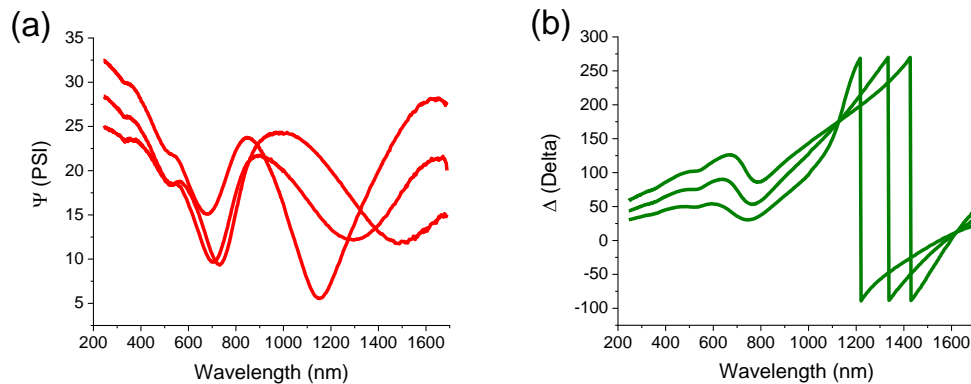
Figure 5.45. Raw data for (a) Psi and (b) Delta collected at angles 65 $^{\circ}$, 70 $^{\circ}$, and 75 $^{\circ}$ for an Mg$_2$Si thin film.

Refractive index values for silica (literature [133]) and MgO/Si (ellipsometry) at the center wavelengths used for synthetic pattern and diatom measurements are tabulated in Table 5.5. Values for MgO/Si are reported to four significant figures based on acceptable MSE values (<50) and satisfactory modelling off sapphire substrate effects.

Table 5.5. Refractive index values for silica from literature and MgO/Si from ellipsometry measurements at wavelengths used for diatom measurements.

Wavelength (nm)	Refractive Index SiO$_2$ [133]	Refractive Index MgO/Si
550	1.460	2.153
650	1.457	2.097
750	1.454	2.065
850	1.453	2.042
950	1.451	2.026
1050	1.450	2.013

5.3.3 *Summary and Conclusions*

In this study, results from ellipsometry measurements on silica, MgO/Si, and Mg$_2$Si thin films were presented for supporting experimental and theoretical analysis regarding the optical properties of native and higher index replica diatom frustules as well as synthetic hole patterns in films of these materials. Initial measurements on samples, all on sapphire substrates, were complicated by spectral oscillations, which were likely caused by interference of potentially coherent back reflections from the front and back surface of sapphire. Roughening the back surface of the sapphire significantly reduced the oscillations such that sapphire itself could be satisfactorily modelled within ± 0.001 of the index values from the literature over the 300-1700 nm wavelength range. This enabled the estimation of the refractive index of MgO/Si with reasonable confidence, which was fit well by an EMA of 65% MgO and 35% Si over the wavelength range 500-1100 and considered suitable for

diatom-relevant experiments and simulations. Due to substantial surface roughness, fitting could not be achieved for thin films of Mg_2Si using either standard or focusing probes methods over 500-1100 nm. Despite this, Mg_2Si films showed evidence of two possible resonances that indicate that anomalous dispersion is present in this material over this wavelength range. However, without such optical properties would be difficult to quantify until surface roughness in Mg_2Si films is greatly reduced.

5.3.4 *Experimental Details*

5.3.4.1 <u>General Details – Spectroscopic Ellipsometry of Silica, MgO/Si and Mg_2Si Thin Films</u>

Refractive index and optical roughness measurements for thin films were carried out using a J. A. Woollam M-2000UI Spectroscopic Ellipsometer with 245-1690 nm wavelength range. Typical scans were acquired at angles of 65°, 70°, and 75°, with 70° as the alignment angle, unless otherwise noted. Model fits in most samples were limited to the wavelength range of interest (ca. 550 – 1100 nm) to improve fit quality. The spot size of the beam for standard and focusing probe measurements was ca. 3 mm and 300 µm in diameter, respectively. All measurements were conducted in ambient conditions. For materials prone to oxidation (MgO/Si and Mg_2Si), measurements were setup prior to removing the sample from a nitrogen-purged glovebox and measured as quickly as possible after removing, typically within 5 minutes.

5.3.4.2 <u>Ellipsometry and Modelling Double Side Polished (DSP) Sapphire Substrate</u>

Prior to measurement, the backside of a 1x1 cm^2 piece of 600 µm thick DSP sapphire substrate (University Wafer #1251, c-m plane 0.2$^\text{o}$) was thoroughly roughened using a diamond scribe to reduce back reflections causing deleterious oscillations. The substrate was modelled as a single layer of sapphire following a Tauc-Lorentz oscillator model over the entire 300-1700 range. [164] The MSE of the fit over this range was 11, with roughness estimated at 4 nm. Compared to sapphire dispersion curves from the literature, all measured data points in the 550-1100 nm range were within ± 0.001 of the reference and thus considered to be accurate for later use in modelling multilayer films. [266]

5.3.4.3   Ellipsometry and Modelling Amorphous Silica Thin Film on DSP Sapphire

Amorphous silica thin films (200 nm thick) were measured using the standard method. As a result of the higher optical transparency of silica compared to MgO/Si and Mg$_2$Si, the oscillations due to sapphire were the most severe of all the samples due to a greater portion of the beam reaching the sapphire and being reflected with minimal attenuation. As was done with all samples, the back surface of the sapphire substrate was roughened considerably, which reduced oscillations but did not completely remove them. The sample was modelled as two layers, the top layer being 200 nm thick amorphous silica and the bottom sapphire.

Modelling as a double layer with no density gradients or EMA gave the best fits (MSE ca. 23) and matched best with the physical nature of the sample. This is expected because this film was made from a spin coated tetraethyl orthosilicate (TEOS) film which, after firing at 700 $^\text{o}$C, forms a single dense layer. Discrepancies were found between the

293

estimated roughness by ellipsometry (4 nm) and AFM (9 nm), which were attributed to macroscopic thickness variations that skew roughness estimations from ellipsometry. To circumvent this, focusing probes were used to reduce the illumination area to ca. 300 μm in diameter. Using the focusing probes, a graded layer method (approximated as 5 layers) provided the best fit (average MSE ca. 20) and gave a roughness of ca. 10 nm, matching more closely to AFM values. However, the indices estimated for the "top" and "bottom" layers of the silica film by the model were much higher than that expected for silica. Due to the closeness of the top layer values to the index of sapphire (i.e. 1.54-1.69 for the "top" layer and 1.37-1.50 for the "bottom" layer in the 500-1100 nm range), the index inflation was thought to be caused by anisotropic effects of sapphire. Since the back surface was etched by hand with a diamond scribe, it is possible that locally (within the 300 μm beam diameter) the back surface of sapphire was not roughened satisfactorily and could have given strong coherent reflections. Based on the discussion above, it was decided that the results obtained by the standard ellipsometry method were less prone to sapphire interference and were thus considered more accurate, although still offset somewhat from literature values. [133]

5.3.4.4   Ellipsometry and Modelling MgO/Si Thin Film on DSP Sapphire

Standard ellipsometry measurements (measurement angles = 58°, 60°, 62°) on a ca. 260 nm MgO/Si thin film were modelled over the 500-1100 nm wavelength range using an effective medium approximation (EMA) assuming a composition of 35% Si and 65% MgO (composition error from fit ± 3.99%), based on molar volume of each component. The resulting fit had an MSE of 45 with an accurately estimated thickness (263.0 ± 1.8 nm) and roughness (19.47 ± 0.45 nm), confirmed by cross-sectional SEM and AFM (as seen in

Figure 5.44), respectively. At first glance, the oscillations due to sapphire were not as noticeable over the entire spectral range as silica, which was tentatively assigned to the generally reduced transparency of MgO/Si relative to silica. However, the MSE was slightly larger than the fit for silica. Further inspection of the fit shows that the portions of the curves at longer wavelengths were not fit as well as those in the visible for MgO/Si (Figure 5.46). This is likely due to the much greater transparency of MgO/Si in the IR compared to the visible (Figure 5.43a), which likely means that wavelengths in that region reach the sapphire substrate and are strongly reflected with minimal attenuation and thus may contribute to broad oscillations that affect the fit.
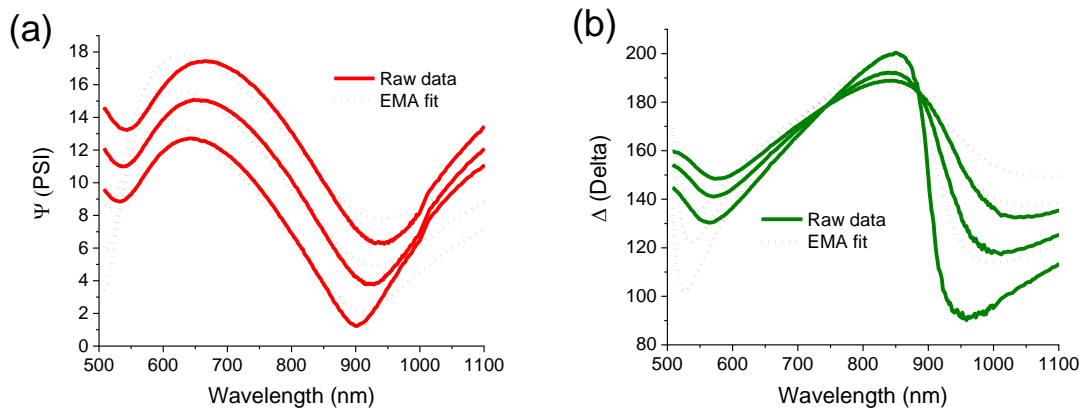
Figure 5.46. (a) Plot of Ψ .vs. wavelength and (b) Plot of Δ .vs. wavelength raw data from MgO/Si thin film.

5.3.4.5 Ellipsometry and Modelling Mg$_2$Si Thin Film on DSP Sapphire

Standard and focusing probe measurements were carried out for Mg$_2$Si thin films on DSP sapphire substrates with non-roughened and roughened back surfaces. Since Mg$_2$Si is substantially less transmissive and much higher in index than silica and MgO/Si, initial measurements were done without roughening the backside of the sapphire, working under

the hypothesis that little-to-no light be make it to the sapphire layer. Later measurements with the backside roughened showed no noticeable changes, confirming this the limited transmission hypothesis. Despite the lack of sapphire reflection, all scans obtained from Mg_2Si could not be fit quantifiably (MSE >100). For the standard measurement method, various angles and spots of the film were tried but did not result in any improvements in the S/N. Cracks in the films (unavoidably consequence of cleaning processes involving HCl washing step) could be seen (Figure 5.47c) over various parts of the film and were thought to contribute to the poor S/N. In an attempt to circumvent this issue, focusing probes were used to reduce the beam size to ca. 300 µm, reducing the chances to part of the beam illuminating a crack, but yielded no improvements in scan quality. AFM on these films confirms surface roughness of 63 nm which, considering the film is ca. 300 nm thick, presents frequent and large changes in thickness over the entirety of the film and is thought to be the cause for poor scan quality.
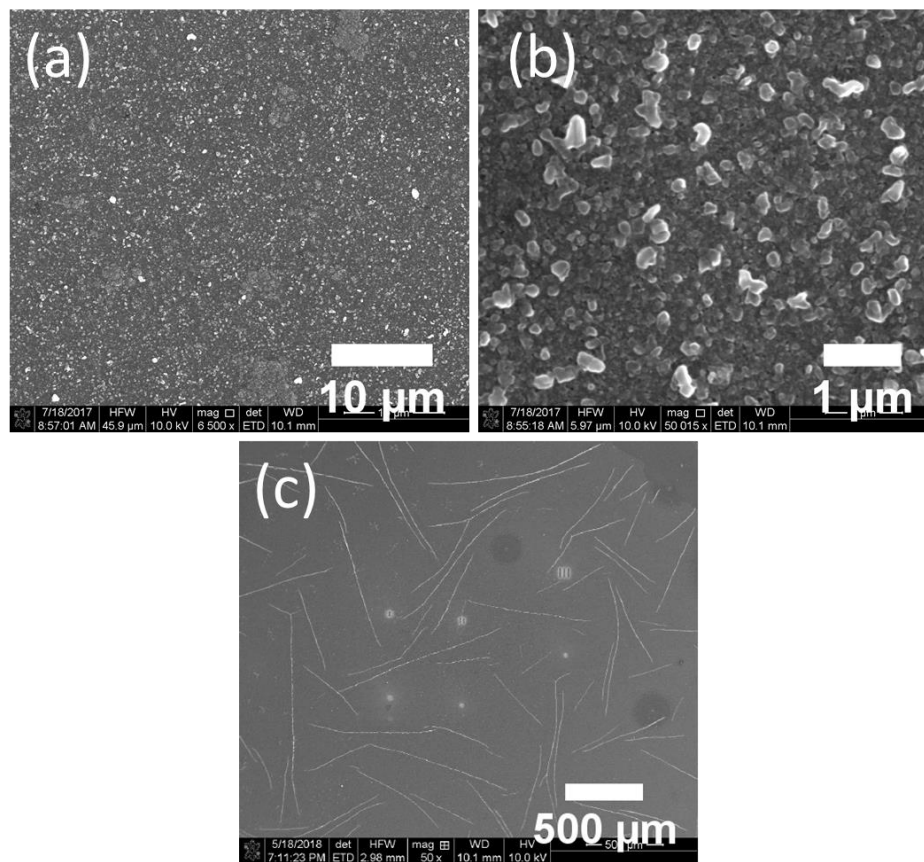
Figure 5.47. (a) Large area SEM image of Mg2Si thin film surface used for ellipsometry (b) Higher magnification SEM of the same Mg2Si film (c) SEM of cracking after HCl washing step – images by Jiaqi Li, Sandhage Group, Purdue.

5.3.4.6 Atomic Force Microscopy of Silica, MgO/Si and Mg$_2$Si Thin Films

Surface topology and roughness measurements were made using a Nanosurf easyscan2 with a 70 µm (±15%) atomic force microscope scan head with maximum scan range = 70 µm, maximum Z-range = 14 µm, drive resolution Z = 0.21 nm, drive resolution XY = 1.1 nm, XY-linearity mean error = <1.2%, Z-measurement noise level (RMS, Dynamic Mode) = 0.5 nm. Three scans per sample were measured in NCLR Dynamic

Mode with a typical with a scan area of 25x25 μm^2. Roughness values reported are the arithmetic mean of the RMS area roughness from three measurements.

5.3.4.7 Preparation of Silica, MgO/Si, and Mg$_2$Si Thin Films

The following procedure is courtesy of Jiaqi Li, Sandhage group, Purdue. Sol formation begings by adding 5 mL of tetraethylorthosilicate (TEOS) drop-wise into 5 mL ethanol (200 proof) and stirring well to ensure mixing. 0.81 mL of DI H$_2$O is added, followed by 0.81 mL of 0.1 M HCl. This solution was refluxed at 70 ^{o}C for 2 hours with stirring. Separately, an aqueous 22% wt methycellulose (MC) solution is made by stirring 287.4 mg MC in 14.1 mL DI H$_2$O for 2 hours. The TEOS and MC solutions are then mixed to obtain a 2% wt final sol-gel solution, which is stirred for 30 hours at room temperature.

Prior to spin coating, sapphire wafers (University wafer) are cut into 1x1 cm^2 squares, then cleaned by ozone, washed with water, and dried with nitrogen. On the spin coating chuck, the MC+TEOS solution is dripped (4-5 drops) onto the substrate and spun at 3000 RPM for 20 seconds. After spinning, the film is aged overnight at room temperature and then dried in a vacuum oven at 60 ^{o}C for 30 min. The as-dried film is then fired in air at 700 ^{o}C fir 15 min (ramping/cooling temperature 2 ^{o}C/min). In converting silica films to MgO/Si, the silica films on sapphire substrates are reacted with Mg vapor using Mg$_2$Si granules as the gas source at 750 ^{o}C for 6 hours with carrier glass a mixture of H$_2$ and Ar, and a low-carbon steel ampoule. Between MgO/Si and Mg$_2$Si, the MgO is dissolved by 3M HCl for 30 min inside an Ar-purged glovebox to yield porous silicon films. These silicon films are then reaction with Mg gas (Mg foil as gas source) at 600 ^{o}C for 4 hours in a stainless-steel

tube with carrier gas mixture of H_2 and Ar. Thicknesses were confirmed by cross-sectional SEM.

5.4 Beam Propagation Simulations of Standardized Pattern in SiO_2 and MgO/Si Films

5.4.1 *Background and Experimental Approach*

The complexity of diatom frustules results in an equally complex superposition of optical waves upon diffraction that characterize the observed interference phenomena, which are difficult to deconvolute. This, among other factors, complicates the characterization of the wavelength-dependence in the focusing behavior of these systems and limits the understanding of how one can use the solid-state chemistries described in section 1.3.2 to extend the optical properties into the IR. Working toward developing a model system that could facilitate this level of understanding, this process begins by understanding the inherent dependence on focusing distance for foramen hole arrays in the refractive index range of interest, i.e. for that of patterns in SiO_2 and MgO/Si thin films. Therefore, it is necessary to design a control experiment such that a direct correlation between focusing distance and index at known wavelengths can be obtained for a given hole pattern. Despite the interest shown for index-dependent focusing phenomena for various types of photonic structures, investigations to-date have found no clear parameterized relationships between focusing distance, as well as other quantities like the full width at half maximum (FWHM) of the focused beam, and refractive index. [127, 270-272] As such, these studies obtained an empirical relationship via BPM simulations, which were used to corroborate experimental observations.

A theoretical investigation by Wang *et al.* [270] regarding micro/nano fiber arrays for the subwavelength-focusing of optical waves provides insights into how diffracting fiber-based elements can be arranged to control the distance at which focusing occurs and how tightly the light is confined at the focus. The fiber bundles discussed in that work are similar to diatom structures in that, like the wavelets diffracted by the fiber tips, the interference patterns from the diatom frustules are thought to originate from diffracted wavelets exiting each hole. The advantage of this similarity is that the experiment design principles by Wang *et al*. [270] can be applied to model the behavior of simple hole arrays with known dimensions so the effect of index on the focusing behavior can be isolated and studied. Although it is noted that, unlike optical fibers, which possess a higher refractive index core than the outer cladding layers, the diatom samples are opposite in their index profile where the holes (analogous to the core) are treated as air voids and the surrounding material (cladding) is silica, MgO/Si, or Mg_2Si. Regardless, the approach to making a standardized hole array for this study will be based on the concentric ring structure illustrated in Figure 5.48a, which at a defined hole size and separation distance (defined by the radius difference between rings) was shown to give a single, intense focal spot as shown in Figure 5.48b.
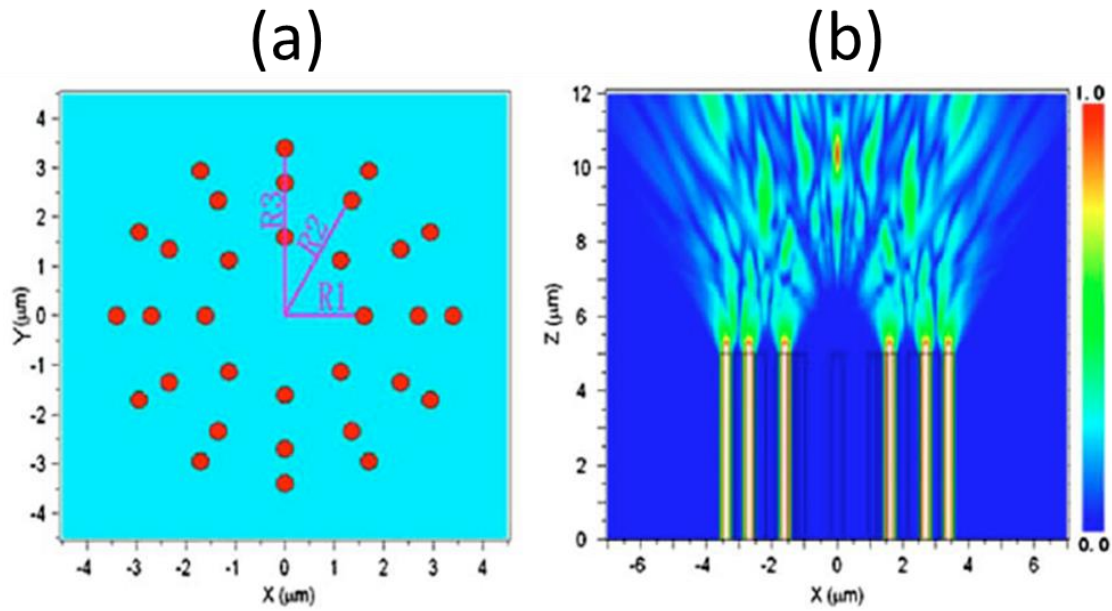
Figure 5.48. (a) Illustration of three concentric rings of fiber arrays that produced focusing results in cross section view "b" (radii R_1: 1.6 µm, R_2: 2.7 µm, R_3: 3.4 µm); (b) Countour plot of focal point cross section from array "a". Adapted from Wang *et al*. [270] with permission. Copyright 2009 Journal of the Optical Society of America.

In the following section, details for BPM simulations used in determining the appropriate hole array geometry and size will be discussed in terms of the pattern's ability to provide a high-contrast focal pattern that is able to be resolved easily by the measurement setup described in section 2.3.5 and Chapter 6. From there, the dependence on refractive index, as a function of wavelength, on the focusing distance will be investigated. Simulations will not be pursued for Mg_2Si, given that the refractive index in this wavelength range is unknown and could not be characterized by ellipsometry (see section 5.3.2 for discussion).

5.4.2   *Results and Discussion*

Determining the hole pattern geometry suitable for this experiment began by taking a simple, analogous pattern like Figure 5.49a and adjusting the hole sizes and spacing (i.e. spacing between holes and the radii separating concentric circles of holes) so that the focal spot would be at a reasonable distance and confined within an approximately 500 µm-wide area in space that could easily be measured within the imaging measurements setup discussed in section 2.3.5 and Chapter 6. The hole array was constructed by plotting 2 µm holes at 8 evenly spaced points (i.e. every $\pi/8$ radians) along the perimeter of three concentric circles of radii 4.5, 8.5 and 13 µm (Figure 5.49a).
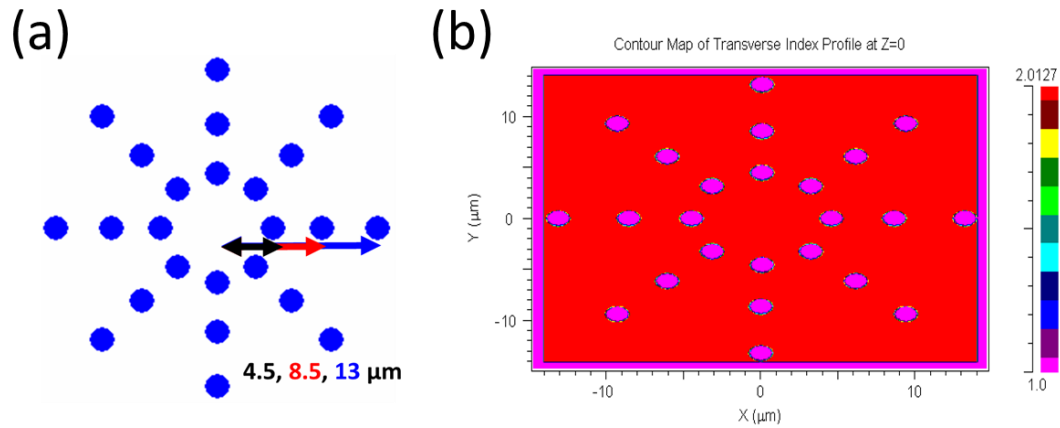
Figure 5.49. (a) Hole pattern as plotted in matlab; (b) Index profile for pattern "a" in a MgO/Si thin film as shown after importing into RSoft.

The binary image of the standardized hole pattern was converted to an index profile format (.ipf) image and imported into RSoft. Figure 5.49b shows the visualization of the index pattern in MgO/Si within the software, where the red areas correspond to the foreground (MgO/Si film) and the pink circles correspond to the holes (air, n = 1). In this configuration the imported pattern reflects the physical description of the film itself but ignores the substrate. However, given that sapphire is a single crystal and highly

transparent in the 500-1100 nm wavelength range of interest, the substrate is assumed to have no contributions to measured values. This greatly reduced the complexity of the simulation and shortens computation time not having to monitor propagation through the 430 µm thick substrate.
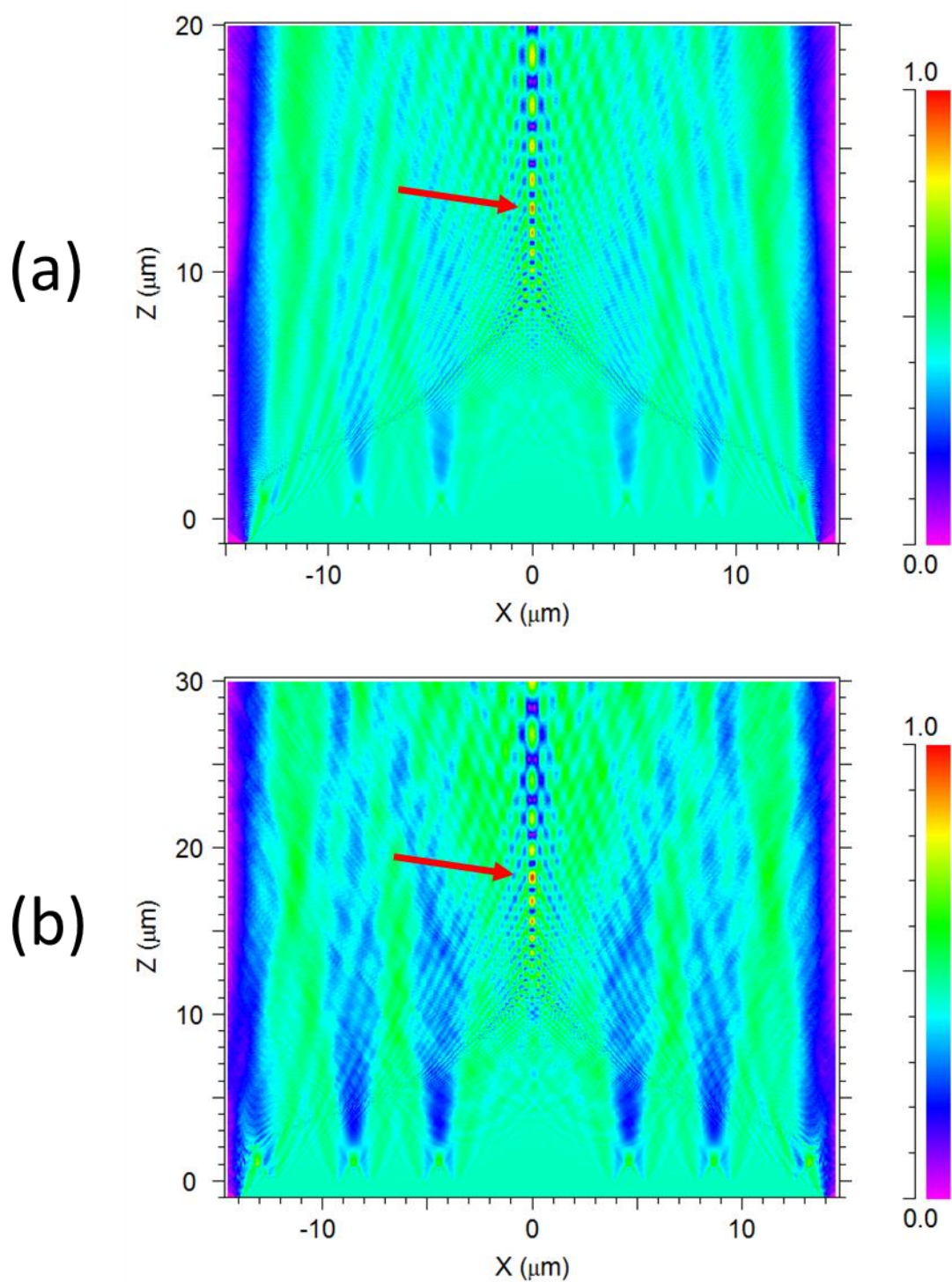
Figure 5.50. Interference resulting from standardized pattern in (a) silica and (b) MgO/Si thin films with the standardized patterns at λ = 850 nm. Arrows point to the brightest focal spots in each scan.

The interference pattern in the plane behind the standardized pattern was monitored in the XZ plane with a resolution of 20 nm in the X and Y directions and taking 50 nm steps in Z. Since only one wavelength could be run at a time (although up to three simulations at different wavelengths could be runs simultaneously and not fail due to memory limitations), these parameters kept simulation time at moderate distances (up to ca. 50 µm in Z direction) down to a few minutes. Figure 5.50a-b shows two example interference patterns from a silica (a) and MgO/Si (b) film at an illumination wavelength of 850 nm. As will be discussed further in Chapter 6, although there are multiple foci predicted by in the simulation, only one spot is observed experimentally. In each simulation, there is one spot (ca. 500 µm at FWHM), usually the 4-5th local maximum, that is significantly more intense than the rest and is immediately followed by spots that are dramatically less intense. To simplify the analysis, the brightest local maximum (i.e. focal distance with the most constructive interference) is taken to be the primary focal spot and is found to match closely with focusing distances obtained from measurements (see section 6.2.2.1). [128] Naturally, there are some assumptions made that could cause discrepancies between the experimental and simulation data such as: thickness variations, light transmission, surface roughness, hole size uniformity, spectral purity of the incoming beam, and error in the actuators controlling stage movement; which will be discussed further in Chapter 6.

Table 5.6. Refractive index data for SiO_2 from reference [133] and MgO/Si index obtained from ellipsometry for simulated focal distances, and respective percent differences in reference to the change for each quantity between SiO_2 and MgO/Si.

λ (nm)	Index SiO_2	Index MgO/Si	Index Percent Difference (%)	Simulated Focal Distance SiO_2 (µm)	Simulated Focal Distance MgO/Si (µm)	Focal Distance Percent Difference (%)
550	1.460	2.153	38	20.1	29.4	38
650	1.457	2.097	36	16.8	24.0	35
750	1.454	2.065	35	14.4	20.2	34
850	1.453	2.043	34	12.6	17.9	35
950	1.451	2.026	33	11.3	15.9	34
1050	1.450	2.013	33	10.3	14.3	33

Using the above convention, the focal distance for the standard patterns in silica and MgO/Si films were tabulated as a function of wavelength as seen in Table 5.6. From this data set, the similarity between the percent differences of the refractive indices and simulated focal distances at each wavelength for silica and MgO/Si shows that the focal distance scales with index. Although the exact cause for this is unclear, there is a clear decrease in the diffraction angle associated with an increase in refractive index that requires longer propagation lengths in the plane behind the pattern to achieve maximum, confined interference. As will be discussed later in the experimental measurements from Chapter 6, this is in semi-quantitative agreement with standardized hole patterns of the same dimensions made into silica and MgO/Si thin films via focused ion beam (FIB) milling.

5.4.3 *Summary and Conclusions*

In this section, the development of a control experiment to determine the index dependence of focusing distance for a given hole pattern was developed and implemented. Beam propagation (BPM) simulations on standardized patterns in silica and MgO/Si thin films showed that the primary focal spot for the higher index MgO/Si pattern was at longer

distances from the plane of the thin than the lower index silica pattern. The origin of this effect is unclear, however, signifies a reduction in diffraction angle with increasing refractive index. In terms of the wavelength dispersion of this trend, focusing distances were found to decrease concomitantly with index as the illumination wavelength was increased by 100 nm steps in over 550-1050 nm, as anticipated.

5.4.4 *Experimental Details*

5.4.4.1 BPM Simulations of Standardized Hole Patterns

Numerical beam propagation simulations of the standardized pattern were performed using the BPM software package BeamPROP in RSoft CAD Environment 7.0 based on the Pade-wide angle technique. [273] All simulations used Pade coefficients (1,1). For customized simulations, it is necessary to import the desired hole patterns as high-contrast index profile. This is done by binarizing the plotted hole pattern and converting into a tab-delimited comma separated value (CSV) format using Matlab. This CSV file is then read into Notepad++, where the first four lines of the file are filled with dimensional information (the height and width of the image in pixels) and saved as a .ipf file (IPF, index profile). In this format, the index profile can be read by RSoft and the dimensions of the hole pattern can be defined within RSoft and will scale correctly as along as the pixel dimensions in the IPF are defined correctly. Simulations at 550, 650, 750, 850, 950, and 1050 nm wavelengths were performed for all samples, accounting for the change in refractive index with wavelength.

For standardized pattern, the grid size was set to 20 nm in the X and Y direction and 50 nm for the Z direction. Simulations are started 1 µm before the sample plane and

307

monitors propagation through the sample until 20 µm and 30 µm in the dark plane behind the silica and MgO/Si patterns, respectively. Typical simulation time for a standardized pattern at a single wavelength is 1-3 minutes, depending on simulation depth in the Z direction. The field shape was set as rectangular and a typical illumination power was 0.1-0.2. Wave propagation is monitored as a contour map in the XZ plane. Film thickness was assumed to be 200 nm, closely matching experimental values.

5.5   Chapter Summary

This chapter presented a combination of theoretical and experimental investigations into material and structural factors necessary for the accurate modeling and analysis of diatom frustules. In section 5.2, the computational calculation of foramen hole patterns in terms of radius and hole-to-hole parameters was explored. The application of CHT and Delaunay triangulation algorithms to binarized images of foramen hole patterns allowed for rapid hole location, radius estimation, and hole-to-hole distance calculation for native silica diatoms and higher index replicas (MgO/Si and Mg_2Si). Statistical analysis of these patterns revealed that no significant differences (i.e. >10%) were found between individual diatoms or between native and replica frustules, confirming high quality shape preservation through different stages of conversion. Analysis was also provided in terms of how resolution affects the accuracy of these methods, which was determined to be semi-quantitative, but physically consistent with the frustules examined.

Section 5.3 detailed a brief set of ellipsometry measurements on thin films of silica, MgO/Si and Mg_2Si in an attempt to obtain the refractive index dispersion in the 550-1050 nm wavelength range. Despite spectral oscillations from the anisotropy of the sapphire

substrate, reliable measurements were obtained for silica and MgO/Si. Silica was found to match closely with the literature and MgO/Si was modelled well by an EMA, assuming a composition of 65% MgO and 35% Si with reasonable MSE (<50) for a polycrystalline sample. Measurements on Mg_2Si thin films did not yield fittable scans due to substantial surface roughness (ca. 63 nm), confirmed by AFM.

The results from ellipsometry were then used to enhance the accuracy in modeling the focusing behavior of standardized hole patterns in silica and MgO/Si thin films in section 5.4. These simulations were conducted as a control experiment to empirically determine the impact of refractive index (as a function of wavelength) on the focusing distance. Taking inspiration from the literature [270], this was accomplished by creating a simple hole pattern that provided a simplified focusing pattern and simulating (BPM) the interference from the same pattern in silica and MgO/Si thin films. The percent difference in the change of the focusing distance correlated strongly with the percent difference of the change in refractive index. Although the origin for this is unclear, there is an apparent decrease in the diffraction angle upon an increase in refractive index.

5.6 References

107. Khorasaninejad, M., Chen, W.T., Devlin, R.C., Oh, J., Zhu, A.Y., and Capasso, F., *Metalenses at visible wavelengths: Diffraction-limited focusing and subwavelength resolution imaging.* Science, 2016. **352**(6290): p. 1190-1194.

115. Khorasaninejad, M., Shi, Z., Zhu, A.Y., Chen, W.T., Sanjeev, V., Zaidi, A., and Capasso, F., *Achromatic Metalens over 60 nm Bandwidth in the Visible and Metalens with Reverse Chromatic Dispersion.* Nano Letters, 2017. **17**(3): p. 1819-1824.

126. Romann, J., Valmalette, J.C., Røyset, A., and Einarsrud, M.A., *Optical properties of single diatom frustules revealed by confocal microspectroscopy.* Optics Letters, 2015. **40**(5): p. 740-743.

127. Stefano, L.D., Rea, I., Rendina, I., Stefano, M.D., and Moretti, L., *Lensless light focusing with the centric marine diatom Coscinodiscus walesii.* Optics Express, 2007. **15**(26): p. 18082-18088.

128. De Tommasi, E., Rea, I., Mocella, V., Moretti, L., De Stefano, M., Rendina, I., and De Stefano, L., *Multi-wavelength study of light transmitted through a single marine centric diatom.* Optics Express, 2010. **18**(12): p. 12203-12212.

132. Green, M.A., *Self-consistent optical parameters of intrinsic silicon at 300K including temperature coefficients.* Solar Energy Materials and Solar Cells, 2008. **92**(11): p. 1305-1310.

133. Malitson, I.H., *Interspecimen Comparison of the Refractive Index of Fused Silica.* Journal of the Optical Society of America, 1965. **55**(10): p. 1205-1209.

163. Jellison, G.E., *3 - Data Analysis for Spectroscopic Ellipsometry*, in *Handbook of Ellipsometry*, H.G. Tompkins and E.A. Irene, Editors. 2005, William Andrew Publishing: Norwich, NY. p. 237-296.

164. Collins, R.W. and Ferlauto, A.S., *2 - Optical Physics of Materials*, in *Handbook of Ellipsometry*, H.G. Tompkins and E.A. Irene, Editors. 2005, William Andrew Publishing: Norwich, NY. p. 93-235.

167. Aspnes, D.E., Theeten, J.B., and Hottier, F., *Investigation of effective-medium models of microscopic surface roughness by spectroscopic ellipsometry.* Physical Review B, 1979. **20**(8): p. 3292-3302.

168. Aspnes, D.E., *Optical properties of thin films.* Thin Solid Films, 1982. **89**(3): p. 249-262.

255. Finkel, Z.V., Vaillancourt, C.J., Irwin, A.J., Reavie, E.D., and Smol, J.P., *Environmental control of diatom community size structure varies across aquatic ecosystems.* Proceedings of the Royal Society B: Biological Sciences, 2009. **276**(1662): p. 1627-1634.

256. Cohoon, G.A., Alvarez, C.E., Meyers, K., Deheyn, D.D., Hildebrand, M., Kieu, K., and Norwood, R.A. *Analysis of quasi-periodic pore-network structure of centric marine diatom frustules*. in *SPIE BiOS*. 2015. SPIE.

257. Atherton, T.J. and Kerbyson, D.J., *Size invariant circle detection*, in *Image and Vision Computing*. 1999. p. 795-803.

258. Yuen, H.K., Princen, J., Illingworth, J., and Kittler, J., *Comparative study of Hough transform methods for circle finding*, in *Image and Vision Computing*. 1990. p. 71-77.

259. MathWorks. *imfindcircles*. 2018 [cited 2018 August 23]; Available from: https://www.mathworks.com/help/images/ref/imfindcircles.html.

260. *Delaunay Triangulation.* 2018 [cited 2018 August 24]; Available from: https://www.mathworks.com/help/matlab/math/delaunay-triangulation.html.

261. de Berg, M., Cheong, O., van Kreveld, M., and Overmars, M., *Delaunay Triangulations*, in *Computational Geometry: Algorithms and Applications*. 2008, Springer: Berlin, DE. p. 191-215.

262. Boas, M.L., *Mathematical Methods in the Physical Sciences*. Third ed. 2006, Hoboken, NJ, USA: John Wiley & Sons, Inc.

263. Wand, M.P. and Jones, M.C., *Kernel Smoothing: Monographs on Statistics and Applied Probability*. First ed. 1995, New York: Chapman and Hall.

264. *ksdensity.* 2018 [cited 2018 August 23]; Available from: https://www.mathworks.com/help/stats/ksdensity.html.

265. Rose, C. and Smith, M.D., *Mathematical Statistics with Mathematica*, ed. G. Casella, S. Fienberg, and I. Olkin. 2001, New York, NY: Springer Texts in Statistics.

266. Dodge, M.J., *Refractive Index*, in *Handbook of Laser Science and Technology*. 1986, CRC Press: Boca Raton, FL. p. 30.

267. Tan, C.Z., *Determination of refractive index of silica glass for infrared wavelengths by IR spectroscopy.* Journal of Non-Crystalline Solids, 1998. **223**(1): p. 158-163.

268. Stephens, R.E. and Malitson, I.H., *Index of refraction of magnesium oxide.* Journal of Research of the National Bureau of Standards, 1952. **49**(4): p. 249-252.

269. Khazaeizhad, R., Kassani, S.H., Jeong, H., Yeom, D.-I., and Oh, K., *Mode-locking of Er-doped fiber laser using a multilayer MoS2 thin film as a saturable absorber in both anomalous and normal dispersion regimes.* Optics Express, 2014. **22**(19): p. 23732-23742.

270. Wang, X., Fu, J., Liu, X., and Tong, L.-M., *Subwavelength focusing by a micro/nanofiber array.* Journal of the Optical Society of America A, 2009. **26**(8): p. 1827-1833.

271. Tingting, W., Cuifang, K., Xiang, H., and Xu, L., *Subwavelength focusing by a microsphere array.* Journal of Optics, 2011. **13**(3): p. 035702.

272. Roy, T., Rogers, E.T.F., and Zheludev, N.I., *Sub-wavelength focusing meta-lens.* Optics Express, 2013. **21**(6): p. 7577-7582.

273. Hadley, G.R., *Wide-angle beam propagation using Padé approximant operators.* Optics Letters, 1992. **17**(20): p. 1426-1428.

CHAPTER 6. SPECTROSCOPIC CHARACTERIZATION AND ANALYSIS OF NATIVE SILICA DIATOM FRUSTULES, HIGH INDEX REPLICAS, AND SYNTHETIC PATTERNS IN THIN FILMS

6.1 Chapter Introduction

This chapter presents an experimental investigation into the influence of refractive index and hole pattern geometries on the focusing behavior in the visible and NIR for synthetic patterns, natural silica diatom valves, and higher index replicas. Results from interference imaging measurements will be discussed in detail in sections 6.2.2.1-6.2.2.2, using theoretical data obtained from Chapter 5 in conjunction with diffraction and interference optics theories to identify the material and structural parameters that contribute to the focusing behavior of these biophotonic systems. Analysis will be provided to describe the limitations of simulations and how uncertainty in specific experimental variables could cause discrepancies in focal distances between theoretical predictions and experimental data. Results from this work will be used to compare diatom valves to state-of-the-art, high numerical aperture objectives and metalenses and thus assess their utility as light-concentrating, micro-photonic elements.

6.2 Focal Spot Mapping Measurements on Standardized and Naturally-Derived Diatom Patterns

6.2.1 *Background and Experimental Approach*

Theoretical data obtained from Chapter 5 showed that, for the same hole pattern in different thin film materials (i.e. silica and MgO/Si), the expected decrease in focusing

distance as one increases wavelength should closely follow the dispersion in refractive index. This agreed with other theoretical investigations [127, 270] and suggests that the same should be true for higher index diatom valves at NIR wavelengths, provided that the shape is well-preserved upon conversion and that the foramen holes patterns are, indeed, the structural parameter that controls the focusing patterns from these frustules (Figure 6.1). Since most studies to-date have focused on the photosynthetic properties of diatom valves, the wavelength dependence in the focusing distance has only been measured over limited parts of the visible spectrum. [128, 129] Further, information about the NIR behavior for *C. wailessii* valves is, to the best of the author's knowledge, limited to theoretical calculations (Figure 6.1b). [127] As such, one of the goals for this chapter is to obtain corroborating experimental data in the NIR for native silica and higher index replicas to extend knowledge in this area.
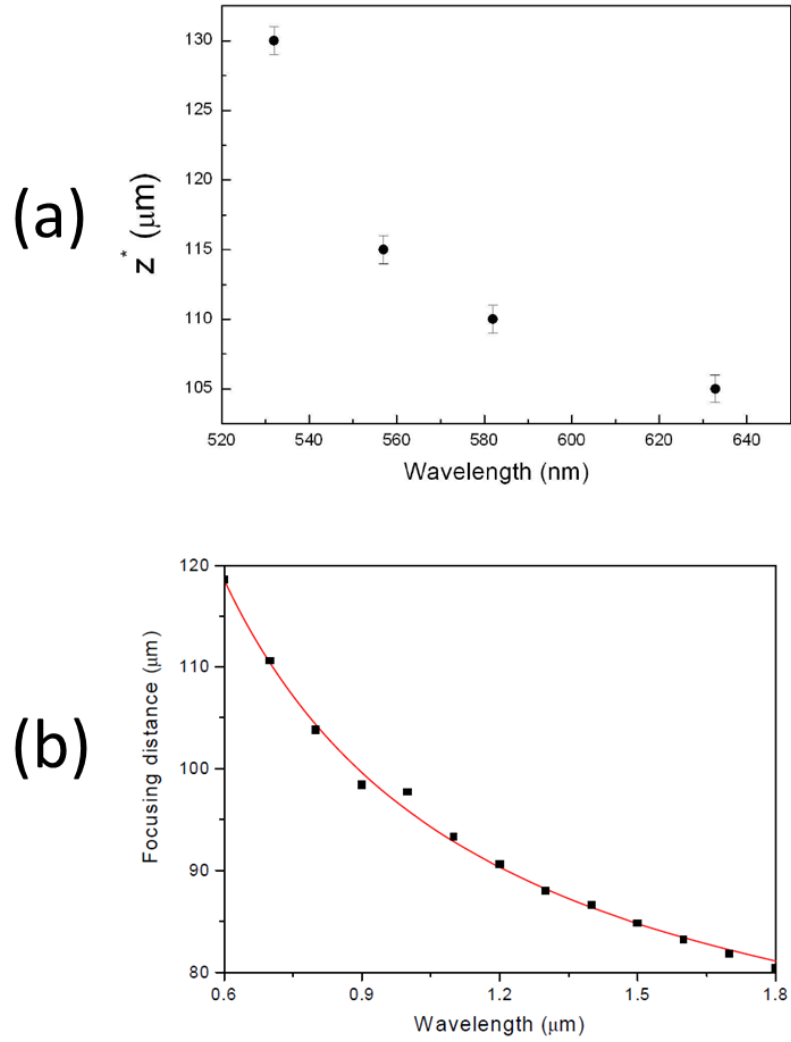
Figure 6.1. (a) Measured focusing distances (labelled as z*) for the focal spots of maximum intensity for a *C. wailessii* valve over 520-640 nm wavelengths. Reproduced from De Tomassi *et al.* [128] with permission. Copyright 2010 Optics Express (b) Calculated focussing distances in the visible and NIR for a *C. wailessii* valve. Reproduced from De Stefano et al. [127] with permission. Copyright 2007 Optics Express.

The most straightforward way to obtain this focusing information is through a far field interference imaging method described previously in the literature. [127, 128] An overview of the setup used in this dissertation is provided in section 2.3.5. Since there is inherent variability between individual diatoms, data for five frustules/replicas of each material will be measured and the arithmetic mean of these focusing distances at each

315

wavelength will be reported. In combination with focusing distances obtained from BPM simulations and computationally-derived hole pattern statistics from Chapter 5, analysis will be presented to determine if the silica and higher index valves studied here follow the trends in the literature and arguments are presented to describe possible explanations for discrepancies.

6.2.2   *Results and Discussion*

6.2.2.1   Focusing Measurements on Standardized Patterns in Silica, MgO/Si, and Mg$_2$Si in the Visible and Near Infrared

High-quality standardized hole patterns that matched well with the dimensions of the simulated patterns discussed in section 5.4, were obtained via focused ion beam (FIB) milling in thin films of silica and MgO/Si made by the TEOS spin coating method (section 6.2.4.3). These patterns (Figure 6.2), where measured using the far field imaging method described in section 2.3.5, however with smaller steps sizes than those typically used for diatom frustule measurements, due to the rapidly evolving interference pattern in the plane ca. 20-30 µm from the film surface.
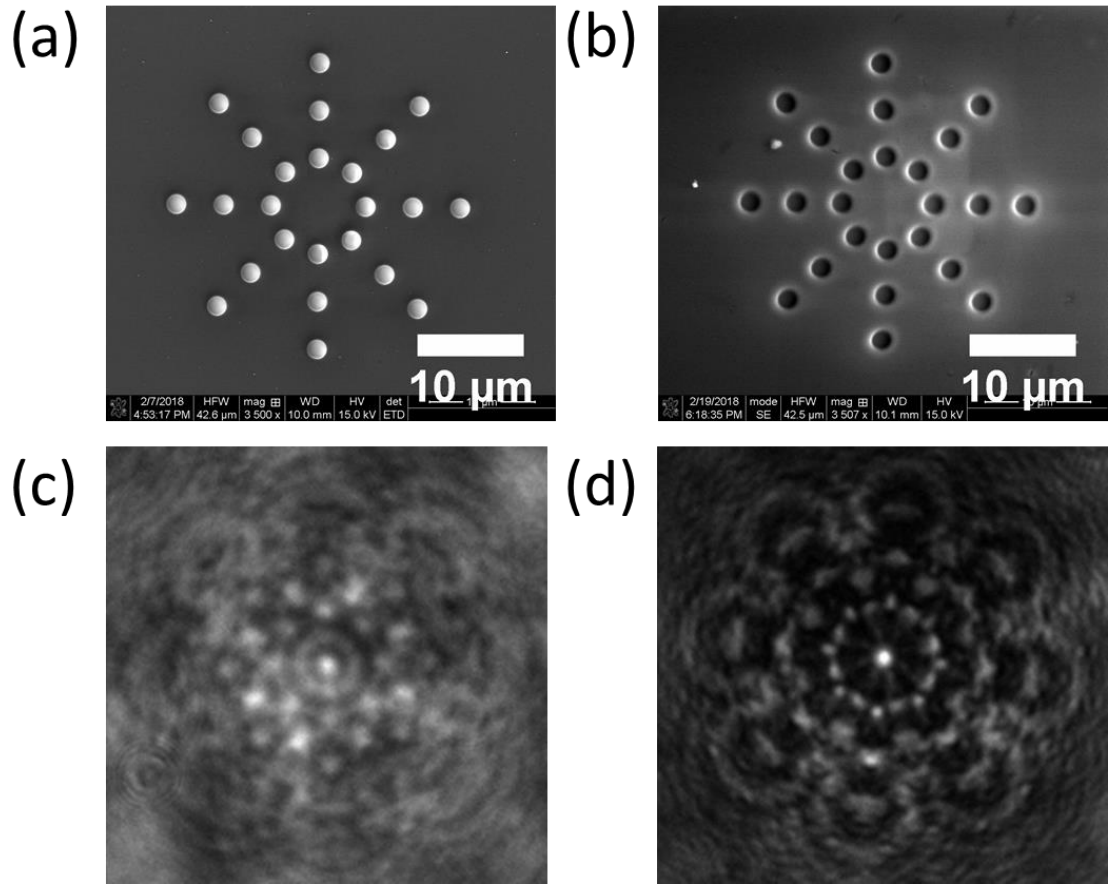
Figure 6.2. (a) SEM of standard pattern in silica thin film; (b) SEM of standard pattern in MgO/Si; (c) Far field image of silica interference pattern at 22 µm, λ = 550 nm; and (d) Far field image of MgO/Si standard pattern interference at 30 µm, λ = 550 nm. Images in "a" and "b" courtesy of Jiaqi Li, Sandhage Group, Purdue.

Results from these measurements are plotted in Figure 6.3 alongside the simulation results from section 5.4. Focal distances (typical focusing spot FWHM ca. 1.5 µm for all wavelengths) were found to decrease with increasing wavelength and the magnitude of the shift agreed well with simulation results (Table 6.1). For silica and MgO/Si experimental data, there was an appreciable offset in focusing distance toward larger values for most data points when compared to simulation. Particularly for MgO/Si, experimental values deviated more significantly from the theoretical trend at longer wavelengths. It was noted,

however, that some data points (i.e. 550 nm for silica and MgO/Si, and 950, 1050 nm for silica) agreed within the experimental margin of error,
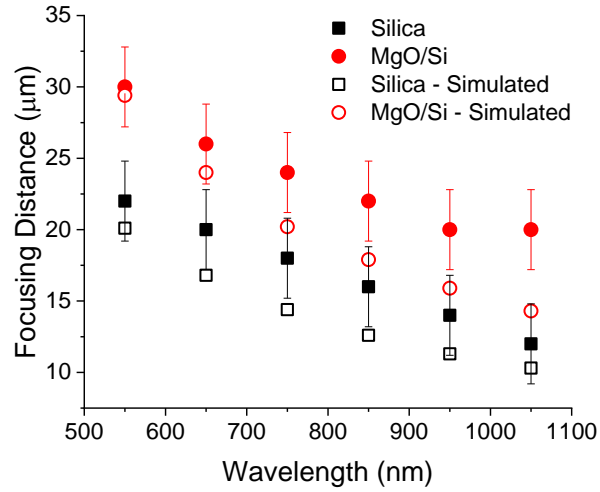
Figure 6.3. Measured and simulated focusing distance .vs. wavelength for silica and MgO/Si standardized patterns. Experimental error bars (±2.8 µm) were calculated based on error propagation analysis of uncertainty in actuator unidirectional repeatability (± 0.15 µm), starting position (±2.0 µm), and step size (±2.0 µm) while translating along the beam axis. Error simulated focusing distances taken to be ±50 nm, based on simulation step size in the Z-direction.

One of the largest contributors to this observation is likely the spectral bandwidth of the laser beams used for measurements, which have a range of incident frequencies compared to the purely monochromatic beam used in simulations. Depending on the broadness of the output peak, the index dispersion of the thin films over even a moderate wavelength range (± 50 nm) could shift the focusing distance away from the idealized value obtained via simulation. As shown in Figure 6.7, the output of the optical parametric amplifier (OPA) used in this study tends to broaden spectrally at NIR wavelengths. Additionally, because a transparent boundary condition is used during simulations, contributions from absorption and/or reflection at the air-film interface was omitted from

the description of this system. [179, 274] This may affect MgO/Si more than silica because of the greater optical density of MgO/Si in the visible and NIR. Additionally, a higher refractive index will increase reflectivity and potentially support lateral waveguide modes due to internal reflection, which could explain the generally greater discrepancy for the standardized pattern in MgO/Si. Another factor could be uncertainty in NIR refractive indices obtained from ellipsometry for MgO/Si that were used in simulations. As discussed in section 5.3.2, due to surface roughness and disruptive oscillations from the sapphire substrate, portions of the Ψ and Δ curves in the NIR were not fit as well as those in the visible and could cause a shift in the index and thus a similar shift in the simulated data points in that spectral region. Additionally, contributions from non-diffracted, transmitted light (i.e. differences in the phases of superimposed waves) could also contribute to this offset. These collective effects are also likely responsible for the observation of only one primary focal spot from measurements, whereas multiple foci, albeit less intense ones, are obtained from simulations (5.3.2).

Table 6.1. Tabulated data for measured focal distances of silica and MgO/Si standardized patterns and comparison of the percent difference in focal distance between measurements and simulations (from section 5.4.2).

λ (nm)	Measured Focal Distance SiO_2 (μm)[a]	Measured Focal Distance MgO/Si (μm)[a]	Measured Percent Difference (%)	Simulated Percent Difference (%)
550	22	30	31	38
650	20	26	26	35
750	18	24	29	34
850	16	22	32	35
950	14	20	35	34
1050	12	20	50	33

(a) Error in measured focal distances estimated to be $\pm$ 2.8 μm.

319

6.2.2.2   <u>Focusing Behavior of Natural Silica Diatom Frustules and Higher Index MgO/Si</u>

<u>and Mg$_2$Si Replicas in the Visible and Near Infrared</u>

Far field interference imaging was performed on five frustules of each type, i.e. native biosilica as well as MgO/Si and Mg$_2$Si replicas (listed in section 5.2.2.5-5.2.2.20 with large area images of the hole patterns and statistical analysis). Results from these measurements are plotted in Figure 6.4 where the average focusing distance for a given MgO/Si replica valve is noticeably longer than that from silica. From the discussion in section 5.4.2, this was attributed to the decrease in diffraction angle of wavelets exiting the foramen holes with increasing index. [270] Although there was no clear trend with regards to the spatial confinement of the focusing and wavelength, generally, FWHM of the foci were in the range of 1-2 µm. Similar results were found in studies of *C. wailessii* valves at visible wavelengths. [128] In terms of the valve's ability to concentrate light, this result shows that incident light on the diatom frustule was confined into an area ca. 1-2% of the diameter of the valve. [125]
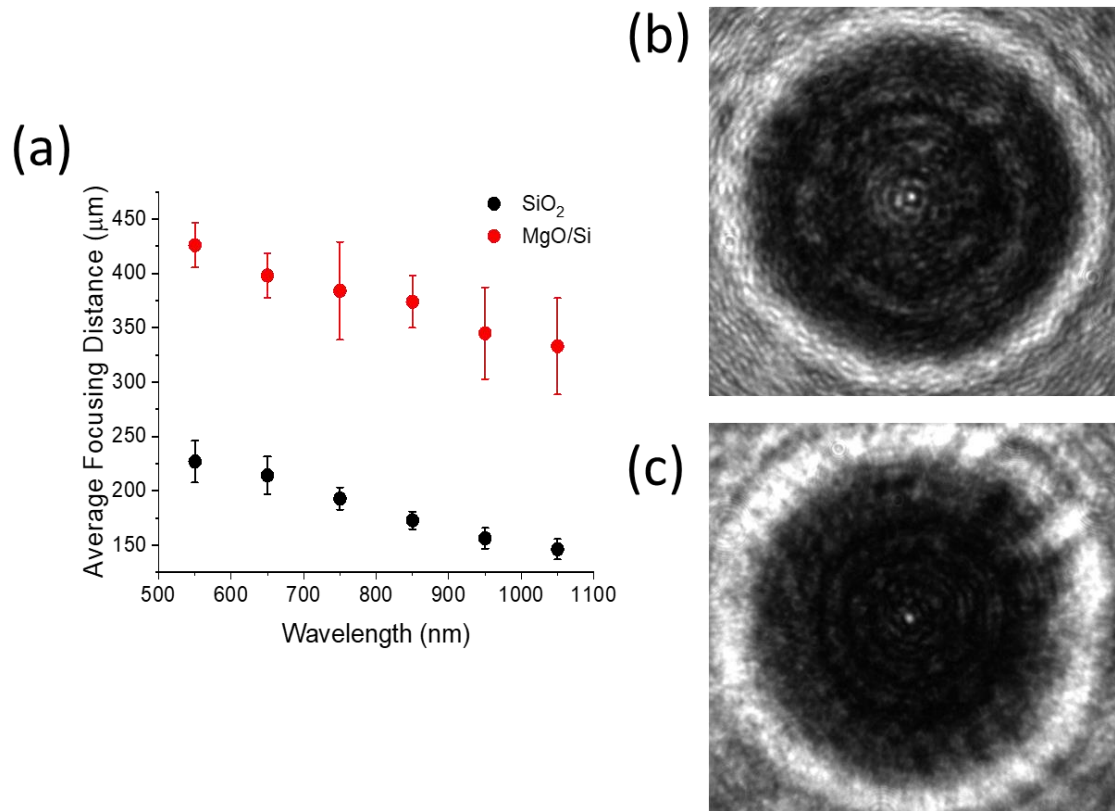
Figure 6.4. (a) Average focusing distance .vs. wavelength obtained from the arithmetic mean of five frustules for native silica and MgO/Si replicas for each material. Error bars calculated based on the standard deviation from each set; (b) Silica valve focusing at $\lambda = 650$ nm; and (c) MgO/Si replica focusing at $\lambda = 650$ nm.

The larger error bars for MgO/Si replicas compared to native silica valves are indicative of greater uncertainties in the quantification of the focusing distances at each wavelength, which are likely a combination of multiple factors. To elaborate, as one images further into the far field, the focusing patterns have lower S/N due to interference from debris, substrate defects, or other diffracting objects lying close to the valve. Further, the combination of decreased S/N and higher attenuation (Figure 5.43a) for MgO/Si replicas was found to reduce the contrast between the focal spots and the surrounding image, which further ambiguates the start and end points of a given focal point. Additionally, diatom-to-diatom variations in hole size and hole-to-hole distances can cause shifting in the observed

321

interference pattern. From section 5.2.2.20, hole size was not found to vary appreciably, but the ca. ± 10% spread in hole-to-hole distance could explain some error bars being as large as ± 13%.

The attenuation issue was exacerbated with Mg_2Si, for which systematic measurements could not be obtained, and is attributed to a simultaneous increase in optical density over the measured range (550-1050 nm) and a volume expansion in the thickness direction of each diatom layer upon complete conversion. Indeed, cross sectional SEM data provided by Jiaqi Li (Sandhage Group, Purdue) at different stages of conversion showed that a 30% increase in thickness occurs from the conversion of silica to MgO/Si and another 27% when converting MgO/Si to Mg_2Si.

Table 6.2. Tabulated focal distance data for natural silica valves and MgO/Si replicas; and the percent difference between these values at each wavelength.

λ (nm)	Measured Focal Distance SiO_2 (μm)	Measured Focal Distance MgO/Si (μm)	Percent Difference (%)
550	230 ± 19	430 ± 21	61
650	210 ± 17	400 ± 20	62
750	190 ± 10	380 ± 45	67
850	170 ± 8	370 ± 24	74
950	160 ± 9	350 ± 42	75
1050	150 ± 9	330 ± 44	75

As shown in Table 6.2, the percent difference between focal distances at a given wavelength between silica valves and MgO/Si replicas were, generally, nearly double what was found for the standardized hole patterns in Table 6.1. Given that hole radii and hole-to-hole distances were found to be consistent within ca. ± 10% (section 5.2.2.20) among the silica valves and MgO/Si replicas (5 samples each material), it is unlikely that diatom-to-diatom foramen hole pattern variations are solely responsible for this trend. This

suggests that the observed focusing pattern is not purely a function of the change in diffraction angle that comes with the index dispersion of each material and must be influenced by other structural components of the diatom valve. Building on the discussion in section 5.1.2, if one assumes that the inner layers of the valve have little-to-no diffractive contributions the focusing behavior, the only other source of diffraction would be that which comes from the circular edge of the frustule, referred to as Poisson-Arago (PA) diffraction (section 2.4.3) or Poisson's spot. [127, 175]

In work by Di Caprio *et al.* [174], the contribution from PA diffraction was investigated by reconstructing the phase profile of the interference pattern from natural *C. wailessii* valves holographically and was found not to have a significant constructive interference until further in the far field past where focusing is typically observed. These diatoms, however, were approximately double the diameter of the diatoms in this dissertation (ca. 90 µm) but possess hole sizes and hole-to-hole distance comparable to the valves discussed here, which likely limits the extrapolation of this explanation to the current samples. To elaborate, Poisson's spot is well-described by the Rayleigh-Sommerfeld diffraction model [172, 175, 176, 275] and has been shown to achieve 50% of its maximum intensity on the beam axis at a distance (z) equal to the radius (a) of the diffracting object (i.e. obeys the relation $1 = z / a$). For the diatoms in this work (radius ca. 45 µm) this means that Poisson's spot reaches 50% of its maximum intensity after only 45 µm of propagation, and 100% (following $4 = z / a$) at 180 µm. Due to appreciable constructive interference in this range, PA diffraction was suspected to have significant contributions to the interference pattern for the relatively smaller frustules and replicas studied here, which gave focal spots within or beyond this range (Figure 6.4 and Table

6.2). As such, the dramatic shift in focusing distance as a function of index for MgO/Si replicas could be explained by the wavelets from PA diffraction overlapping strongly with the wavelets from the foramen holes and destructively interfering in the plane near the diatom but then undergoing partial constructive interference further in the far field.
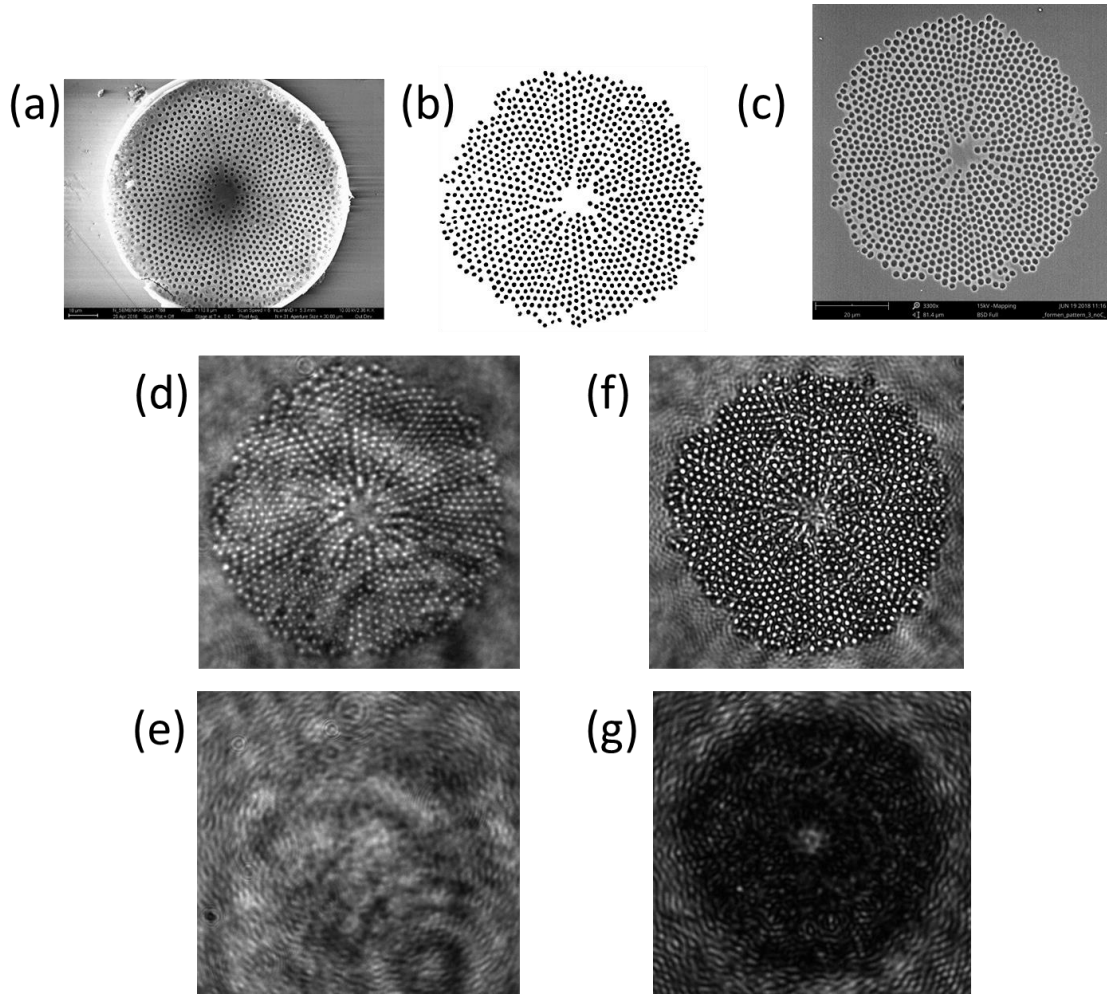
Figure 6.5. (a) SEM image of native silica diatom use for foramen hole pattern extraction – SEM by Nikolay Semenikhin, Sandhage Group, Georgia Tech; (b) Foramen hole pattern extracted from SEM image "a" via binarization – some manual editing done reshape or remove poorly shaped holes; (c) SEM of FIB milled foramen pattern "b" in a silica thin film – SEM by Jiaqi Li, Sandhage Group, Purdue; (d) 40x micrograph of foramen pattern in silica at focus $\lambda = 850$ nm; (e) Same pattern from "d" at 140 µm showing no little-to-no localized constructive interference at $\lambda = 850$ nm; (f) 40x micrograph of foramen pattern in MgO/Si at focus $\lambda = 850$ nm; (g) Same pattern from "f" at 125 µm showing some constructive interference but no clear focusing $\lambda = 850$ nm.

In testing the impact of edge diffraction on the interference pattern of a diatom-like hole array, two different foramen patterns were FIB milled into silica and MgO/Si thin films using hole patterns extracted via careful image processing (original and binary images for one shown in Figure 6.5a-b). Interference imaging of these samples demonstrated that, regardless of material identity, no unambiguous focusing was observed, opposite of what was found in reference [174]. This is shown in Figure 6.5d-g, where the interference pattern obtained from measurement was seemingly random and largely destructive in nature at distances from the plane of the film that typically provide focal spots for diatom valves made of the same material. This observation suggests that the pseudo-random hole patterns of the foramen layer are not conducive to strongly localized interference. To offer some evidence that this effect is dictated by the hole pattern and not related to random sources of error such as film thickness variations and or defects, focusing measurements were done on vogel patterns (Figure 6.6a) of similar diameter to foramen patterns FIB milled into a silica thin films, which possess a periodic hole pattern, albeit angular. Indeed, a focusing-like spot was found by vogel patterns in thin films of silica in the absence of a boundary (Figure 6.6c).
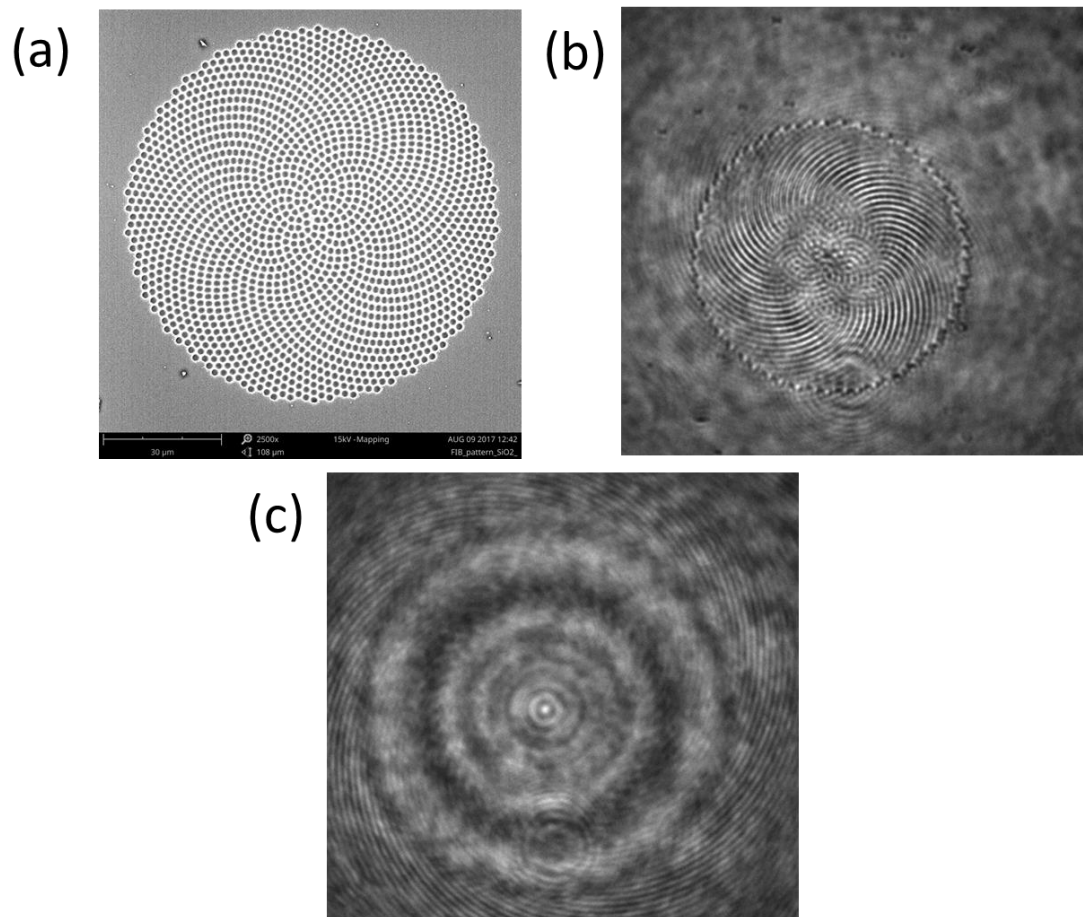
Figure 6.6. (a) SEM image of 1800 hole vogel pattern FIB milled into a silica thin film – SEM by Sunghwan Hwang, Sandhage Group, Purdue; (b) 40x micrograph of 1800 hole vogel pattern in focus at λ = 850 nm; (c) 40x micrograph of same pattern in "b" at 254 µm from film plane, showing bright focal spot in the center of the pattern surrounding by concentric rings.

Although this is not a quantitative measure of how periodicity influences focusing from diffractive hole arrays, this observation does support the argument that patterns with greater periodicity are more likely to provide the conditions for obtaining well-defined interference patterns that enable focusing-like behavior. Further, the lack of focusing from foramen hole arrays likely means that the contributions from PA diffraction the focusing behavior are more significant the previously anticipated for these smaller diameter valves and replicas. [127, 129, 174]

6.2.3 *Summary and Conclusions*

A study was presented comparing the experimental results from interference mapping measurements for silica diatom frustules, MgO/Si replicas, and synthetic patterns in thin films of silica and MgO/Si. Regarding the standardized patterns, reasonable agreement was found between the values expected from simulations and the actual decrease in focusing distance with wavelength, which matched closely with the refractive index dispersion over the 550-1050 nm wavelength range for patterns in silica and MgO/Si (Table 6.1). This trend, however, did not translate to natural silica frustules and MgO/Si replica valves where the increase in focusing distance as a function of index was found to be nearly twice that from standardized patterns (Table 6.2). Additionally, no clear focusing was observed for Mg_2Si replicas, which was primarily attributed to significant transmission losses. Computational hole mapping results from Chapter 5, showed that the standard deviations in the average hole radius and hole-to-hole distance over different diatom valves and different materials were reasonably small (within $\pm$ 10%) and thus diatom-to-diatom variations could not fully describe this discrepancy.

Having no evidence to suggest that diffraction from the inner layers of the frustules has any contribution to the observed interference pattern, this observed difference in focusing distance between silica and MgO/Si valves was attributed to PA diffraction potentially causing destructive interference at shorter distances away from the plane of the valve but partially interfering at further distances, making it appear as though the foci were located much further in the far field than previously anticipated. Also, as noted in section 5.2.2.21, the edge of the diatom can experience roughening over different stages of conversion (Figure 5.41). For more ideal-shaped spheres, edge roughness has been shown

to distort the interference profile obtained from PA diffraction. [176] In terms of Mg_2Si replicas, working under the assumption that PA diffraction contributes significantly to the observed interference patterns, the roughening experienced by some samples (Figure 5.41) would also explain why no clear focusing was observed for these replicas.

It is noted that BPM simulations were attempted for foramen patterns from silica valves and MgO/Si replicas, in a manner similar to that reported in references [127, 128, 276] and for the standardized patterns from section 5.4. However, results were not conclusive and thus are not reported in detail here. Like the shortcomings in the transparent boundary conditions discussed with the standardized samples, the ambiguity in the results from these simulations is tentatively ascribed to improperly accounting for the non-transmissive light-matter interactions at the interface in the presence of a large number of holes and with much thicker films (foramen thickness estimated to be 900 nm, compared to ca. 200 nm for thin films). Additionally, the possibility for waveguiding within the hole-bearing silica slab (i.e. the mode propagates in the X-Y direction) making up the foramen may not be accurately accounted for in the current BPM framework, which could also contribute to simulation consistency issues. [277, 278]

Native frustules and MgO/Si replicas ca. 90 µm in diameter were found to concentrate light into circular areas approximately 1-2 µm wide. Compared to state-of-the-art objectives and metalenses [107, 115], the spot size of the typical focal spot from diatoms is approximately twice the diameter in a similar wavelength range. Additionally, even silica diatoms show some absorption-related attenuation in the visible, which is only worsened in MgO/Si, and Mg_2si replicas with higher optical density in the visible and NIR and likely results in poor focusing efficiency as described in Khorasaninejad *et al*. [107]. Further,

there is limited experimental evidence regarding the ability for diatoms to preserve the polarization of the incident beam. [174, 276] These present drawbacks in terms of using diatoms or diatom-like structures for imaging applications, but there is still the possibility for using these in applications where only localized intensity is desired and nonuniform beam quality is not critical.

6.2.4 *Experimental Details*

6.2.4.1 Far Field Interference Imaging

Far field interference imaging was accomplished using a custom-built, modular microscope system (described in section 2.3.5) for which the light source was a TOPAS-C OPA (pulse widths typically <100 fs) pumped by a regeneratively amplified femtosecond system at 795 nm (Solstice, Spectraphysics, pulse widths typically <90 fs, repetition rate 1 kHz). All samples were measured at 550, 650, 750, 860, 950, and 1050 nm. For some wavelengths, the internal motors controlling the angles of the nonlinear crystals for the TOPAS-C were adjusted to obtain output at the desired wavelength and spectral narrowness. All measurements were done at a vertical polarization. Prior to arriving at the sample, the incoming beam is attenuating with neutral density filters to limit the power going through the objective to approximately a few milliwatts to avoid damaging the objective. To achieve the best contrast and S/N, a 200 µm aperture was placed before the sample to limit the illumination area to the area specifically around the features of interest. The stage for moving the sample was mounted on a 460P-XYZ stage (Newport) with 1.00 ich travel, with TRA25PPD actuators (Newport) and controlled by an ESP300 Motion Controller (Newport) via LabVIEW. Since the sample needed to be held vertically but still

allow optical beams through, the center of the sample holder was a coverslip bearing a

PDMS (high transmission at optical wavelengths) film on which the sample could stick.

Imaging was done using a 40x objective (Olympus, UPlanFLN, NA = 0.75, WD = 0.5 mm)

and a Lumera Infinity 2 CCD camera.

    Measurements for standardized patterns were carried out by finding the focal plane

for the hole arrays at a certain wavelength, maximizing the brightness registered in the

image to ensure even illumination, and then gradually translating the sample 2 µm away

from the objective toward the far field; taking pictures at each step. Interference imaging

of synthetic foramen hole arrays, natural diatoms, and high index replicas were done

similarly, however, because the interference patter did not evolve as rapidly as the

standardized pattern, a step size of 5 µm was used. Image were taken until 2-3 unambiguous

foci and their positions of appearance along the beam axis were identified.
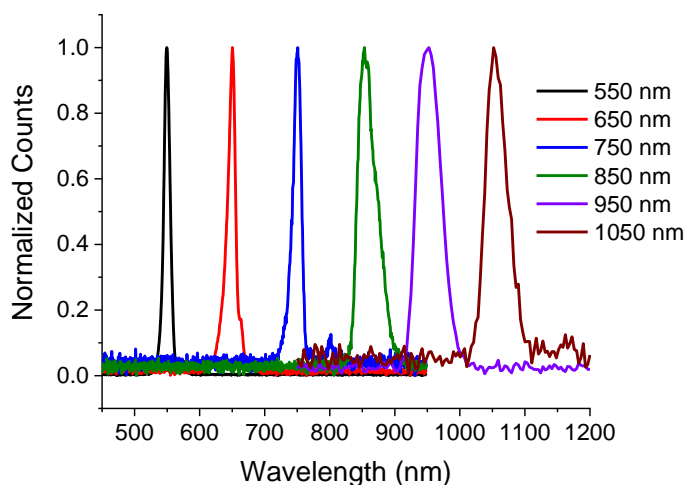
Figure 6.7. Plot of spectra output for TOPAS-C OPA 550 nm (FWHM: 11 nm), 650 nm (FWHM 13 nm), 750 nm (FWHM: 16 nm), 860 nm (FWHM: 35 nm), 950 nm (FWHM 43 nm), and 1050 nm (FHWM: 62 nm).

6.2.4.2 Focused Ion Beam (FIB) Milling of Synthetic Patterns

FIB milling of synthetic patterning was achieved by first obtaining high quality binarized images for the patterns of interest. For naturally-derived diatom patterns, this was accomplished by binarizing the high contrast SEM images in Matlab and then manually cleaning up the image (i.e. removing noise, removing odd shaped holes, filling in holes not picked up well by binarization) in ImageJ. This pattern is imported into FIB machine and milled into film using a FEI Quanta 3D FEG Dual-beam SEM (Purdue) with an accelerating voltage of 30 kV and ion beam current of 3 nA. FIB milling performed by Sunghwan Hwang and Jiaqi Li, Sandhage Group, Purdue.

6.2.4.3 Preparation of Silica, MgO/Si, and Mg_2Si Thin Films

The following procedure is courtesy of Jiaqi Li, Sandhage group, Purdue. Sol formation begins by adding 5 mL of tetraethylorthosilicate (TEOS) drop-wise into 5 mL ethanol (200 proof) and stirring well to ensure mixing. 0.81 mL of DI H_2O is added, followed by 0.81 mL of 0.1 M HCl. This solution was refluxed at 70 ^{o}C for 2 hours with stirring. Separately, an aqueous 22% wt methycellulose (MC) solution is made by stirring 287.4 mg MC in 14.1 mL DI H_2O for 2 hours. The TEOS and MC solutions are then mixed to obtain a 2% wt final sol-gel solution, which is stirred for 30 hours at room temperature.

Prior to spin coating, sapphire wafers (University wafer) are cut into 1x1 cm^2 squares, then cleaned by ozone, washed with water, and dried with nitrogen. On the spin coating chuck, the MC+TEOS solution is dripped (4-5 drops) onto the substrate and spun at 3000 RPM for 20 seconds. After spinning, the film is aged overnight at room temperature and then dried in a vacuum oven at 60 ^{o}C for 30 min. The as-dried film is then fired in air at

700 °C fir 15 min (ramping/cooling temperature 2 °C/min). In converting silica films to MgO/Si, the silica films on sapphire substrates are reacted with Mg vapor using Mg$_2$Si granules as the gas source at 750 °C for 6 hours with carrier glass a mixture of H$_2$ and Ar, and a low-carbon steel ampoule. Between MgO/Si and Mg$_2$Si, the MgO is dissolved by 3M HCl for 30 min inside an Ar-purged glovebox to yield porous silicon films. These silicon films are then reaction with Mg gas (Mg foil as gas source) at 600 °C for 4 hours in a stainless-steel tube with carrier gas mixture of H$_2$ and Ar. Thicknesses were confirmed by cross-sectional SEM.

6.3   Chapter Summary

In this chapter, interference imaging measurements on standardized patterns, native silica valves, and high index replicas were performed in an effort to quantify the impact of hole pattern arrangements and refractive indices on the focusing behavior of these biophotonic systems. As anticipated, all samples measured showed a decrease in focusing distance with an increase in wavelength and an increase in focusing distance with an increase in refractive index. [128, 170, 270] In reference to simulations, the change in focusing distance for standardized patterns matched reasonably well with simulations, although experimental values were offset to larger values. Though the exact cause of this discrepancy was unclear, a discussion of uncertainties and inconsistencies from an experimental and theoretical perspective was provided regarding the many factors that control the agreement with simulations and measurements while maintaining physical consistency. From these measurements, ideally, the focusing distance should decrease with increasing wavelength at a rate that is controlled by the dispersion of the refractive index of that material. This result was achievable because of the precise control over the

simplified hole array that was patterned into different materials to maximize consistency and eliminate errors associated with hole pattern reproducibility. Additionally, this was facilitated by ellipsometry measurements and modeling, discussed in section 5.3.

For natural silica valves and MgO/Si replicas, the increase in focusing distance with refractive index was greater than that seen in the standardized patterns. Given that no significant deviations in hole size (radius) and hole-to-hole distance were found (within ± 10%) based on the average of these quantities from several diatoms in Chapter 5, the dramatic increase in focusing distance could not be directly ascribed to changes in index nor hole pattern variations between sets of diatoms. As such, an argument was presented to suggest that diffraction originating from the edge of the diatom, known as Poisson-Arago diffraction, could contribute more significantly to the interference pattern than previous anticipated. To test this hypothesis, interference imaging was done on synthetic foramen hole patterns in silica and MgO/Si films (no edge present), which did not yield any unambiguous focusing. On the other hand, vogel patterns, with angular periodicity, were found to give focal spots in silica thin films, indicating that the pseudo-randomness of the foramen patterns was not conducive to concentrating wavelets and achieving localized constructive interference.

This result was in qualitative disagreement with the literature [174], however, the valves studied in that work were approximately twice as large as the valves studied here. Consequently, the distance from the valve at which constructive interference from PA diffraction becomes significant is longer in the literature study than the frustules examined in this dissertation. As predicted by the Rayleigh-Sommerfield diffraction model, the PA diffraction could overlap significantly with wavelets originating from the foramen hole

patterns as close as 45 µm away from the valve plane, well before focal spots are observed experimentally. [175]

Although further experiments are necessary to confirm the degree to which PA diffraction may contribute to these interference patterns, the results presented here provide a detailed initial study into the complex interference effects that diatom frustules afford and how their optical properties can be changed by hole pattern alterations and changes in refractive index such that favorable focusing properties in the NIR can be obtained. In terms of a diatom valve's ability to concentrate light, the observed spatial confinement was appreciable (1-2 µm) considering most diatoms were ca. 90 µm in diameter. However, compared to state-of-the-art objectives and metalenses, the circular focal spots obtained here are approximately twice as large and the focusing efficiency is low (currently not quantifiable) due to absorption losses and scattering from debris and other surface defects. [107] As such, the utility for diatoms as imaging lenses is likely limited but could possibly be useful for other applications where focal spot quality is not critical and control over polarization and phase is not required.

6.4 References

107.   Khorasaninejad, M., Chen, W.T., Devlin, R.C., Oh, J., Zhu, A.Y., and Capasso, F., *Metalenses at visible wavelengths: Diffraction-limited focusing and subwavelength resolution imaging.* Science, 2016. **352**(6290): p. 1190-1194.

115.   Khorasaninejad, M., Shi, Z., Zhu, A.Y., Chen, W.T., Sanjeev, V., Zaidi, A., and Capasso, F., *Achromatic Metalens over 60 nm Bandwidth in the Visible and Metalens with Reverse Chromatic Dispersion.* Nano Letters, 2017. **17**(3): p. 1819-1824.

125.   De Tommasi, E., De Luca, A.C., Lavanga, L., Dardano, P., De Stefano, M., De Stefano, L., Langella, C., Rendina, I., Dholakia, K., and Mazilu, M., *Biologically enabled sub-diffractive focusing.* Optics Express, 2014. **22**(22): p. 27214-27227.

127. Stefano, L.D., Rea, I., Rendina, I., Stefano, M.D., and Moretti, L., *Lensless light focusing with the centric marine diatom Coscinodiscus walesii.* Optics Express, 2007. **15**(26): p. 18082-18088.

128. De Tommasi, E., Rea, I., Mocella, V., Moretti, L., De Stefano, M., Rendina, I., and De Stefano, L., *Multi-wavelength study of light transmitted through a single marine centric diatom.* Optics Express, 2010. **18**(12): p. 12203-12212.

129. Romann, J., Valmalette, J.-C., Chauton, M.S., Tranell, G., Einarsrud, M.-A., and Vadstein, O., *Wavelength and orientation dependent capture of light by diatom frustule nanostructures.* Scientific Reports, 2015. **5**: p. 17403.

170. Hecht, E. and Ganesan, A.R., *Diffraction*, in *Optics*. 2002, Pearson: New York, USA. p. 420-480.

172. Hecht, E. and Ganesan, A.R., *Interference*, in *Optics*. 2002, Pearson: New York, USA. p. 366-416.

174. Di Caprio, G., Coppola, G., Stefano, L.D., Stefano, M.D., Antonucci, A., Congestri, R., and Tommasi, E.D., *Shedding light on diatom photonics by means of digital holography.* Journal of Biophotonics, 2014. **7**(5): p. 341-350.

175. Robert, L.L., *Rayleigh–Sommerfeld diffraction and Poisson's spot.* European Journal of Physics, 2006. **27**(2): p. 193.

176. Harvey, J.E. and Forgham, J.L., *The spot of Arago: New relevance for an old phenomenon.* American Journal of Physics, 1984. **52**(3): p. 243-247.

179. Hadley, G.R., *Transparent boundary condition for the beam propagation method.* IEEE Journal of Quantum Electronics, 1992. **28**(1): p. 363-370.

270. Wang, X., Fu, J., Liu, X., and Tong, L.-M., *Subwavelength focusing by a micro/nanofiber array.* Journal of the Optical Society of America A, 2009. **26**(8): p. 1827-1833.

274. Hadley, G.R., *Transparent boundary condition for beam propagation.* Optics Letters, 1991. **16**(9): p. 624-626.

275. Harvey, J.E., Forgham, J.L., and Bieren, K.V. *The Spot Of Arago And Its Role In Wavefront Analysis*. in *26th Annual Technical Symposium*. 1983. SPIE.

276. Ferrara, M.A., Dardano, P., De Stefano, L., Rea, I., Coppola, G., Rendina, I., Congestri, R., Antonucci, A., De Stefano, M., and De Tommasi, E., *Optical Properties of Diatom Nanostructured Biosilica in Arachnoidiscus sp: Micro-Optics from Mother Nature.* PLoS One, 2014. **9**(7): p. e103750.

277. Fuhrmann, T., Landwehr, S., El Rharbi-Kucki, M., and Sumper, M., *Diatoms as living photonic crystals.* Applied Physics B, 2004. **78**(3): p. 257-260.

278. Polini, A., Pagliara, S., Camposeo, A., Cingolani, R., Wang, X., Schröder, H.C., Müller, W.E.G., and Pisignano, D., *Optical properties of in-vitro biomineralised silica.* Scientific Reports, 2012. **2**: p. 607.

CHAPTER 7. CONCLUSIONS AND FUTURE OUTLOOK

7.1 Comments on Chapter 3

The work in this chapter presented advances in understanding the influence of judicious bulky substitution on the linear and NLO properties of chalcogenopyrylium-terminated heptamethine dyes in solution and solid-state. A set of thio- and selenopyrylium dyes demonstrated satisfactory 2PA-FOMs ($|Re(\chi^{(3)})/ Im(\chi^{(3)})| \geq 12$) and linear loss (ca. 4 dB cm^{-1}) in neat and APC blend films and thus present an opportunity for demonstrating AOSP with improved performance over previous studies of anionic heptamethines with comparable values of $|Re(\chi^{(3)})|$ but much lower 2PA-FOMs. [29] However, film processing work detailed in section 3.4 showed that the lack of adhesion and mechanical strength for APC likely makes it an inadequate host for device-fabrication when blended with a thiopyrylium dye, although surface modification with APC-like groups made some improvements in this regard.

Despite the success found with a 50% wt thiopyrylium dye blend in PMMA, the processing methods in this dissertation are not optimal as higher concentrations (loading percentage) and better film quality can be achieved. This presents a significant opportunity to improve the NLO performance of these blends and demonstrate disruptive all-optical switching based on SOH-devices with low linear loss (ca. ≤ 1 dB cm^{-1}). [23] Based on the results from section 3.2, thiopyryliums (**Ib** and **If**) and selenopyryliums (**Ij** and **Io**) are attractive candidate materials for such studies. Another opportunity in this area is to pair these cationic chalcogenopyrylium dyes with anionic polymethines as shown by Li *et al.* [279] , which can offer some control over aggregation and increase the overall number

density of polymethines in the solid-state. Further, Li et al. [280] and others [281] have shown that changing the host environment to have more ionic character is another pathway to control aggregation and increase miscibility in the solid state. Furthermore, this could substantially improve linear loss and the maximum achievable dye loading percentage before phase separation occurs as well as potentially enhance NLO response.

7.2 Comments on Chapter 4

Spectroscopic measurements in chloroform solutions revealed that a series of fused-ring, quadrupolar A-π-D-π-A chromophores demonstrated large 2PA cross sections in the NIR. Although the values of δ at the 2PA maximum were comparable to some discrete porphyrins and small porphyrin oligomers, they did not surpass those found for larger, more delocalized porphyrin oligomers at similar excitation wavelengths. [226, 227, 252, 253] Outside of the obvious strategy to increase the acceptor strength, more molecular engineering pathways are available to tune the 2PA response of these materials to achieve even larger and further red-shifted 2PA. In the series F6IC, F8IC, and F10IC, the presence of additional thiophenes in the core, compared to the indacene-based compounds, resulted in large increases for δ and substantial red-shifted 1PA and 2PA; highlighting the impact that heteroatoms can have on the optical properties of these compounds. This effect can be extended by substituting larger heteroatoms (Se and Te) to further reduce transition energies and enhance charge transfer, similar to what was shown by Liu *et al*. [282] and Rath *et al*. [283] for aza-BODIPY and porphyrin compounds, respectively. Furthermore, the influence of isomerization, such as that studied by Wang et al. [235], for heteroatom-containing rings could be an altnerate pathway for optimizing 2PA behavior. Additionally, numerous studies have shown that the addition of the appropriate donor or acceptor group

338

on the center ring of a π-conjugated bridge can significantly enhance charge transfer. [83, 85, 105, 235] This can be applied to indacene compounds by substituting strong donor groups on the central ring of the core to facilitate greater charge transfer from the donor core to the acceptor groups at the molecule's edge. In terms of film processability, the out-of-plane groups (R, Figure 7.1) can be modified to change solubility and crystallinity. [284]
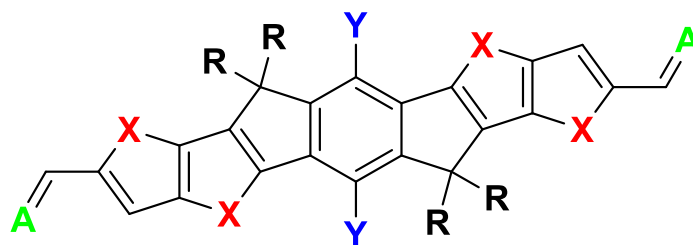

Figure 7.1. Example structure of a fused-7-ring core showing sites for synthetic modification. Red X's are sites for heteroatoms, blue Y's are sites to attached donor groups, green A's are acceptor end groups, and black R's are out-of-plane groups.

7.3   Comments on Chapters 5-6

Although there is still much to learn about the complex optical behavior of diatoms, the theoretical and experimental work in these chapters presented incremental advances in understanding the origin of these phenomena and how changing the index of these frustules can inform the design of higher refractive index, inorganic, microphotonic elements operating at visible and NIR wavelengths. As naturally-derived, lensless focusing microsctructures, diatoms do not achieve the same efficiency and polarization control as man-made metastructure arrays, but they do enable light concentration within 1-2 µm diameter focal areas and can be harvested renewably at large scales. [107, 115, 130] As such, diatom valves are likely not useful for imaging applications but could find success as light concentrators for optofluidic applications utilizing microfluorescence where the phase

and beam profile are not critical but delivery of moderately intense light beams to micron-sized areas is highly desired. [95, 108, 285, 286] Further, significant efforts have been put into mapping the genome for diatoms, which opens up the possibility for controlling structural features such as hole size and spacing in the foramen layers for *C. wailessii* valves. [124]

7.4   References

23.   Koos, C., Vorreau, P., Vallaitis, T., Dumon, P., Bogaerts, W., Baets, R., Esembeson, B., Biaggio, I., Michinobu, T., Diederich, F., Freude, W., and Leuthold, J., *All-optical high-speed signal processing with silicon–organic hybrid slot waveguides.* Nature Photonics, 2009. **3**: p. 216.

29.   Li, Z.a., Liu, Y., Kim, H., Hales, J.M., Jang, S.-H., Luo, J., Baehr-Jones, T., Hochberg, M., Marder, S.R., Perry, J.W., and Jen, A.K.-Y., *High-Optical-Quality Blends of Anionic Polymethine Salts and Polycarbonate with Enhanced Third-Order Non-linearities for Silicon-Organic Hybrid Devices.* Advanced Materials, 2012. **24**(44): p. OP326-OP330.

83.   Albota, M., Beljonne, D., Brédas, J.-L., Ehrlich, J.E., Fu, J.-Y., Heikal, A.A., Hess, S.E., Kogej, T., Levin, M.D., Marder, S.R., McCord-Maughon, D., Perry, J.W., Röckel, H., Rumi, M., Subramaniam, G., Webb, W.W., Wu, X.-L., and Xu, C., *Design of Organic Molecules with Large Two-Photon Absorption Cross Sections.* Science, 1998. **281**(5383): p. 1653.

85.   Rumi, M., Ehrlich, J.E., Heikal, A.A., Perry, J.W., Barlow, S., Hu, Z., McCord-Maughon, D., Parker, T.C., Röckel, H., Thayumanavan, S., Marder, S.R., Beljonne, D., and Brédas, J.-L., *Structure−Property Relationships for Two-Photon Absorbing Chromophores: Bis-Donor Diphenylpolyene and Bis(styryl)benzene Derivatives.* Journal of the American Chemical Society, 2000. **122**(39): p. 9500-9510.

95.   Göppert-Mayer, M., *Über Elementarakte mit zwei Quantensprüngen.* Annalen der Physik, 1931. **401**(3): p. 273-294.

105.   Pond, S.J.K., Rumi, M., Levin, M.D., Parker, T.C., Beljonne, D., Day, M.W., Brédas, J.-L., Marder, S.R., and Perry, J.W., *One- and Two-Photon Spectroscopy of Donor−Acceptor−Donor Distyrylbenzene Derivatives: Effect of Cyano Substitution and Distortion from Planarity.* The Journal of Physical Chemistry A, 2002. **106**(47): p. 11470-11480.

107. Khorasaninejad, M., Chen, W.T., Devlin, R.C., Oh, J., Zhu, A.Y., and Capasso, F., *Metalenses at visible wavelengths: Diffraction-limited focusing and subwavelength resolution imaging.* Science, 2016. **352**(6290): p. 1190-1194.

108. Erickson, D., Sinton, D., and Psaltis, D., *Optofluidics for energy applications.* Nature Photonics, 2011. **5**: p. 583.

115. Khorasaninejad, M., Shi, Z., Zhu, A.Y., Chen, W.T., Sanjeev, V., Zaidi, A., and Capasso, F., *Achromatic Metalens over 60 nm Bandwidth in the Visible and Metalens with Reverse Chromatic Dispersion.* Nano Letters, 2017. **17**(3): p. 1819-1824.

124. Hildebrand, M., *Diatoms, Biomineralization Processes, and Genomics.* Chemical Reviews, 2008. **108**(11): p. 4855-4874.

130. Hildebrand, M., Davis, A.K., Smith, S.R., Traller, J.C., and Abbriano, R., *The place of diatoms in the biofuels industry.* Biofuels, 2012. **3**(2): p. 221-240.

226. Kurotobi, K., Kim, K.S., Noh, S.B., Kim, D., and Osuka, A., *A Quadruply Azulene-Fused Porphyrin with Intense Near-IR Absorption and a Large Two-Photon Absorption Cross Section.* Angewandte Chemie, 2006. **118**(24): p. 4048-4051.

227. Yoon, M.-C., Noh, S.B., Tsuda, A., Nakamura, Y., Osuka, A., and Kim, D., *Photophysics of meso-β Doubly Linked Ni(II) Porphyrin Arrays: Large Two-Photon Absorption Cross-Section and Fast Energy Relaxation Dynamics.* Journal of the American Chemical Society, 2007. **129**(33): p. 10080-10081.

235. Wang, J., Zhang, J., Xiao, Y., Xiao, T., Zhu, R., Yan, C., Fu, Y., Lu, G., Lu, X., Marder, S.R., and Zhan, X., *Effect of Isomerization on High-Performance Nonfullerene Electron Acceptors.* Journal of the American Chemical Society, 2018. **140**(29): p. 9140-9147.

252. Ahn, T.K., Kwon, J.H., Kim, D.Y., Cho, D.W., Jeong, D.H., Kim, S.K., Suzuki, M., Shimizu, S., Osuka, A., and Kim, D., *Comparative Photophysics of [26]- and [28]Hexaphyrins(1.1.1.1.1.1): Large Two-Photon Absorption Cross Section of Aromatic [26]Hexaphyrins(1.1.1.1.1.1).* Journal of the American Chemical Society, 2005. **127**(37): p. 12856-12861.

253. Drobizhev, M., Stepanenko, Y., Rebane, A., Wilson, C.J., Screen, T.E.O., and Anderson, H.L., *Strong Cooperative Enhancement of Two-Photon Absorption in Double-Strand Conjugated Porphyrin Ladder Arrays.* Journal of the American Chemical Society, 2006. **128**(38): p. 12432-12433.

279. Li, Z.a., Mukhopadhyay, S., Jang, S.-H., Brédas, J.-L., and Jen, A.K.Y., *Supramolecular Assembly of Complementary Cyanine Salt J-Aggregates.* Journal of the American Chemical Society, 2015. **137**(37): p. 11920-11923.

280. Li, Z.a., Ensley, T.R., Hu, H., Zhang, Y., Jang, S.-H., Marder, S.R., Hagan, D.J., Van Stryland, E.W., and Jen, A.K.-Y., *Conjugated Polycyanines: A New Class of Materials with Large Third-Order Optical Nonlinearities.* Advanced Optical Materials, 2015. **3**(7): p. 900-906.

281. Harrison, W.J., Mateer, D.L., and Tiddy, G.J.T., *Liquid-Crystalline J-Aggregates Formed by Aqueous Ionic Cyanine Dyes.* The Journal of Physical Chemistry, 1996. **100**(6): p. 2310-2321.

282. Liu, X., Zhang, J., Li, K., Sun, X., Wu, Z., Ren, A., and Feng, J., *New insights into two-photon absorption properties of functionalized aza-BODIPY dyes at telecommunication wavelengths: a theoretical study.* Physical Chemistry Chemical Physics, 2013. **15**(13): p. 4666-4676.

283. Rath, H., Sankar, J., PrabhuRaja, V., Chandrashekar, T.K., Nag, A., and Goswami, D., *Core-Modified Expanded Porphyrins with Large Third-Order Nonlinear Optical Response.* Journal of the American Chemical Society, 2005. **127**(33): p. 11608-11609.

284. Lin, Y., Zhao, F., He, Q., Huo, L., Wu, Y., Parker, T.C., Ma, W., Sun, Y., Wang, C., Zhu, D., Heeger, A.J., Marder, S.R., and Zhan, X., *High-Performance Electron Acceptor with Thienyl Side Chains for Organic Photovoltaics.* Journal of the American Chemical Society, 2016. **138**(14): p. 4955-4961.

285. Lin, S.-W., Chang, C.-H., and Lin, C.-H., *High-throughput Fluorescence Detections in Microfluidic Systems.* Genomic Medicine, Biomarkers, and Health Sciences, 2011. **3**(1): p. 27-38.

286. Lim, J., Gruner, P., Konrad, M., and Baret, J.-C., *Micro-optical lens array for fluorescence detection in droplet-based microfluidics.* Lab on a Chip, 2013. **13**(8): p. 1472-1475.